



UNIVERZA V LJUBLJANI
FAKULTETA ZA MATEMATIKO IN FIZIKO

DOKTORSKA DISERTACIJA

Peter Smerkol

2013



UNIVERSITY OF LJUBLJANA
FACULTY OF MATHEMATICS AND PHYSICS
DEPARTMENT OF PHYSICS

Peter Smerkol

MEASUREMENT OF CP VIOLATION PARAMETER
 \mathcal{A}_{CP} IN WEAK DECAYS OF CHARMED BARYONS
 Λ_c WITH THE BELLE DETECTOR

Doctoral Thesis

ADVISER: Prof. Dr. Boštjan Golob

LJUBLJANA, 2013



UNIVERZA V LJUBLJANI
FAKULTETA ZA MATEMATIKO IN FIZIKO
ODDELEK ZA FIZIKO

Peter Smerkol

MERITEV PARAMETRA KRŠITVE SIMETRIJE CP
(\mathcal{A}_{CP}) PRI ŠIBKIH RAZPADIH ČAROBNIH
BARIONOV Λ_c Z DETEKTORJEM BELLE

Doktorska Disertacija

MENTOR: Prof. Dr. Boštjan Golob

LJUBLJANA, 2013

POVZETEK

V delu je predstavljena meritev parametrov šibke asimetrije α_{Λ_c} in kršitve simetrije CP \mathcal{A}_{CP} za razpade $\Lambda_c \rightarrow \Lambda\pi$. Analiza je narejena na vzorcu z integrirano luminoznostjo 785 fb^{-1} , zbranim z detektorjem Belle na asimetričnem trkalniku e^+e^- KEKB. Naša metoda meritve je zasnovana tako, da najprej izmerimo povprečni parameter šibke asimetrije za združena vzorca razpadov Λ_c^+ in $\bar{\Lambda}_c^-$, nato pa z uporabo te vrednosti določimo parameter kršitve simetrije CP. Dobljena rezultata sta ob privzeti izmerjeni kršitvi simetrije CP v razpadu $\Lambda \rightarrow p\pi$ [1] enaka $|\langle\alpha_{\Lambda_c}\rangle| = 0.964 \pm 0.014(\text{stat.}) \pm 0.033(\text{syst.})$ in $\mathcal{A}_{CP}^{\Lambda_c} = -0.012 \pm 0.010(\text{stat.}) \pm 0.022(\text{syst.})$, ob predpostavki, da v razpadu $\Lambda \rightarrow p\pi$ kršitve simetrije CP ni, pa sta enaka $|\langle\alpha_{\Lambda_c}\rangle| = 0.958 \pm 0.014(\text{stat.}) \pm 0.025(\text{syst.})$ in $\mathcal{A}_{CP}^{\Lambda_c} = -0.006 \pm 0.010(\text{stat.}) \pm 0.005(\text{syst.})$.

Ključne besede:

detektor Belle, kršitev simetrije CP, čarobni barioni

PACS:

14.20.Lq (Barioni z kvarkom c)

13.30.Eg (Hadronski razpadi barionov)

11.30.Er (CP invariantnost)

ABSTRACT

We present measurements of the weak asymmetry parameter α_{Λ_c} and the CP-violating parameter $\mathcal{A}_{\text{CP}}^{\Lambda_c}$ for the $\Lambda_c \rightarrow \Lambda\pi$ decay. The measurement is based on a 785 fb^{-1} data sample recorded with the Belle detector at the KEKB asymmetric-energy e^+e^- collider. We use a method based on first measuring the average weak asymmetry parameter for joined Λ_c^+ and $\bar{\Lambda}_c^-$ decays and then using this value to measure the CP-violating parameter, and we find $|\langle\alpha_{\Lambda_c}\rangle| = 0.964 \pm 0.014(\text{stat.}) \pm 0.033(\text{syst.})$ and $\mathcal{A}_{\text{CP}}^{\Lambda_c} = -0.012 \pm 0.010(\text{stat.}) \pm 0.022(\text{syst.})$ assuming the measured CP-violation in the $\Lambda \rightarrow p\pi$ decay [1], or $|\langle\alpha_{\Lambda_c}\rangle| = 0.958 \pm 0.014(\text{stat.}) \pm 0.025(\text{syst.})$ and $\mathcal{A}_{\text{CP}}^{\Lambda_c} = -0.006 \pm 0.010(\text{stat.}) \pm 0.005(\text{syst.})$ assuming no CP-violation in the $\Lambda \rightarrow p\pi$ decay.

Keywords:

the Belle detector, CP violation, charmed baryons

PACS:

14.20.Lq (Charmed baryons)

13.30.Eg (Hadronic decays of baryons)

11.30.Er (CP invariance)

ZAHVALA

Najprej gre zahvala mentorju Boštjanu Golobu za ravno pravšnjo mešanico usmerjanja, kritičnih pripomb in dobre volje. Brez njegovega znanja in izkušenj mi tega doktorskega dela ne bi uspelo dokončati.

Posebej se moram zahvaliti še Marku Petriču, Marku Stariču in Marku Bračku za vse razlage in neskončne diskusije, ki so pomagale razjasniti še tako zapleten problem.

K delu so pripomogli še Anže Zupanc, Peter Križan, Luka Gabršček, Liza Mijovič, Jure Klučar, Shohei Nishida, Tomaž Podobnik in Jolanta Brodzicka.

Na koncu bi se rad zahvalil še vsem sodelavcem odseka za eksperimentalno fiziko delcev da so ustvarili izjemno vzdušje, zaradi katerega je bilo v veselje priti v službo, ter družini in prijateljem, ki so me podpirali in vzpodbujali pri pisanju doktorske disertacije.

CONTENTS

1	INTRODUCTION	1
1.1	The Standard Model and its fundamental symmetries	1
1.2	Violation of CP symmetry	4
1.2.1	Kobayashi Maskawa mechanism	5
1.3	CP violation in charm decays	8
1.4	CP-violation in weak decays of the Λ_c baryon	9
1.4.1	Λ_c decay chain angular distribution - nonrelativistic derivation	10
1.4.2	Λ_c decay chain angular distribution - relativistic derivation	14
2	EXPERIMENTAL SETUP	15
2.1	The KEKB asymmetric e^+e^- collider	15
2.2	The Belle detector	17
2.2.1	Beam pipe	19
2.2.2	Silicon vertex detector - SVD	20
2.2.3	Central drift chamber - CDC	21
2.2.4	Aerogel Cherenkov Counter - ACC	23
2.2.5	Time-of-flight counters - TOF	25
2.2.6	Electromagnetic calorimeter - ECL	27
2.2.7	K_L and muon detector - KLM	28
2.3	Trigger and data acquisition	30
2.3.1	L1 trigger	32
2.3.2	L3 trigger	33
2.3.3	L4 trigger	33
2.3.4	Data acquisition system	34
2.4	Particle identification	35
2.4.1	Charged hadron identification	35
2.4.2	Electron identification	37
2.4.3	Muon identification	38
2.5	Monte Carlo simulation	38
3	METHOD OF MEASUREMENT	41
3.1	Method of measurement of the average weak asymmetry parameter	42
3.2	Method of measurement of the CP-violating parameter	43
3.3	$\langle\alpha_{\Lambda_c}\rangle$ and $\mathcal{A}_{CP}^{\Lambda_c}$ parameters for Λ_c decays	45
4	DEVELOPMENT OF THE MEASUREMENT METHOD ON MONTE CARLO SIMULATION	47
4.1	Preselection - hadronic event selection	47
4.2	Reconstruction of the Λ_c decay chain	48
4.3	Construction of the skim sample	48
4.3.1	Comparison of Monte Carlo simulation and data event samples	49

	4.3.2	Reweighting of the Monte Carlo simulation $\cos \theta_h$ angular distribution	51
4.4		Construction of the analysis sample	54
	4.4.1	Optimization of selection criteria	54
	4.4.2	Analysis sample	56
4.5		Fit of Λ_c mass in bins of $\cos \theta_h$	56
	4.5.1	General fit method	57
	4.5.2	Signal MC simulation fit	58
	4.5.3	Generic MC simulation fit	60
4.6		Deconvolution	62
4.7		Reconstruction efficiency	64
4.8		Determination of the average weak asymmetry parameter	65
4.9		Fit of Λ_c^+ and $\bar{\Lambda}_c^-$ mass in bins of $\cos \theta_h$	67
4.10		Deconvolution of Λ_c^+ and $\bar{\Lambda}_c^-$ events and \mathcal{A}_{CP} determination	69
4.11		Linearity and consistency test	70
4.12		Summary	72
5		ANALYSIS OF REAL DATA	75
	5.1	MC simulation tuning	75
		5.1.1 Re-optimization of the Λ_c CMS momentum selection criterion	78
		5.1.2 Real data reconstruction efficiency determination	78
	5.2	Λ_c fit of the real data analysis sample	78
	5.3	$\langle \alpha \rangle$ and $\langle \alpha_{\Lambda_c} \rangle$ determination	81
	5.4	Λ_c^+ and $\bar{\Lambda}_c^-$ fits of the real data analysis sample	82
	5.5	\mathcal{A}_{CP} and $\mathcal{A}_{CP}^{\Lambda_c}$ determination	82
6		SYSTEMATIC UNCERTAINTY	85
	6.1	Tracking efficiency uncertainty	85
	6.2	Deconvolution matrix uncertainty	86
	6.3	Fit model uncertainty	86
	6.4	Peaking background uncertainty	88
	6.5	Uncertainty due to \mathcal{A}_{FB}	89
	6.6	Uncertainty due to \mathcal{A}_ϵ	91
	6.7	Summary	93
7		SUMMARY	97
8		POVZETEK DOKTORSKEGA DELA	99
	8.1	Uvod	99
		8.1.1 Standardni Model in njegove simetrije	99
		8.1.2 Kršenje simetrije CP in mehanizem Kobayashi-Maskawa	101
		8.1.3 Kršenje simetrije CP pri razpadu bariona Λ_c	102
	8.2	Trkalnik KEKB in detektor Belle	104
		8.2.1 Trkalnik KEKB	105
		8.2.2 Detektor Belle	105
		8.2.3 Identifikacija nabitih delcev	107
	8.3	Metoda meritve	107
		8.3.1 Meritev povprečnega parametra šibke asimetrije	108
		8.3.2 Meritev parametra kršenja simetrije CP	109

8.3.3	Določanje parametrov za razpad Λ_c	111
8.4	Razvoj metode meritve na simuliranih podatkih	111
8.4.1	Rekonstrukcija razpadne verige Λ_c	111
8.4.2	Primerjava vzorcev iz simulacije in pravih podatkov	112
8.4.3	Konstrukcija analiznega vzorca	114
8.4.4	Prilagajanje porazdelitev po masi Λ_c v intervalih $\cos\theta_h$	115
8.4.5	Dekonvolucija	117
8.4.6	Učinkovitost rekonstrukcije za razpad Λ_c	118
8.4.7	Določanje povprečnega parametra šibke asimetrije	119
8.4.8	Določanje parametra \mathcal{A}_{CP}	120
8.5	Rezultati	122
8.5.1	Popravljanje MC simulacije	122
8.5.2	Rezultati	123
8.6	Sistematska napaka	126
8.7	Povzetek	129
A	FIT RESULTS	131
A.1	Λ_c signal MC simulation fit	131
A.2	Λ_c generic MC simulation fit	131
A.3	Λ_c^+ and $\bar{\Lambda}_c^-$ generic MC simulation fit	131
A.4	Λ_c real data fit	131
A.5	Λ_c^+ and $\bar{\Lambda}_c^-$ real data fit	131
A.6	Σ^{*+} and Σ^{*-} real data fit	131
B	DERIVATIONS OF COVARIANCE MATRICES AND ERRORS	157
B.1	Error propagation	157
B.2	Covariance matrix for the $\langle\alpha\rangle$ fit	157
B.3	Error for the $\langle\alpha\rangle$ fit	159
B.4	Error on the deconvolution matrix element	159
B.5	Covariance matrix for the \mathcal{A}_{CP} fit	160
B.6	Error on the \mathcal{A}_{CP} fit	162
	BIBLIOGRAPHY	163

INTRODUCTION

1.1 THE STANDARD MODEL AND ITS FUNDAMENTAL SYMMETRIES

The Standard Model of particle physics (SM) is a theory which describes the fundamental particles and the interactions between them. It is a relativistic quantum gauge field theory, based on the gauge symmetry group $SU(3)_C \times SU(2)_L \times U(1)_Y$, which describes the three interactions found in Nature - the electromagnetic, the weak and the strong interactions [2, 3, 4]. The interactions are mediated by spin 1 particles, called gauge bosons, between the spin $\frac{1}{2}$ constituents of matter, called fermions. Another spin 0 particle, called the Higgs boson, generates the masses of the particles via interaction and the spontaneous breaking of the gauge symmetry [5].

If a system exhibits a certain symmetry, this means that a certain feature of the system is unchanged under some transformation. This unchanged feature of the system is said to be invariant under the transformation. Mathematically, transformations that leave a quantity unchanged are described by groups. The transformations can be continuous or discrete, with continuous transformations described by Lie groups, and discrete transformations by discrete groups. It is important to note that according to Noether's theorem [6], every symmetry is associated with a conservation law.

The particles in the SM are described using quantum fields, with the dynamics of the SM determined via the principle of least action, by a Lagrangian function, built from these fields. Since the SM is a relativistic quantum gauge field theory, its Lagrangian is invariant to two continuous transformations - the Poincare transformations, described by the Poincare Lie group translation $\times SO(1,3)$ and the gauge transformations, described by the mentioned $SU(3)_C \times SU(2)_L \times U(1)_Y$ Lie group.

The Poincare symmetry is a global spacetime symmetry of the SM, which follows from the principles of special relativity - all physical quantities and laws must be the same in every inertial frame of reference for every point of the Minkowski spacetime. Since the inertial frames are connected via Poincare transformations, the physical quantities and laws must be invariant under the Poincare group of transformations and the corresponding conserved quantities are the energy, the momentum and the angular momentum of the system. Also, in order for the theory to be causal, it has to have an exact Poincare symmetry [7].

The gauge symmetry is an internal symmetry (independent of spacetime coordinates) of a quantum field theory, which arises because a quantum field,

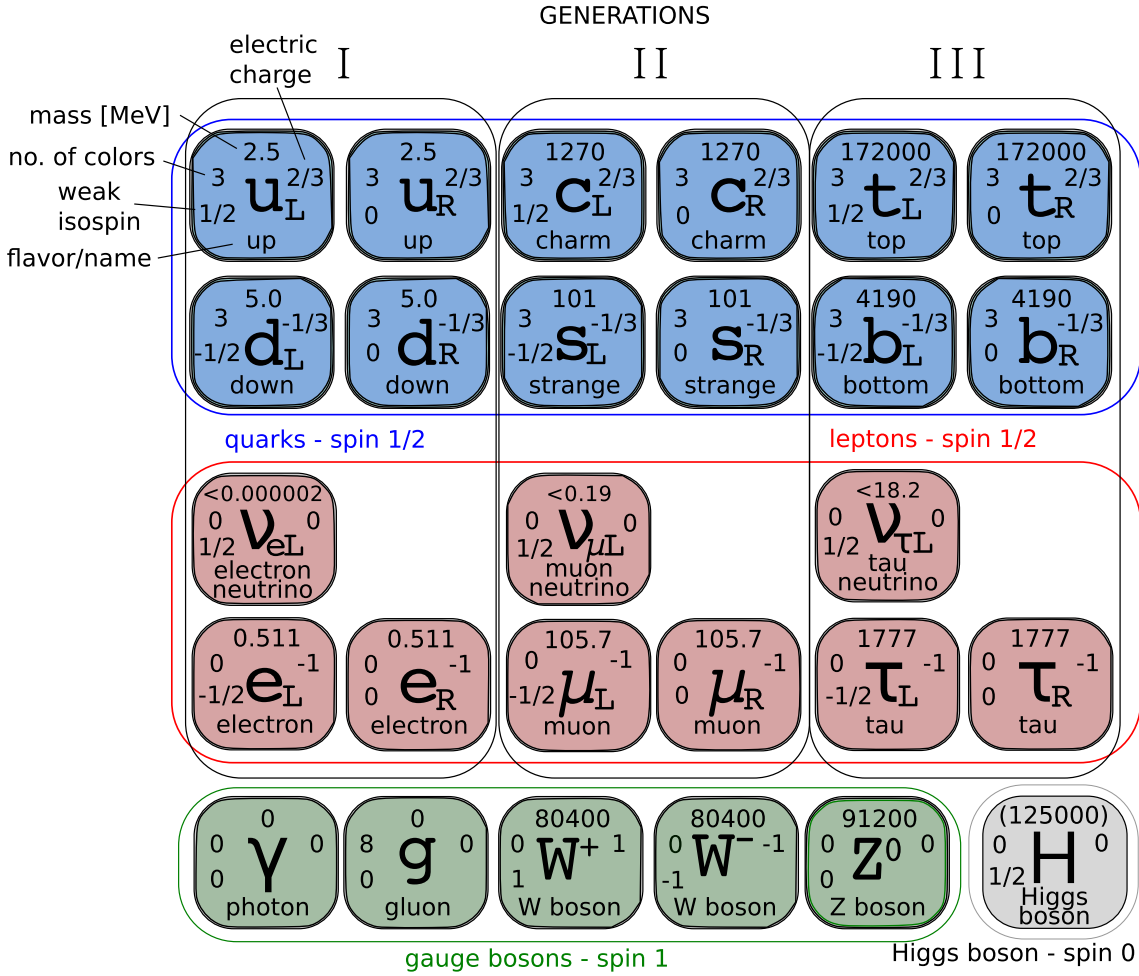


Figure 1: Standard Model particles and their properties.

which is not an observable quantity, can have different configurations, which result in the same observable quantities. The transformation from one to the other field configuration is called a gauge transformation. We can associate a gauge symmetry group for every interaction described by the SM. The fields transform as a $SU(3)_C$ group under the strong interaction and the conserved quantity under these transformations is the quark color. Under the electroweak interaction, the fields transform as a $SU(2)_L \times U(1)_Y$ group and the conserved quantities are the weak hypercharge and the weak isospin. So the SM has a $SU(3)_C \times SU(2)_L \times U(1)_Y$ gauge symmetry. In the SM, this symmetry is then spontaneously broken by the non-zero vacuum expectation value of the theory to the $SU(3)_C \times U(1)_{em}$ symmetry group, which gives the strong, weak and electromagnetic interactions.

The fundamental quantum fields in the SM are divided into several categories, based on their spin and quantum numbers, which are conserved by the gauge transformations (see figure 1).

The spin 1 gauge bosons, which mediate the interactions, are divided into:

- Eight massless gluons g , which carry the strong interaction. They carry a color-anticolor charge, and interact with quarks and between themselves.

- The three massive weak gauge bosons W^+ , W^- and Z^0 , which carry the weak interaction. In addition to weak isospin, the W bosons also carry an electric charge. They interact with quarks and leptons of different flavors and also between themselves.
- The massless photon γ , which carries the electromagnetic force between charged particles.

The spin $\frac{1}{2}$ fermions are organized into three generations, which have identical properties according to the interactions, the only difference between the generations being the masses of the particles and the flavor quantum number. In one generation, we have a pair of left-handed quarks (an up-type and a down-type quark), a pair of left-handed leptons (a lepton and its corresponding neutrino), a right-handed up-type quark, a right-handed down-type quark, and a right-handed lepton. For every particle, there is a corresponding antiparticle, which has the same mass and reversed quantum numbers. The left-handed particle fields are $SU(2)_L$ doublets, and the right-handed particle fields are $SU(2)_L$ singlets.

- There are thus six quarks of different flavor, the up-type quarks u , c and t , and the down-type quarks d , s and b . The quarks carry color charge, and hence they interact via the strong interaction. In addition, they also carry an electric charge and the weak isospin, so they can also interact via the electromagnetic and weak interaction.
- There are also six flavors of leptons, which do not carry color charge. The leptons are e , μ and τ , and they interact via the electromagnetic and weak interactions. To each of the leptons there corresponds a neutrino, ν_e , ν_μ and ν_τ . They are electrically neutral and can therefore interact only via the weak interaction.

The Higgs boson is a spin 0 particle, a $SU(2)_L$ doublet, and does not carry color or electric charge.

Every described particle except the Higgs boson has been experimentally confirmed, and a new particle, which is consistent with the Higgs boson, was discovered by the ATLAS and CMS collaborations in 2012 [8, 9].

In addition to these exact symmetries, we can also define other transformations under which the SM is only approximately conserved. For example, we can define approximate continuous symmetries, such as the quark flavor symmetry, the chiral symmetry, etc. We can also define three discrete symmetries:

- the P symmetry - the symmetry under parity transformation, which reverses the spatial coordinates, \vec{r} to $-\vec{r}$,
- the C symmetry - the symmetry under charge conjugation, which transforms a particle into its antiparticle by conjugating all internal quantum numbers,
- the T symmetry - the symmetry under time reversal, which transforms t to $-t$.

The electromagnetic and strong interaction terms in the SM Lagrangian conserve all three of these symmetries, so they also conserve any combination, and the weak interaction violates the P and C symmetries maximally - only the left-handed particles and the right-handed antiparticles interact with the weak gauge bosons.

For a long time, it was thought that the combined CP symmetry is conserved by all three interactions and is therefore a fundamental symmetry of the SM, until Cronin and Fitch discovered a small CP-violating effect in the system of neutral kaons in 1964 [10]. Later, CP-violation was also discovered in decays of B mesons by the Belle and Babar collaborations [11]. CP-violation was not yet discovered in other meson decays, baryon decays or lepton decays.

It can be shown that the combined CPT symmetry has to be conserved in order for the SM to be a Lorentz (Poincare) invariant local quantum field theory with a Hermitian Hamiltonian [12] or alternatively, that the violation of CPT symmetry implies a violation of Lorentz (Poincare) symmetry [13], so CPT symmetry is a fundamental symmetry of the SM.

1.2 VIOLATION OF CP SYMMETRY

CP-transformation changes a particle into its antiparticle. Because of this, violation of CP symmetry is one of the key ingredients that explain why the Universe is predominantly composed out of matter and not antimatter. It is one of the three Sakharov conditions for baryogenesis, which are necessary for the matter-antimatter asymmetry [14].

To quantify the asymmetry between baryonic and antibaryonic matter, we can compare the number of baryons and the number of photons found in the universe today, as this number is related to the asymmetry between quarks and antiquarks in the early Universe ($\sim 10^{-6}$ seconds after the Big Bang). The baryon number asymmetry of the Universe, deduced from nucleosynthesis and cosmic microwave background radiation [15, 16], is:

$$\Delta|_{t \gtrsim 10^{-6}} = \frac{n_B - n_{\bar{B}}}{n_\gamma} \simeq 10^{-10}. \quad (1)$$

It is usually assumed that earlier than $\sim 10^{-6}$ seconds after the Big Bang, the Universe underwent inflation, which evened out the initial asymmetries between quarks and antiquarks, so $\Delta|_{t \lesssim 10^{-6}} = 0$ must have held, and the asymmetry between quarks and antiquarks would have to come from violation of CP symmetry alone. The Sakharov conditions are necessary to explain how a non-vanishing Δ could arise dynamically from the starting symmetric situation $\Delta = 0$. The three conditions are:

- There must be baryon number violation interactions:

$$H_{\text{eff}}(\Delta B \neq 0) \neq 0. \quad (2)$$

- There must be CP-violating interactions, because if CP were an exact symmetry, every process mediated by $H_{\text{eff}}(\Delta B \neq 0)$ would still have the same

decay rate as the CP-conjugated one, so the matter-antimatter asymmetry would still be 0.

- The universe must have been out of thermal equilibrium. This is because CPT is conserved, and in an equilibrium state, time becomes irrelevant on a global scale, so CPT symmetry reduces to CP symmetry, and the second condition is not fulfilled.

In the SM, the only source of CP-violation in quark interactions comes from the Kobayashi-Maskawa (KM) mechanism, explained in section 1.2.1, however, this mechanism alone does not account for the baryon number asymmetry (1) seen today. Therefore it is important to search for as-yet undiscovered CP-violating effects included in the SM (namely, CP-violation in the leptonic sector, as it is the only other possibility), or in models that extend the SM.

1.2.1 Kobayashi Maskawa mechanism

In order to describe CP-violation in the SM, let us denote the fermionic particle fields in figure 1 by (in this derivation, we will follow [17] and [18]):

$$P_{Hf}(r_{SU(3)}, r_{SU(2)})_Y, \quad (3)$$

where P is the particle, H the handedness, f the flavor/generation index, $r_{SU(3)}$ and $r_{SU(2)}$ the representations of $SU(3)_C$ and $SU(2)_L$ that the particle belongs in, and Y the hypercharge. With this notation, we have for fermions:

$$Q_{Li}(3, 2)_{1/6} = \begin{bmatrix} U_{Li} \\ D_{Li} \end{bmatrix}, \quad U_{Ri}(3, 1)_{2/3}, \quad D_{Ri}(3, 1)_{-1/3}, \quad (4)$$

$$L_{Li}(1, 2)_{-1/2} = \begin{bmatrix} \nu_{Li} \\ E_{Li} \end{bmatrix}, \quad E_{Ri}(1, 1)_{-1},$$

and for the Higgs field we have

$$\phi(1, 2)_{1/2}. \quad (5)$$

The SM Lagrangian can be divided into multiple parts:

$$\mathcal{L} = \mathcal{L}_{\text{gaugeKT}} + \mathcal{L}_{\text{fermionKT}} + \mathcal{L}_{\text{Higgs}} + \mathcal{L}_{\text{Yukawa}}, \quad (6)$$

where the parts contain the gauge fields kinetic terms, the fermion fields kinetic terms, the Higgs field potential and the Yukawa interaction terms. The only

part of the SM Lagrangian that is CP-violating is the Yukawa term.¹ The quark Yukawa terms are:

$$-\mathcal{L}_{\text{Yukawa}}^{\text{quark}} = Y_{ij}^d \overline{Q_{Li}} \phi D_{Rj} + Y_{ij}^u \overline{Q_{Li}} \tilde{\phi} U_{Rj} + (Y_{ij}^d)^* \overline{D_{Ri}} \phi^\dagger Q_{Lj} + (Y_{ij}^u)^* \overline{U_{Ri}} \tilde{\phi}^\dagger Q_{Lj}, \quad (7)$$

where $\tilde{\phi} = \begin{bmatrix} 0 & 1 \\ -1 & 0 \end{bmatrix} \phi^*$.

We spontaneously break the $SU(3)_C \times SU(2)_L \times U(1)_Y$ symmetry into $SU(3)_C \times U(1)_{em}$ by letting the Higgs field acquire a nonzero vacuum expectation value:

$$\langle \phi \rangle = \begin{bmatrix} 0 \\ \frac{v}{\sqrt{2}} \end{bmatrix}, \quad v = 246 \text{ GeV}. \quad (8)$$

After the spontaneous symmetry breaking, the Yukawa interactions become the mass terms:

$$-\mathcal{L}_{\text{Yukawa}}^{\text{mass}} = (M_d)_{ij} \overline{D_{Li}} D_{Rj} + (M_u)_{ij} \overline{U_{Li}} U_{Rj} + (M_d)_{ij}^* \overline{D_{Ri}} D_{Lj} + (M_u)_{ij}^* \overline{U_{Ri}} U_{Lj}. \quad (9)$$

These fields, however, are written in the interaction basis and so the mass matrices in equation (9) are not diagonal. If we want to obtain the physical masses of the quarks, we need to write the terms in the mass basis, where the mass matrices are diagonal. We can always find two unitary matrices V_{qL} and V_{qR} so that $V_{qL} M_q V_{qR}^\dagger = M_q^{\text{diag}}$, ($q = u, d$). The quark mass eigenstates are then $q'_{Li} = (V_{qL})_{ij} q_{Lj}$, $q'_{Ri} = (V_{qR})_{ij} q_{Rj}$, ($q = u, d$).

With these transformations, the charged current weak interactions, which we get from the $\mathcal{L}_{\text{fermionKT}}$ part of the Lagrangian in (6), now transform to:

$$\begin{aligned} -\mathcal{L}_{cc, \text{flavor}} &= \frac{g}{2} \overline{Q_{Li}} \gamma^\mu W_\mu^a \tau^a Q_{Li}, \quad a = 1, 2 \rightarrow \\ -\mathcal{L}_{cc, \text{mass}} &= \frac{g}{\sqrt{2}} \left[\overline{u}'_L, \overline{c}'_L, \overline{t}'_L \right] \gamma^\mu W_\mu^+ (V_{uL} V_{dL}^\dagger) \begin{bmatrix} d'_L \\ s'_L \\ b'_L \end{bmatrix} + \\ &\quad \frac{g}{\sqrt{2}} \left[\overline{d}'_L, \overline{s}'_L, \overline{b}'_L \right] \gamma^\mu W_\mu^- (V_{uL} V_{dL}^\dagger)^* \begin{bmatrix} u'_L \\ c'_L \\ t'_L \end{bmatrix}, \end{aligned} \quad (10)$$

where $W_\mu^\pm = \frac{1}{\sqrt{2}} (W_\mu^1 \mp W_\mu^2)$.

The 3×3 unitary matrix:

$$V_{\text{CKM}} = V_{uL} V_{dL}^\dagger, \quad (11)$$

¹ There can also be a CP violating term in the QCD gauge field kinetic term: $\mathcal{L}_\theta = \frac{\theta_{\text{QCD}}}{32\pi^2} \varepsilon_{\mu\nu\rho\sigma} F^{\mu\nu\alpha} F^{\rho\sigma\alpha}$. This term can be estimated by measuring the electric dipole moment of the neutron, which leads to the bound $\theta_{\text{QCD}} < 10^{-10}$. There is no requirement in SM that this parameter should be so small, and understanding why CP-violation is so small in strong interactions is called the strong CP problem [19].

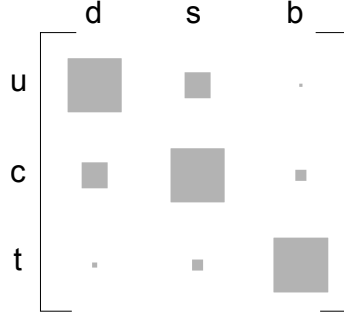


Figure 2: Magnitudes of the CKM matrix elements, represented by an area.

is called the Cabibbo-Kobayashi-Maskawa (CKM) matrix. The elements of the CKM matrix are free parameters in the SM, and their magnitudes determine the probability of the weak charged W^\pm boson couplings between quarks of different generations (flavors), so we can label the elements as:

$$V_{\text{CKM}} = \begin{bmatrix} V_{ud} & V_{us} & V_{ub} \\ V_{cd} & V_{cs} & V_{cb} \\ V_{td} & V_{ts} & V_{tb} \end{bmatrix}. \quad (12)$$

Every 3×3 unitary matrix can be parameterized by 3 real parameters and 1 complex phase. One particularly useful parameterization is called the Wolfenstein parameterization [20]:

$$V_{\text{CKM}} = \begin{bmatrix} 1 - \frac{1}{2}\lambda^2 & \lambda & A\lambda^3(\rho - i\eta) \\ -\lambda & 1 - \frac{1}{2}\lambda^2 & A\lambda^2 \\ A\lambda^3(1 - \rho - i\eta) & -A\lambda^2 & 1 \end{bmatrix} + \mathcal{O}(\lambda^4). \quad (13)$$

The global fit on all available measurements and SM unitarity constraints, gives for the parameters:

$$\lambda = 0.22535 \pm 0.00065, \quad A = 0.811^{+0.022}_{-0.012}, \quad \rho = 0.131^{+0.026}_{-0.013}, \quad \eta = 0.345^{+0.013}_{-0.014}. \quad (14)$$

From these values we can see that the CKM matrix is almost diagonal, in a sense that the absolute values of its elements are smaller the further away one goes from the diagonal (see figure 2), so the quarks are more likely to couple to quarks in the same generation.

The complex phase parameter in the CKM matrix is the only source of CP-violation in the SM. This can be explained intuitively by CP transforming the

charged current weak interaction Lagrangian (10) and comparing it to the untransformed one:

$$\begin{aligned}
-\mathcal{L}_{cc,\text{mass}} &= \frac{g}{\sqrt{2}} \left[\bar{u}'_L, \bar{c}'_L, \bar{t}'_L \right] \gamma^\mu W_\mu^+ V_{\text{CKM}} \begin{bmatrix} d'_L \\ s'_L \\ b'_L \end{bmatrix} + \\
&\quad \frac{g}{\sqrt{2}} \left[\bar{d}'_L, \bar{s}'_L, \bar{b}'_L \right] \gamma^\mu W_\mu^- V_{\text{CKM}}^* \begin{bmatrix} u'_L \\ c'_L \\ t'_L \end{bmatrix}, \\
&\xrightarrow{\text{CP}} \\
-\mathcal{L}_{cc,\text{mass}}^{\text{CP}} &= \frac{g}{\sqrt{2}} \left[\bar{d}'_L, \bar{s}'_L, \bar{b}'_L \right] \gamma^\mu W_\mu^- V_{\text{CKM}} \begin{bmatrix} u'_L \\ c'_L \\ t'_L \end{bmatrix} + \\
&\quad \frac{g}{\sqrt{2}} \left[\bar{u}'_L, \bar{c}'_L, \bar{t}'_L \right] \gamma^\mu W_\mu^+ V_{\text{CKM}}^* \begin{bmatrix} d'_L \\ s'_L \\ b'_L \end{bmatrix},
\end{aligned} \tag{15}$$

We see that the Lagrangian (10) is CP symmetry conserving only if $V_{\text{CKM}} = V_{\text{CKM}}^*$ holds, in other words, if the CKM matrix elements are real. This will be true only if the complex phase is equal to 0.

A similar derivation can be performed for the leptons, but in the SM, the leptonic CP-violation is equal to 0, because in the SM the neutrinos do not have masses. However, recent neutrino oscillation experiments have shown that neutrinos mix among themselves and therefore must have masses [21], so we also have a possibility of CP-violation in the leptonic sector. So far, no CP-violation in this sector has been experimentally confirmed.

1.3 CP VIOLATION IN CHARM DECAYS

CP violation in the SM for tree-level charm decays is expected to be very small. This is due to the fact that the t quark is so heavy that it decays before it can form hadrons, so all the charmed hadronic states that participate in weak decays are composed of quarks that belong to the first two generations. The 2×2 matrix for the first two generations (the Cabibbo matrix) is real to the order of λ^2 in the Wolfenstein parametrization (13). The complex phase that causes CP violation enters only in the λ^4 order, and this yields a CP violating effect of the order $\mathcal{O}(10^{-3})$.

CP-violation can also occur in next order decays (box and penguin decays), however, the CP violating effects that can occur are highly suppressed by the smallness of the typical CKM matrix element combinations $V_{cq} V_{uq}^*$ that determine the coupling probability in the second order weak charm decays. To estimate the order of magnitude of the CP violating effects, we look for example

at the factor $V_{cs}V_{us}^*$ (this is a factor relevant to the box diagram process). Using CKM matrix unitarity, this factor can be expressed as:

$$V_{cs}V_{us}^* = -V_{cd}V_{ud}^* \left(1 + \frac{V_{cb}V_{ub}^*}{V_{cd}V_{ud}^*} \right). \quad (16)$$

The second term's absolute value is small, and we can express the magnitude of the imaginary part for the term $V_{cs}V_{us}^*$ as:

$$\arg(V_{cs}V_{us}^*) \approx \text{Im} \left(\frac{V_{cb}^*V_{ub}}{V_{cd}^*V_{ud}} \right) \approx 7 \times 10^{-4}. \quad (17)$$

Both contributions are therefore of the order of $\mathcal{O}(10^{-3})$, so any observation of CP violation significantly larger than this would present a clean signal of physics not described by the SM. Searches for CP violation in charm decays are therefore a promising way to discover physics beyond the SM.

1.4 CP-VIOLATION IN WEAK DECAYS OF THE Λ_c BARYON

The Λ_c^+ baryon is a spin 1/2 particle composed of (udc) quarks. In this work, we will search for CP-violation in a specific decay chain of Λ_c^+ , where the Λ_c^+ baryon decays weakly to the Λ^0 baryon, also a spin 1/2 baryon, composed of (uds) quarks and a π^+ , a spin 0 meson with a quark content of (u \bar{d}). The Λ^0 baryon then decays weakly to a proton, again a spin 1/2 baryon composed of quarks (uud), and a π^- , a spin 0 meson with a quark content of (d \bar{u}). (see figure 3).

Weak decays of a spin 1/2 particle to spin 1/2 and spin 0 particles ($B_0 \rightarrow B_1M$) can be described by an amplitude:

$$A(B_0 \rightarrow B_1M) = \overline{u}_{B_1}(p_{B_1}, s_{B_1})[A_S - \gamma_5 A_P]u_{B_0}(p_{B_0}, s_{B_0}). \quad (18)$$

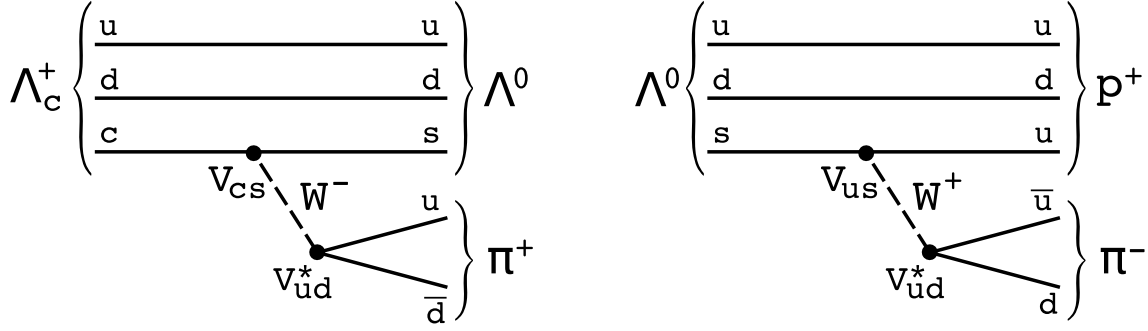
If we CP transform this amplitude, we get:

$$A(B_0 \rightarrow B_1M) \xrightarrow{\text{CP}} \overline{v}_{B_0}(p_{B_0}, s_{B_0})[A_S + \gamma_5 A_P]v_{B_1}(p_{B_1}, s_{B_1}). \quad (19)$$

From these amplitudes we can calculate the angular distribution in the decay, which is a linear function of the $\cos \theta$ of the decay (see section 1.4.1). If CP symmetry is conserved in these decays, the parameter of B_0 decay, α_{B_0} , will be the opposite of the parameter of $\overline{B_0}$ decay, $\alpha_{\overline{B_0}}$, because of (18) and (19). If we define an asymmetry:

$$\mathcal{A}_{\text{CP}}^{B_0} = \frac{\alpha_{B_0} + \alpha_{\overline{B_0}}}{\alpha_{B_0} - \alpha_{\overline{B_0}}}, \quad (20)$$

we can determine the amount of CP-violation in this decay.

Figure 3: Feynman diagrams of the Λ_c^+ baryon decay chain.

1.4.1 Λ_c decay chain angular distribution - nonrelativistic derivation

In this section and in section 1.4.2, we follow [22]. The two decays that we are analyzing are both weak decays of a spin 1/2 particle to a spin 1/2 particle and a spin 0 particle. We look first at just the decay $\Lambda_c \rightarrow \Lambda\pi$. Because this decay is weak, the parity is not conserved and there is no restriction on the parity of the final state. If we take the initial state to be completely polarized (for example, we choose the initial state with spin up), then by angular momentum conservation, the $\Lambda\pi$ final state can have an angular momentum of $l = 0$ (S-wave) or $l = 1$ (P-wave). The following spin configurations are allowed:

$$\begin{aligned}
 \psi_1 &= A_S Y_0^0 s_{1/2} = A_S \begin{bmatrix} 1 \\ 0 \end{bmatrix}, \\
 \psi_2 &= -A_P \left(-\sqrt{\frac{1}{3}}\right) Y_0^1 s_{1/2} = -A_P \left(-\sqrt{\frac{1}{3}}\right) (\sqrt{3} \cos \theta) \begin{bmatrix} 1 \\ 0 \end{bmatrix}, \\
 \psi_3 &= -A_P \left(\sqrt{\frac{2}{3}}\right) Y_1^1 s_{-1/2} = -A_P \left(\sqrt{\frac{2}{3}}\right) \left(-\sqrt{\frac{3}{2}} \sin \theta e^{i\varphi}\right) \begin{bmatrix} 0 \\ 1 \end{bmatrix},
 \end{aligned} \tag{21}$$

where A_S and A_P are the amplitudes of the S and P angular momentum state, Y_j^i are orbital momentum eigenfunctions, the factors $-\sqrt{\frac{1}{3}}$ and $\sqrt{\frac{2}{3}}$ are Clebsch-Gordon coefficients for the decomposition of the initial spin 1/2 state into two spins, 1/2 and 1, and $s_{1/2}$ and $s_{-1/2}$ are the Pauli spin functions.

The final state is a superposition of all three possible spin configurations:

$$\psi_f = \psi_1 + \psi_2 + \psi_3 = (A_S + A_P \cos \theta) \begin{bmatrix} 1 \\ 0 \end{bmatrix} + (A_P e^{i\varphi} \sin \theta) \begin{bmatrix} 0 \\ 1 \end{bmatrix}. \tag{22}$$

This gives for the angular distribution of the decay as measured in the Λ_c center-of-mass system (CMS) (see figure 4):

$$\frac{dN}{d \cos \theta} = \psi_f^* \psi_f = 1 + \alpha_{\Lambda_c} \cos \theta, \tag{23}$$

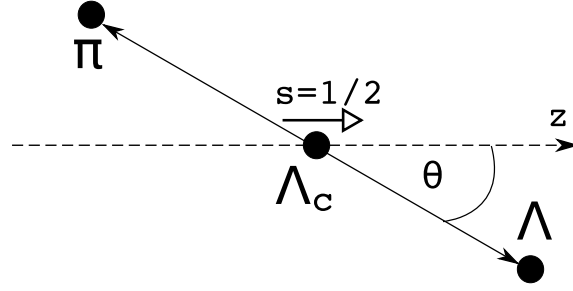


Figure 4: Definition of the angle in the angular distribution of Λ_c decay in Λ_c CMS.

where α_{Λ_c} is the weak asymmetry decay parameter for the Λ_c decay:

$$\alpha_{\Lambda_c} = \frac{2\text{Re}(A_S^* A_P)}{|A_S|^2 + |A_P|^2}. \quad (24)$$

Theoretically, this parameter can for example be calculated in the framework of heavy quark effective theory [23]. In addition, we can also define two other decay parameters:

$$\begin{aligned} \beta_{\Lambda_c} &= \frac{2\text{Im}(A_S^* A_P)}{|A_S|^2 + |A_P|^2}, \\ \gamma_{\Lambda_c} &= \frac{|A_S|^2 - |A_P|^2}{|A_S|^2 + |A_P|^2}. \end{aligned} \quad (25)$$

We would like to determine the polarization of the Λ particle coming from this decay. For this, we need the spin state of the Λ . The most general spin state of a spin 1/2 particle can be written as:

$$\psi = a \begin{bmatrix} 1 \\ 0 \end{bmatrix} + b \begin{bmatrix} 0 \\ 1 \end{bmatrix}, \quad (26)$$

where a and b are complex numbers normalized to 1:

$$|a|^2 + |b|^2 = 1. \quad (27)$$

Since the final state wave function (22) contains all information about the spin of the Λ , we just need to normalize it to get the correct spin state of the Λ . We will also set φ to 0. With this, we set the emission direction of the Λ into the $z-x$ plane, which does not affect generality. The Λ spin state is then:

$$\psi_{\Lambda} = \frac{\psi_f}{|\psi_f|^2} = \frac{A_S + A_P \cos \theta}{1 + \alpha_{\Lambda_c} \cos \theta} \begin{bmatrix} 1 \\ 0 \end{bmatrix} + \frac{A_P \sin \theta}{1 + \alpha_{\Lambda_c} \cos \theta} \begin{bmatrix} 0 \\ 1 \end{bmatrix}. \quad (28)$$

The polarization vector for spin 1/2 particles is defined as

$$\vec{P} = 2 \langle \vec{J} \rangle = \psi^* \vec{\sigma} \psi, \quad (29)$$

where $\vec{\sigma}$ are the Pauli matrices. From equations (28) and (29) we can now determine the components of the Λ polarization vector:

$$\begin{aligned} (1 + \alpha_{\Lambda_c} \cos \theta) P_{\Lambda_x} &= \alpha_{\Lambda_c} \sin \theta + 2|A_p|^2 \cos \theta \sin \theta, \\ (1 + \alpha_{\Lambda_c} \cos \theta) P_{\Lambda_y} &= \beta_{\Lambda_c} \sin \theta, \\ (1 + \alpha_{\Lambda_c} \cos \theta) P_{\Lambda_z} &= \gamma_{\Lambda_c} + \alpha_{\Lambda_c} \cos \theta + 2|A_p|^2 \cos^2 \theta. \end{aligned} \quad (30)$$

Now we generalize to the case where the initial Λ_c particle is not completely polarized ($P_{\Lambda_c} < 1$). We can define the initial polarization of a sample of Λ_c particles as:

$$P_{\Lambda_c} = \frac{N_{\uparrow} - N_{\downarrow}}{N_{\uparrow} + N_{\downarrow}}, \quad (31)$$

where N_{\uparrow} and N_{\downarrow} are the numbers of Λ_c particles in the sample with spin up and spin down, respectively. Equation (23) now becomes:

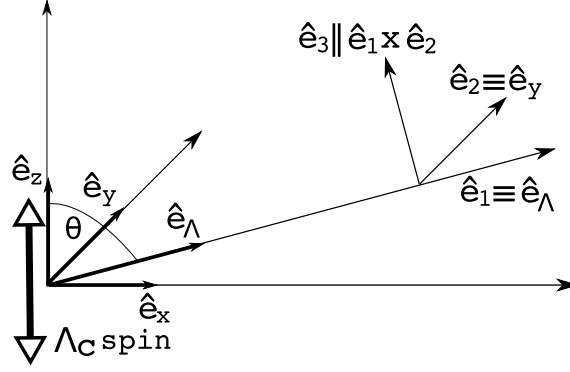
$$\frac{dN}{d \cos \theta} = 1 + P_{\Lambda_c} \alpha_{\Lambda_c} \cos \theta, \quad (32)$$

and for calculation of the Λ polarization, we must reweigh both spin terms in equation (28) by $\frac{N_{\uparrow}}{N_{\uparrow} - N_{\downarrow}}$ and $\frac{N_{\downarrow}}{N_{\uparrow} - N_{\downarrow}}$, respectively. For the spin down state, we must also make the transformation $y \rightarrow -y, z \rightarrow -z, \theta \rightarrow \pi - \theta$, as the Λ_c spin points in the negative z direction in this case. When we take this into account, the Λ polarization for a Λ_c source with polarization P_{Λ_c} in the Λ_c CMS is:

$$\begin{aligned} P_{\Lambda_x} &= \frac{\alpha_{\Lambda_c} \sin \theta + 2P_{\Lambda_c} |A_p|^2 \cos \theta \sin \theta}{1 + P_{\Lambda_c} \alpha_{\Lambda_c} \cos \theta}, \\ P_{\Lambda_y} &= \frac{P_{\Lambda_c} \beta_{\Lambda_c} \sin \theta}{1 + P_{\Lambda_c} \alpha_{\Lambda_c} \cos \theta}, \\ P_{\Lambda_z} &= \frac{P_{\Lambda_c} \gamma_{\Lambda_c} + \alpha_{\Lambda_c} \cos \theta + 2P_{\Lambda_c} |A_p|^2 \cos^2 \theta}{1 + P_{\Lambda_c} \alpha_{\Lambda_c} \cos \theta}. \end{aligned} \quad (33)$$

These expressions simplify if we write them in the Λ emission CMS, where the x -axis is defined with the Λ emission direction in the Λ_c CMS, the y -axis direction is the same as before, and the z -axis is defined to be perpendicular to the x and y axes in the usual way (see figure 5). If we transform the Λ polarization vector to this coordinate system, we get (we will denote the axes with indices 1, 2 and 3 for this system):

$$\begin{aligned} P_{\Lambda 1} &= \frac{\alpha_{\Lambda_c} + P_{\Lambda_c} \cos \theta}{1 + P_{\Lambda_c} \alpha_{\Lambda_c} \cos \theta}, \\ P_{\Lambda 2} &= \frac{P_{\Lambda_c} \beta_{\Lambda_c} \sin \theta}{1 + P_{\Lambda_c} \alpha_{\Lambda_c} \cos \theta}, \\ P_{\Lambda 3} &= \frac{P_{\Lambda_c} \gamma_{\Lambda_c} \sin \theta}{1 + P_{\Lambda_c} \alpha_{\Lambda_c} \cos \theta}. \end{aligned} \quad (34)$$

Figure 5: Definition of the Λ emission coordinate system.

Now we look at the decay $\Lambda \rightarrow p\pi$. We know that this is also a weak decay of a spin 1/2 particle to a spin 1/2 particle and a spin 0 particle, so according to the equation (32), the angular distribution of the decay in the Λ CMS is:

$$\frac{dN}{d \cos \theta_p} = 1 + P_\Lambda \alpha_\Lambda \cos \theta_p, \quad (35)$$

where α_Λ is the weak asymmetry parameter for the decay of Λ , P_Λ is the Λ polarization and the θ_p angle is defined for the $\Lambda \rightarrow p\pi$ decay in the same way as the θ angle for the $\Lambda_c \rightarrow \Lambda\pi$ decay in figure 4.

In our case, the Λ sample has this angular distribution with respect to the direction of the polarization \vec{P}_Λ . We now want to write the angular distributions of the decay with respect to the directions 1, 2 and 3 in figure 5. It can be shown that the distribution (35) remains the same for all three directions, if we write it with the polar angle and the right component of polarization for the specific direction. So, for all three directions, we will have:

$$\frac{dN}{d \cos \vartheta_k}(\theta) = 1 + \alpha_\Lambda P_{\Lambda k}(\theta) \cos \vartheta_k, \quad k = 1, 2, 3. \quad (36)$$

The components (34) are written for a specific angle θ . In our sample however, for each Λ that is emitted, this angle will be different, so if we want the angular distributions in Λ CMS of the whole sample, we need to average the polarization components over θ :

$$\frac{dN}{d \cos \vartheta_k} = 1 + \alpha_\Lambda \langle P_{\Lambda k} \rangle \cos \vartheta_k, \quad k = 1, 2, 3. \quad (37)$$

$\langle P_{\Lambda k} \rangle$ is the statistical average of the polarization components over the θ decay angle:

$$\langle P_{\Lambda k} \rangle = \int P_{\Lambda k}(\theta) f(\theta) d\Omega, \quad (38)$$

where $f(\theta)$ is the normalized distribution (32). If we calculate this, we arrive to our final distributions:

$$\begin{aligned}\frac{dN}{d \cos \vartheta_1} &= 1 + \alpha_{\Lambda_c} \alpha_{\Lambda} \cos \vartheta_1, \quad \cos \vartheta_1 = \hat{e}_p \cdot \hat{e}_1, \\ \frac{dN}{d \cos \vartheta_2} &= 1 + \frac{\pi}{4} P_{\Lambda_c} \beta_{\Lambda_c} \alpha_{\Lambda} \cos \vartheta_2, \quad \cos \vartheta_2 = \hat{e}_p \cdot \hat{e}_2, \\ \frac{dN}{d \cos \vartheta_3} &= 1 + \frac{\pi}{4} P_{\Lambda_c} \gamma_{\Lambda_c} \alpha_{\Lambda} \cos \vartheta_3, \quad \cos \vartheta_3 = \hat{e}_p \cdot \hat{e}_3,\end{aligned}\tag{39}$$

where \hat{e}_1, \hat{e}_2 and \hat{e}_3 have been defined in figure 5 and \hat{e}_p is the emission direction of the proton in the Λ CMS.

As one can see from the first of equations (39), we can determine the parameter α_{Λ_c} regardless of the initial polarization of the Λ_c sample, if α_{Λ} is known.

1.4.2 Λ_c decay chain angular distribution - relativistic derivation

In section 1.4.1, we derived the angular distributions nonrelativistically. Specifically, we did not distinguish between the Λ_c CMS where the decay orbital momentum is strictly defined, and the Λ CMS where the Λ spin is strictly defined. To find a relativistic generalization, we need to write down the relativistic decay state of the Λ_c in its CMS. This state can be written as a superposition of states:

$$|L, M, s, m \rangle = \int d\Omega_{\vec{p}} Y_L^M(\Omega_{\vec{p}}) \varphi_{\vec{p}} \Gamma_{\vec{p}} \chi_s^m, \tag{40}$$

where:

- $\Omega_{\vec{p}}$ are the angles $\theta_{\vec{p}}, \phi_{\vec{p}}$, denoting the direction of the Λ momentum \vec{p} in the Λ_c CMS.
- $Y_L^M(\Omega_{\vec{p}})$ is the decay orbital momentum state with angular momentum L and z component M .
- $\varphi_{\vec{p}}$ is a plane wave state $e^{i\vec{p}\vec{x}}$ for Λ in the Λ_c CMS.
- χ_s^m is the spin eigenstate of Λ in the Λ CMS, which is defined so that the coordinate axes are parallel to the axes in the Λ_c CMS.
- $\Gamma_{\vec{p}}$ is the matrix that transforms the Λ spin state from the Λ CMS to the Λ_c CMS.

It can be shown that the rotation properties of the relativistic states (40) do not depend on the Λ momentum \vec{p} , which means that they transform under rotations in the Λ_c CMS as the corresponding nonrelativistic states. If this is true, then the nonrelativistic derivation which considers only angular momentum in the Λ_c CMS is identical to the relativistic one. The only difference is that caution must be taken when transforming from the Λ CMS to Λ_c CMS. Since every Λ in the sample has its own CMS, defined by the Λ_c CMS, we need to first transform every quantity from the laboratory system to the Λ_c CMS, and from there to the Λ CMS, where we have calculated the angular distribution.

EXPERIMENTAL SETUP

This work has been done by analyzing a 785 fb^{-1} data sample collected by the Belle detector. The Belle detector is a particle detector constructed around the crossing point of the electron and positron beams of the KEKB asymmetric e^+e^- collider, located at the High Energy Accelerator Research Organization in Tsukuba, Japan. In this chapter, the KEKB collider and the Belle detector will be described. For a complete description, see [24] for the KEKB collider and [25, 26] for the Belle detector.

2.1 THE KEKB ASYMMETRIC e^+e^- COLLIDER

KEKB is a two-ring, asymmetric energy electron-positron collider. Its two rings with a circumference of $\sim 3 \text{ km}$ are installed 11 m below the ground level in a tunnel which was previously used for the TRISTAN collider. In one of the rings, the electrons are stored at the energy of 8.5 GeV (the high energy ring - HER) and in the other, positrons are stored at the energy of 3.5 GeV (the low energy ring - LER). The electrons and positrons are injected into the rings by a linac complex at full energies. The two rings intersect at an angle of 22 mrad in a single point, called the interaction point (IP), where the e^+e^- collisions occur. The Belle detector is built around the IP in order to catch the particles produced by the collisions (see figure 6).

The beam energies are chosen so that the center-of-mass (CM) energy is :

$$E_{\text{CM}} = 2\sqrt{E_{\text{HER}}E_{\text{LER}}} = 10.58 \text{ GeV}, \quad (41)$$

which corresponds to the mass of the $\Upsilon(4S)$ resonance, an excited bound state of $b\bar{b}$ quarks [1]. Because the mass of $\Upsilon(4S)$ is approximately equal to 2 times the mass of the B meson, this resonance is just above the threshold for the B meson production, and it decays exclusively to a pair of B mesons (either charged or neutral). Because the cross-section for the $e^+e^- \rightarrow \Upsilon(4S) \rightarrow B\bar{B}$ reaction at this energy is large, the KEKB collider produces a large amount of B mesons (it is a so-called 'B-factory'). This setup that gives a large B meson production is chosen because the Belle collaboration's main goal was to study CP violation in decays of B mesons.

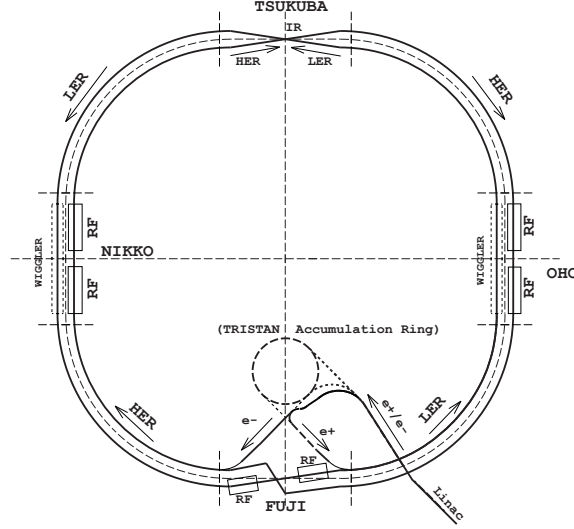


Figure 6: A schematic of the KEKB collider [24].

interaction type	σ [nb]
$e^+e^- \rightarrow \Upsilon(4S) \rightarrow B\bar{B}$	1.1
$e^+e^- \rightarrow c\bar{c}$	1.3
$e^+e^- \rightarrow q\bar{q}, (q = u, d, s)$	2.1
$e^+e^- \rightarrow \tau^+\tau^-$	0.93
Bhabha, radiative Bhabha	37.8
$\gamma\gamma$	11.1

Table 1: Cross sections for possible e^+e^- interactions in the KEKB collider [25].

The beam energies are asymmetric, and therefore the produced $\Upsilon(4S)$ particle is boosted in the laboratory system by:

$$\beta\gamma = \frac{E_{\text{HER}} - E_{\text{LER}}}{E_{\text{CMS}}} = 0.425. \quad (42)$$

The $B\bar{B}$ pair produced from $\Upsilon(4S)$ has approximately the same boost, as they are produced almost at rest in the CMS of the $\Upsilon(4S)$, so the decay vertices of both mesons are $\sim 200 \mu\text{m}$ apart in the laboratory system, which allows for the measurement of time-dependent CP-violation.

In addition to collecting data at this energy, the accelerator also collected data at energies corresponding to other $\Upsilon(NS)$ resonances, and at an energy of 60 MeV below the $\Upsilon(4S)$ resonance (see figure 7).

The colliding e^+e^- can also undergo interactions other than the $\Upsilon(4S) \rightarrow B\bar{B}$ production. The interactions include all other quark pair production except for $t\bar{t}$ pairs, muon and tau pair production, Bhabha scattering and two photon events. The cross-sections for each interaction are written in table 1. As we can see, the collider also produces a large amount of $c\bar{c}$ pairs, which can be used to study charm physics.

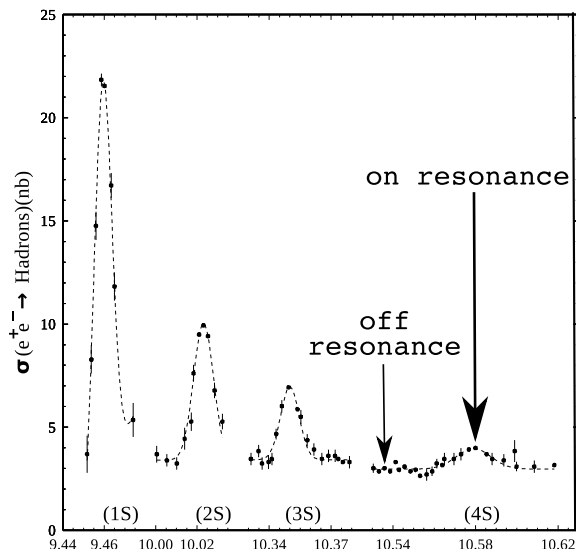


Figure 7: Cross section for $e^+e^- \rightarrow \text{hadrons}$ at the center-of mass energies near the Υ resonances [1].

The performance of an accelerator is characterized by its luminosity, which equals the number of particles per area per unit of time times the opacity of the target. For the intersecting ring collider, it is equal to:

$$\mathcal{L} = fn \frac{N_1 N_2}{A}, \quad (43)$$

where f is the revolution frequency, n the number of particle bunches in an individual ring, N_1 and N_2 the number of particles in each colliding bunch, and A the cross-section of the beam.

The luminosity relates the rate of particle collisions to the interaction cross-section:

$$\frac{dN}{dt} = \mathcal{L}\sigma. \quad (44)$$

The KEKB collider's design luminosity was $1.0 \times 10^{34}/\text{cm}^2\text{s}$, and in June 2009, it achieved a luminosity of $2.11 \times 10^{34}/\text{cm}^2\text{s}$, which is the current world record for colliders.

The integrated luminosity

$$L = \int \mathcal{L} dt, \quad (45)$$

is a measure of total collected data. In its running period, the KEKB collider has produced a total of more than 1000 fb^{-1} of data, 711 fb^{-1} of this amount at the $\Upsilon(4S)$ resonance and 100 fb^{-1} at 60 MeV below the $\Upsilon(4S)$ resonance (see table 2).

2.2 THE BELLE DETECTOR

The Belle detector (figure 8) is constructed around the interaction point of the KEKB accelerator. Its purpose is to measure the energy, momentum and identity

Resonance	collected data [fb^{-1}]
$\Upsilon(1S)$	6
$\Upsilon(2S)$	25.0
$\Upsilon(3S)$	3
60 MeV below $\Upsilon(4S)$	100
$\Upsilon(4S)$	711
$\Upsilon(5S)$	121
all data	> 1000

Table 2: The amount of data produced at various energies of different resonances in the KEKB collider [27].

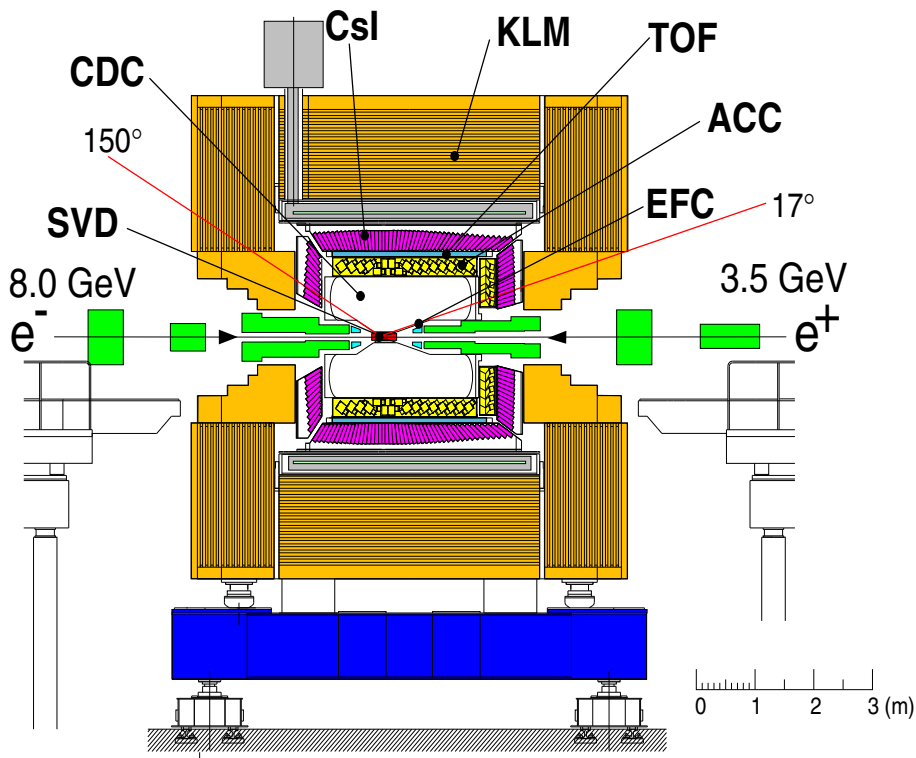


Figure 8: Side view of the Belle detector [25].

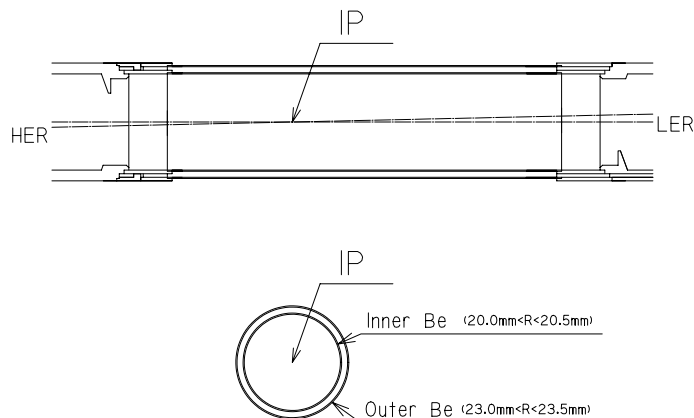


Figure 9: Cross-section of the beam pipe at the interaction region [25].

of various long-lived particles which are final products of the e^+e^- collisions in the accelerator. It is configured around the 1.5 T solenoid magnet and iron structure which surround the KEKB beams.

The detector is composed of various subdetector systems, all of which have specific tasks. Just outside the beryllium beam pipe is the silicon vertex detector (SVD), which measures the decay vertices of B mesons. Looking radially outward, after the SVD there is the multiwire drift chamber (CDC), used for charged particle tracking and via measurements of the specific ionization $\frac{dE}{dx}$, also for particle identification. The aerogel Cherenkov counters (ACC) and the time-of-flight counters (TOF) outside the CDC are also used for particle identification. Following those in the radial direction, there is an electromagnetic calorimeter (ECL), used for measuring the energy of the electromagnetic showers, composed of an array of CsI(Tl) crystals. All of these subdetectors are located inside the superconducting solenoid magnet. The outermost subdetector is the K_L meson and muon detector (KLM), composed of arrays of resistive plate counters interspersed in the iron yoke.

The detector covers a polar angle of $17^\circ < \theta < 150^\circ$ ¹. A part of the uncovered polar angle is measured by a pair of extreme forward calorimeters (EFC), composed of an array of BGO crystals.

In order to reduce the Bhabha and $\gamma\gamma$ background events and to reduce the rate of data that needs to be written by the data acquisition system, the Belle detector employs a hardware and a software trigger.

In the following the most important parts of the detector for the performed measurement are described in more details.

2.2.1 Beam pipe

The beam pipe in the interaction region ($-4.6 \text{ cm} \leq z \leq 10.1 \text{ cm}$) is a double-wall beryllium cylinder (see figure 9). The inner radius is 15 mm for the new beam pipe and 20 mm for the old beam pipe (see chapter 2.2.2). Because of the

¹ The laboratory system is defined with the z -axis pointing in the opposite direction of the LER beam, the x -axis pointing in the horizontal direction, and the y -axis pointing in the vertical direction.

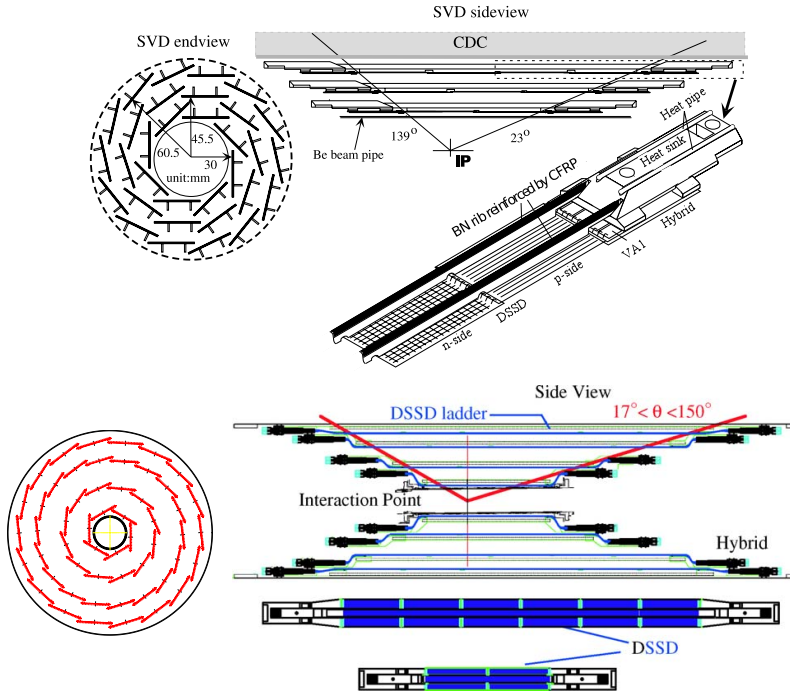


Figure 10: Detector configurations of SVD1 (top) and SVD2 (bottom) [25, 26].

heat induced by the beam, it is He-gas cooled. Both beryllium walls are 0.5 mm thick and represent 0.3% of the radiation length. On the outside wall, a 60 μm thick gold sheet is attached in order to reduce the low energy X-ray background from HER. Its thickness corresponds to 0.6% of the radiation length.

2.2.2 Silicon vertex detector - SVD

In order to study the time-dependent CP-violation in B meson decays, one needs a precision of $\sim 100 \mu\text{m}$ in the measurement of the difference of the z decay vertex positions for B meson pairs. This measurement is provided by the silicon vertex detector (SVD), which in addition is also useful for measuring the decay vertex positions of D and τ mesons and also contributes to tracking. As the resolution that can be achieved is dominated by the multiple Coulomb scattering, the SVD needs to be placed as close to the IP as possible and it must be low in mass but rigid.

The SVD is composed of layers of detectors, where each layer is built out of independent DSSD (double-sided silicon detector) ladders (see figure 10). The DSSD is a depleted p – n junction in which a passing charged particle excites electrons from the valence to the conducting band, thus creating electron-hole pairs, which create currents in the p^+ and n^+ strips on the surface of the DSSD. Each DSSD in SVD has 1280 sense strips and 640 readout pads on opposite sides.

In the Belle detector, there have been two different silicon vertex detectors (denoted by SVD1 and SVD2), where SVD1 was operating from the beginning of the measuring period until 2003, and SVD2 was operating from 2003 until the end of the measuring period.

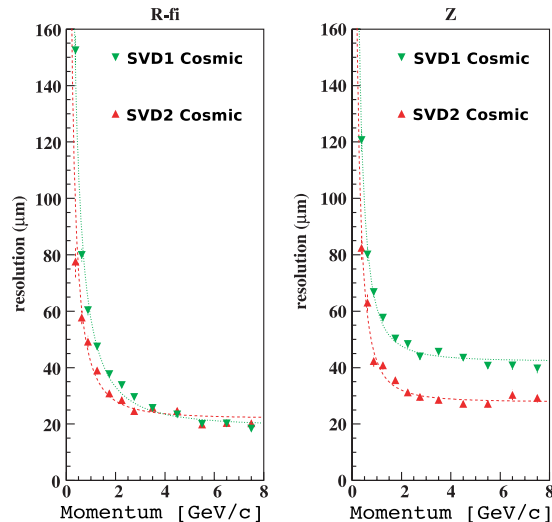


Figure 11: Impact parameter resolutions of SVD1 and SVD2 in the z direction and the $r - \phi$ plane [25].

SVD1 had 3 layers placed at 30, 45.5 and 60 mm radially from the IP, consisting out of 8, 10 and 14 DSSD ladders respectively, where in each ladder there were 2, 3 or 4 ladders, depending on the layer. It covered a solid of angle of $23^\circ \leq \theta \leq 139^\circ$ and at $\theta = 90^\circ$, corresponded to 1.85% of the radiation length.

SVD2 had 4 layers placed at 20, 43.5, 70 and 80 mm radially from the IP, consisting out of 6, 12, 18 and 18 DSSD ladders respectively, where in each ladder there were 2, 3, 5 or 6 ladders, depending on the layer. It covered a solid of angle of $17^\circ \leq \theta \leq 150^\circ$, thus matching the angular coverage of the CDC, and at $\theta = 90^\circ$, corresponded to 2.6% of the radiation length.

Both detectors provided sufficient accuracy in measuring the coordinates of the decay vertices of B mesons in the z direction and also in the $r - \phi$ plane, as confirmed by the measurements of the impact parameter resolution. The momentum and angular dependence of the impact parameter resolution in the z direction and $r\phi$ plane can be expressed by the formula

$$\sigma_z = a \oplus \frac{b}{p\beta \sin^{5/2} \theta} \mu\text{m}, \quad \sigma_{r\phi} = c \oplus \frac{d}{p\beta \sin^{3/2} \theta} \mu\text{m}, \quad (46)$$

where $a = 36, b = 42, c = 19, d = 50$ for SVD1, and $a = 28, b = 32, c = 22, d = 36$ for SVD2 (see figure 11).

2.2.3 Central drift chamber - CDC

Virtually all measurements done with the Belle detector need an efficient reconstruction of individual charged particle tracks and the precise determination of their momenta. This is accomplished with the main tracking detector, the CDC.

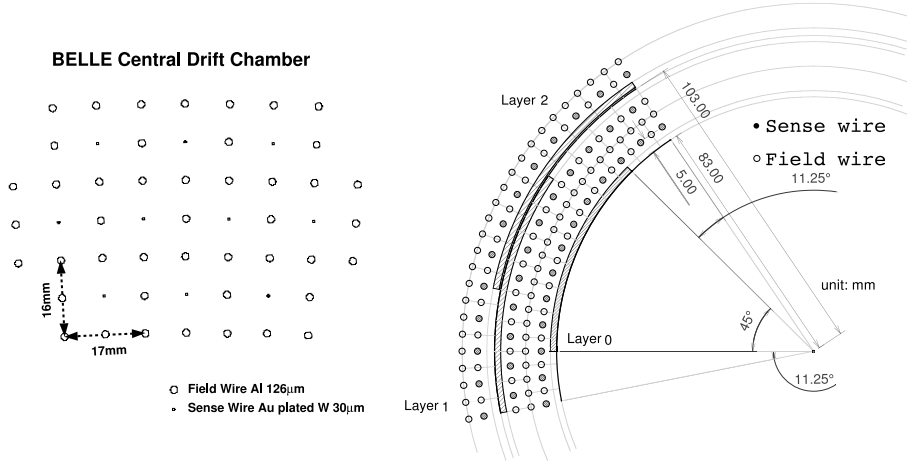


Figure 12: The Belle CDC cell structure [25].

Physics goals for the Belle experiment require a momentum resolution of the reconstructed charged tracks to be:

$$\frac{\sigma_{p_T}}{p_T} \sim 0.5\% \sqrt{1 + p_T^2 [\text{GeV}/c]}, \quad (47)$$

for all particles with $p_T \geq 100 \text{ MeV}/c$ in the polar angle of $17^\circ \leq \theta \leq 150^\circ$. The tracking system must also provide information for the trigger and particle identification information in the form of precise measurements of the specific ionization $\frac{dE}{dx}$.

The CDC is designed and constructed to meet these requirements. It is a multiwire drift chamber, filled with gas, with strung anode sense and field wires centered between cathode planes, forming cells (see figure 12). A charged particle traveling through the chamber ionizes the gas, which causes the ionized electrons and ions to drift to the anode wires and cathode planes, respectively. In the strong electric field close to the anode wire, the electrons trigger an avalanche, which induces an electric pulse on the anode wire. The position of the track is then determined by measuring the drift time of the electrons, that is the time difference between the passing of the particle, determined by a scintillation counter, and the appearance of the pulse in the wire. The drift speed must be as constant as possible, and for this reason there are additional field wires strung between the sense wires, to ensure the uniformity of the electric field in the gap between the anode sense wires.

The Belle CDC has an inner radius of 103.5 mm and an outer radius of 874 mm (see figure 13). It has 50 cylindrical layers, each containing between 3 and 6 axial or small-angle-stereo layers and 3 cathode layers, which amounts to a total of 8400 drift cells. The z -coordinate is measured by cathode strips glued on the inner surface of the cylinder (see figure 12). The gas is a low- Z mixture of 50% helium-50% ethane. It has a long radiation length, and the drift velocity saturates at a relatively low electric field to provide a constant drift velocity, but still provides a good resolution on the measurement of the specific ionization because of the large ethane component.

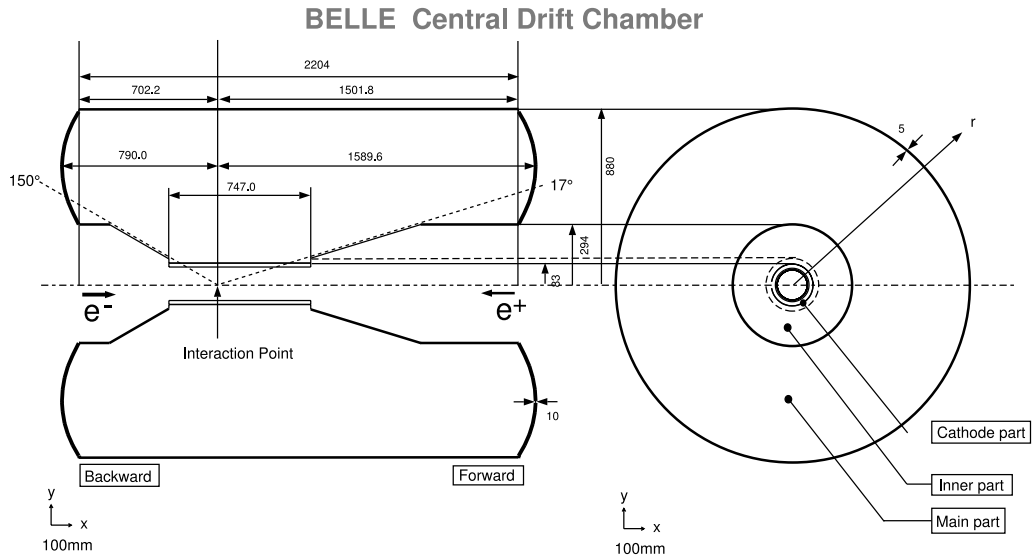


Figure 13: Geometry of the Belle CDC [25].

The spatial resolution of the CDC measured with cosmic ray data is between $120 \mu\text{m}$ and $150 \mu\text{m}$, depending on the incident angle and layer. To extract the transverse momentum $p_T = \sqrt{p_x^2 + p_y^2}$ and the p_z component of the momentum, a tracking algorithm sorts CDC hits into helical tracks, where the p_T and p_z are then extracted from the curvature radius and the slope of the helix. The relative uncertainty of the measured p_T is between 0.5% and 1.1%, depending on the magnitude of the p_T .

The CDC also measures the specific ionization - the energy loss of a charged particle ($\frac{dE}{dx}$) in the chamber gas. This measurement is used for particle identification, as the loss depends on the velocity of the particle. The specific ionization is determined by measuring the amplitude of the pulse in the anode sense wires, which is proportional to $\frac{dE}{dx}$. The resolution of the truncated mean energy loss for a track in CDC is 7.8%, and with this, the CDC is able to discriminate between pions and kaons with momenta up to $0.8 \text{ GeV}/c$ on a 3σ level (see figure 14).

2.2.4 Aerogel Cherenkov Counter - ACC

For all measurements with the Belle detector, the ability to distinguish between different types of particles, especially between π^\pm and K^\pm , is crucial. The aerogel Cherenkov counter (ACC) extends the momentum coverage for particle identification beyond the $\frac{dE}{dx}$ measurement of the CDC and the time-of-flight measurements by TOF (see chapters 2.2.3, 2.2.5, 2.4).

The ACC is an array of silica aerogel threshold Cherenkov counters. The threshold Cherenkov counter discriminates particles by using the fact that when a particle travels through a medium faster than light in that medium, it emits Cherenkov radiation. The threshold for emittance of Cherenkov radiation depends on the refractive index of the medium:

$$\beta_{\text{threshold}} = \frac{1}{n}. \quad (48)$$

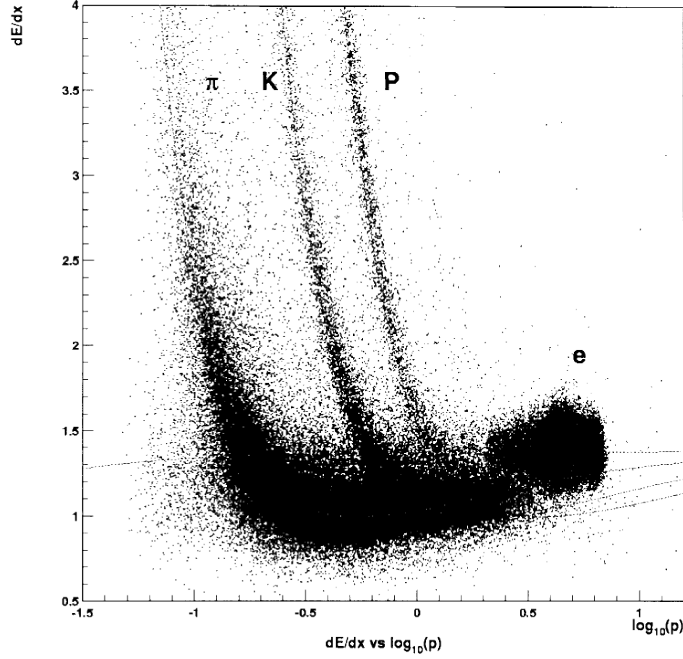


Figure 14: Truncated mean of $\frac{dE}{dx}$ vs. the momentum observed in the CDC [25].

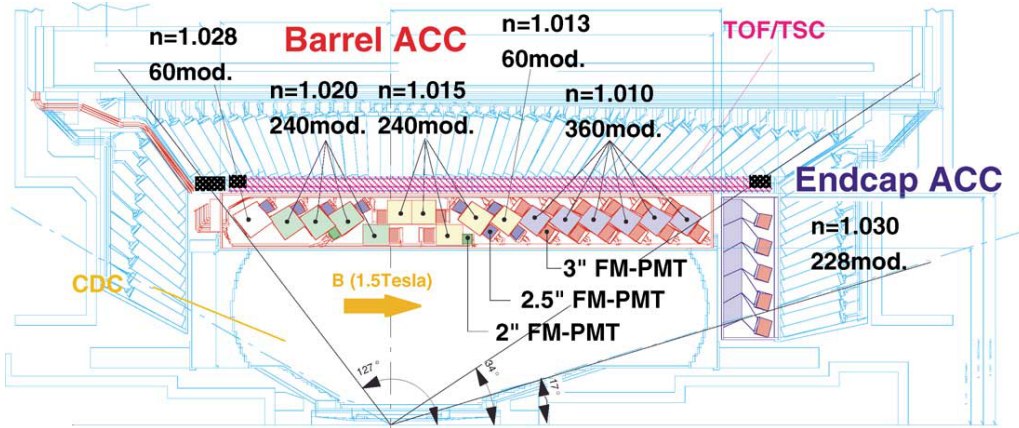


Figure 15: The geometry of the ACC system [25].

The silica aerogel used for the medium is suitable because it can be produced with a very well known refractive index ($\Delta n/(n-1) \sim 3\%$). The ACC is therefore able to discriminate between pions and kaons in the momentum range of $1.2 - 3.5 \text{ GeV}/c$, since pions in this momentum range produce Cherenkov light, whereas kaons, which are heavier, do not.

In Belle, the ACC consists of 960 counter modules, segmented into 60 cells in the ϕ direction for the barrel part and 228 modules, laid out in 5 concentric layers for the forward end-cap part (see figure 15). A single module consists of 5 aerogel tiles in a thin aluminum box with dimensions $12 \times 12 \times 12 \text{ cm}^3$. The refractive indices of aerogel tiles are between 1.01 and 1.03, depending on the azimuthal angle region in order to obtain a good K/π separation for the whole kinematical range. The Cherenkov light is collected by fine-mesh photomultiplier tubes attached directly to the aerogel, chosen because of their large effective area and high gain ($\sim 10^8$) (see figure 16).

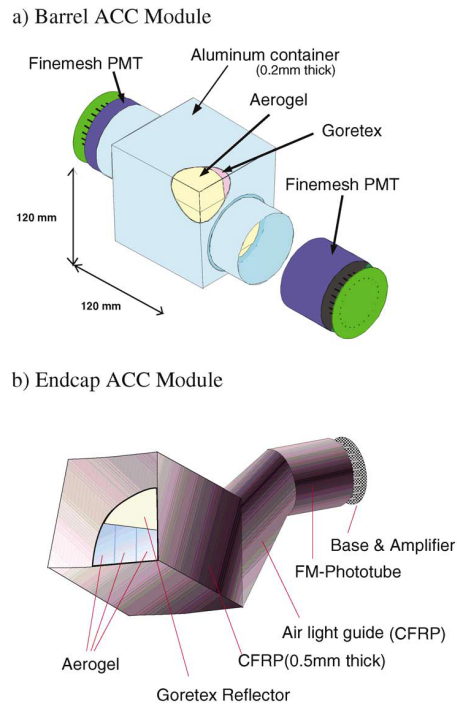


Figure 16: ACC counter modules for a) barrel and b) end-cap regions [25].

2.2.5 Time-of-flight counters - TOF

The time-of-flight counter (TOF) is used for particle identification in a momentum range of 0.8 – 1.2 GeV, a range that lies between the ranges of the CDC and ACC particle identification systems.

The TOF measures the time between the e^+e^- collision in the IP and the passage of a charged particle through it. The mass of the particle is then calculated with

$$m = \frac{p}{c} \sqrt{\left(\frac{ct}{l}\right)^2 - 1}, \quad (49)$$

where p is the particle momentum, measured by the CDC, l the length of the helix that the particle has traveled on, determined by the CDC tracking algorithm, and t the measured time by TOF. The time measurement has to have a resolution of ~ 100 ps, in order to obtain a 3σ separation power between pions and kaons on a travel path of about 1.2 m.

The TOF system uses fast plastic scintillators with an attenuation length longer than 2 m. The TOF system also provides fast timing signals for the trigger system, and to avoid pile-up in the trigger queue, the TOF scintillation counters must be augmented by thin trigger scintillation counters (TSC) to keep the trigger rate below 70 kHz. The whole system consists of 128 TOF counters and 64 TSC counters, with 2 TOF and 1 TSC counter forming one module (see figure 17). The system covers a polar angle range of $34^\circ - 120^\circ$. The scintillation photons are picked up by fine-mesh-dynode photomultiplier tubes, mounted directly on the scintillation counters and placed in a magnetic field of 1.5 T. This configuration meets the ~ 100 ps time resolution goal for the Belle detector (see figure 18).

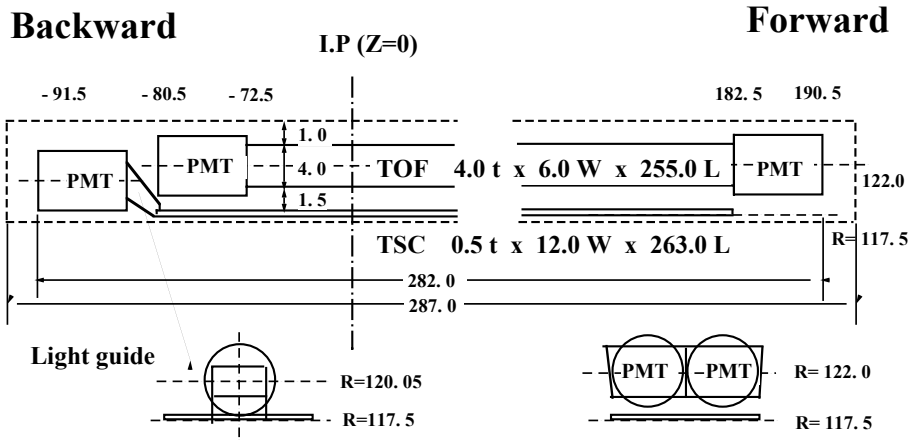


Figure 17: The layout of the TOF/TSC module [25].

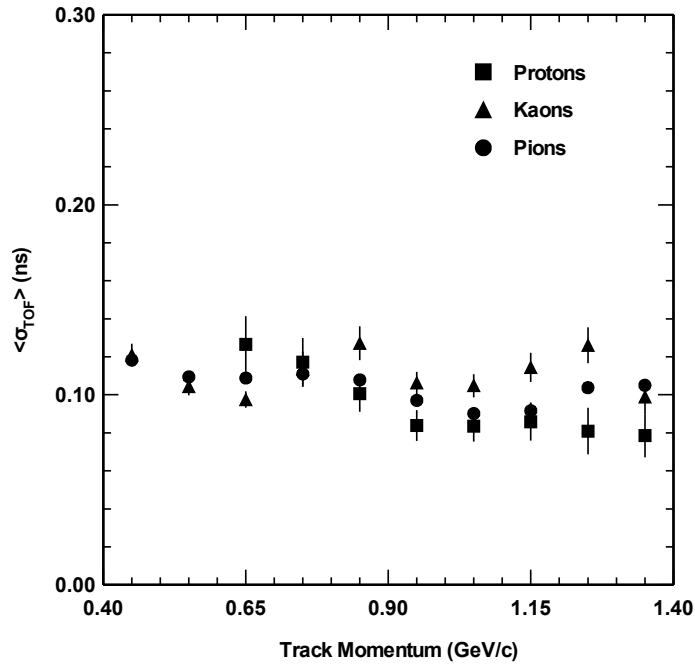


Figure 18: The averaged time resolution of the TOF over all counters and z , for different particle types [25].

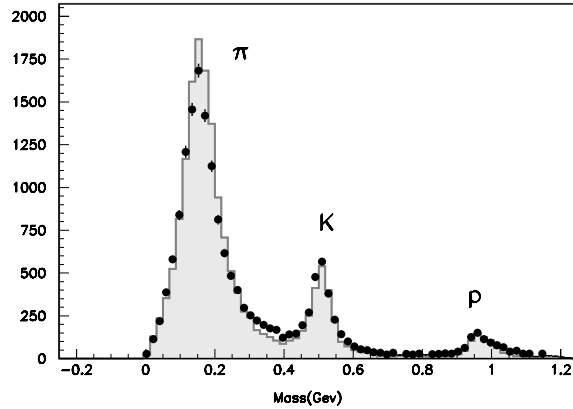


Figure 19: Mass distribution for TOF measurements for particle momenta below 1.2 GeV [25].

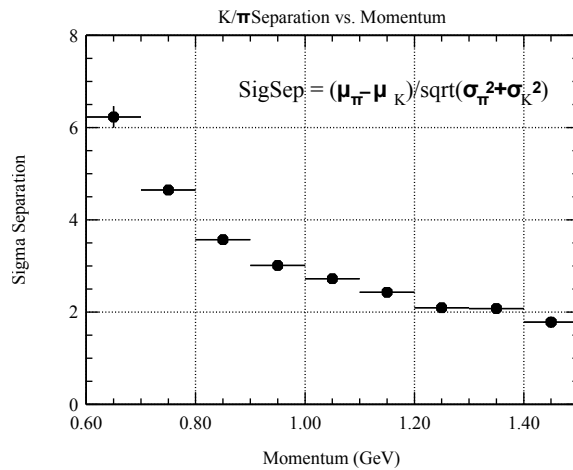


Figure 20: π^\pm/K^\pm separation by TOF [25].

For particle momenta below 1.2 GeV (which encompasses 90% of the particles produced by the $\Upsilon(4S)$ decays), a clear separation of peaks at the π , K and p masses is observed (see figure 19). The separation power depends on the particle momentum, as shown on figure 20.

2.2.6 Electromagnetic calorimeter - ECL

The main purpose of the electromagnetic calorimeter (ECL) is the detection of photons with high efficiency and good resolutions in energy and position. Good performance for energies below 500 GeV is especially important as most photons are the end products of cascade decays. The ECL also helps with the electron identification by comparing the momenta and the energy deposits of the charged particles.

The detection of high momentum π^0 which decay into two photons requires a precise determination of their opening angle and this requires a fine grained segmentation of the calorimeter. The ECL therefore uses a highly segmented array of CsI(Tl) crystals with a silicone photodiode readout in a magnetic field of 1.5 T. When an electron or a photon interacts with the crystal, it produces

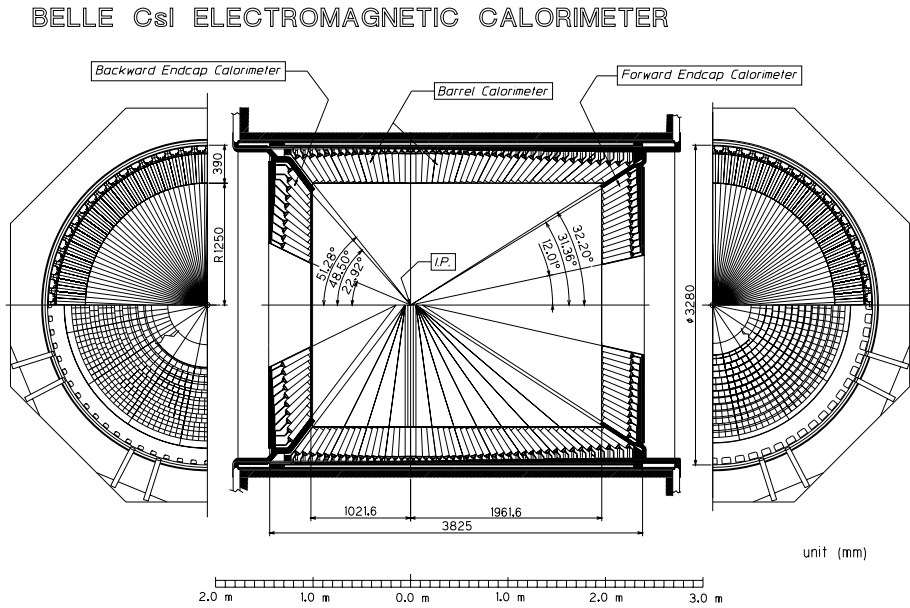


Figure 21: The configuration of ECL [25].

an electromagnetic shower by bremsstrahlung and pair creation, which is then detected.

The Belle ECL covers an angle of $17^\circ \leq \theta \leq 150^\circ$, and contains 8736 CsI(Tl) counters (see figure 21). The transverse area of each crystal is about $6 \times 6 \text{ cm}^2$. This transverse area size ensures that $\sim 80\%$ of the deposited energy by the EM shower remains in the same crystal, which improves the energy resolution. A smaller size would improve the position resolution, but decrease the energy resolution. The length of the crystal is 30 cm, corresponding to 16.2 radiation lengths, which ensures a good energy resolution for high energy particles by minimizing the shower leakage out of the rear of the counter. This resolution is $\sim 2.5\%$ for electron energies above 1 GeV.

The ECL is also used for distinguishing electrons and pions, as the pions deposit much less energy than electrons with the same momentum, due to their lower probability of bremsstrahlung and pair creation (see figure 22). The misidentification probability is found to be less than 1% for momenta above 2 GeV.

The energy calibration of the ECL has been carried out by using Bhabha and $e^+e^- \rightarrow \gamma\gamma$ events. The energy resolution achieved (for ECL and EFC) was 1.7% (see figure 23).

2.2.7 K_L and muon detector - KLM

The K_L and muon detector (KLM) identifies K_L and muon particles with a high efficiency over a broad momentum range greater than 600 MeV/c. It covers an angular range of $20^\circ - 155^\circ$ and consists of alternating layers of charged particle detectors and 4.7 cm thick iron plates. There are 15 detector and 14 iron layers in the barrel region and 14 detector layers in each of the forward and backward end caps.

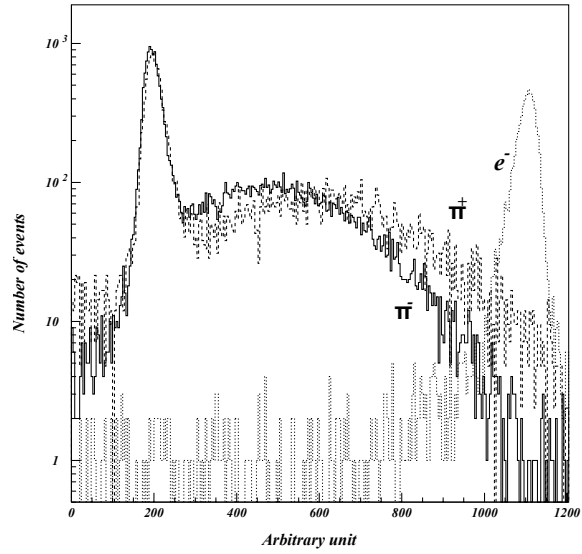


Figure 22: Distributions of the energy deposits in the ECL by e^- , π^+ and π^- at the momentum of 1 GeV/c [25].

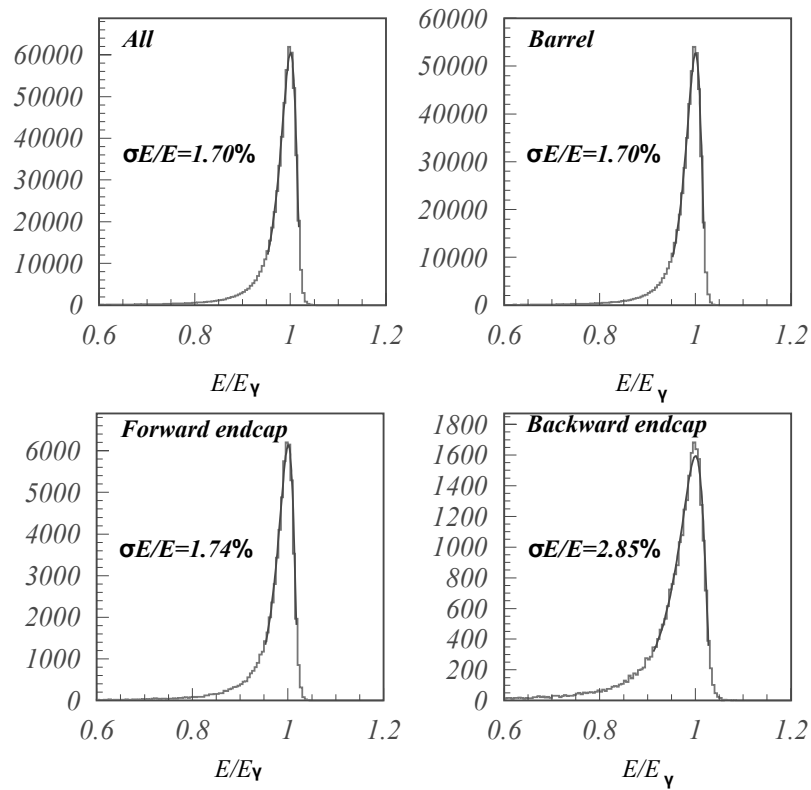


Figure 23: Energy resolutions measured from Bhabha events for overall, barrel, forward and backward end-cap calorimeters [25].

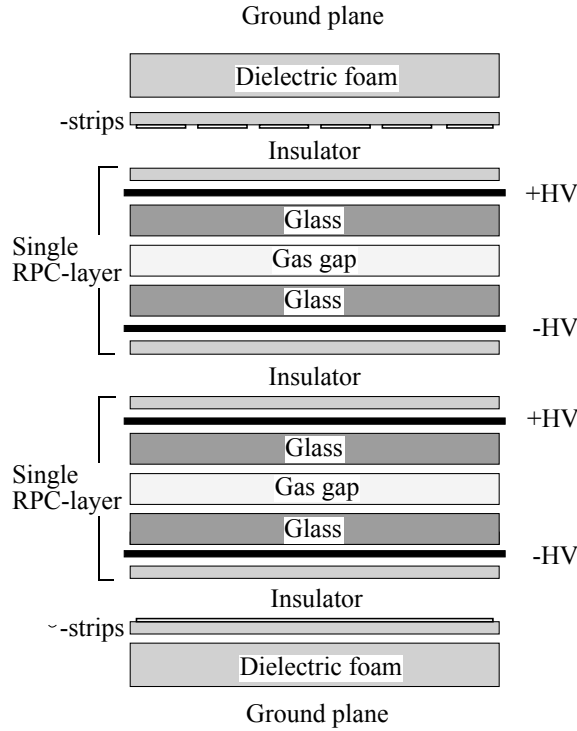


Figure 24: Cross-section of a KLM superlayer [25].

The iron layers provide 3.9 interaction lengths of material, and the ECL system provides an additional 0.8 of interaction length for K_L conversion. The K_L that interact in the ECL or iron produce a shower of ionizing particles, which determines the K_L direction. The multiple layers and detectors also provide $\mu/(K, \pi)$ discrimination by measuring their range and transverse scattering, as the muons penetrate material easier than other particles with smaller deflections.

The charged particle detection layers are glass-electrode-resistive plate counters (RPC). They have two parallel plate electrodes with high resistivity ($> 10^{10} \Omega\text{cm}$), separated by a gas filled gap. The ionizing particle initiates a streamer that results in a local discharge of the plates, which induces a signal on the external pickup strips. Two RPCs are sandwiched between the orthogonal θ and ϕ pickup strips to form a superlayer (see figure 24). The gas used in the KLM is a mixture of 62% HFC-134a (CH_2FCF_3), 30% argon and 8% butane-silver (C_4H_{10}).

The muon identification efficiency for the KLM is better than 90% with a fake rate of less than 5%, and the spatial resolution is found out to be 1.2 cm (see figure 25).

2.3 TRIGGER AND DATA ACQUISITION

At a luminosity of $10^{34}/\text{cm}^2\text{s}$, the trigger rates for various physical processes are listed in table 3. The trigger system is needed to keep the background rates within the tolerance of the data acquisition system (DAQ) (max 500 Hz), while maximizing the efficiency for physics events of interest. The trigger system imposes a set of selection criteria on an event to select the events for which the raw

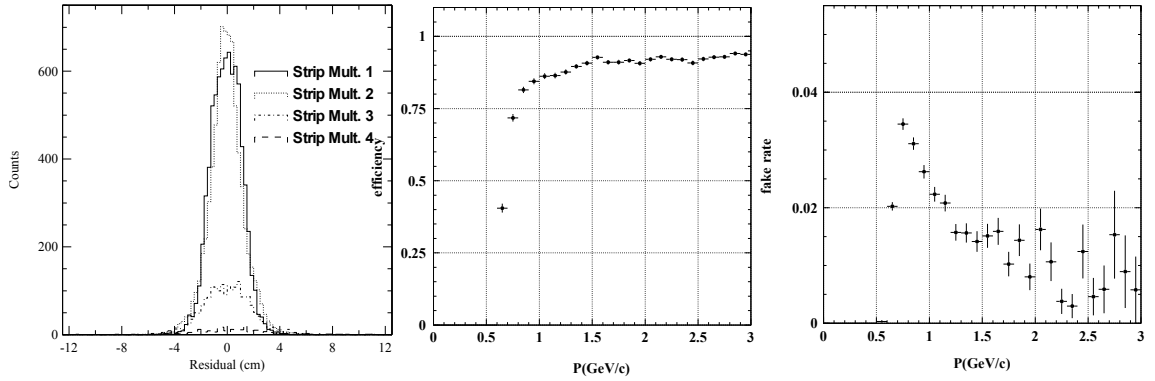


Figure 25: Left - Spatial resolution of a KLM superlayer, middle - Muon detection efficiency vs. momentum in the KLM, right - Muon fake rate vs. momentum in the KLM [25].

process	trigger rate [Hz]
$\Upsilon(4S) \rightarrow B\bar{B}$	12
$e^+e^- \rightarrow q\bar{q}, (q = u, d, s, c)$	28
$e^+e^- \rightarrow \tau^+\tau^-$ or $\mu^+\mu^-$	16
Bhabha, radiative Bhabha	500
$\gamma\gamma(p_T \leq 0.3 \text{ GeV}/c)$	35
beam induced bkg	$\mathcal{O}(100)$
cosmic rays	20

Table 3: Trigger rates for various physical processes for the Belle detector [25].

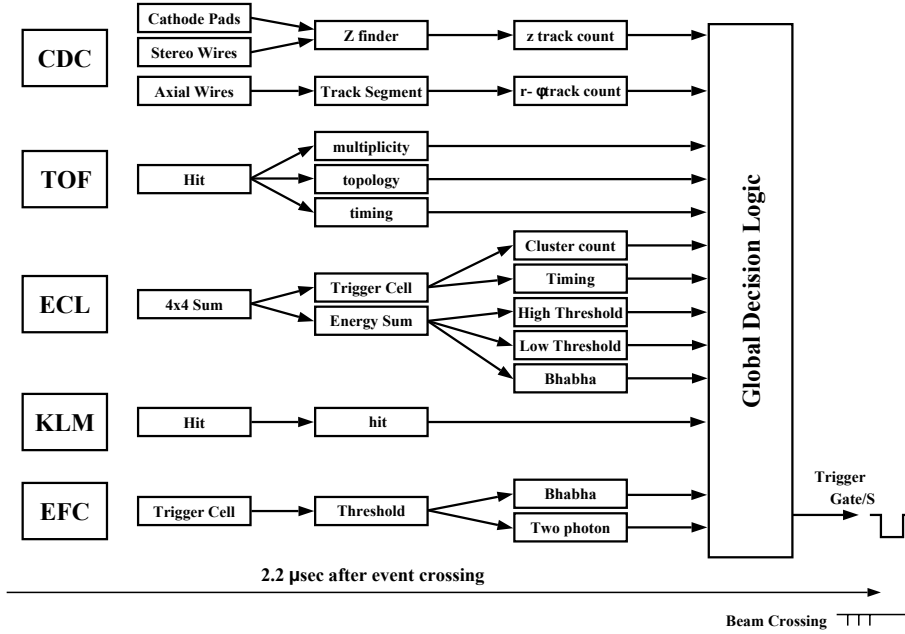


Figure 26: The level 1 trigger system for the Belle detector [25].

data should be transferred by the DAQ from the detector to the data storage system.

The Belle trigger system consists of a level 1 (L1) hardware trigger, a level 3 (L3) software trigger and a level 4 (L4) offline trigger.

2.3.1 L1 trigger

The L1 hardware trigger system consists of the sub-detector trigger systems (CDC, TOF, ECL, KLM and EFC) and a central trigger system called the global decision logic (GDL) (see figure 26). The sub-detector triggers fall into two categories, the track triggers and the energy triggers. The GDL receives the sub-detector trigger signals within 1.85 μs and provides the trigger signal 2.2 μs after the e^+e^- collision.

The CDC provides two types of triggers; the $r-\phi$ trigger, which is based on signals from the axial superlayers and the z-trigger, which takes information from the cathode strips. The CDC trigger is required to be fully efficient for tracks originating from the IP and to be relatively insensitive to background tracks from other sources.

The TOF trigger provides an event timing signal and information on the hit multiplicity and topology. Because the timing of the event must be sufficiently precise, it has to have a time jitter of less than 10 ns.

The ECL trigger must generate fast trigger signals in order to provide a fully efficient trigger both for neutral and charged particles. Two kinds of triggers are implemented, a total energy trigger, which is sensitive to events with high electromagnetic energy deposits, and a cluster counting trigger, which is sensitive to multi-hadronic events that contain low-energy clusters and minimum ionizing particles.

The KLM trigger has to save events which include muon tracks with a high efficiency, even if the cleanliness of the signal is not high.

The EFC trigger provides two types of information; the energy and the location of signals in the BGO crystals. The trigger can discriminate between Bhabha events, which have a coplanar forward/backward coincidence of energetic electromagnetic showers, and two photon events, which produce a single electromagnetic shower together with some CDC tracks or ECL clusters.

The GDL receives up to 48 trigger signals from the sub-detector trigger systems and makes global correlations between them. It takes 350 ns to generate the final trigger signal. The final triggers fed into the GDL are:

- Multi track triggers - they require at least 3 tracks from the $r - \phi$ CDC trigger and 1 track from the CDC z-trigger.
- Total energy triggers - they use the ECL energy sum trigger and are vetoed by ECL Bhabha and cluster triggers.
- Isolated cluster counting trigger - requires at least 4 ECL isolated clusters, which avoids Bhabha events.
- Bhabha triggers - take 2 tracks in the CDC $r - \phi$ trigger and 1 track in the CDC z-trigger.
- Muon triggers - require at least 2 CDC $r - \phi$ tracks and the KLM trigger.
- Monitor triggers - a random trigger and prescaled triggers for monitoring purposes.

The combined efficiency for all triggers is more than 99.5% for multi-hadronic data samples.

2.3.2 *L3 trigger*

The L3 trigger is a software trigger which has to further reduce the events selected for storage. It performs a fast reconstruction of events and rejects events with no tracks with an impact parameter of $|z| < 5$ cm and a total ECL energy deposit of less than 3 GeV. If the L1 trigger categorizes an event as a Bhabha event, the L3 trigger passes it through. The L3 trigger reduces the event rate by 50%, while retaining 99% of hadronic events.

2.3.3 *L4 trigger*

The L4 trigger is an offline trigger that decides which events shall undergo full reconstruction and thus reduces the CPU time needed for the data summary tape production (see section 2.3.4). It requires events with the ECL deposited energy of more than 4 GeV, at least one track with a transverse momentum larger than 300 MeV/c and an impact parameter with $r < 1$ cm and $|z| < 4$ cm. It rejects 78% of all triggered events while keeping nearly all the hadronic events.

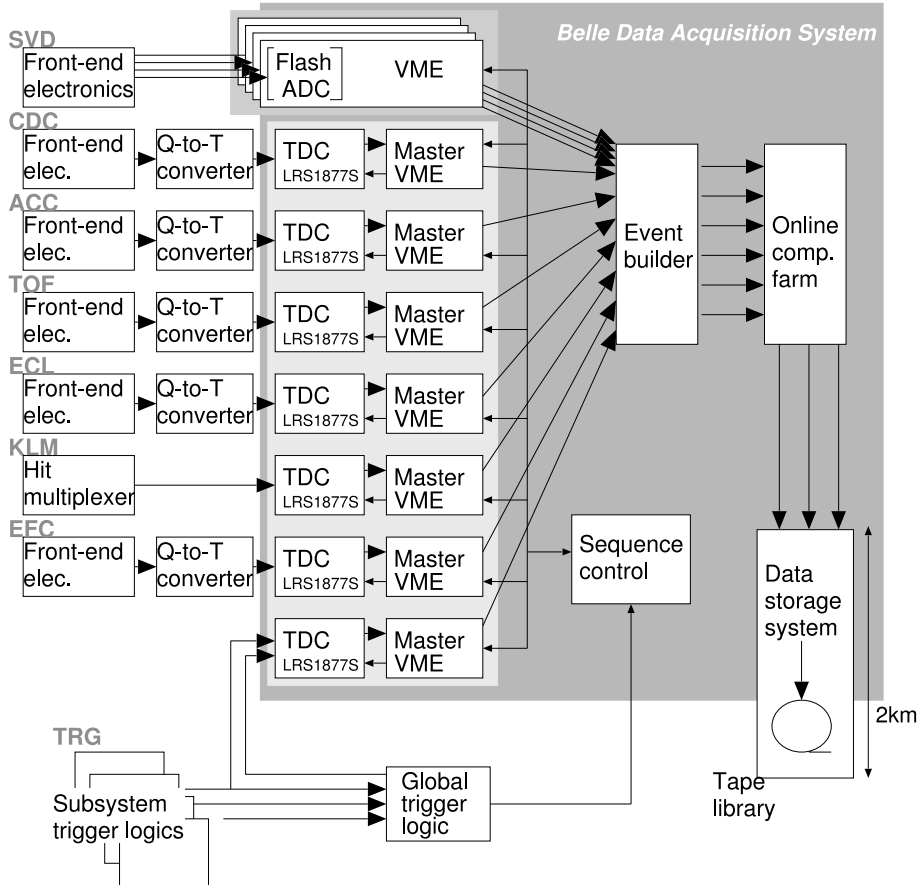


Figure 27: The data acquisition system scheme for the Belle detector [25].

2.3.4 Data acquisition system

To satisfy the 500 Hz working rate with a deadtime fraction of less than 10%, the data acquisition system is devised in a parallel scheme. The system is divided into 7 subsystems running in parallel, each system handling the data from a sub-detector. The data is then combined into a single event record, converting the "detector-by-detector" parallel data streams to a single "event-by-event" data stream. This data stream is sent through the L3 software trigger and then to a mass storage system (see figure 27).

The event builder then constructs a complete event data from detector signals. Before the full event reconstruction, the data is sent through the L4 trigger. The events accepted by the L4 trigger are then fully reconstructed and the information is stored to the DST. In this stage, the raw data is converted into physics objects, such as position and momentum 4-vectors, particle identification information, and so on.

For physics analyses, the complete data from the DST is not needed, so minimal sets of data required for physics analyses are stored in a "mini-DST" format. At this level, the hadronic event size is about 40 kB.

2.4 PARTICLE IDENTIFICATION

The particle identification at Belle is done by combining measurements from different subdetectors capable of discriminating between particle types. For each subdetector, a probability for the subdetector to identify a particle as a particle of type f ($f = \pi, K, p, e, \mu$) $P_{f,i}$ is determined. Then, the product of the different probabilities $P_f = \prod_i P_{f,i}$ is calculated, and this product is used to calculate a probability ratio, which discriminates between particles of type f and f' :

$$R_{f/f'} = \frac{P_f}{P_f + P_{f'}}. \quad (50)$$

This ratio can take a value in the range $[0, 1]$ and is a single variable which can be used to discriminate between two types of particles.

2.4.1 Charged hadron identification

The probability P_f , ($f = K, \pi, p$) is determined from information from three subdetectors:

- the $\frac{dE}{dx}$ measurement in the CDC,
- the time-of-flight measurement in TOF,
- the number of detected photons in ACC.

For each of the subdetectors, a probability that the subdetector detected a particle of type f is calculated, and the probability P_f is calculated as a product of all subdetector probabilities:

$$P_f = P_f^{\text{dE/dx}} \cdot P_f^{\text{ACC}} \cdot P_f^{\text{TOF}}. \quad (51)$$

The dE/dx probability is based on a difference between the measured and expected value of the energy loss for particle type f and is parameterized by a Gaussian distribution:

$$P_f^{\text{dE/dx}} = \frac{e^{-\chi^2/2}}{\sqrt{2\pi}\sigma_{\text{dE/dx}}}, \quad \chi^2 = \left(\frac{(\text{dE/dx})_{\text{measured}} - (\text{dE/dx})_{f,\text{expected}}}{\sigma_{\text{dE/dx}}} \right)^2, \quad (52)$$

where $(\text{dE/dx})_{\text{measured}}$ is the measured energy loss, $(\text{dE/dx})_{f,\text{expected}}$ is the expected energy loss for particle of type f , and $\sigma_{\text{dE/dx}}$ is the (expected) resolution of the dE/dx measurement.

The TOF probability is based on the measured and expected times for each photo-tube. The χ^2 is constructed by taking the difference between two two-

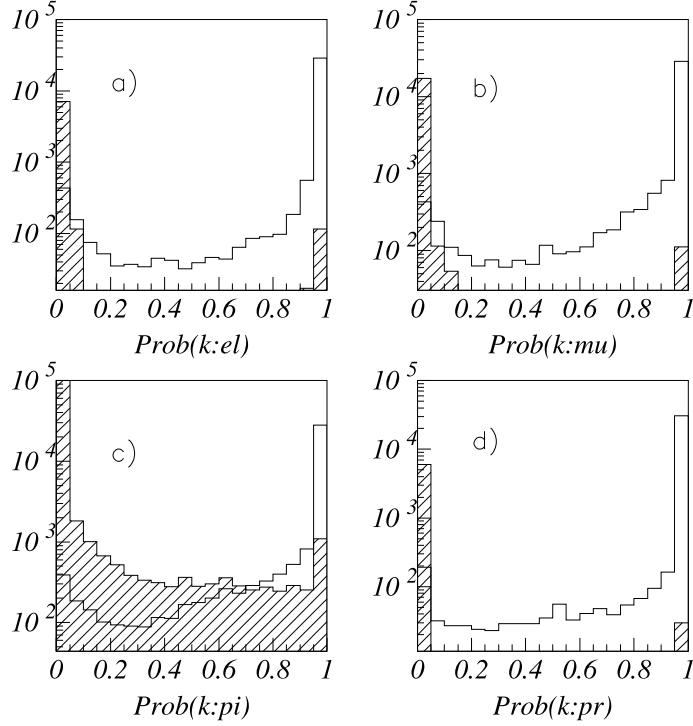


Figure 28: The likelihood ratio distributions for signal kaons and assumed background particle tracks, $R_{K/*}$, where $*$ = a) e , b) μ , c) π and d) p . The empty histograms are distributions of K tracks, and the dashed histograms are background tracks in each case.

vectors, one containing the observed times for each of the two photo-tubes and the other containing the predicted times:

$$\begin{aligned}\Delta^i &= t_o^i - t_p^i, \quad i = 0, 1, \\ \chi^2 &= \sum_j \vec{\Delta}_j \mathbf{E}_j^{-1} \vec{\Delta}_j,\end{aligned}\quad (53)$$

where j denotes the j -th TOF hit and \mathbf{E}_j is the 2×2 error matrix for the j -th TOF hit two vector $\vec{\Delta}_j$. The probability is then constructed as a Gaussian distribution:

$$P_f^{\text{TOF}} = \frac{e^{-\chi^2/2}}{\sqrt{2\pi} \prod_j \sigma_j}, \quad (54)$$

where σ_j is the expected timing resolution.

The ACC probability is based on comparing the observed number of photoelectrons (N_{pe}) with a threshold value ($N_{pe,f}^{\text{th}}$), using the expected efficiency ε at the measured momentum:

$$P_f^{\text{ACC}} = \begin{cases} \varepsilon_f, & N_{pe} \geq N_{pe,f}^{\text{th}} \\ 1 - \varepsilon_f, & N_{pe} \leq N_{pe,f}^{\text{th}} \end{cases}. \quad (55)$$

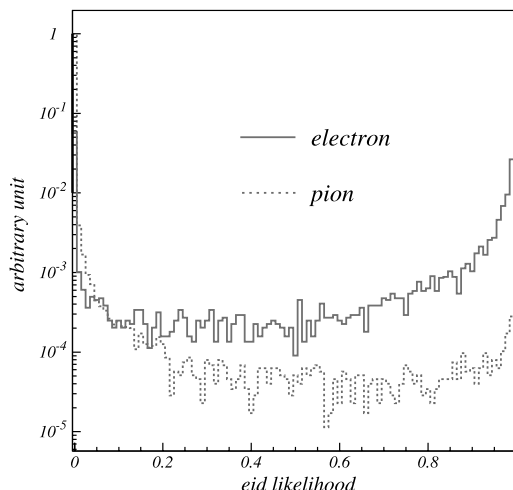


Figure 29: Electron identification likelihood ratio for electrons - solid line and pions - dashed line [25].

If information from a certain sub-detector is not available, the probability for any particle type is set to $P_i^k = 0.5$, $i = \pi, K, p$, $k = dE/dx, TOF, ACC$. In this way, this sub-detector has no effect in the combined likelihood ratio.

Figure 28 shows the likelihood ratios for signal kaons and assumed background particle tracks, $R_{K/*}$, $* = e, \mu, \pi, p$.

2.4.2 Electron identification

In order to distinguish electrons from hadrons, muons and photons, two approaches are used [28]. The first exploits the difference between the electromagnetic showers induced by electrons and the ones induced by hadrons. The second approach makes use of the difference in velocity between electrons and hadrons at the same momentum, which can be determined by the dE/dx measurement and the observation of light yield in the ACC array. These two approaches are then combined into a single likelihood.

The discriminants used are (see figure 29):

- Position matching between the track, extrapolated into the ECL, and the cluster position measured in the ECL. The χ^2 is calculated as

$$\chi^2 = \left(\frac{\Delta\phi}{\sigma_{\Delta\phi}}\right)^2 + \left(\frac{\Delta\theta}{\sigma_{\Delta\theta}}\right)^2, \quad (56)$$

where $\Delta\phi$ and $\Delta\theta$ are the differences between the cluster position and an electron track in the azimuth and polar angles, respectively, and $\sigma_{\Delta\phi}$ and $\sigma_{\Delta\theta}$ are the widths obtained by fitting the $\Delta\phi$ and $\Delta\theta$ distributions for electrons with Gaussian functions.

- The ratio of energy E measured in the ECL and the charged track momentum p . For electrons, which have negligible mass compared to their momentum, this ratio is 1 within measurement errors, whereas the other hadrons have this ratio typically smaller than 1.

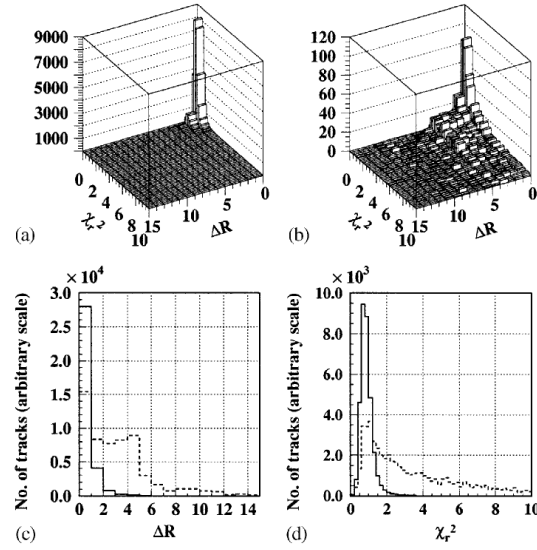


Figure 30: a) ΔR vs. χ_r^2 for single muons, b) ΔR vs. χ_r^2 for single pions, c) ΔR , d) χ_r^2 for muons - solid histograms and pions - dashed histograms [25].

- The transverse shower shape in the ECL. The shape is quantified by the variable $E9/E25$, defined as a ratio of energy deposited in a 3×3 array of crystals surrounding the crystal in the center of the shower to the energy deposited in a 5×5 array of crystals with the same center. Electrons exhibit a peak at 0.95, while the other hadrons have the value at a lower range.
- The dE/dx measurement probability, which is defined in the same way as with charged particle identification (see chapter 2.4.1).
- The light yield in ACC, which distinguishes between electrons and hadrons in the momentum region below ~ 1.0 GeV, as the Cherenkov threshold for electrons is only a few MeV, while that of other hadrons is 0.5 – 1.0 GeV.

2.4.3 Muon identification

The muon probability is constructed using two quantities; ΔR , which is the difference between the measured and expected range of the track, and χ_r^2 , the goodness of fit of the transverse deviations of all hits associated with the track [29]. This is calculated at each detector plane with Kalman filtering, energy loss and multiple scattering effects (see figure 30).

2.5 MONTE CARLO SIMULATION

The physics analyses require a very good understanding of physics processes undergoing in decays of particles and in the interaction of particles with the detector material in order to correctly interpret the results, thus reducing the error. These processes are highly complex, and many of them are not yet measured, and so can not be described analytically and thus taken into account when interpreting the results. That is why the processes are modeled by a Monte Carlo

(MC) simulation, and samples of data are generated by this simulation, mimicking the real decays and detector responses as closely as possible.

There are currently 6 so-called "streams" of Monte Carlo data samples produced by the Belle collaboration, where each stream corresponds to the same amount of real data as collected in the whole Belle data-taking period. The amount of all Monte Carlo data samples is bigger than the amount of real data collected in order to reduce the possible uncertainties.

The Monte Carlo sample generation has two steps. In the first step, the e^+e^- collision is simulated, producing sets of outgoing particles, called events. This is done by two event generators, the EvtGen generator [30], which is used to model the $B\bar{B}$ events and incorporates known properties of particles, such as mass, charge, branching ratios, spin, etc., measured by numerous experiments in form of world averages [1], and the JetSet generator [31], which is used to model the continuum events. The hadronization of quarks is simulated with the Lund string fragmentation model [32].

The second step is the detector response simulation, which is done by the CERN package GEANT [33]. GEANT also uses data from as many measurements of detector responses and particle - material interactions as possible to simulate the detector response as accurately as possible. The output of GEANT is then reconstructed in the same way as the real data, and saved in the mini-DST format to be used in an analysis.

METHOD OF MEASUREMENT

In this analysis, we measure the CP-violation parameter $\mathcal{A}_{\text{CP}}^{\Lambda_c}$, defined in equation (20) for the $\Lambda_c \rightarrow \Lambda\pi$ decay ¹. For this measurement, we will use the first of the equations (39). To use this equation, we must determine the angular distribution for the cosine of the helicity angle θ_h , the angle between the proton momentum and the momentum of the pion coming from Λ_c in the Λ CMS (see figure 31). Note that this is the same angle as the angle between the Λ emission direction in the Λ_c system and the direction of the p emission in the Λ system, defined in (39). The normalized angular distribution for our signal sample is then:

$$\frac{dN}{d \cos \theta_h} = \frac{N}{2} (1 + \alpha \cos \theta_h), \quad (57)$$

where N is the number of reconstructed events in the analysis data sample and with α we denoted the product $\alpha_{\Lambda_c} \alpha_{\Lambda}$ of the weak asymmetry parameters for the $\Lambda_c \rightarrow \Lambda\pi$ and $\Lambda \rightarrow p\pi$ decays as defined in (32) and (35), respectively.

So far, the best measurement of CP violation in the $\Lambda_c \rightarrow \Lambda\pi$ decay was done by the FOCUS collaboration [34], which obtained the results:

$$\alpha_{\Lambda_c} = -0.78 \pm 0.16 \pm 0.13, \quad \mathcal{A}_{\text{CP}}^{\Lambda_c} = -0.07 \pm 0.19 \pm 0.12, \quad (58)$$

where the first cited error is statistical and the second is systematic. Their method of measurement was to measure the angular distribution (57) for Λ_c^+ and $\bar{\Lambda}_c^-$ decays separately and with the known α_{Λ} coefficient obtain the coefficients α_{Λ_c} and $\alpha_{\bar{\Lambda}_c}$, which were then used to calculate the $\mathcal{A}_{\text{CP}}^{\Lambda_c}$ parameter with the equation (20).

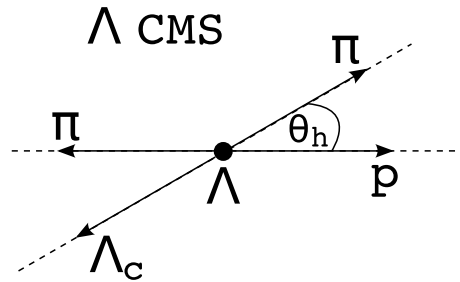


Figure 31: Definition of the helicity angle used in the analysis.

¹ Whenever we write Λ_c without a sign, it implies both the Λ_c^+ and its charge conjugate.

Given an expected 100 times larger number of $\Lambda_c \rightarrow \Lambda\pi$ decays in our analysis sample, we employed a different method of measuring $\mathcal{A}_{\text{CP}}^{\Lambda_c}$. First, we assume that the CP-violating effects are small compared to P-violation and measure the α parameter, averaged over Λ_c^+ and $\overline{\Lambda}_c^-$ decays, and then measure the small deviation from the average α , which is linked to the \mathcal{A}_{CP} parameter, which measures the amount of CP violation in the $\Lambda_c \rightarrow \Lambda\pi, \Lambda \rightarrow p\pi$ decay chain. From this parameter, we can get the $\mathcal{A}_{\text{CP}}^{\Lambda_c}$ parameter by using the best known measurement of $\mathcal{A}_{\text{CP}}^{\Lambda}$. The method is described in the two subsequent sections.

3.1 METHOD OF MEASUREMENT OF THE AVERAGE WEAK ASYMMETRY PARAMETER

First, we assume that the CP violation in the Λ_c decay chain is small (see chapter 1.3). This means,

$$d\alpha \ll \langle \alpha \rangle, \quad \langle \alpha \rangle \approx \alpha \approx \overline{\alpha}, \quad (59)$$

where $d\alpha$ is the difference between the α and $\overline{\alpha}$ coefficients, and $\langle \alpha \rangle$ is their average.

With the above assumption, we can first measure the average weak asymmetry parameter $\langle \alpha \rangle$ by joining the Λ_c^+ and $\overline{\Lambda}_c^-$ samples and determining the angular distribution (57).

The angular distribution is determined by reconstructing the joined Λ_c^+ and $\overline{\Lambda}_c^-$ events and selecting only events from the whole data sample that satisfy a number of selection criteria, thus obtaining the analysis data sample. Then, for the selected events, $\cos \theta_h$ is calculated and the events are divided into bins in the $\cos \theta_h$ variable.

We can express the number of reconstructed signal events in each bin of the joined Λ_c^+ and $\overline{\Lambda}_c^-$ analysis data sample as:

$$N_i^{\text{rec,join}}(\cos \theta_{h,i}) = N_i^{0,\text{join}}(\cos \theta_{h,i}) \text{Br}(\Lambda_c \rightarrow \Lambda\pi)(\cos \theta_{h,i}) \text{Br}(\Lambda \rightarrow p\pi)(\cos \theta_{h,i}) \langle \varepsilon \rangle_i(\cos \theta_{h,i}), \quad (60)$$

where $N_i^{\text{rec,join}}$ is the number of reconstructed Λ_c^+ and $\overline{\Lambda}_c^-$ decay chain signal events in the i -th bin, $N_i^{0,\text{join}}$ is the number of all produced Λ_c^+ and $\overline{\Lambda}_c^-$ signal events that fall into the i -th bin, $\text{Br}(\Lambda_c \rightarrow \Lambda\pi)(\cos \theta_{h,i})$ and $\text{Br}(\Lambda \rightarrow p\pi)(\cos \theta_{h,i})$ are the angular dependent branching ratios for the decays of Λ_c and Λ , $\cos \theta_{h,i}$ is the value of $\cos \theta_h$ in the i -th bin, and $\langle \varepsilon \rangle_i$ is the efficiency for the reconstruction of both the $\Lambda_c^+ \rightarrow \Lambda\pi^+, \Lambda \rightarrow p^+\pi^-$ decay chain and the charged conjugated one in the i -th bin.

We can express the angular dependence of the branching ratios as derived in the chapter 1.4.1:

$$\text{Br}(\Lambda_c \rightarrow \Lambda\pi)(\cos \theta_{h,i}) \text{Br}(\Lambda \rightarrow p\pi)(\cos \theta_{h,i}) = \text{Br}^0 \frac{1}{2} (1 + \langle \alpha \rangle \cos \theta_{h,i}), \quad (61)$$

where with Br^0 we denoted the product of the absolute branching ratios for the $\Lambda_c \rightarrow \Lambda\pi$ and $\Lambda \rightarrow p\pi$ decays. The angular dependence of the number of

all produced signal events is tied to the Λ_c^+ and $\bar{\Lambda}_c^-$ production asymmetry; the forward-backward asymmetry (see [1] and chapter 3.2), however, this asymmetry is an antisymmetric function with respect to particles and antiparticles, and since we joined the Λ_c^+ and $\bar{\Lambda}_c^-$ samples, this dependence cancels out. With this, we have the expression for the number of reconstructed signal events in each bin:

$$N_i^{\text{rec,join}}(\cos \theta_{h,i}) = N_i^{0,\text{join}} \text{Br}^0 \frac{1}{2} (1 + \langle \alpha \rangle \cos \theta_{h,i}) \langle \varepsilon \rangle_i(\cos \theta_{h,i}). \quad (62)$$

For each $\cos \theta_h$ bin, the number of reconstructed signal events is determined by fitting the Λ_c mass distribution in this bin. This number is then divided by the efficiency for reconstructing the Λ_c decay chain in this bin.

We also need to account for the detector measurement resolution, which causes the measured particle masses and momenta to be slightly different than the actual ones, and when calculating the $\cos \theta_h$, this results in events migrating from the actual $\cos \theta_h$ bin to which they belong to. To correct this, we perform a deconvolution of the numbers of events, with the deconvolution matrix determined from Monte Carlo simulation.

After this procedure, we are left with the true $\cos \theta_h$ distribution (57) of Λ_c signal events. From this distribution, we can determine the $\langle \alpha \rangle$ parameter by fitting the distribution with a linear function.

3.2 METHOD OF MEASUREMENT OF THE CP-VIOLATING PARAMETER

For measuring \mathcal{A}_{CP} , we reconstruct the Λ_c^+ and $\bar{\Lambda}_c^-$ samples separately and make analysis samples by selecting events which satisfy the selection criteria. We then measure the reconstructed asymmetry in bins of $\cos \theta_h$, where for the i -th bin, the reconstructed asymmetry is:

$$\mathcal{A}_i^{\text{rec}}(\cos \theta_{h,i}) = \frac{N_i^{\text{rec}}(\cos \theta_{h,i}) - \bar{N}_i^{\text{rec}}(\cos \theta_{h,i})}{N_i^{\text{rec}}(\cos \theta_{h,i}) + \bar{N}_i^{\text{rec}}(\cos \theta_{h,i})}, \quad (63)$$

where N_i^{rec} and \bar{N}_i^{rec} are the numbers of reconstructed Λ_c^+ and $\bar{\Lambda}_c^-$ events in the i -th bin, respectively. These numbers can be expressed as:

$$\begin{aligned} N_i^{\text{rec}}(\cos \theta_{h,i}) &= \\ & N^0(\cos \theta_{h,i}) \text{Br}(\Lambda_c^+ \rightarrow \Lambda \pi^+)(\cos \theta_{h,i}) \text{Br}(\Lambda \rightarrow p^+ \pi^-)(\cos \theta_{h,i}) \varepsilon_i(\cos \theta_{h,i}), \\ \bar{N}_i^{\text{rec}}(\cos \theta_{h,i}) &= \\ & \bar{N}^0(\cos \theta_{h,i}) \text{Br}(\bar{\Lambda}_c^- \rightarrow \bar{\Lambda} \pi^-)(\cos \theta_{h,i}) \text{Br}(\bar{\Lambda} \rightarrow \bar{p}^- \pi^+)(\cos \theta_{h,i}) \bar{\varepsilon}_i(\cos \theta_{h,i}), \end{aligned} \quad (64)$$

where N^0 is the produced numbers of Λ_c^+ , ε_i is the efficiency of reconstruction for Λ_c^+ events, and the quantities with bars are the corresponding quantities for the $\bar{\Lambda}_c^-$ events.

We again express the angular dependence of the branching ratios as:

$$\text{Br}(\Lambda_c^+ \rightarrow \Lambda \pi^+)(\cos \theta_{h,i}) \text{Br}(\Lambda \rightarrow p^+ \pi^-)(\cos \theta_{h,i}) = \text{Br}^0 \frac{1}{2} (1 + \alpha \cos \theta_{h,i}), \quad (65)$$

$$\text{Br}(\overline{\Lambda}_c \rightarrow \overline{\Lambda} \pi^-)(\cos \theta_{h,i}) \text{Br}(\overline{\Lambda} \rightarrow \overline{p}^- \pi^+)(\cos \theta_{h,i}) = \text{Br}^0 \frac{1}{2} (1 + \overline{\alpha} \cos \theta_{h,i}),$$

where $\alpha = \alpha_{\Lambda_c^+} \alpha_\Lambda$ and $\overline{\alpha} = \alpha_{\overline{\Lambda}_c} \alpha_{\overline{\Lambda}}$ are the products of asymmetry parameters for the Λ_c^+ and $\overline{\Lambda}_c$ decay chains, respectively, and Br^0 is the product of the absolute branching ratios which is the same for both decays. The numbers of reconstructed signal events are thus:

$$N_i^{\text{rec}}(\cos \theta_{h,i}) = N^0(\cos \theta_{h,i}) \text{Br}^0 \frac{1}{2} (1 + \alpha \cos \theta_{h,i}) \varepsilon_i(\cos \theta_{h,i}), \quad (66)$$

$$\overline{N}_i^{\text{rec}}(\cos \theta_{h,i}) = \overline{N}^0(\cos \theta_{h,i}) \text{Br}^0 \frac{1}{2} (1 + \overline{\alpha} \cos \theta_{h,i}) \overline{\varepsilon}_i(\cos \theta_{h,i}).$$

Additionally to assuming a small CP-violating effect as in the previous section, we also assume that the produced number of Λ_c^+ and $\overline{\Lambda}_c$ particles is approximately the same for each bin (this means that we assumed a small forward-backward asymmetry, see below) and that the efficiencies for reconstructing either Λ_c^+ or $\overline{\Lambda}_c$ in each bin are approximately the same:

$$\begin{aligned} N_i^0 &\approx \overline{N}_i^0 \approx \langle N^0 \rangle_i, \\ \varepsilon_i &\approx \overline{\varepsilon}_i \approx \langle \varepsilon \rangle_i. \end{aligned} \quad (67)$$

With these assumptions, we can write to the first order in small quantities dN^0 , $d\alpha$ and $d\varepsilon$:

$$\begin{aligned} N_i^0 &= \langle N^0 \rangle_i + dN_i^0, \quad dN_i^0 \ll \langle N^0 \rangle_i, \\ \overline{N}_i^0 &= \langle N^0 \rangle_i - dN_i^0, \\ \alpha &= \langle \alpha \rangle + d\alpha, \quad d\alpha \ll \langle \alpha \rangle, \\ \overline{\alpha} &= \langle \alpha \rangle - d\alpha, \\ \varepsilon_i &= \langle \varepsilon \rangle_i + d\varepsilon_i, \quad d\varepsilon_i \ll \langle \varepsilon \rangle_i, \\ \overline{\varepsilon}_i &= \langle \varepsilon \rangle_i - d\varepsilon_i. \end{aligned} \quad (68)$$

If we put expressions (68) into equations (66) and then into the definition of the reconstructed asymmetry (63), we get to the first order in small quantities:

$$\begin{aligned} \mathcal{A}_i^{\text{rec}}(\cos \theta_{h,i}) &= \mathcal{A}_i^{\text{FB}}(\cos \theta_{h,i}) + \mathcal{A}_i^\varepsilon(\cos \theta_{h,i}) + \mathcal{A}_{\text{CP}} \frac{\cos \theta_{h,i}}{1 + \langle \alpha \rangle \cos \theta_{h,i}}, \\ \mathcal{A}_i^{\text{FB}} &= \frac{N_i^0 - \overline{N}_i^0}{N_i^0 + \overline{N}_i^0}, \\ \mathcal{A}_i^\varepsilon &= \frac{\varepsilon_i - \overline{\varepsilon}_i}{\varepsilon_i + \overline{\varepsilon}_i}, \\ \mathcal{A}_{\text{CP}} &= \frac{\alpha - \overline{\alpha}}{\alpha + \overline{\alpha}}. \end{aligned} \quad (69)$$

Here \mathcal{A}^{FB} is the forward-backward asymmetry, the asymmetry in production of Λ_c^+ and $\overline{\Lambda}_c^-$. This asymmetry arises because of the asymmetry in the production of $c\bar{c}$ (and actually any fermion anti-fermion pair) in e^+e^- collisions. It occurs at tree level because of the interference between the two possible $e^+e^- \rightarrow c\bar{c}$ processes - one mediated by a virtual γ , and one by a Z^0 particle. This process is well understood and contributes at the percent level [1]. It can also come from higher-order QED effects where it is expected to peak sharply in the forward and backward directions, but the precise shape is not known [35]. The asymmetry is an odd function of the c quark (and of the Λ_c) polar angle in the CMS and hence cancels out when integrated over that angle.

Due to CP symmetry conservation in the production of Λ_c baryons through the EM and strong interaction, we know that \mathcal{A}_{FB} must be an antisymmetric function in the polar angle:

$$\mathcal{A}^{\text{FB}}(\cos \theta^*) = -\mathcal{A}^{\text{FB}}(-\cos \theta^*). \quad (70)$$

In our analysis, however, we can assume that there is no angular dependence of \mathcal{A}^{FB} on the angle θ_h , since this angle is defined in the Λ CMS, which is different for every event, so any angular dependence of \mathcal{A}^{FB} on θ_h will be evened out. We will check this assumption with the Monte Carlo simulation and estimate the systematic error on the result.

The \mathcal{A}^ε is the asymmetry for reconstruction of particles and antiparticles. It arises because of different interactions of final state particles and antiparticles with the matter in the detector. We can again assume that it has no angular dependence on the angle θ_h , for the same reasons as for the \mathcal{A}^{FB} asymmetry. This assumption can be checked using the decay chain $\Sigma^* \rightarrow \Lambda\pi$, $\Lambda \rightarrow p\pi$, which has the same final state particles, but no present CP-violation. This is because $\Sigma^* \rightarrow \Lambda\pi$ is a strong decay and is therefore not CP violating, and $\Lambda \rightarrow p\pi$, which is a weak decay and could have CP violation, has the measured CP asymmetry $\mathcal{A}_{\text{CP}}^\Lambda = (\alpha_\Lambda + \alpha_{\overline{\Lambda}})/(\alpha_\Lambda - \alpha_{\overline{\Lambda}})$ of 0.006 ± 0.021 [1] and is consistent with 0. With measuring this decay chain, we can again estimate the systematic error on the result.

With these assumptions, the reconstructed asymmetry is:

$$\mathcal{A}_i^{\text{rec}}(\cos \theta_{h,i}) = \mathcal{A}_i^{\text{FB}} + \mathcal{A}_i^\varepsilon + \mathcal{A}_{\text{CP}} \frac{\cos \theta_{h,i}}{1 + \langle \alpha \rangle \cos \theta_{h,i}}, \quad (71)$$

and the only angular dependence arises because of the \mathcal{A}_{CP} asymmetry. This way, we can determine the magnitude of \mathcal{A}_{CP} by fitting the reconstructed asymmetry with a function of the form $f(x) = k + \mathcal{A}_{\text{CP}}(x/(1 + \langle \alpha \rangle x))$, with using the measured $\langle \alpha \rangle$.

3.3 $\langle \alpha_{\Lambda_c} \rangle$ AND $\mathcal{A}_{\text{CP}}^{\Lambda_c}$ PARAMETERS FOR Λ_c DECAYS

The $\langle \alpha \rangle$ parameter that we measure using equation (62) is the decay parameter for the $\Lambda_c \rightarrow \Lambda\pi$, $\Lambda \rightarrow p\pi$ decay chain. To get the α_{Λ_c} decay parameter for the

$\Lambda_c \rightarrow \Lambda\pi$ decay, assuming that the CP-violation in this decay is 0 within the uncertainty of the measurement, we use the definition of $\langle\alpha\rangle$:

$$\langle\alpha\rangle = \frac{\alpha_{\Lambda_c} \alpha_{\Lambda} + \alpha_{\bar{\Lambda}_c} \alpha_{\bar{\Lambda}}}{2}. \quad (72)$$

If we assume no CP-violation in the $\Lambda_c \rightarrow \Lambda\pi$ decay, this means that

$$|\alpha_{\Lambda_c}| = |\alpha_{\bar{\Lambda}_c}| = |\langle\alpha_{\Lambda_c}\rangle|. \quad (73)$$

We can then calculate $\langle\alpha_{\bar{\Lambda}_c}\rangle$ by using the world averages of measurements of α_{Λ} and $\mathcal{A}_{\text{CP}}^{\Lambda}$ from [1]:

$$\begin{aligned} \alpha_{\Lambda} &= 0.642 \pm 0.013, \\ \mathcal{A}_{\text{CP}}^{\Lambda} &= \frac{\alpha_{\Lambda} + \alpha_{\bar{\Lambda}}}{\alpha_{\Lambda} - \alpha_{\bar{\Lambda}}} = 0.006 \pm 0.021. \end{aligned} \quad (74)$$

We use α_{Λ} and $\mathcal{A}_{\text{CP}}^{\Lambda}$ as independent parameters because $\bar{\alpha}_{\Lambda}$ is measured with significantly lower precision [1]. The measurements of α_{Λ} and $\mathcal{A}_{\text{CP}}^{\Lambda}$ with the dominant precision are from [36] and [37], respectively. The former is performed on Λ produced in $p\pi^-$ collisions, while the latter on $\Lambda\bar{\Lambda}$ pairs produced in $p\bar{p}$ annihilations. Hence the correlations between the two measurements are negligible.

With these quantities, we calculate $\langle\alpha_{\Lambda_c}\rangle$ as

$$\langle\alpha_{\Lambda_c}\rangle = \frac{\langle\alpha\rangle}{\alpha_{\Lambda}} (1 + \mathcal{A}_{\text{CP}}^{\Lambda}). \quad (75)$$

If we also assume no CP-violation in the $\Lambda \rightarrow p\pi$ decay (the world average for $\mathcal{A}_{\text{CP}}^{\Lambda}$ is consistent with this assumption), $\langle\alpha_{\Lambda_c}\rangle$ can be calculated as:

$$\langle\alpha_{\Lambda_c}\rangle = \frac{\langle\alpha\rangle}{\alpha_{\Lambda}}. \quad (76)$$

From equation (71) we get the asymmetry parameter \mathcal{A}_{CP} , which is linked to CP-violation in the $\Lambda_c \rightarrow \Lambda\pi, \Lambda \rightarrow p\pi$ decay chain. To get the CP asymmetry parameter $\mathcal{A}_{\text{CP}}^{\Lambda_c}$ linked to CP-violation in the $\Lambda_c \rightarrow \Lambda\pi$ decay, we again take the best measured value for the CP asymmetry parameter for $\Lambda \rightarrow p\pi$ decays, written in the second equation of (74) and with this value, we calculate the CP asymmetry parameter for $\Lambda_c \rightarrow \Lambda\pi$ decays as:

$$\mathcal{A}_{\text{CP}}^{\Lambda_c} = \frac{\alpha_{\Lambda_c} + \alpha_{\bar{\Lambda}_c}}{\alpha_{\Lambda_c} - \alpha_{\bar{\Lambda}_c}} = \frac{\mathcal{A}_{\text{CP}} - \mathcal{A}_{\text{CP}}^{\Lambda}}{1 - \mathcal{A}_{\text{CP}} \mathcal{A}_{\text{CP}}^{\Lambda}}. \quad (77)$$

With the assumption of no CP-violation in the $\Lambda \rightarrow p\pi$ decay, the $\mathcal{A}_{\text{CP}}^{\Lambda_c}$ parameter is the same as the \mathcal{A}_{CP} parameter:

$$\mathcal{A}_{\text{CP}}^{\Lambda_c} = \mathcal{A}_{\text{CP}}. \quad (78)$$

DEVELOPMENT OF THE MEASUREMENT METHOD ON MONTE CARLO SIMULATION

In order to ensure that the measurement method described in chapter 3 is valid, i.e. produces un-biased results, we first check the method by using a sample of events generated by a Monte Carlo (MC) simulation (see chapter 2.5).

4.1 PRESELECTION - HADRONIC EVENT SELECTION

Before we reconstruct our signal decays, the events must pass a hadronic event selection. This selection consists of a number of requirements, used to suppress non-hadronic events and select $e^+e^- \rightarrow \Upsilon(4S) \rightarrow B\bar{B}$, or $e^+e^- \rightarrow q\bar{q}$, $q=u,d,s,c$ events. The requirements are:

- For each event, there must be at least 3 reconstructed charged tracks and two reconstructed neutral clusters in the ECL barrel region.
- The charged track must have a transverse momentum bigger than 100 MeV/c, and impact parameters dr less than 2.0 cm and $|dz|$ less than 4.0 cm.
- The neutral clusters must have a deposited energy of bigger than 100 MeV in the polar angle region of $17^\circ < \theta < 150^\circ$.
- The primary vertex of the event must lie in the region $dr < 1.5$ cm and $|dz| < 3.5$ cm.
- To suppress the background from $\gamma\gamma$ processes and the beam induced background, the sum of momentum magnitudes in the z direction, calculated in the e^+e^- CMS, must be less than half the total available energy \sqrt{s} .
- To further suppress the QED processes, the energy sum of all clusters in the ECL should be greater than $0.18\sqrt{s}$.
- To suppress the background from $e^+e^- \rightarrow \tau^+\tau^-$ processes, the invariant mass of particles in each of the two hemispheres, divided by a plane perpendicular to the boost, must be greater than 1.8 GeV.

These requirements are satisfied by 99% of the $e^+e^- \rightarrow \Upsilon(4S) \rightarrow B\bar{B}$ events and 79.5% of $e^+e^- \rightarrow q\bar{q}$ events, while keeping only 5% of non-hadronic events. The efficiencies for various processes are shown in table 4.

process	ε	$\sigma \cdot \varepsilon$ [nb]
$B\bar{B}$	0.991	1.09
$q\bar{q}$	0.795	2.70
$\tau^+\tau^-$	0.049	0.05
Bhabha	0.00002	0.001
$\gamma\gamma$	0.004	0.04
Beam gas	0.09	0.11

Table 4: Efficiencies of the hadronic event selection for various processes [25].

4.2 RECONSTRUCTION OF THE Λ_c DECAY CHAIN

To reconstruct the Λ_c decay chain in each recorded event, we take the reconstructed charged tracks from the detector and by using the $R_{f/f'}$ probability ratios described in chapter 2.4, identify tracks as pions or protons. For protons we use the ratios $R_{p/K}$ and $R_{p/\pi'}$, and for both pions the ratios $R_{\pi/K'}$, $R_{\pi/p'}$, $R_{\pi/e}$ and $R_{\pi/\mu}$. We also separate p^+ and \bar{p}^- and π^+ and π^- tracks by the reconstructed charge of the track. We then combine the selected p^+ and π^- to form Λ particles, and combine the Λ particles with the reconstructed π^+ into Λ_c^+ particles. We form the $\bar{\Lambda}_c^-$ particle in the same way, using the reconstructed charge conjugate particles. Out of all formed Λ_c^+ and $\bar{\Lambda}_c^-$ particles, we select the best signal candidates by performing vertex fits on the Λ and π tracks and selecting the combination that has the best confidence level of the vertex fit.

4.3 CONSTRUCTION OF THE SKIM SAMPLE

We select a sample of events by applying a set of loose selection criteria from 6 times the available data (streams) of generic MC simulation events that passed preselection. These are simulated events of all possible physical processes coming from $e^+e^- \rightarrow \Upsilon(4S) \rightarrow B\bar{B}$, or $e^+e^- \rightarrow q\bar{q}$, $q = u, d, s, c$. This sample we call a 'skim' sample. In addition to using the selection criteria on the variables described in section 4.2, we employ selection criteria on the invariant mass of the Λ and Λ_c particles and on the Λ_c momentum in the e^+e^- CMS. The invariant mass of a particle P is defined using the momentum four-vector P_P conservation as:

$$m_P = m(P_0 \dots P_N) = \sqrt{P_P^2} = \sqrt{E_P^2 - |\vec{p}_P|^2} = \sqrt{\left(\sum_i \sqrt{|\vec{p}_i|^2 + m_i^2} \right)^2 - \left| \sum_i \vec{p}_i \right|^2}, \quad (79)$$

where i runs over all N final state particles P_i that form the particle P .

The loose selection criteria used to create the skim sample are shown in table 5.

selection variable	value
$R_{\pi/K}, R_{\pi/p}, R_{p/K}, R_{p/\pi}$	≥ 0.6
$R_{\pi/e}, R_{\pi/\mu}$	≤ 0.9
$m(p\pi)$	$\geq 1.10 \text{ GeV}/c^2, \leq 1.13 \text{ GeV}/c^2$
$m(p\pi\pi)$	$\geq 2.19 \text{ GeV}/c^2, \leq 2.38 \text{ GeV}/c^2$
$p_{\text{CMS}}(\Lambda_c)$	$\geq 1.5 \text{ GeV}/c$

Table 5: Selection criteria used to make the skim sample out of all generic MC simulated events.

4.3.1 Comparison of Monte Carlo simulation and data event samples

To check the method with a Monte Carlo simulation generated event sample, we need to ensure that the simulation describes the relevant processes as closely to the real data as possible. Small differences between MC simulation and real data arise mostly from inadequate simulation of the fragmentation of $c\bar{c}$ quarks into hadrons and need to be taken into account when estimating the systematic uncertainty of the measurement.

We first look at the Λ_c invariant mass distribution and separate the reconstructed events according to their origin, since this way we can explain the features of the distribution. We find out that we can divide the sample into 5 categories (see figure 32)¹:

- Signal - this category consists of the signal events $\Lambda_c^+ \rightarrow \Lambda\pi^+$, $\Lambda \rightarrow p^+\pi^-$, with Λ_c^+ coming directly from the fragmentation ($c\bar{c} \rightarrow \Lambda_c^+X$), from fragmentation via the various Σ_c ($\Sigma_c^0, \Sigma_c^+, \Sigma_c^{++}, \Sigma_c^{*0}, \Sigma_c^{*+}, \Sigma_c^{*++}$) baryons ($c\bar{c} \rightarrow \Sigma_c X \rightarrow \Lambda_c^+ \pi$), which decay strongly exclusively into Λ_c^+ and a pion, directly from B mesons ($B \rightarrow \Lambda_c^+ X$), or from B mesons via the Σ_c baryons ($B \rightarrow \Sigma_c X \rightarrow \Lambda_c^+ \pi$).
- Low mass background - events that fall into this category are events coming from the $\Lambda_c^+ \rightarrow \Sigma^0 \pi^+$, $\Sigma^0 \rightarrow \Lambda\gamma$, $\Lambda \rightarrow p^+\pi^-$ decay chain, where the photon is not reconstructed, thus resulting in a slightly lower invariant mass.
- High mass background - these events come from decay chains:
 - $\Xi_c^0 \rightarrow \Xi^- \pi^+, \Xi^- \rightarrow \Lambda\pi^-$,
 - $\Xi_c^+ \rightarrow \Xi^0 \pi^+, \Xi^0 \rightarrow \Lambda\pi^0$,
 - $\Xi_c^0 \rightarrow \bar{K}^0 \Lambda, \bar{K}^0 \rightarrow \pi^+\pi^-$,
 with Λ reconstructed in the $\Lambda \rightarrow p^+\pi^-$ mode for each decay channel.
- Peaking background - these events are true decays of Λ_c , with exactly the same final state ($p\pi^+\pi^-$) as the signal decays, but with different intermediate states:

¹ Here, we write only the Λ_c^+ categories as the categories for $\bar{\Lambda}_c^-$ are charge conjugates of the Λ_c^+ ones.

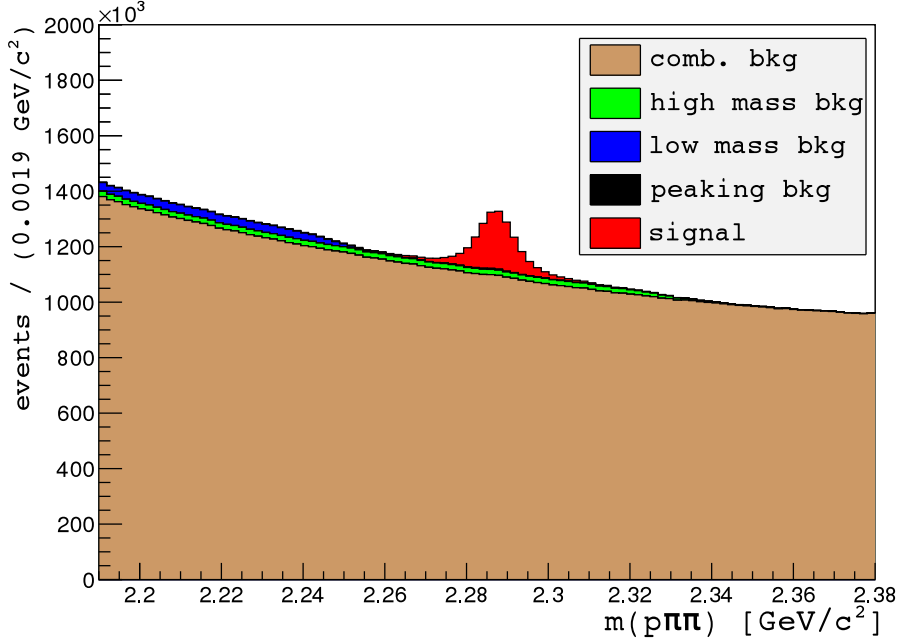


Figure 32: Breakdown of the generic MC simulation skim sample according to the origin of final state particles.

- $\Lambda_c^+ \rightarrow f_0 p^+, f_0 \rightarrow \pi^+ \pi^-$,
- $\Lambda_c^+ \rightarrow K^0 p^+, K^0 \rightarrow K_S^0 \rightarrow \pi^+ \pi^-$,
- $\Lambda_c^+ \rightarrow p^+ \pi^+ \pi^-$,

- Combinatorial background - events mostly from random combinations of final state particles or other statistically nonsignificant decays.

Now we can compare the generic MC simulation and real data Λ_c mass distributions by forming probability density functions (PDFs) out of histograms for the signal ($SIG(m(p\pi\pi))$), the high mass background ($HM(m(p\pi\pi))$), the low mass background ($LM(m(p\pi\pi))$) and the combinatorial ($C(m(p\pi\pi))$) background (we leave out the peaking background, because it is negligibly small for this purpose) and fitting the combined PDF:

$$f(m(p\pi\pi)) = a \cdot SIG(m(p\pi\pi)) + b \cdot HM(m(p\pi\pi)) + c \cdot LM(m(p\pi\pi)) + d \cdot C(m(p\pi\pi)), \quad (80)$$

to the data histogram. If we divide the coefficients a, b, c and d obtained from this fit by the total number of events in the combined histogram, we get the scale factors by which we must multiply the MC simulation events so that they give the best possible match between MC simulation and data. The scaling coefficients for the signal, low mass and combinatorial background are, although statistically significant, not extremely far from unity, and reflect the unperfect modeling of the $c\bar{c}$ fragmentation and poorly known branching ratios of various charmed baryons entering the MC simulation. The results of the fit are shown in figure 33 and the scaling coefficients are written in table 6. We see that the events coming from the high mass background are not present in the data at all,

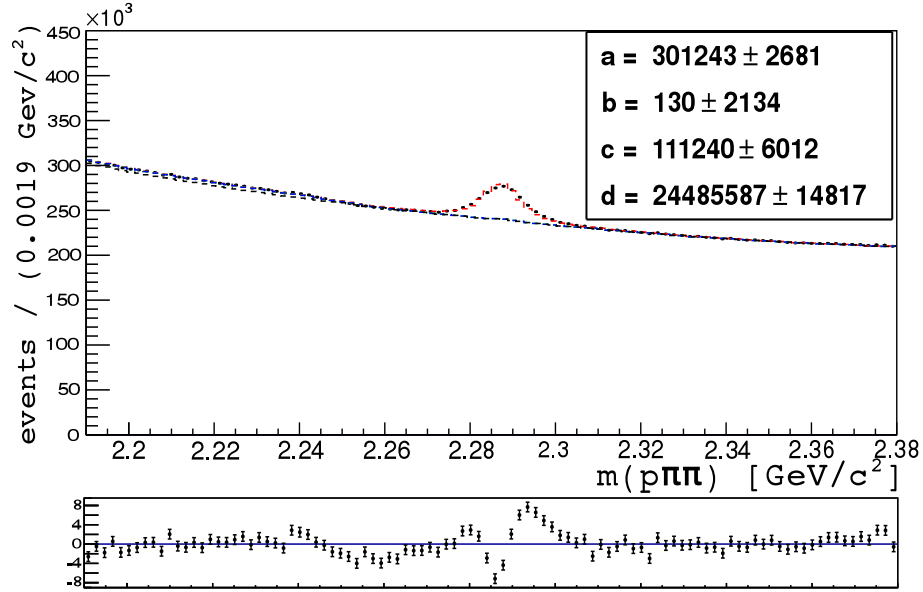


Figure 33: Fit of the combined histogram PDF (80), obtained from the MC simulated Λ_c mass distribution, to the data Λ_c mass distribution.

event category	scaling coefficient
Signal	1.090 ± 0.010
Low mass bkg	0.726 ± 0.039
High mass bkg	0.000 ± 0.009
Combinatorial bkg	1.330 ± 0.001

Table 6: Scale coefficients between data and MC simulation for different event categories, obtained from the fit shown in figure 33.

which shows that the production of Ξ_c and the branching ratios for their decays to final states with a Λ particle are highly overestimated. This overestimation is due to the fact that the relevant quantities concerning Ξ_c decays are very poorly known.

4.3.2 Reweighting of the Monte Carlo simulation $\cos \theta_h$ angular distribution

In the generic MC simulation, the $\cos \theta_h$ angular distribution is flat (see figure 34) - the linear angular dependence due to parity non-conserving weak decays is not simulated. To be able to check the method with the generic MC simulation, we have to reweigh events to the correct angular distribution.

We therefore reweigh the signal for the $c\bar{c} \rightarrow \Lambda_c X$ and $c\bar{c} \rightarrow \Sigma_c X \rightarrow \Lambda_c \pi$ events (see figure 34), whereas the $B \rightarrow \Lambda_c X$, $B \rightarrow \Sigma_c X \rightarrow \Lambda_c \pi$ ², and the background events are not reweighed, but scaled, so that the ratio of signal and background events remains the same.

² The events coming from B mesons are not reweighed, since after the optimization of the selection criteria (see chapter 4.4.1) we reject almost all of these events.

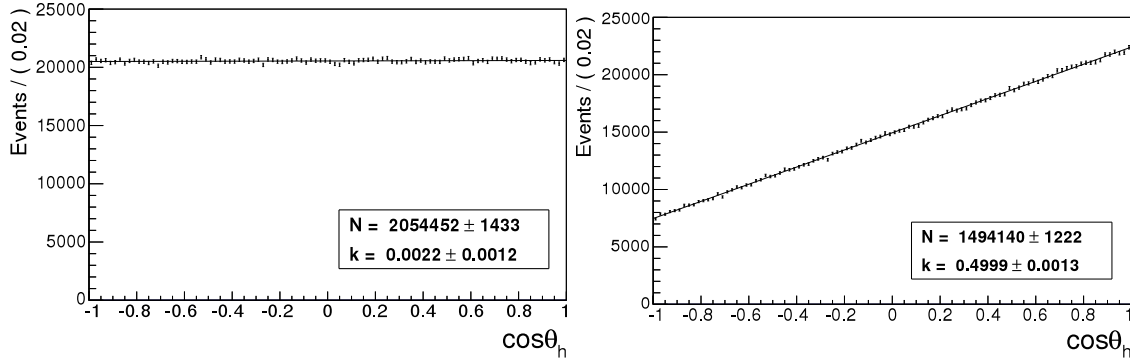


Figure 34: Fit with a linear function on $\cos \theta_h$ angular distribution of the generic MC simulation for events with Λ_c^+ coming from fragmentation. Left - before reweighing, right - after reweighing.

This is done using a random number generator used to generate a number r between 0 and 1, which is then compared to the expression $y = (1 + \alpha \cos \theta_h)/(1 + \alpha)$ for each event in the case of reweighing, and to $y = 1/(1 + \alpha)$ in the case of scaling. If $r < y$, the event is accepted, otherwise it is discarded. For α we chose the value 0.5 for both Λ_c^+ and Λ_c^- decays, as obtained in [34] (see figure 34). Because we use a random number generator, the α coefficients have slightly different values between streams. Their values are shown in table 7.

In the analysis, there are five angles to consider when reweighing the events; the three angles defined in (39) and the two angles from (32) and (35). The first angle ϑ_1 from equations (39) is the helicity angle, and the distribution of signal events over this angle is independent of the polarization of Λ_c and must be reweighed to the distribution described by the equation. The distributions of events over all other angles are dependent on the polarization of the Λ_c sample, however in our case, the Λ_c either come from the $(c\bar{c} \rightarrow \Lambda_c X)$ fragmentation, which can not produce a polarized Λ_c sample, or from B mesons, which in principle could produce a polarized Λ_c sample, but after we produce the analysis sample by optimizing the selection criteria, we reject almost all of these events (see chapter 4.4.1). We can therefore assume that the Λ_c sample is unpolarized ($P_{\Lambda_c} = 0$). With this assumption, the distributions over the second and third angle from (39) and over the angle from (32) are flat, whereas the distribution over the angle from (35) is identical to the one over the helicity angle.

If we plot all the angle distributions in the simulation, we see that the only distribution we have to reweigh is the helicity angle distribution, as the other distributions remain flat or reweigh correctly as we reweigh the helicity angle distribution (see figure 35).

After scaling and reweighing the generic MC simulation, we obtain an equivalent of 4 streams of simulated events. These events are now scaled to match the data and are reweighed to the correct $\cos \theta_h$ angular distribution.

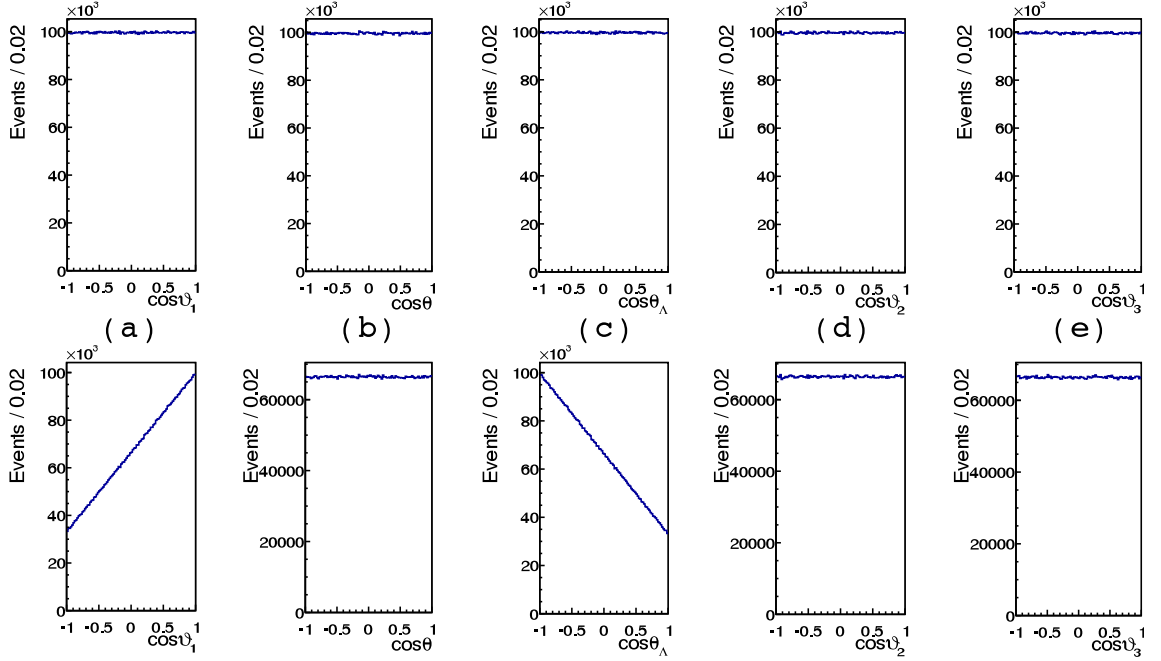


Figure 35: Angles defined in (39) (a, d, e), (32) (b) and (35) (c) before reweighing the angle (a) - top row, and after reweighing the angle (a) - bottom row.

stream	$\alpha_{\Lambda_c^+}$	$\alpha_{\Lambda_c^-}$
0	0.5014 ± 0.0026	0.5048 ± 0.0026
1	0.4971 ± 0.0026	0.5006 ± 0.0026
2	0.5016 ± 0.0026	0.5035 ± 0.0026
3	0.4994 ± 0.0026	0.4944 ± 0.0026
all	0.4999 ± 0.0013	0.5008 ± 0.0013

Table 7: α coefficients used to reweigh streams of generic MC simulation.

selection variable	value
$R_{\pi/\kappa}, R_{\pi/p}$ (for both pions)	≥ 0.6
$R_{\pi/e}, R_{\pi/\mu}$ (for both pions)	≤ 0.9
$R_{p/\kappa}, R_{p/\pi}$	≥ 0.6
$p\pi, p\pi\pi$ vertex fit conf. level	$\geq 10^{-3}$
$m(p\pi)$	$\geq 1.1126 \text{ GeV}/c^2, \leq 1.1186 \text{ GeV}/c^2$
$m(p\pi\pi)$	$\geq 2.19 \text{ GeV}/c^2, \leq 2.38 \text{ GeV}/c^2$
$p_{\text{CMS}}(\Lambda_c)$	$\geq 2.2 \text{ GeV}/c$

Table 8: Selection criteria used to make the analysis sample out of all generic MC simulation events.

4.4 CONSTRUCTION OF THE ANALYSIS SAMPLE

4.4.1 Optimization of selection criteria

To create the analysis sample, we perform an optimization of all the selection criteria used. In addition to criteria used to create the skim sample, we also use the Λ and Λ_c vertex fit confidence levels.

For optimization, we define a figure-of-merit (FOM) function:

$$\text{FOM} = \varepsilon \cdot P, \quad (81)$$

where ε is the efficiency and P is the purity, defined as:

$$\varepsilon = \frac{N_{\text{sig}}^{\text{rec}}}{N_{\text{sig}}^0}, \quad P = \frac{N_{\text{sig}}^{\text{rec}}}{N_{\text{all}}^{\text{rec}}}, \quad (82)$$

with $N_{\text{sig}}^{\text{rec}}$ denoting the number of reconstructed signal events, N_{sig}^0 the number of all signal events and $N_{\text{all}}^{\text{rec}}$ the number of all reconstructed events.

A selection criterion is optimized when the FOM calculated with this criterion is at its maximum value. This definition of the FOM gives us the best significance for the signal yield ($N_{\text{sig}}^{\text{rec}}/\sigma_{N_{\text{sig}}^{\text{rec}}}$) in the sample. After an automated iterative procedure, we get the selection criteria shown on figure 36.

Since for all selection criteria except the $m(p\pi)$ invariant mass and the Λ_c momentum in the e^+e^- CMS criteria, the FOM does not depend very strongly on the cut, we do not use the selection criteria suggested by the optimization, to retain a larger number of signal events. For confidence levels for both vertex fits we use the standard value $\geq 10^{-3}$, and for the three mentioned criteria, we use the values from the optimization procedure. The results of the procedure are shown in table 8.

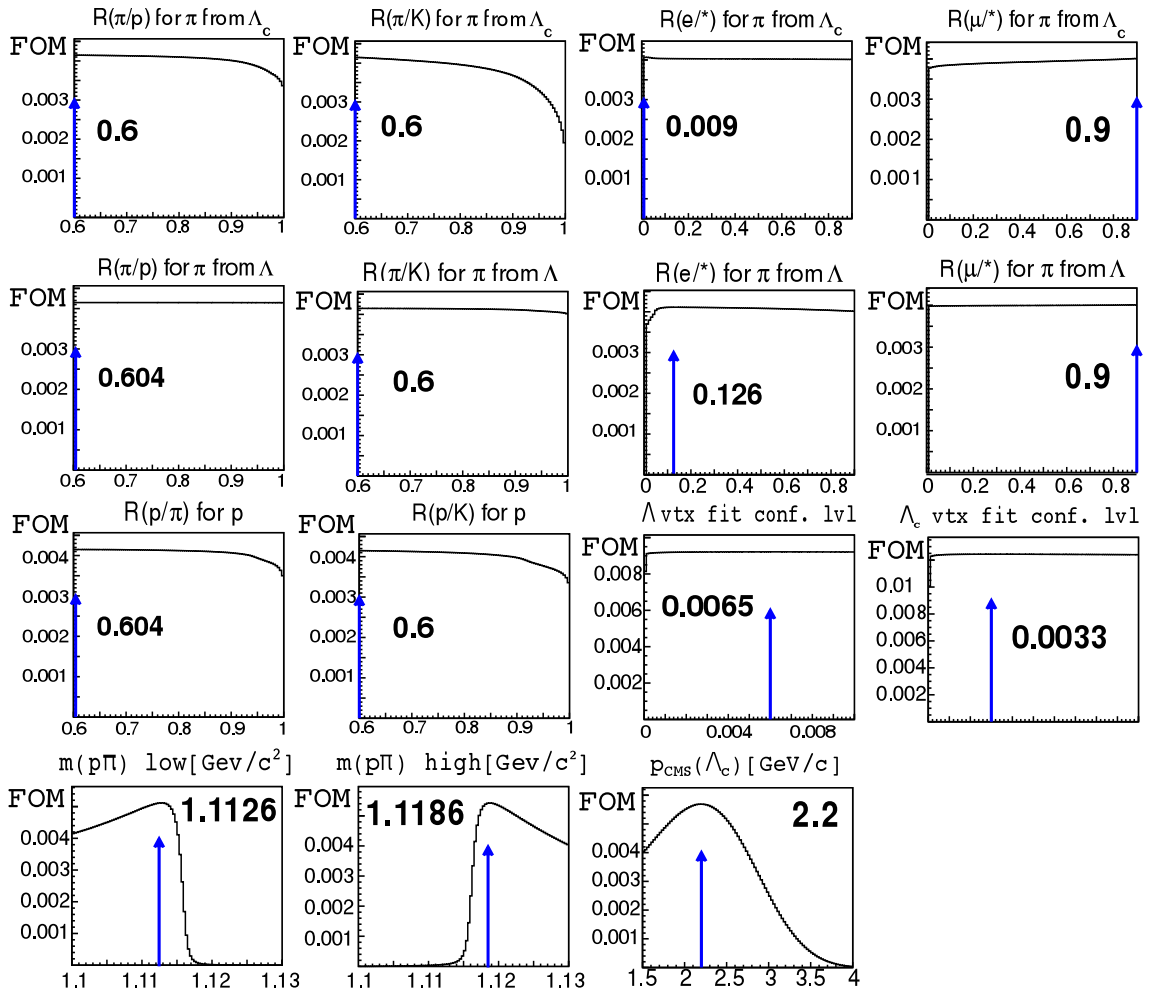


Figure 36: The results of an automated iterative optimization of all used selection criteria, showing the value of FOM on the y-axis and the chosen selection criterion on the x-axis. The arrow indicates where the maximum of FOM has been found and the value of the selection criterion at the maximum is written in the graph.

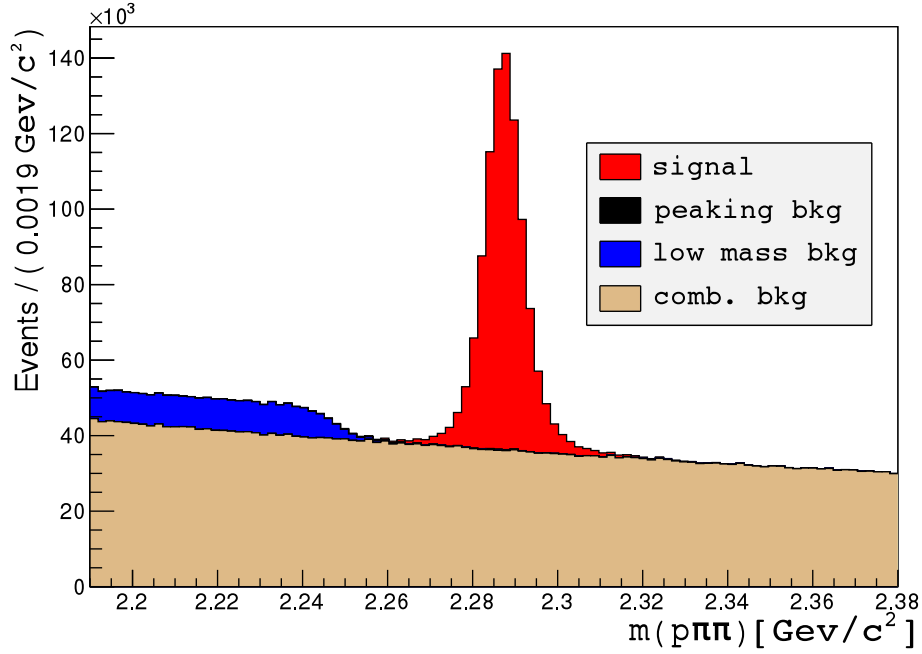


Figure 37: Breakdown of the generic MC simulation analysis sample according to the origin of the final state particles.

	skim sample	analysis sample
efficiency	0.28	0.18
purity	0.10	0.65
FOM	0.03	0.12
S/B	0.11	1.88

Table 9: Efficiency, purity, FOM and signal-to-background ratio for the $[-2\sigma, +2\sigma]$ interval around the Λ_c signal peak for the analysis and skim samples.

4.4.2 Analysis sample

Using the selection criteria shown in table 8, we obtain the Λ_c analysis sample. The Λ_c mass distribution in the simulated sample separated into categories according to their origin is shown in figure 37.

The signal-to-background ratio (S/B) in the analysis sample is now significantly better than in the skim sample (see table 9).

4.5 FIT OF Λ_c MASS IN BINS OF $\cos \theta_h$

In the next step, reconstructed Λ_c decays are divided into bins according to $\cos(\theta_h)$ values. Since we perform a deconvolution (see chapter 4.6), the chosen bin width should have no influence on the uncertainty of the result, however we would nevertheless like to reduce the bin-to-bin event migration due to a finite

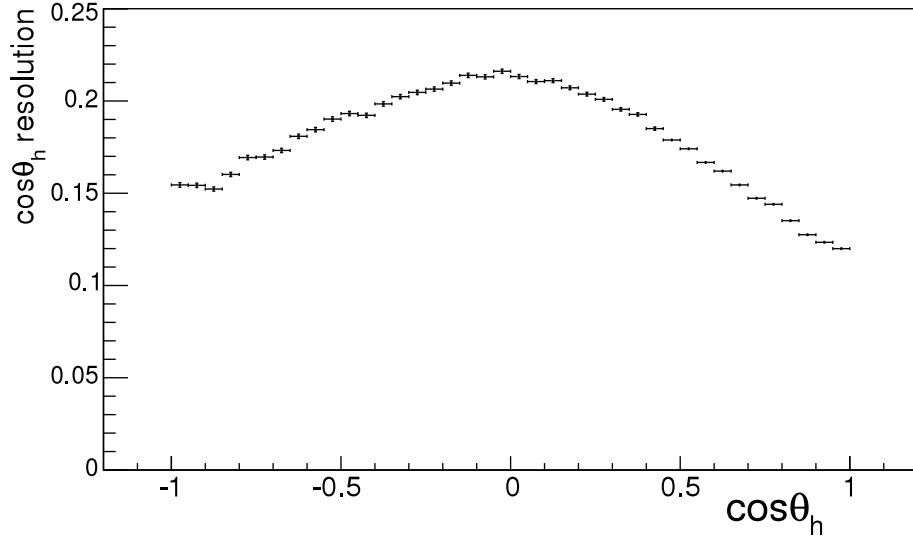


Figure 38: Detector resolution for measuring $\cos\theta_h$.

$\cos(\theta_h)$ resolution³, while still dividing the $\cos\theta_h$ distribution into as many bins as possible. This is the reason that we choose the width of the bin according to an estimate of the detector resolution for measuring $\cos\theta_h$. The resolution is estimated with the signal MC simulation by calculating the difference between the reconstructed and generated values of $\cos\theta_h$ in the sample in bins of $\cos\theta_h$ and then taking the root mean square (RMS) of each histogram formed that way. The results are shown in figure 38.

According to the results, we decided to divide the $\cos\theta_h$ distribution into 10 equidistant bins, setting the bin width at 0.2, as this is roughly the largest resolution estimate.

4.5.1 General fit method

The fit method used to fit the Λ_c mass histograms in bins of $\cos\theta_h$ is the extended binned maximum likelihood. With this method, we do not define probability density functions, normalized to 1 to describe the distributions, but models (M_i), normalized to the expected number of events $N_{\text{exp}}(\vec{p})$ which this model describes. The model for the whole data sample (M) is thus a sum of individual models:

$$M(x; \vec{p}) = \sum_i N_i M_i(x; \vec{p}_i), \quad \int M(x; \vec{p}) dx \equiv N_{\text{exp}}(\vec{p}). \quad (83)$$

Here, x is the observable, \vec{p} is the vector of all model parameters, N_i are the expected numbers of events for each model and \vec{p}_i is the subset of parameters for the i -th model. The model is normalized to $N_{\text{exp}} = \sum_i N_i$, which is the sum of number of events in histograms for all $\cos\theta_h$ bins.

³ The reconstructed value of θ_h for a given decay may differ from the true one due to the resolution effects.

We estimate the parameter values by minimizing the extended likelihood function in a simultaneous fit to histograms for all $\cos \theta_h$ bins:

$$-\ln L(\vec{p}) = - \sum_{j=1}^{N_{\text{bin}}=10} \sum_{H_j(x_i)} M(x_i; \vec{p}_j) - \text{Poisson}(N_{\text{obs}} | \sum_{j=1}^{N_{\text{bin}}=10} N_{\text{exp},j}(\vec{p}_j)), \quad (84)$$

where the index j runs over bins in $\cos \theta_h$, $H_j(x_i)$ is the histogram for the j -th $\cos \theta_h$ bin with i bins, x_i is the i -th bin center in the histogram H_j , \vec{p}_j are the parameters used in the model that describes the histogram in the j -th $\cos \theta_h$ bin and N_{obs} is the sum of the observed event count in all $\cos \theta_h$ histograms, modeled by a Poisson distribution with the expected event count for all histograms as mean.

4.5.2 Signal MC simulation fit

To ensure the convergence of fits, we need to fix some of the fit parameters. We do this by first fitting just the signal events (the signal MC simulation) and fixing some of the fit parameters to the values obtained by this fit when fitting all the events in the analysis sample. For the signal MC simulation, we perform a simultaneous fit to the $m(p\pi\pi)$ mass distribution in all bins of $\cos \theta_h$, where for each bin, we use two Gaussian functions and one asymmetric Gaussian function with a common peak value as a model and the ratios of numbers of events and widths between the second Gaussian and the first Gaussian and between the asymmetric Gaussian and the first Gaussian are common for all bins:

$$\begin{aligned} M_S(m_{p\pi\pi}; \vec{p}) &= \sum_{i=1}^{N_{\text{bin}}=10} N_{1,i} [G(m_{p\pi\pi}; m_i, \sigma_{1,i}) + n_{12} G(m_{p\pi\pi}; m_i, s_{12}\sigma_{1,i}) + \\ &\quad + n_{13} \text{AG}(m_{p\pi\pi}; m_i, s_{13l}\sigma_{1,i}, s_{13r}\sigma_{1,i})], \\ G(x; m, \sigma) &= \frac{1}{\sqrt{2\pi}\sigma} \exp\left[-\frac{(x-m)^2}{2\sigma^2}\right], \\ \text{AG}(x; m, \sigma_l, \sigma_r) &= \frac{1}{\sqrt{2\pi}\sigma_l} (1 - \theta(x-m)) \exp\left[-\frac{(x-m)^2}{2\sigma_l^2}\right] + \\ &\quad + \frac{1}{\sqrt{2\pi}\sigma_r} \theta(x-m) \exp\left[-\frac{(x-m)^2}{2\sigma_r^2}\right], \end{aligned} \quad (85)$$

where $\theta(x)$ is the Heaviside step function.

We fit the signal MC simulation histograms in the range $[2.25 \text{ GeV}/c^2 - 2.33 \text{ GeV}/c^2]$ and use streams 0 and 1 of the analysis sample to increase statistics, which results in a smaller uncertainty for the fixed parameters. The parameters which are fixed on the generic MC simulation analysis sample fit (see next section), are shown in table 10 and an example of the fit for bin 4 ($-0.2 < \cos \theta_h < 0.0$) is shown on figure 39. Results of fits for all $\cos \theta_h$ bins are shown in appendix A.1.

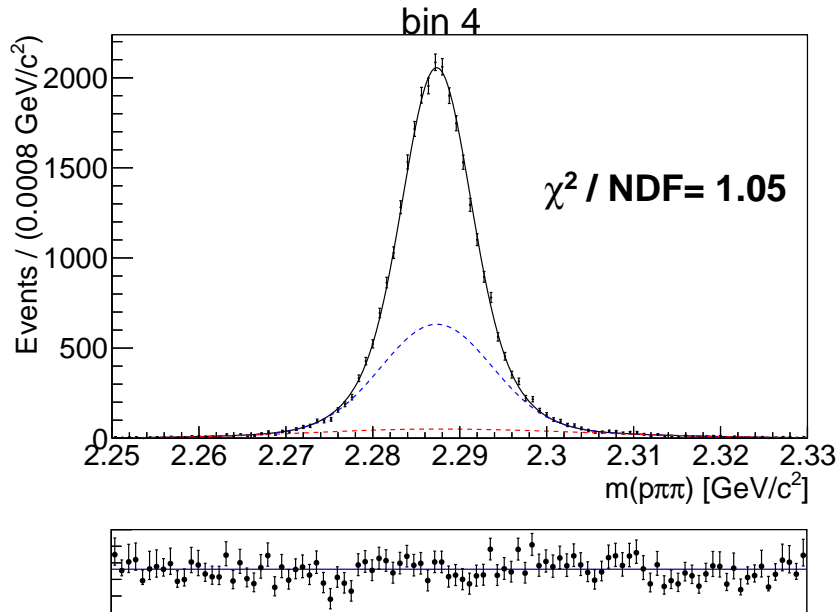


Figure 39: An example of the fit on the signal MC simulation for bin 4 ($-0.2 < \cos\theta_h < 0.0$). The black, blue and red lines mark the narrow Gaussian, the wide Gaussian and the asymmetric Gaussian, respectively. The bottom plot shows the fit residuals.

parameter	value
n_{12}	0.710 ± 0.060
n_{13}	0.156 ± 0.010
s_{12}	1.741 ± 0.018
s_{13l}	4.008 ± 0.056
s_{13r}	4.856 ± 0.071

Table 10: Values and errors of parameters obtained from the signal MC simulation, which are then fixed in the generic MC simulation analysis sample fit.

4.5.3 Generic MC simulation fit

For the fit on the generic MC simulation, we perform a simultaneous fit to the $m(p\pi\pi)$ mass distribution in all bins of $\cos\theta_h$, where for each bin, the model is a sum of the model for the signal peak, defined in (85), with all the common ratios fixed to the values determined from the fit on the signal MC simulation, a sigmoid function for the low mass background and a Chebyshev polynomial of the second order for the combinatorial background. The common parameters for all bins are the width and the position of the sigmoid and the two Chebyshev polynomial coefficients:

$$\begin{aligned}
M_G(m_{p\pi\pi}; \vec{p}) &= \sum_{i=1}^{N_{\text{bin}}=10} \left[N_{1,i} \left(G(m_{p\pi\pi}; m_i, \sigma_{1,i}) + n_{12} G(m_{p\pi\pi}; m_i, s_{12}\sigma_{1,i}) + \right. \right. \\
&\quad \left. \left. + n_{13} \text{AG}(m_{p\pi\pi}; m_i, s_{13l}\sigma_{1,i}, s_{13r}\sigma_{1,i}) \right) + \right. \\
&\quad \left. + N_{b1,i} S(m_{p\pi\pi}; m_b, w_b) + N_{b2,i} \text{CH}(m_{p\pi\pi}; c_1, c_2) \right], \\
G(x; m, \sigma) &= \frac{1}{\sqrt{2\pi}\sigma} \exp \left[-\frac{(x-m)^2}{2\sigma^2} \right], \\
\text{AG}(x; m, \sigma_l, \sigma_r) &= \frac{1}{\sqrt{2\pi}\sigma_l} (1 - \theta(x-m)) \exp \left[-\frac{(x-m)^2}{2\sigma_l^2} \right] + \\
&\quad + \frac{1}{\sqrt{2\pi}\sigma_r} \theta(x-m) \exp \left[-\frac{(x-m)^2}{2\sigma_r^2} \right], \\
S(x; m, w) &= \frac{1}{1 + \exp \left[\frac{x-m}{w} \right]}, \\
\text{CH}(x; c_1, c_2) &= 1 + c_1 x + c_2 (x^2 - 1).
\end{aligned} \tag{86}$$

The number of signal events (R_i) and the statistical uncertainty on the number of signal events (σ_{R_i}) for each bin are calculated as:

$$R_i = N_{1,i}(1 + n_{12} + n_{13}), \quad \sigma_{R_i} = \sigma_{N_{1,i}}(1 + n_{12} + n_{13}), \tag{87}$$

where $\sigma_{N_{1,i}}$ is the statistical error on the parameter $N_{1,i}$ from the fit on generic MC simulation. The number of signal events from the generic MC simulation fit for all $\cos\theta_h$ bins is shown in table 41b and figure 41a and an example of the fit on generic MC simulation for bin 4 ($-0.2 < \cos\theta_h < 0.0$) is shown in figure 40. Results of fits for all $\cos\theta_h$ bins are shown in appendix A.2.

To check if the fit correctly reproduces the number of signal events, we look at the fit residuals, defined as:

$$\frac{N_{\text{fit}} - N_{\text{actual}}}{\sigma_{N_{\text{fit}}}}, \tag{88}$$

where N_{fit} is the number of signal events determined from the fit, N_{actual} is the actual number of events determined by counting on the generic MC simulation, and $\sigma_{N_{\text{fit}}}$ is the statistical error on the number of signal events determined from the fit. The residuals are fitted with a constant function with a χ^2 fit. The result is 0.06 ± 0.32 with a χ^2/NDF of 8.75/9, which corresponds to a probability of

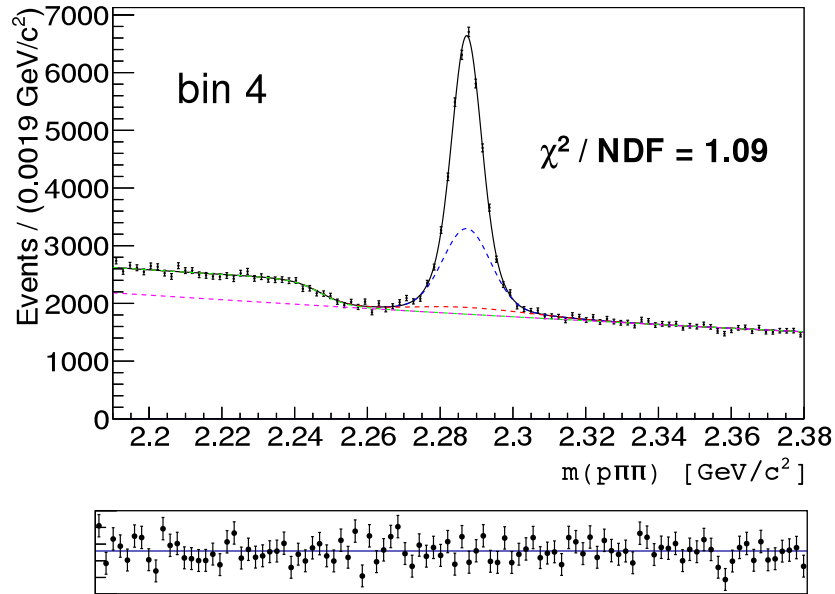


Figure 40: An example of the fit on the generic MC simulation for bin 4 ($-0.2 < \cos\theta_h < 0.0$). The black, blue, red, green and purple lines mark the narrow Gaussian, the wide Gaussian, the asymmetric Gaussian (all describing signal events), the sigmoid function and the 2nd order Chebyshev polynomial (all describing the backgrounds), respectively. The bottom plot shows the fit residuals.

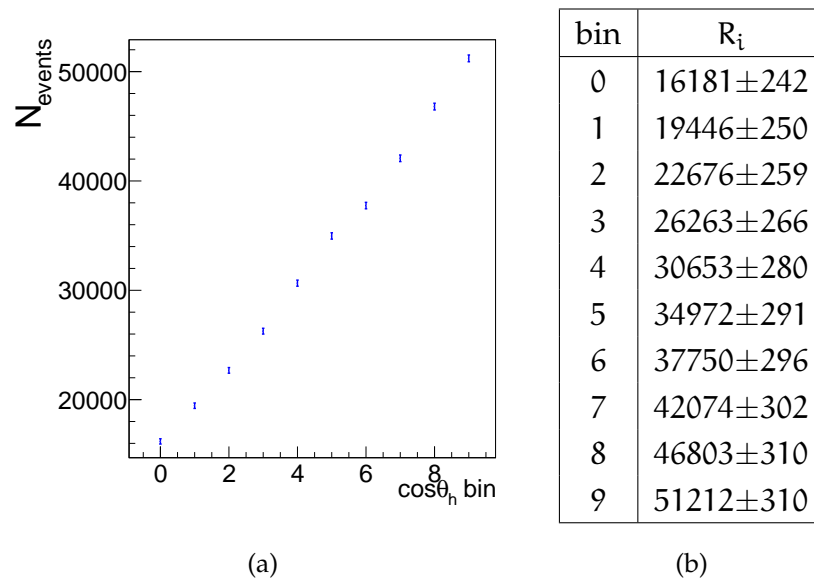


Figure 41: Numbers and statistical uncertainties for signal events for each $\cos\theta_h$ bin, determined from the generic MC simulation fit. Note that the histogram is zero-suppressed.

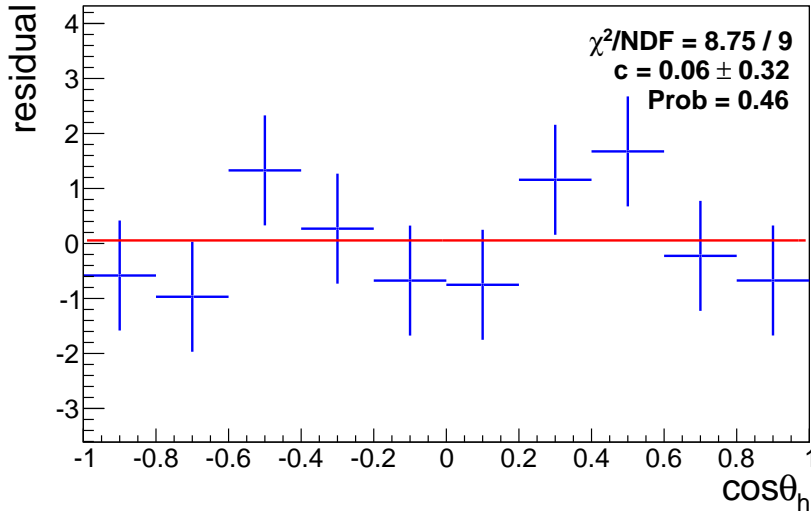


Figure 42: Residuals between fitted and actual number of events for the generic MC simulation fit, fitted with a constant function with a χ^2 fit.

0.46, hence we can conclude that the fit model correctly reproduces the number of reconstructed events (see figure 42).

4.6 DECONVOLUTION

The Belle detector has a finite resolution of measurement of the θ_h angle (see figure 38), which means that the measured value of $\cos \theta_h$ for an event can slightly deviate from its true value. As a consequence, events migrate across the bins. Mathematically, this means that the true $\cos \theta_h$ distribution is convoluted with a resolution function:

$$\left(\frac{dN}{d \cos \theta_h} \right)_{\text{rec}} = \left(\frac{dN}{d \cos \theta_h} \right) \otimes \text{Res}(\cos \theta_h). \quad (89)$$

To correct this we deconvolute the reconstructed $\cos \theta_h$ distribution, using a deconvolution matrix determined from the Monte Carlo simulation.

First, we determine the event migration from the MC simulation by distributing signal events into 2D bins according to their reconstructed and generated $\cos \theta_h$ values and counting the number of events that fall into each 2D bin (see figure 43). As expected, a large majority of events concentrates in the diagonal of the plot, showing that their $\cos \theta_h$ value is correctly reproduced. With this procedure, we get a resolution map in the form of a matrix, which maps the resolution function into chosen bins of $\cos \theta_h$. We will denote this map by M_{ij} , where index i runs over the reconstructed $\cos \theta_h$ bins and index j over the generated $\cos \theta_h$ bins.

In order to get the convolution matrix, we need the probability that after reconstruction, each event with a generated value of $\cos \theta_h$ in the j -th bin will fall into the i -th bin of the reconstructed $\cos \theta_h$ distribution. We know that the probability for an event to fall into any bin must be 1, since we do not lose events

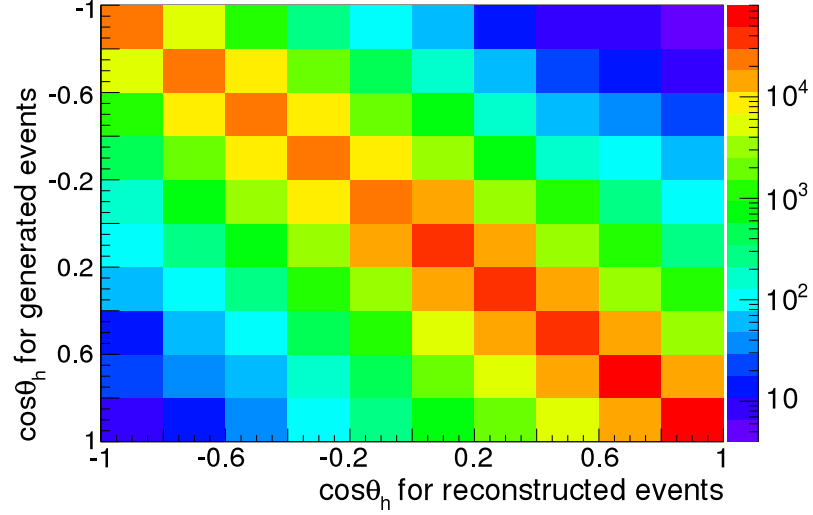


Figure 43: Distribution of events in bins of reconstructed and generated $\cos\theta_h$. (Note: the color axis is shown in a logarithmic scale.)

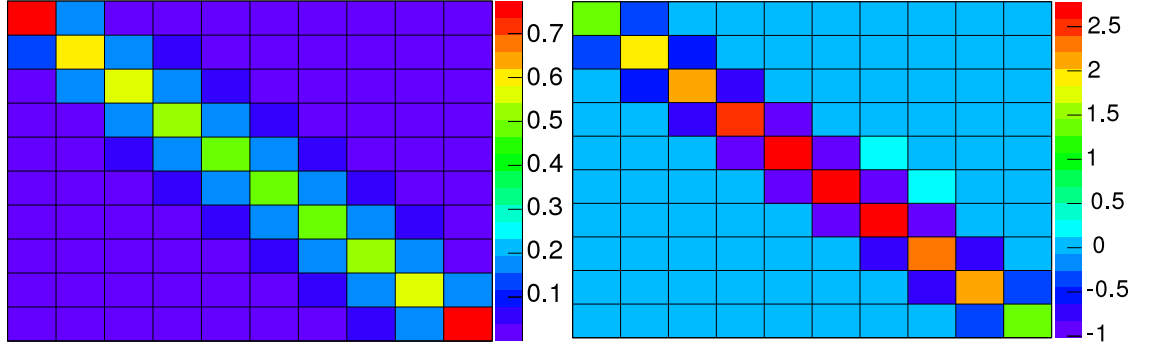


Figure 44: Convolution (left) and deconvolution (right) matrices in bins of reconstructed and generated $\cos\theta_h$.

because of the detector resolution, so for the convolution matrix the following normalization must hold:

$$\sum_i p_{ij} = 1, \quad (90)$$

where with p_{ij} we denoted the element of the convolution matrix, with index i running over the reconstructed $\cos\theta_h$ bins and index j over the generated $\cos\theta_h$ bins.

To get the convolution matrix, we must therefore normalize the resolution map row-wise (see figure 44):

$$p_{ij} = \frac{M_{ij}}{\sum_k M_{kj}}. \quad (91)$$

Now, the normalization (90) holds, because:

$$\sum_i p_{ij} = \sum_i \frac{M_{ij}}{\sum_k M_{kj}} = \frac{\sum_i M_{ij}}{\sum_k M_{kj}} = 1. \quad (92)$$

With the convolution matrix P , we can calculate the numbers of reconstructed events in bins of the $\cos \theta_h$ distribution (\vec{R}), given the generated $\cos \theta_h$ distribution (\vec{G}), from the matrix equation:

$$\vec{R} = P\vec{G}. \quad (93)$$

In our case, we need to determine the generated distribution from the reconstructed one. We multiply the matrix equation (93) with P^{-1} from the left side, and get:

$$\vec{G} = P^{-1}\vec{R} = Q\vec{R}, \quad (94)$$

where we defined the deconvolution matrix with $Q = P^{-1}$ (see figure 44).

The deconvoluted number of events in the i -th bin of the $\cos \theta_h$ distribution (G_i) is therefore calculated from the reconstructed $\cos \theta_h$ distribution (R_j) as

$$G_i = \sum_j q_{ij} R_j, \quad (95)$$

where q_{ij} is the element of the deconvolution matrix Q .

The error on the deconvoluted number of events (which we denote as G_i) can be expressed in terms of convoluted numbers of events and their errors (here denoted as R_i and σ_{R_i}) from (87) and the coefficients of the deconvolution matrix and their errors (q_{ij} and $\sigma_{q_{ij}}$). For a derivation, see appendix B.3.

$$\sigma_{G_i}^2 = \sum_j R_j^2 \sigma_{q_{ij}}^2 + \sum_j \sum_k q_{ij} q_{ik} R_{jk} \sigma_{R_j} \sigma_{R_k}, \quad (96)$$

where the error on the deconvolution coefficient can be expressed with numbers of events in bins of the resolution map M_{ij} as (see appendix B.4 for a derivation):

$$\sigma_{q_{ij}}^2 = \sum_a \sum_b q_{ia}^2 \frac{M_{ab} \sum_{c \neq a} M_{cb}}{(\sum_c M_{ab})^3} q_{bj}^2, \quad (97)$$

and R_{jk} is the correlation coefficient between R_j and R_k , which is equal to 1 when $j = k$ and has a value between -1 and 1 when $j \neq k$. The variables R_j and R_k are correlated because we use a simultaneous fit to all bins to determine them. The calculated errors on the deconvolution matrix coefficients are shown in figure 45.

4.7 RECONSTRUCTION EFFICIENCY

Reconstruction efficiency in $\cos \theta_h$ bins must be determined since the $\cos \theta_h$ dependence of the efficiency changes the reconstructed $\cos \theta_h$ distribution. The efficiency in each bin is defined as

$$\langle \varepsilon_i \rangle = \frac{N_{R,i}}{N_{G,i}}. \quad (98)$$

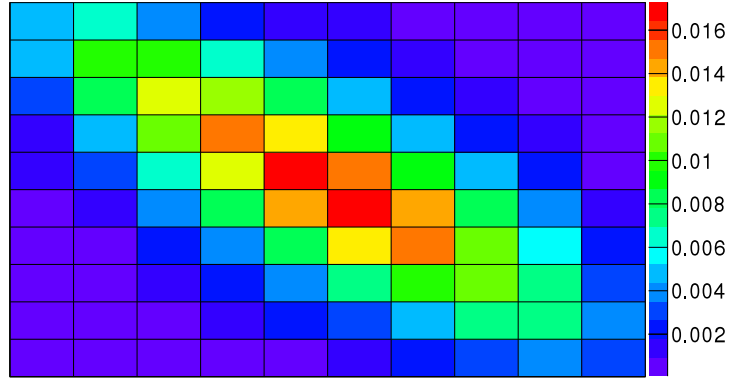


Figure 45: Errors on the deconvolution matrix coefficients in bins of reconstructed and generated $\cos \theta_h$.

It is determined by counting the reconstructed (N_R) and generated (N_G) events for each bin. For counting the reconstructed events we reconstruct a generated sample of reweighed signal MC. The generated events are counted on the same sample before any selection is used (including Hadron B preselection).

The error on the efficiency is calculated as an error of the Poisson distribution, since for one event it distributes as a binomial distribution (the event either passes the selection criteria, or it does not) and we have a large number of events:

$$\sigma_{\langle \varepsilon \rangle_i} = \sqrt{\frac{N_{R,i}(N_{G,i} + N_{R,i})}{N_{G,i}^3}}. \quad (99)$$

The determined efficiencies for each bin are shown in figures 46a and 46b.

4.8 DETERMINATION OF THE AVERAGE WEAK ASYMMETRY PARAMETER

To determine $\langle \alpha \rangle$, we fit the efficiency corrected deconvoluted numbers of events (T_i) in bins of $\cos \theta_h$:

$$T_i = \frac{G_i}{\langle \varepsilon \rangle_i}, \quad (100)$$

with a linear function of the form:

$$f(x; N, \langle \alpha \rangle) = \frac{1}{2}N(1 + \langle \alpha \rangle x). \quad (101)$$

The errors on G_i and $\langle \varepsilon \rangle_i$ are not correlated, so the errors on T_i are

$$\sigma_{T_i}^2 = T_i^2 \left(\frac{\sigma_{G_i}^2}{G_i^2} + \frac{\sigma_{\langle \varepsilon \rangle_i}^2}{\langle \varepsilon \rangle_i^2} \right), \quad (102)$$

with σ_{G_i} and $\sigma_{\langle \varepsilon \rangle_i}$ defined in equations (96) and (99), respectively.

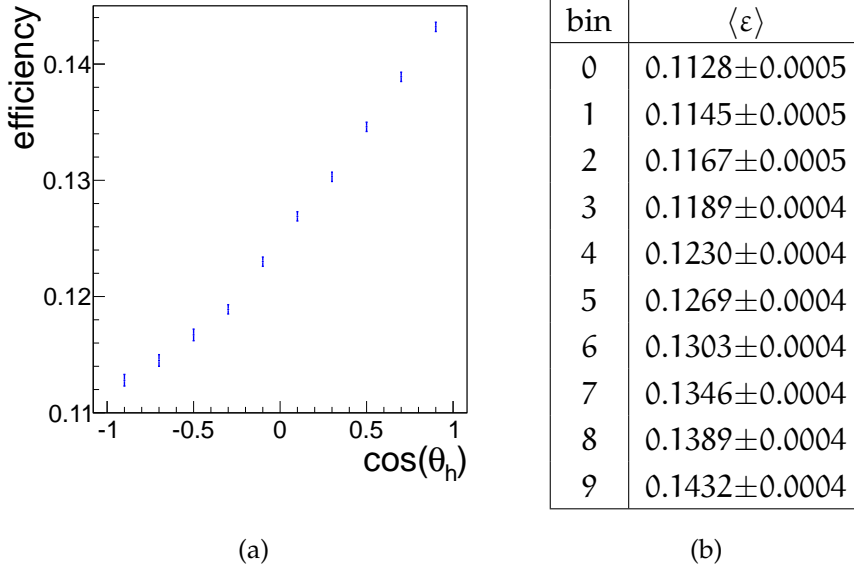


Figure 46: Plot 46a shows the graphical representation of the reconstruction efficiency and table 46b the numerical values in individual $\cos \theta_h$ bins. Note that the histogram in 46a has a suppressed zero and that the total change of the reconstruction efficiency over the whole $\cos \theta_h$ interval amounts to only around 2% – 3%.

The fit we perform is a multi-variate χ^2 fit [1], since the errors on G_i are correlated because of the deconvolution. We minimize the function:

$$\chi^2(N, \langle \alpha \rangle) = (\vec{T} - \vec{f}(x; N, \langle \alpha \rangle))^T V^{-1} (\vec{T} - \vec{f}(x; N, \langle \alpha \rangle)), \quad (103)$$

where \vec{T} is the vector of determined T_i values, \vec{f} is the corresponding vector of values for the function $f(x; N, \langle \alpha \rangle)$, defined in (101), evaluated at centers of bins, and V is the covariance matrix of the T_i values, which can be expressed as (see appendix B.2 for a derivation):

$$V_{ij} = T_i T_j \left(\frac{\sum_k \sum_l q_{ik} q_{jl} R_{kl} \sigma_{R_k} \sigma_{R_l}}{G_i G_j} + \delta_{ij} \frac{\sum_k R_k^2 \sigma_{q_{ik}} \sigma_{q_{jk}}}{G_i G_j} + \delta_{ij} \frac{\sigma_{\langle \varepsilon \rangle_i} \sigma_{\langle \varepsilon \rangle_j}}{\langle \varepsilon \rangle_i \langle \varepsilon \rangle_j} \right). \quad (104)$$

The fit is shown in figure 47. We compare the result to the value obtained by fitting the true generated distribution (see figure 34 and table 7) for streams 0 and 1. The results are in a good agreement within the error:

$$\langle \alpha \rangle_{\text{rec}} = 0.498 \pm 0.008, \quad \langle \alpha \rangle_{\text{st12gen}} = 0.501 \pm 0.001. \quad (105)$$

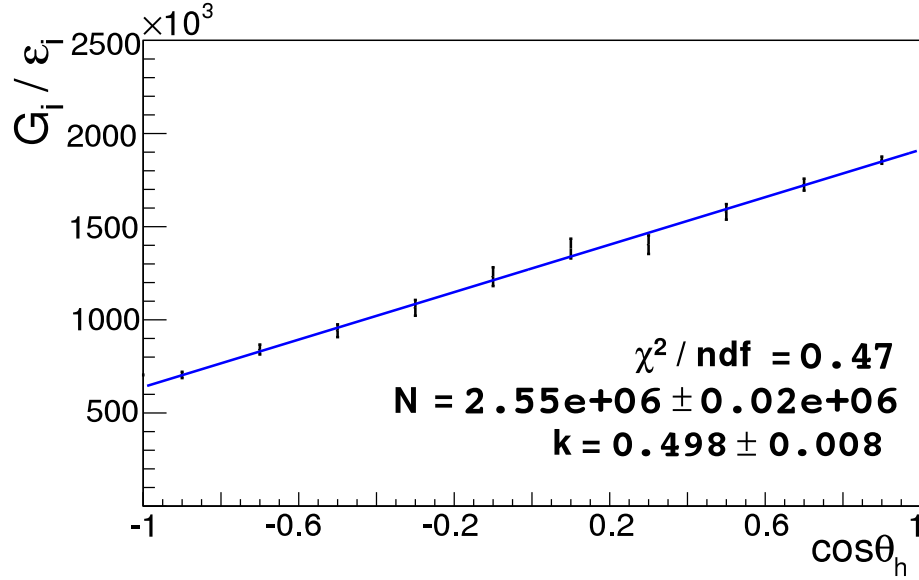


Figure 47: Fit on efficiency corrected deconvoluted $\cos\theta_h$ distribution of events, used to determine $\langle\alpha\rangle$, which is denoted as k in the plot.

4.9 FIT OF Λ_c^+ AND $\bar{\Lambda}_c^-$ MASS IN BINS OF $\cos\theta_h$

For measuring \mathcal{A}_{CP} , we take the same analysis sample as for the $\langle\alpha\rangle$ measurement, described in section 4.4. This is a scaled, reweighed MC sample obtained with optimized selection criteria.

We divide the analysis sample into separate samples for Λ_c^+ and $\bar{\Lambda}_c^-$ and for each sample distribute the events according to the bins in $\cos\theta_h$ angle, chosen in section 4.5.

We then perform an extended likelihood fit, defined in section 4.5.1, with the model defined in (86), separately to the Λ_c^+ and $\bar{\Lambda}_c^-$ samples. We take the values for the fixed parameters n_{12} , n_{13} , s_{12} , s_{13l} and s_{13r} from the fit on the signal MC simulation (see table 10) in both cases. Examples of Λ_c^+ and $\bar{\Lambda}_c^-$ fits on the generic MC simulation for bin 7 ($0.4 < \cos\theta_h < 0.6$) are shown in figure 48. Results of fits in all bins of $\cos\theta_h$ are shown in appendix A.3. With this fit, we calculate the number of signal events in each bin for the Λ_c^+ and $\bar{\Lambda}_c^-$ samples (R_i and \bar{R}_i) as:

$$\begin{aligned} R_i &= N_{1,i}(1 + n_{12} + n_{13}), & \sigma_{R_i} &= \sigma_{N_{1,i}}(1 + n_{12} + n_{13}), \\ \bar{R}_i &= \bar{N}_{1,i}(1 + n_{12} + n_{13}), & \sigma_{\bar{R}_i} &= \sigma_{\bar{N}_{1,i}}(1 + n_{12} + n_{13}), \end{aligned} \quad (106)$$

where $\sigma_{N_{1,i}}$ is the statistical error on the parameter $N_{1,i}$ from the fit on generic MC simulation for the Λ_c^+ fit, and the corresponding quantities with bars are defined for the $\bar{\Lambda}_c^-$ fit (see figure 49 and table 11).

The χ^2 fits with a constant function on residuals (see figure 50), defined in the same way as in (88), yield a result of 0.27 ± 0.32 with a $\chi^2/\text{NDF} = 4.08/9$ for the Λ_c^+ fit and -0.15 ± 0.32 with a $\chi^2/\text{NDF} = 8.36/9$ for the $\bar{\Lambda}_c^-$ fit, corresponding to probabilities 0.90 and 0.50 respectively, so we can conclude that the method correctly reproduces the number of signal events.

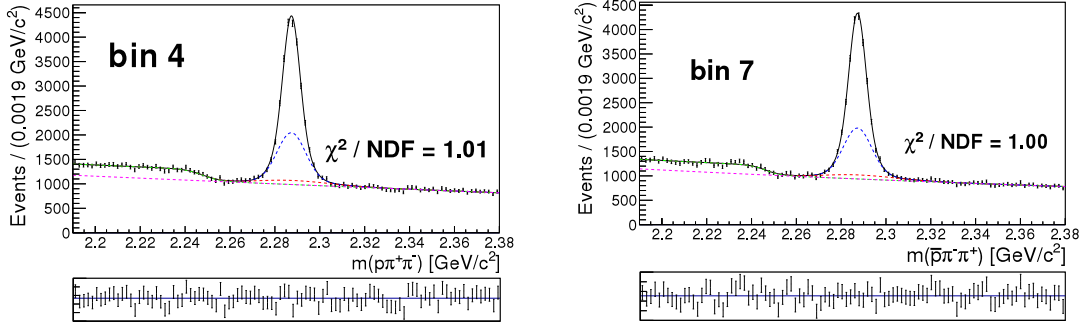


Figure 48: Examples of Λ_c^+ and $\bar{\Lambda}_c^-$ fits on the generic MC simulation for bin 7 ($0.4 < \cos\theta_h < 0.6$). The black, blue, red, green and purple lines mark the narrow Gaussian, the wide Gaussian, the asymmetric Gaussian (all describing signal events), the sigmoid function and the 2nd order Chebyshev polynomial (all describing the backgrounds), respectively. The bottom plots show the fit residuals.

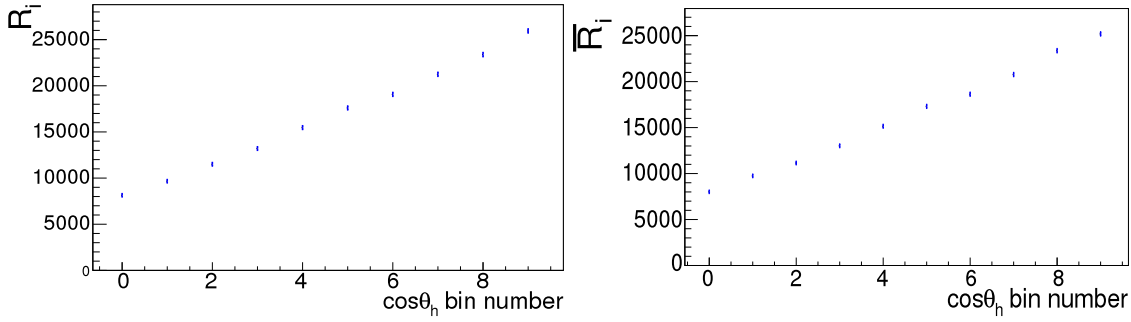


Figure 49: Numbers of events in bins of $\cos\theta_h$, determined from the separate fit to Λ_c^+ and $\bar{\Lambda}_c^-$ invariant mass distributions. Left - numbers of events for Λ_c^+ , right - numbers of events for $\bar{\Lambda}_c^-$.

bin	R_i	\bar{R}_i
0	8137 ± 174	8013 ± 169
1	9661 ± 177	9747 ± 176
2	11497 ± 188	11147 ± 178
3	13202 ± 191	13018 ± 186
4	15470 ± 200	15144 ± 195
5	17599 ± 207	17306 ± 204
6	19067 ± 211	18629 ± 207
7	21242 ± 216	20770 ± 211
8	23378 ± 222	23364 ± 217
9	25943 ± 222	25190 ± 216

Table 11: Numbers of events in bins of $\cos\theta_h$, determined from the separate fit to Λ_c^+ and $\bar{\Lambda}_c^-$ distributions.

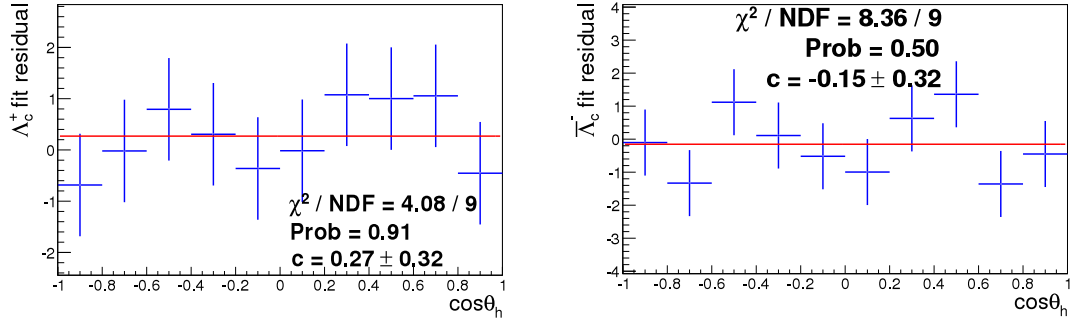


Figure 50: Residuals for fits on the generic MC simulation: left - fit on $\Lambda_c^+ \cos \theta_h$ distribution, right - fit on $\bar{\Lambda}_c^- \cos \theta_h$ distribution, both fitted with a constant function with a χ^2 fit.

4.10 DECONVOLUTION OF Λ_c^+ AND $\bar{\Lambda}_c^-$ EVENTS AND \mathcal{A}_{CP} DETERMINATION

Next we need to use the deconvolution matrix Q , determined from the signal MC simulation (see figure 44), to get the deconvoluted numbers of events for each bin (G_i, \bar{G}_i):

$$G_i = \sum_j q_{ij} R_j, \quad \bar{G}_i = \sum_j q_{ij} \bar{R}_j. \quad (107)$$

To determine \mathcal{A}_{CP} , we fit the reconstructed asymmetry distribution in bins of $\cos \theta_h$:

$$\mathcal{A}_{rec}^i = \frac{G_i - \bar{G}_i}{G_i + \bar{G}_i}, \quad (108)$$

with a function of the form (compare with equation 69):

$$g(x; k, \mathcal{A}_{CP}) = k + \mathcal{A}_{CP} \frac{x}{1 + \langle \alpha \rangle x}, \quad (109)$$

where we use the value of $\langle \alpha \rangle$, determined in section 4.8 using a joined Λ_c^+ and $\bar{\Lambda}_c^-$ sample.

The errors on \mathcal{A}_{rec}^i can be calculated with (see appendix B.6 for a derivation):

$$\begin{aligned} \sigma_{\mathcal{A}_{rec}^i}^2 = & \frac{4}{(G_i + \bar{G}_i)^4} \left(\bar{G}_i^2 \sum_k \sum_l q_{ik} q_{il} R_{kl} \sigma_{R_k} \sigma_{R_l} + \right. \\ & \left. + G_i^2 \sum_k \sum_l q_{ik} q_{il} \bar{R}_{kl} \sigma_{\bar{R}_k} \sigma_{\bar{R}_l} + \sum_k (R_k \bar{G}_i - \bar{R}_k G_i)^2 \sigma_{q_{ik}}^2 \right), \end{aligned} \quad (110)$$

where σ_{R_i} and $\sigma_{\bar{R}_i}$ are the errors on the number of signal events in the i -th bin for the Λ_c^+ and $\bar{\Lambda}_c^-$ distributions, respectively, determined from the fit, R_{ij} and \bar{R}_{ij} are the correlation coefficients between R_i and R_j and between \bar{R}_i and \bar{R}_j , respectively, determined from the fit, and $\sigma_{q_{ij}}$ is the error on the deconvolution matrix element, defined in (97).

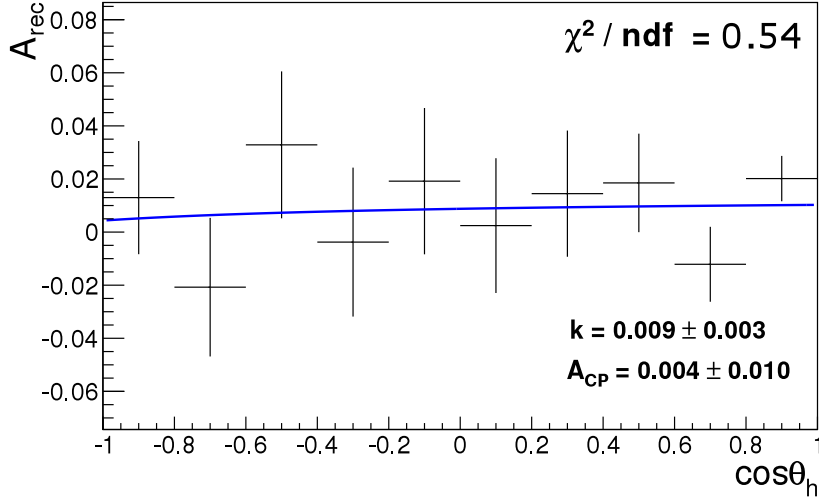


Figure 51: Fit on the reconstructed asymmetry \mathcal{A}_{rec} , used for the determination of \mathcal{A}_{CP} .

Since the errors on \mathcal{A}_{rec}^i are correlated, we again use the multivariate χ^2 fit, where we minimize the function:

$$\chi^2(k, \mathcal{A}_{CP}) = (\vec{\mathcal{A}}_{rec} - \vec{g}(x; k, \mathcal{A}_{CP}))^T V^{-1} (\vec{\mathcal{A}}_{rec} - \vec{g}(x; k, \mathcal{A}_{CP})), \quad (111)$$

where $\vec{\mathcal{A}}_{rec}$ is the vector of determined \mathcal{A}_{rec}^i values, \vec{g} is the corresponding vector of values for the function $g(x; k, \mathcal{A}_{CP})$, defined in (109), evaluated at centers of bins, and V is the covariance matrix of the \mathcal{A}_{rec}^i values, which can be expressed as (see appendix B.5 for a derivation):

$$\begin{aligned} V_{ij} = & \frac{4}{(G_i + \bar{G}_i)^2 (G_j + \bar{G}_j)^2} \left(\bar{G}_i \bar{G}_j \sum_k \sum_l q_{ik} q_{jl} R_{kl} \sigma_{R_k} \sigma_{R_l} + \right. \\ & + G_i G_j \sum_k \sum_l q_{ik} q_{jl} \bar{R}_{kl} \sigma_{\bar{R}_k} \sigma_{\bar{R}_l} + \\ & \left. + \delta_{ij} \sum_k (R_k \bar{G}_i - \bar{R}_k G_i) (R_k \bar{G}_j - \bar{R}_k G_j) \sigma_{q_{ik}} \sigma_{q_{jk}} \right). \end{aligned} \quad (112)$$

The fit is shown in figure 51. We compare the result with the value calculated from the fit on the true signal event $\cos \theta_h$ distribution (figure 34 and table 7) and get a good agreement within the error:

$$\mathcal{A}_{CP}^{rec} = 0.004 \pm 0.010, \quad \mathcal{A}_{CP}^{gen} = -0.003 \pm 0.003. \quad (113)$$

4.11 LINEARITY AND CONSISTENCY TEST

We check the method developed in this chapter with a linearity test which checks if the method gives accurate results regardless of the values of $\langle \alpha \rangle$ and \mathcal{A}_{CP} (in the limits of assumptions in (68)). To perform the check, we generated analysis samples with different values of $\langle \alpha \rangle$ and \mathcal{A}_{CP} (see table 12) from streams 0 and 1 and used the same method as described in this chapter to reconstruct $\langle \alpha \rangle$

Sample ID	α_{gen}	$\bar{\alpha}_{\text{gen}}$	$\langle \alpha \rangle_{\text{gen}}$	$\langle \Delta \rangle$	$\mathcal{A}_{\text{CP gen}}$	Δ^{CP}
0	0.499	0.503	0.501	0.0	-0.003	0.0
1	0.451	0.452	0.451	-6.3	-0.001	0.2
2	0.475	0.474	0.474	-3.4	0.001	0.4
3	0.492	0.493	0.493	-1.0	0.000	0.3
4	0.508	0.510	0.509	1.0	-0.001	0.2
5	0.531	0.531	0.531	3.8	0.000	0.3
6	0.551	0.551	0.551	6.3	0.000	0.3
7	0.474	0.527	0.500	-0.1	-0.052	-4.9
8	0.487	0.520	0.503	0.3	-0.032	-2.9
9	0.499	0.506	0.502	0.1	-0.006	-0.3
10	0.506	0.498	0.502	0.1	0.009	1.2
11	0.518	0.487	0.502	0.1	0.031	3.4
12	0.528	0.478	0.503	0.3	0.049	5.2
13	0.303	0.302	0.302	-24.9	0.002	0.5
14	0.700	0.700	0.700	24.9	0.000	0.3
15	0.349	0.703	0.526	3.1	-0.336	-33.3
16	0.452	0.554	0.503	0.3	-0.100	-9.7
17	0.552	0.453	0.503	0.3	0.099	10.2
18	0.702	0.355	0.528	3.4	0.329	33.2
19	0.301	0.351	0.326	-21.9	-0.077	-7.4
20	0.353	0.303	0.328	-21.6	0.076	7.9
21	0.649	0.700	0.675	21.8	-0.037	-3.4
22	0.702	0.653	0.677	22.0	0.037	4.0

Table 12: Data on different analysis samples used for the linearity test. The $\langle \Delta \rangle$ and Δ^{CP} are the normalized differences between the current and the original sample, defined as $\langle \Delta \rangle_i = \frac{\langle \alpha \rangle_{\text{gen},i} - \langle \alpha \rangle_{\text{gen},0}}{\sigma_{\langle \alpha \rangle}}$ and $\Delta_i^{\text{CP}} = \frac{\mathcal{A}_{\text{CP gen},i} - \mathcal{A}_{\text{CP gen},0}}{\sigma_{\mathcal{A}_{\text{CP}}}}$.

and \mathcal{A}_{CP} . The generated samples are divided into two categories, samples 1 – 12 have values of α and/or \mathcal{A}_{CP} within 6.3σ of the original sample, and samples 13 – 22 have either one or both quantities more than 9.7σ away from the original sample.

The residuals for both quantities, defined as:

$$\text{Res}_i^{\langle \alpha \rangle} = \frac{\langle \alpha \rangle_0 - \langle \alpha \rangle_i}{\sigma_{\langle \alpha \rangle}}, \quad \text{Res}_i^{\mathcal{A}_{\text{CP}}} = \frac{\mathcal{A}_{\text{CP}0} - \mathcal{A}_{\text{CP}i}}{\sigma_{\mathcal{A}_{\text{CP}}}}, \quad (114)$$

are shown in figures 52.

Next, the method is checked with a consistency test which checks if the method gives accurate results for statistically independent samples. To do this, we again generated analysis samples with different values of $\langle \alpha \rangle$ and \mathcal{A}_{CP} (see table 13),

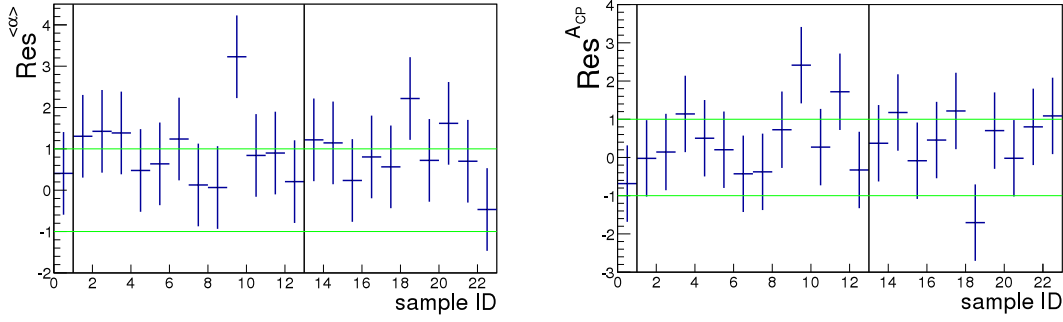


Figure 52: Fit residuals for $\langle\alpha\rangle$ - left, \mathcal{A}_{CP} - right, defined in (114), of different samples for the linearity test with the ± 1 band marked by green lines and different sample categories separated by black lines.

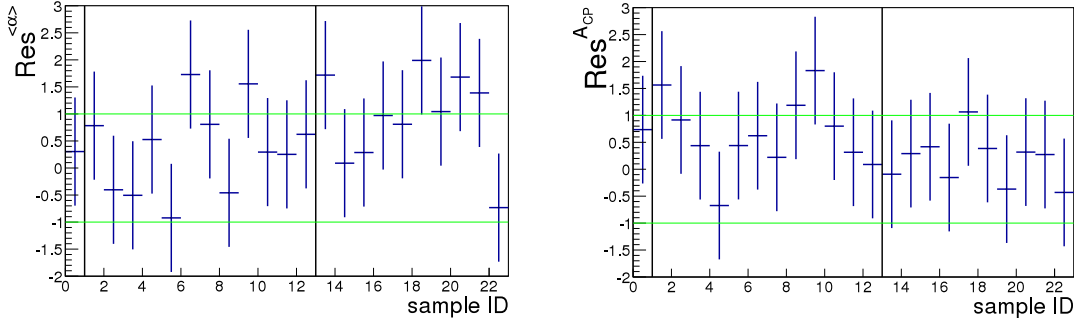


Figure 53: Fit residuals for $\langle\alpha\rangle$ - left, \mathcal{A}_{CP} - right, defined in (114), of different samples for the consistency test with the ± 1 band marked by green lines and different sample categories separated by black lines.

but this time only from stream 2 to ensure that the method is accurate not only for a statistically independent sample, but also for the same number of events as there are in the data sample. Next, we used the same method as described in this chapter to reconstruct $\langle\alpha\rangle$ and \mathcal{A}_{CP} . The generated samples are again divided into two categories, defined in the same way as in the linearity test.

The residuals for both quantities are defined in (114), and are shown in figure 53. For both tests, we see that all residuals (except for one) lie roughly in the 2σ band and show no systematic biases, therefore we can conclude that the method used to reconstruct $\langle\alpha\rangle$ and \mathcal{A}_{CP} has a linear response and is consistent on statistically independent samples.

4.12 SUMMARY

The method developed on simulated data incorporates all sources of statistical uncertainties and the checks show that the results it gives are accurate and unbiased.

Since the statistical uncertainty of a pure signal sample scales as $1/\sqrt{N}$, where N is the number of events in the sample, the expected uncertainty on the data sample is $\lesssim \sqrt{2}$ times the uncertainty obtained from the simulated data, as we used an equivalent of two times the actual collected data to develop the method

Sample ID	α_{gen}	$\bar{\alpha}_{\text{gen}}$	$\langle\alpha\rangle_{\text{gen}}$	$\langle\Delta\rangle$	$\mathcal{A}_{\text{CP gen}}$	Δ^{CP}
0	0.502	0.503	0.502	0.0	0.000	0.0
1	0.458	0.456	0.457	-4.1	0.002	0.1
2	0.470	0.471	0.471	-2.8	0.000	0.0
3	0.492	0.496	0.494	-0.7	-0.003	-0.2
4	0.512	0.516	0.514	1.1	-0.003	-0.2
5	0.529	0.532	0.531	2.6	-0.002	-0.1
6	0.553	0.554	0.554	4.7	0.000	0.0
7	0.480	0.528	0.504	0.2	-0.047	-3.4
8	0.486	0.519	0.502	0.0	-0.032	-2.3
9	0.497	0.507	0.502	0.0	-0.009	-0.6
10	0.509	0.498	0.504	0.2	0.011	0.8
11	0.515	0.485	0.500	-0.2	0.030	2.1
12	0.528	0.473	0.500	-0.2	0.055	3.9
13	0.300	0.308	0.304	-18.0	-0.012	-0.9
14	0.700	0.700	0.700	18.0	0.000	0.0
15	0.355	0.703	0.529	2.5	-0.328	-23.4
16	0.450	0.549	0.500	-0.2	-0.098	-7.0
17	0.554	0.452	0.503	0.1	0.101	7.2
18	0.704	0.351	0.528	2.4	0.335	23.9
19	0.305	0.352	0.329	-15.7	-0.071	-5.1
20	0.352	0.304	0.328	-15.8	0.073	5.2
21	0.651	0.697	0.674	15.6	-0.033	-2.4
22	0.705	0.653	0.679	16.1	0.038	2.7

Table 13: Data on different analysis samples used for the consistency test. The $\langle\Delta\rangle$ and Δ^{CP} are the normalized differences between the current and the original sample, defined as $\langle\Delta\rangle_i = \frac{\langle\alpha\rangle_{\text{gen},i} - \langle\alpha\rangle_{\text{gen},0}}{\sigma_{\langle\alpha\rangle_0}}$ and $\Delta_i^{\text{CP}} = \frac{\mathcal{A}_{\text{CP gen},i} - \mathcal{A}_{\text{CP gen},0}}{\sigma_{\mathcal{A}_{\text{CP}0}}}$.

and the fit results for the number of signal events scale more softly with N because they are correlated with the number of background events in the sample.

For the $\langle\alpha\rangle$ measurement, the expected uncertainty is thus $\lesssim \pm 0.011$ and for the \mathcal{A}_{CP} measurement, $\lesssim \pm 0.014$.

ANALYSIS OF REAL DATA

5.1 MC SIMULATION TUNING

In order to use the method developed in chapter 4, we again need to take into account the small differences between MC simulation and data, coming from the inadequate simulation of the $c\bar{c}$ quark fragmentation into hadrons, a consequence of which is that the produced hadrons have slightly different momenta in the MC simulation compared to the real data.

The different momentum distributions of the hadrons also reflect in the $\cos\theta_h$ distribution as $\cos\theta_h$ is calculated from the magnitudes and directions of the momenta.

Because of these differences, we need to correct the quantities, determined from the MC simulation, that change in the real data. In our method, there are two such quantities, the optimized selection criterion on Λ_c CMS momentum, and the reconstruction efficiency.

To correct this, we need to tune the MC simulation so that the momentum distribution of the Λ_c momentum will match the distribution in the real data. We can do this by comparing the $(p_T, \cos\theta)$ phase spaces in the MC simulation and data, where $p_T = \sqrt{p_x^2 + p_y^2}$ is the transversal momentum of Λ_c in the e^+e^- CM system and θ is the polar angle of the Λ_c flight direction in the e^+e^- CM system.

The phase space for simulated and real data is divided into 2D bins of p_T and $\cos\theta$. Numbers of signal events in the real data phase space bins are determined by sideband subtraction, where by fitting the Λ_c invariant mass distribution the number of signal and background events in a signal window of $\pm 3\sigma$ around the peak value is first determined. A sideband interval in Λ_c invariant mass is then chosen on both sides of the signal interval in such a way that the total number of (background) events in the sideband equals the fitted number of background events in the signal interval (see figure 54). The 2D $(p_T, \cos\theta)$ distribution of events in the sideband is then subtracted from the distribution of events in the signal interval thus providing the $(p_T, \cos\theta)$ distribution of signal events.

The phase space distributions of simulated signal events and real data signal events are shown on figure 55. The differences between distributions are small but non-negligible.

The existing sample of simulated events can be tuned to match the data by appropriately removing simulated events from the sample. For this the following procedure (also known as "hit-or-miss" method) is applied:

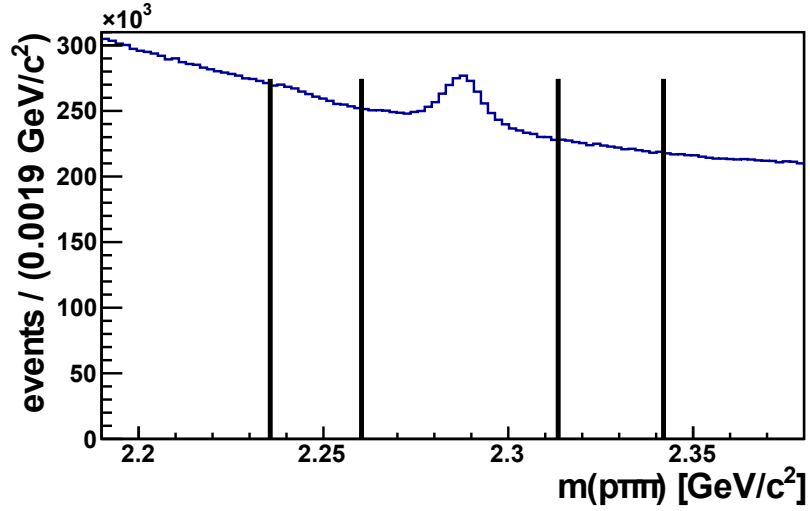


Figure 54: Signal and sideband windows of $p\pi\pi$ invariant mass used to determine the $(p_T, \cos\theta)$ phase space distribution in real data.

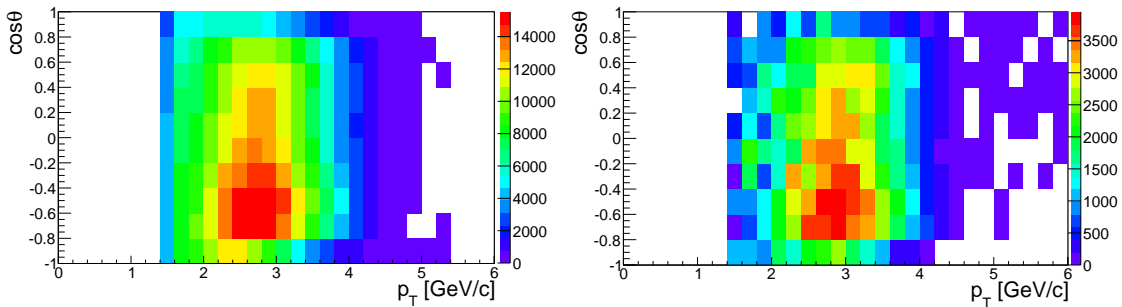


Figure 55: The $(p_T, \cos\theta)$ phase space distributions for: left - simulated signal events, right - for real data signal events obtained by sideband subtraction for Λ_c in the e^+e^- CM system.

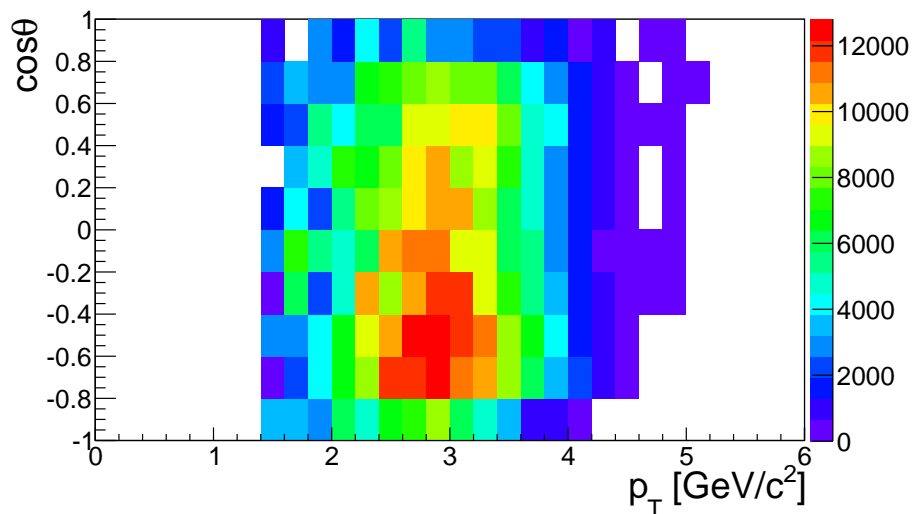


Figure 56: The $(p_T, \cos \theta)$ phase space distribution in the tuned MC simulation for Λ_c in the e^+e^- CM system.

- Because we have bins in the phase space with a small number of events, which are dominated by statistical uncertainties, we choose a only a section of the phase space to be tuned: $[-0.8, 0.6]$ for $\cos \theta$ and $[2.0\text{GeV}, 3.8\text{GeV}]$ for p_T .
- In this section we normalize both the MC simulation and the real data phase space distributions by dividing them with the total number of events in the section, thus obtaining probabilities.
- We calculate the real data/MC simulation ratios of probabilities for all bins in the section, and multiply the number of events in each bin of the MC simulation by the corresponding ratio to obtain the ratio-corrected MC simulation.
- The ratio-corrected/original MC simulation ratios in all bins in the section are used to tune the MC simulation by generating a random number between 0 and 1 for each event, which is then kept if the random number is smaller than the ratio and discarded if the random number is bigger than the ratio.
- For the bins that lie outside the section, we multiply the number of events for each bin with the ratio of the total number of events in the tuned and original MC simulation ($q = 0.72$).

In this way, we obtain a MC simulation with the same $(p_T, \cos \theta)$ phase space distribution (in the tuned section) as the real data. The tuned MC simulation $(p_T, \cos \theta)$ phase space is shown in figure 56.

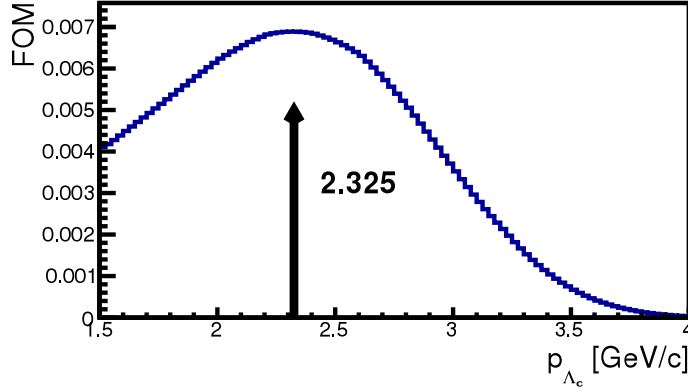


Figure 57: Result of the automated procedure for optimization of the $p_{\text{CMS}}(\Lambda_c)$ selection criterion on tuned MC simulation.

5.1.1 Re-optimization of the Λ_c CMS momentum selection criterion

Because we tuned the momentum of the Λ_c , we need to re-optimize the $p_{\text{CMS}}(\Lambda_c)$ selection criterion. We use the same automated iterative optimization procedure as in section 4.4.1 on the tuned MC simulation sample and find the selection criterion where the $\text{FOM} = \varepsilon \cdot P$ is maximal. The result is shown in figure 57. We find out that the criterion has increased from $p_{\text{CMS}}(\Lambda_c) > 2.2$ GeV to $p_{\text{CMS}}(\Lambda_c) > 2.325$ GeV because the events in real data have a higher average $p_{\text{CMS}}(\Lambda_c)$ than events in the MC simulation.

5.1.2 Real data reconstruction efficiency determination

The reconstruction efficiency, determined from the MC simulation in chapter 4.7, also needs to be updated, since the $\cos\theta_h$ distribution also changes slightly when we tune the Λ_c momentum. The procedure is the same as in chapter 4.7, except that we count the reconstructed and generated events on the tuned MC simulation. The results are shown in figures 58a and 58b.

5.2 Λ_c FIT OF THE REAL DATA ANALYSIS SAMPLE

We create the real data analysis sample by selecting the events satisfying the final selection criteria summarized in table 14.

The distribution of the $m(p\pi\pi)$ invariant mass in bins of $\cos\theta_h$ for the events in the final data sample is fitted using the extended maximum likelihood method (see chapter 4.5.1) and the p.d.f. as defined in chapter 4.5.3. Values of parameters of the p.d.f. which are fixed to the values obtained from MC simulation, are shown in table 10.

An example of the fit for bin 2 ($-0.6 < \cos\theta_h < -0.4$) is shown in figure 59. Results of fits in all $\cos\theta_h$ bins are shown in appendix A.4.

We calculate the number of signal events and the statistical uncertainty as in equation (87) and the results are shown in figures 60b and 60a.

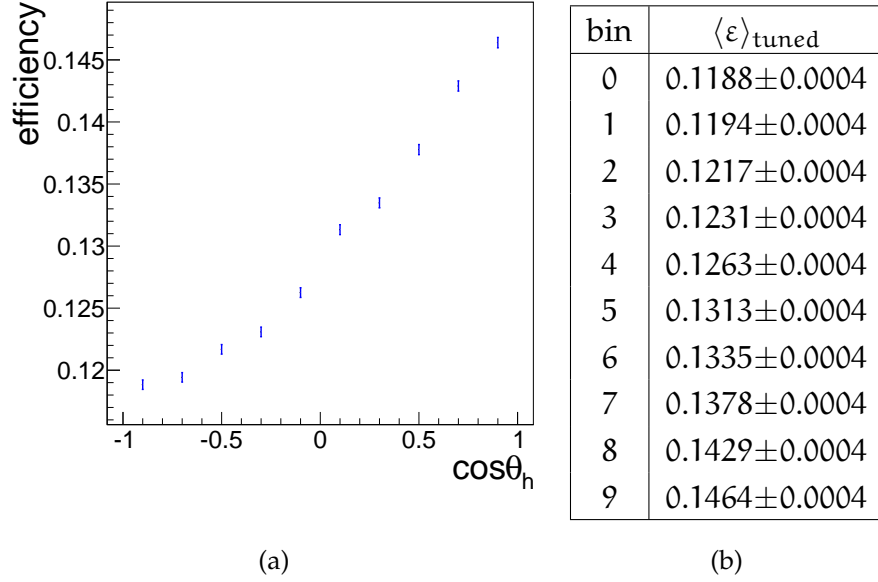


Figure 58: Plot 58a shows the graphical representation of the tuned reconstruction efficiency and table 58b the numerical values in individual $\cos\theta_h$ bins. Note that the histogram in 58a has a suppressed zero and that the total change of the tuned reconstruction efficiency over the whole $\cos\theta_h$ interval amounts to only around 2% – 3%.

selection variable	value
$R_{\pi/K}, R_{\pi/p}$ (for both pions)	≥ 0.6
$R_{\pi/e}, R_{\pi/\mu}$ (for both pions)	≤ 0.9
$R_{p/K}, R_{p/\pi}$	≥ 0.6
$p\pi, p\pi\pi$ vertex fit conf. level	$\geq 10^{-3}$
$m(p\pi)$	$\geq 1.1126 \text{ GeV}/c^2, \leq 1.1186 \text{ GeV}/c^2$
$m(p\pi\pi)$	$\geq 2.19 \text{ GeV}/c^2, \leq 2.38 \text{ GeV}/c^2$
$p_{\text{CMS}}(\Lambda_c)$	$\geq 2.325 \text{ GeV}/c$

Table 14: Selection criteria used to create the real data analysis sample.

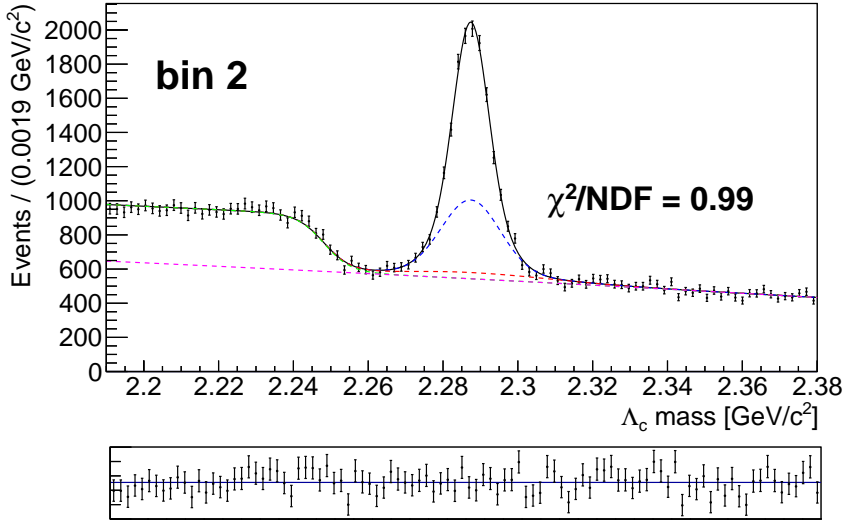


Figure 59: An example of the fit on real data for bin 2 ($-0.6 < \cos\theta_h < -0.4$). The black, blue, red, green and purple lines mark the narrow Gaussian, the wide Gaussian, the asymmetric Gaussian (all describing signal events), the sigmoid function and the 2nd order Chebyshev polynomial (all describing the backgrounds), respectively. The bottom plot shows the fit residuals.

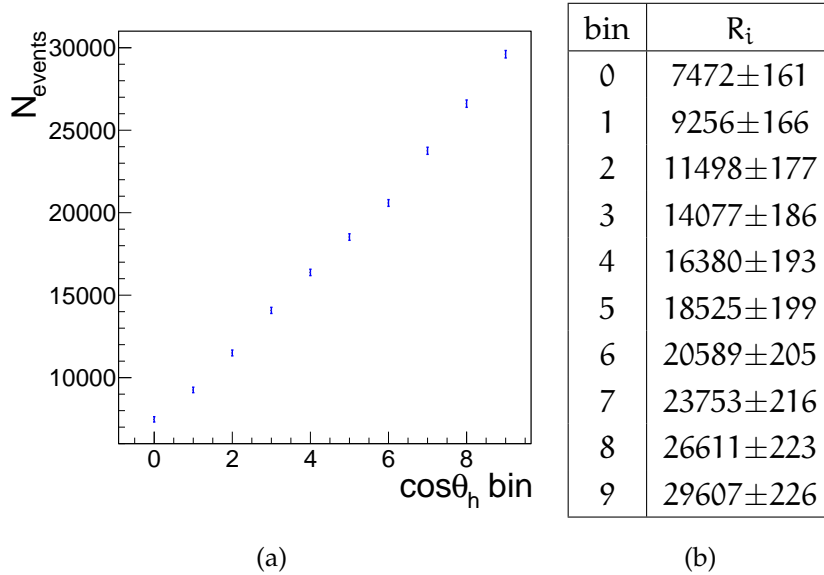


Figure 60: Numbers and statistical uncertainties for signal events for each $\cos\theta_h$ bin, determined from the real data fit. Note that the histogram is zero suppressed.

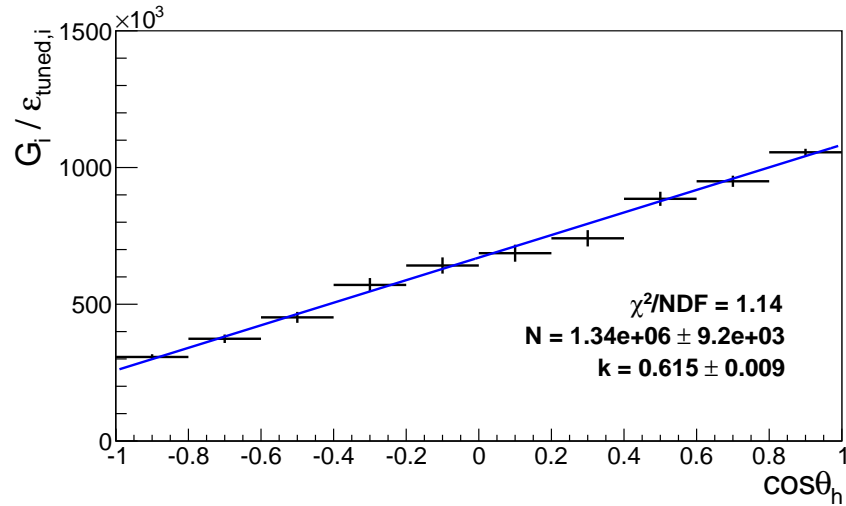


Figure 61: Fit of efficiency corrected deconvoluted $\cos\theta_n$ distribution of signal events on real data used for determination of $\langle\alpha\rangle$. The $\langle\alpha\rangle$ parameter is denoted as k in the plot.

5.3 $\langle\alpha\rangle$ AND $\langle\alpha_{\Lambda_c}\rangle$ DETERMINATION

We now deconvolute the numbers of events obtained from the fit in section 5.2 as explained in section 4.6, using the deconvolution matrix determined from the MC simulation (see figure 44). To determine the $\langle\alpha\rangle$ parameter, we then fit the efficiency corrected deconvoluted numbers of events (T_i):

$$T_i = \frac{G_i}{\langle\epsilon\rangle_{\text{tuned},i}}, \quad (115)$$

with the linear function, defined in (101), using the multivariate χ^2 fit, defined in (103). The fit is shown in figure 61.

The result for $\langle\alpha\rangle$ is:

$$\langle\alpha\rangle = 0.615 \pm 0.009, \quad (116)$$

where the uncertainty includes the statistical uncertainties from the fit, the deconvolution matrix, and the efficiency. With this result, we can use the values of α_Λ and $\mathcal{A}_{\text{CP}}^\Lambda$ from (74) and equation (75) to calculate $\langle\alpha_{\Lambda_c}\rangle$ (look also at the commentary for equation (74)):

$$|\langle\alpha_{\Lambda_c}\rangle| = 0.964 \pm 0.014(\text{stat.}) \pm 0.020(\alpha_\Lambda) \pm 0.020(\mathcal{A}_{\text{CP}}^\Lambda) = 0.964 \pm 0.032, \quad (117)$$

where in the first step we divided the uncertainty into three parts; the first part is the statistical uncertainty of this measurement, the second is the uncertainty of the α_Λ measurement and the third one is the uncertainty of the $\mathcal{A}_{\text{CP}}^\Lambda$ measurement.

If we assume no CP-violation in the $\Lambda \rightarrow p\pi$ decay (i.e. assume $\mathcal{A}_{\text{CP}}^\Lambda = 0$), we use the equation (76), and the result is:

$$|\langle\alpha_{\Lambda_c}\rangle| = 0.958 \pm 0.014(\text{stat.}) \pm 0.019(\alpha_\Lambda) = 0.958 \pm 0.024, \quad (118)$$

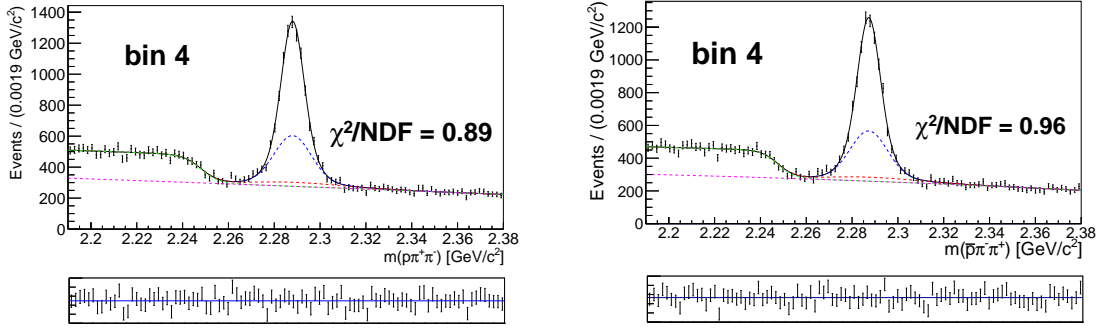


Figure 62: Examples of Λ_c^+ and $\overline{\Lambda}_c^-$ fits on the real data for bin 4 ($-0.2 < \cos\theta_h < 0.0$). The black, blue, red, green and purple lines mark the narrow Gaussian, the wide Gaussian, the asymmetric Gaussian (all describing signal events), the sigmoid function and the 2nd order Chebyshev polynomial (all describing the backgrounds), respectively. The bottom plots show the fit residuals.

where the first part of the uncertainty is the statistical uncertainty of this measurement and the second part is the uncertainty of the α_Λ measurement.

Both results are in agreement with the current world average, taken from [1] (-0.91 ± 0.15) and have an order of magnitude smaller uncertainty.

5.4 Λ_c^+ AND $\overline{\Lambda}_c^-$ FITS OF THE REAL DATA ANALYSIS SAMPLE

In the next step we divide the final data sample used to determine α_{Λ_c} into separate samples of Λ_c^+ and $\overline{\Lambda}_c^-$ decays.

We fit both samples with the extended maximum likelihood fit defined in the chapter 4.5.1, with the fit function defined in the chapter 4.5.3, where we use the values for fixed parameters, determined by the fit on the signal MC simulation, shown in table 10 for both samples.

Additionally, for the Λ_c^+ fit, we fix the m_{bl} and w_{bl} parameters to the values obtained from the Λ_c^+ generic MC fit to ensure the convergence of the fit. The fixed values and their errors, obtained from the generic MC fit, are:

$$\begin{aligned} m_{bl} &= 2.2480 \text{ GeV} \pm 0.0004 \text{ GeV}, \\ w_{bl} &= 0.0039 \text{ GeV} \pm 0.0004 \text{ GeV}. \end{aligned} \quad (119)$$

Examples of Λ_c^+ and $\overline{\Lambda}_c^-$ fits on the real data for bin 4 ($-0.2 < \cos\theta_h < 0.0$) are shown in figure 62. Results of fits for all $\cos\theta_h$ bins are shown in appendix A.5.

The numbers of signal events and their statistical uncertainties for both Λ_c^+ and $\overline{\Lambda}_c^-$ fits are calculated as in equation (106) and are shown in figure 63 and table 15.

5.5 \mathcal{A}_{CP} AND $\mathcal{A}_{CP}^{\Lambda_c}$ DETERMINATION

To determine \mathcal{A}_{CP} , we first deconvolute (see chapter 4.6) the numbers of signal events obtained from the fit in section 5.4 for Λ_c^+ and $\overline{\Lambda}_c^-$ using the deconvolu-

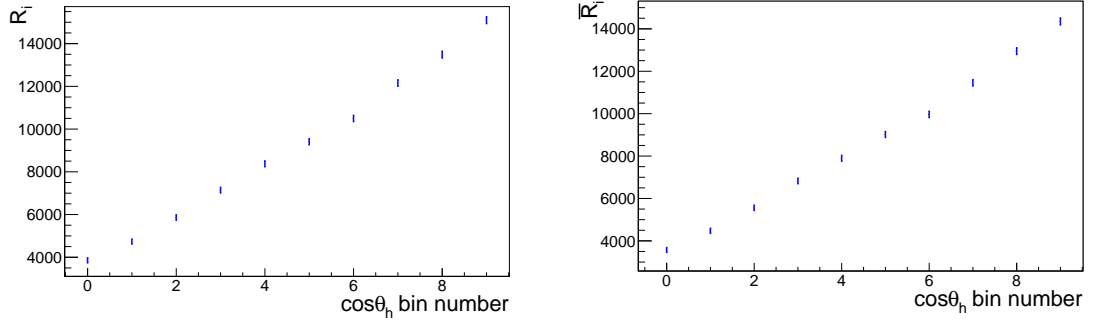


Figure 63: Numbers of events in bins of $\cos\theta_h$, determined from the separate fit to Λ_c^+ and Λ_c^- real data invariant mass distributions. Left - numbers of events for Λ_c^+ , right - numbers of events for Λ_c^- . Note that the histograms are zero suppressed.

bin	R_i	\bar{R}_i
0	3854 ± 116	3571 ± 96
1	4736 ± 114	4475 ± 106
2	5861 ± 123	5559 ± 127
3	7140 ± 130	6826 ± 132
4	8374 ± 137	7894 ± 138
5	9408 ± 141	9016 ± 146
6	10495 ± 145	9963 ± 147
7	12156 ± 152	11456 ± 159
8	13485 ± 157	12950 ± 163
9	15098 ± 158	14352 ± 167

Table 15: Numbers of events in bins of $\cos\theta_h$, determined from the separate fit to Λ_c^+ and Λ_c^- samples.

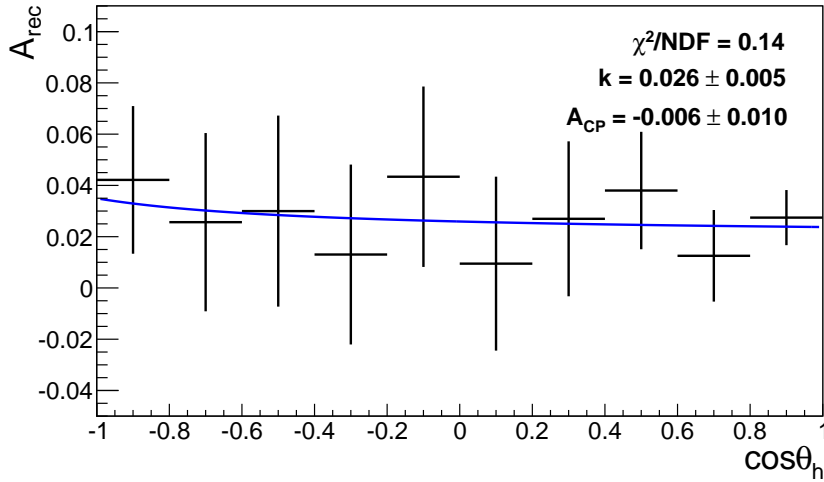


Figure 64: Fit to the reconstructed asymmetry in bins of $\cos \theta_h$ on real data used to determine \mathcal{A}_{CP} .

tion matrix, determined on the MC simulation (see figure 44). With the deconvoluted numbers of signal events, we calculate the reconstructed asymmetry A_{rec}^i , defined in equation (108) in bins of $\cos \theta_h$.

We then fit A_{rec}^i with a multivariate χ^2 fit, defined in (111), with the function, defined in (109). The fit is shown in figure 64.

The result for \mathcal{A}_{CP} is:

$$\mathcal{A}_{CP} = -0.006 \pm 0.010, \quad (120)$$

where the uncertainty is statistical only.

With this result, we can use the value of \mathcal{A}_{CP}^Λ from (74) and equation (77) to calculate $\mathcal{A}_{CP}^{\Lambda_c}$:

$$\mathcal{A}_{CP}^{\Lambda_c} = -0.012 \pm 0.010(\text{stat.}) \pm 0.021(\mathcal{A}_{CP}^\Lambda) = -0.012 \pm 0.023. \quad (121)$$

where in the first step, we divided the statistical uncertainty into two parts, the first is the statistical uncertainty of this measurement and the second the uncertainty of the \mathcal{A}_{CP}^Λ measurement.

If we assume no CP-violation in the $\Lambda \rightarrow p\pi$ decay, the result is the \mathcal{A}_{CP} itself:

$$\mathcal{A}_{CP}^{\Lambda_c} = -0.006 \pm 0.010. \quad (122)$$

Both results are consistent with no CP-violation and are in agreement with the world average [1] (-0.07 ± 0.19), with an order of magnitude smaller uncertainty.

SYSTEMATIC UNCERTAINTY

In this chapter, we evaluate the systematic uncertainty of the result. This uncertainty is present due to several sources; for the present analysis we identified the following possible sources of systematic uncertainty:

- The difference in the tracking efficiency between the real data and the MC simulation introduces an uncertainty for each charged track used in the reconstruction of the Λ_c particle.
- Uncertainty on the deconvolution matrix, which comes from the fact that we calculated the deconvolution matrix based on specific numbers of events from the distribution of events in bins of reconstructed and generated $\cos\theta_h$, obtained from the MC simulation.
- Uncertainty of the fit model, which arises because we fixed various parameters in the fit function based on the MC simulation.
- Uncertainty due to neglecting of the peaking background component in our fit model.
- Uncertainty due to the assumption that the forward-backward asymmetry \mathcal{A}_{FB} is not a function of $\cos\theta_h$.
- Uncertainty due to the assumption that the particle-antiparticle reconstruction asymmetry \mathcal{A}_ε is not a function of $\cos\theta_h$.

6.1 TRACKING EFFICIENCY UNCERTAINTY

This uncertainty affects only the measurement of $\langle\alpha\rangle$, since for the \mathcal{A}_{CP} measurement, it affects the nominator and the denominator in the calculation of the \mathcal{A}_{CP} in the same way and therefore cancels out.

The tracking efficiency systematic error is 0.35% (i.e. the average difference between the tracking efficiency as estimated in MC events and that of real data events) for each charged track used in the reconstruction for tracks which have momentum larger than $200 \text{ MeV}/c^1$ [38].

The systematic uncertainty is treated as correlated among different charged tracks. Since in our measurement we use 3 charged tracks for the reconstruction

¹ The difference between the simulated and real events tracks is measured using partially reconstructed D^* decays.

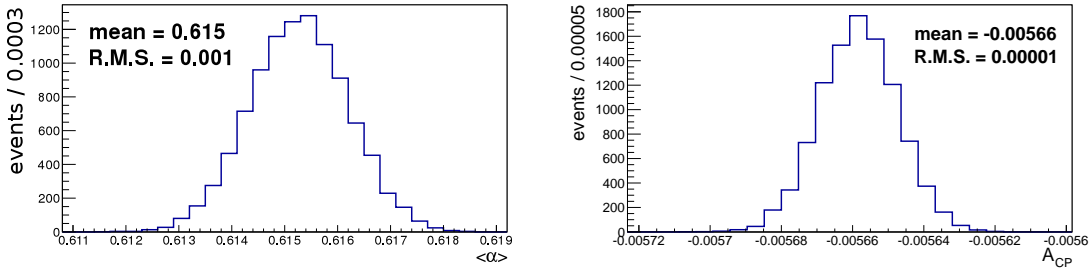


Figure 65: Distributions of $\langle\alpha\rangle$ - left and \mathcal{A}_{CP} - right, obtained by varying the deconvolution matrix and recalculating both quantities. The R.M.S. of the distribution is used as the systematic uncertainty of the two observables due to the uncertainty of the deconvolution matrix.

of the Λ_c particle, we evaluate the systematic uncertainty of the tracking efficiency as 1.05%. The efficiency enters directly into the estimation of $\langle\alpha\rangle$, which therefore carries the same relative uncertainty. This translates into the absolute uncertainty of

$$\sigma_{\text{tracking},\langle\alpha\rangle}^{\text{syst}} = 0.011. \quad (123)$$

6.2 DECONVOLUTION MATRIX UNCERTAINTY

We determined the deconvolution matrix by counting reconstructed and generated events in bins of $\cos\theta_h$ in the MC simulation, thus obtaining the resolution map in chapter 4.6. The procedure depends on the specific counted numbers of events in individual 2D bins of the resolution map. However, the numbers of simulated events are subject to statistical fluctuations and these are treated as a source of systematic uncertainty of the final result.

To evaluate this uncertainty, we vary the number of events in each i, j -th bin in the resolution map stochastically according to a Gaussian distribution with a mean equal to the number of events in this bin (M_{ij}) and a width equal to the standard deviation in this bin, evaluated as $\sqrt{M_{ij}}$.

With the varied resolution map, we again used our measurement method to determine $\langle\alpha\rangle$ and \mathcal{A}_{CP} . This procedure was repeated 10000 times, where each time the deconvolution matrix was varied randomly. The root mean squares of the $\langle\alpha\rangle$ and \mathcal{A}_{CP} distributions obtained this way are taken as the evaluation of the systematic uncertainty (see figure 65):

$$\sigma_{\text{deconvolution},\langle\alpha\rangle}^{\text{syst}} = 0.001. \quad (124)$$

The systematic uncertainty on \mathcal{A}_{CP} due to this source is negligible.

6.3 FIT MODEL UNCERTAINTY

The systematic uncertainty on the fit model comes from the fact that we fixed the ratios $n_{12}, n_{13}, s_{12}, s_{13l}, s_{13r}$ (see chapters 4.5.2 and 4.5.3) and the sigmoid

function parameters m_{bl} and w_{bl} (see chapter 5.4) to values obtained from the MC simulation.

We estimate the systematic uncertainty by varying each of the fixed parameters stochastically according to a Gaussian distribution with a mean equal to the value to which the parameter was fixed, and a width equal to the uncertainty of the fixed parameter, obtained from the signal MC simulation fit for the fixed ratios and from the generic MC simulation fit for the sigmoid function parameters.

We need to take into account the statistical correlations between the parameters, which we also obtained from the signal MC simulation and generic MC simulation fits (see chapters 4.5.2 and 4.5.3). For that purpose, we arrange the original and varied fixed parameters into vectors:

$$\begin{aligned} \mathbf{R} &= [n_{12}, s_{12}, n_{13}, s_{13l}, s_{13r}, m_{bl}, w_{bl}], \\ \tilde{\mathbf{R}} &= [\tilde{n}_{12}, \tilde{s}_{12}, \tilde{n}_{13}, \tilde{s}_{13l}, \tilde{s}_{13r}, \tilde{m}_{bl}, \tilde{w}_{bl}]. \end{aligned} \quad (125)$$

We can now write the correlation matrix for the original fixed parameters as:

$$C = \begin{bmatrix} 1.000 & -0.610 & 0.904 & 0.408 & 0.254 & 0.000 & 0.000 \\ -0.610 & 1.000 & -0.795 & 0.244 & 0.396 & 0.000 & 0.000 \\ 0.904 & -0.795 & 1.000 & 0.063 & -0.118 & 0.000 & 0.000 \\ 0.408 & 0.244 & 0.063 & 1.000 & 0.805 & 0.000 & 0.000 \\ 0.254 & 0.396 & -0.118 & 0.805 & 1.000 & 0.000 & 0.000 \\ 0.000 & 0.000 & 0.000 & 0.000 & 0.000 & 1.000 & -0.139 \\ 0.000 & 0.000 & 0.000 & 0.000 & 0.000 & -0.139 & 1.000 \end{bmatrix}, \quad (126)$$

and the varied fixed parameters are uncorrelated.

To obtain the same correlation between the varied fixed parameters, we find a matrix \mathbf{U} , such that $\mathbf{U}^T \mathbf{U} = C$. This matrix can be found with the Cholesky decomposition. Using this matrix, we can now generate correlated varied fixed parameters from:

$$\mathbf{R}_C = \mathbf{R} + (\tilde{\mathbf{R}} - \mathbf{R})\mathbf{U}. \quad (127)$$

New values for fixed parameters obtained in the described way are then used in determining the $\langle \alpha \rangle$ and \mathcal{A}_{CP} parameters with our measurement method.

We repeat this procedure 10000 times and obtain a distribution for both parameters (see figure 66). The root mean square of these distributions are taken as the systematic uncertainty.

The uncertainties on $\langle \alpha \rangle$ and \mathcal{A}_{CP} due to the fit model are:

$$\begin{aligned} \sigma_{\text{fit model}, \langle \alpha \rangle}^{\text{sys}} &= 0.003. \\ \sigma_{\text{fit model}, \mathcal{A}_{CP}}^{\text{sys}} &= 0.001. \end{aligned} \quad (128)$$

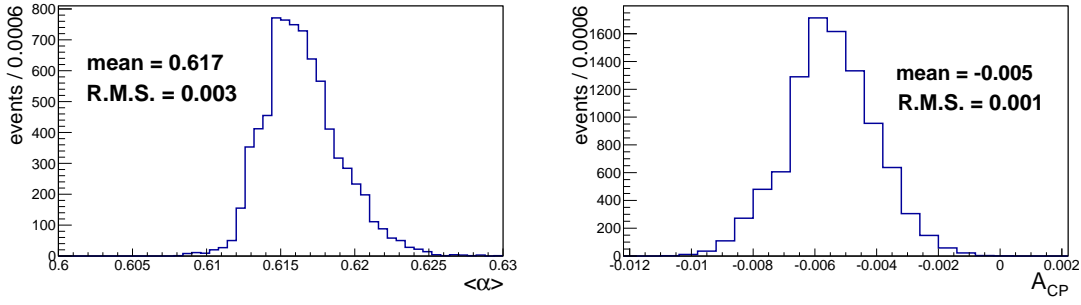


Figure 66: Distributions of $\langle\alpha\rangle$ - left and \mathcal{A}_{CP} - right, obtained by varying the fixed parameters of the fit model and recalculating both quantities. The R.M.S. of these distributions are used as the systematic uncertainty of the two observables due to the uncertainty of the fit model.

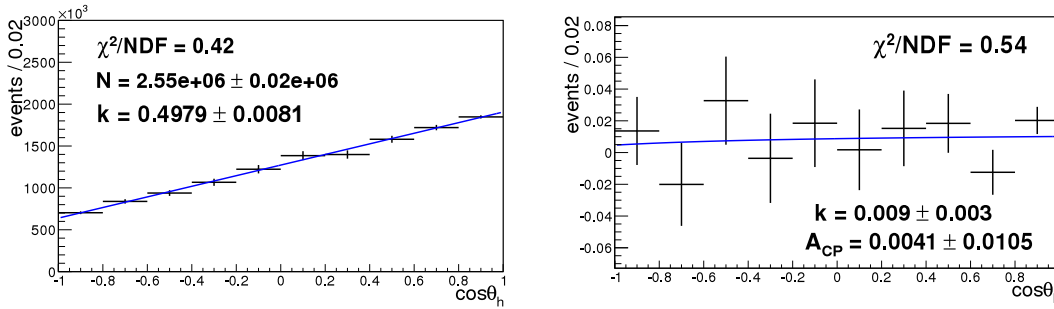


Figure 67: Results of the analysis on MC simulation without the peaking background events. Left - result for $\langle\alpha\rangle$, right - result for \mathcal{A}_{CP} .

6.4 PEAKING BACKGROUND UNCERTAINTY

In chapter 4.3.1, we made a breakdown of the $m(p\pi\pi)$ distribution on the skim sample according to the origin of the Λ_c particle in the MC simulation. We found out that we have a small number of events which have the same $m(p\pi\pi)$ distribution as the signal, but come from other decays - the peaking background. We neglected these events in the subsequent analysis, and therefore introduced a systematic uncertainty.

Since the peaking background arises from some rare processes, there may be a difference between the probability for such events as generated in simulation and the true occurrence rate.

We estimate this uncertainty by generating the same MC simulation as before with the peaking background events left out and repeating the analysis. In this way, we get the biggest possible difference between the values obtained on the MC simulation with and without the peaking background events, which we then take as the uncertainty.

The results of the analysis on MC simulation without peaking background events are shown in figure 67. Systematic uncertainty is in both cases less than 0.001 and thus negligible.

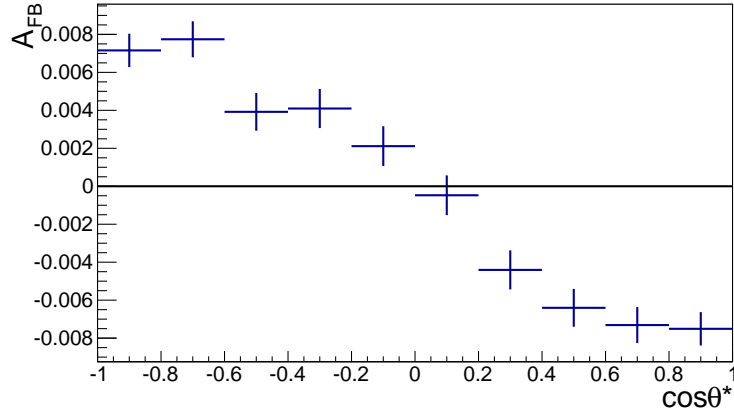


Figure 68: \mathcal{A}_{FB} in bins of the polar angle $\cos\theta^*$ in a signal MC simulation without any selection.

6.5 UNCERTAINTY DUE TO \mathcal{A}_{FB}

This uncertainty arises because we assumed that the $\cos\theta_h$ distribution does not depend on the forward-backward asymmetry or, in other words, that the $\cos\theta^*$ distribution in the CMS and the $\cos\theta_h$ distributions are uncorrelated. In that case in each bin of $\cos\theta_h$ an integral over all $\cos\theta^*$ values is present and thus the forward-backward asymmetry cancels out. If not all values of $\cos\theta^*$ are present in each bin of $\cos\theta_h$, the integral over those values may not vanish in this specific bin and this can lead to asymmetries between Λ_c^+ and $\bar{\Lambda}_c^-$. This uncertainty only affects the \mathcal{A}_{CP} measurement.

First, we check that the \mathcal{A}_{FB} angular dependence is evened out in $\cos\theta_h$ by generating a large MC simulation signal sample on which no selection is applied (not even HadronB preselection). In this sample, we have no \mathcal{A}_{CP} and no \mathcal{A}_c . We know that the forward-backward asymmetry is simulated (to the leading order). We can check this by counting each produced Λ_c^+ and $\bar{\Lambda}_c^-$ in bins of $\cos\theta^*$, where θ^* is the polar angle and calculating \mathcal{A}_{FB} as (see figure 68):

$$\mathcal{A}_{\text{FB}} = \frac{N_{\Lambda_c^+} - N_{\bar{\Lambda}_c^-}}{N_{\Lambda_c^+} + N_{\bar{\Lambda}_c^-}}. \quad (129)$$

To see if this distribution evens out in the θ_h angle, we fit the \mathcal{A}_{FB} distribution with a standard χ^2 fit in bins of $\cos\theta_h$ with the function:

$$f(x; k, \mathcal{A}_{\text{FB}}) = k + \mathcal{A}_{\text{FB}} \frac{x}{1 + \langle\alpha\rangle x}, \quad (130)$$

where we take the value for $\langle\alpha\rangle$ from our reweighed skim sample, as it is in this sample that we would like to check the \mathcal{A}_{FB} . The result is (see figure 69):

$$\begin{aligned} k &= -0.0001 \pm 0.0003, \\ \mathcal{A}_{\text{FB}} &= -0.0004 \pm 0.0010. \end{aligned} \quad (131)$$

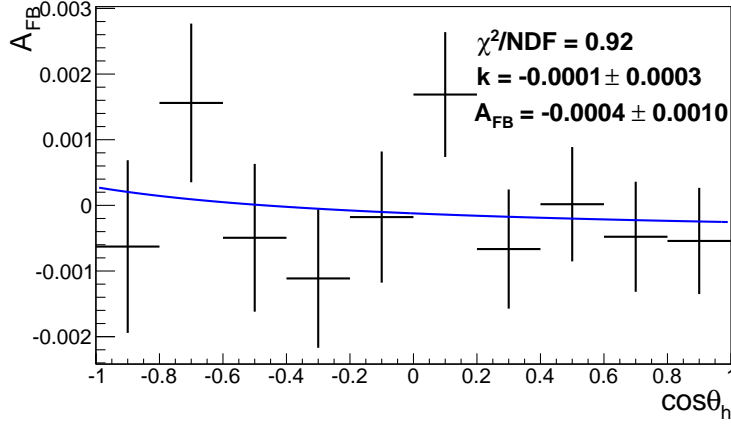


Figure 69: Fit on the \mathcal{A}_{FB} distribution in bins of $\cos\theta_h$ in a signal MC simulation without any selection to determine the evening out of the \mathcal{A}_{FB} distribution in the Λ CM system.

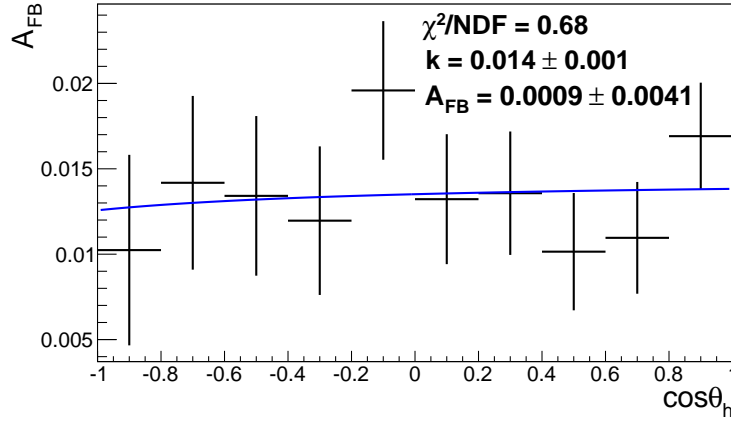


Figure 70: Fit on the \mathcal{A}_{FB} distribution in bins of $\cos\theta_h$ in the analysis sample signal MC simulation to determine the systematic uncertainty.

The asymmetry in $\cos\theta_h$ induced by the forward-backward asymmetry is thus consistent with zero to a high accuracy.

In the next step we check if the selection criteria introduce acceptance effects that may cause asymmetry in $\cos\theta_h$ due to \mathcal{A}_{FB} . We fit the function (130) to the same \mathcal{A}_{FB} distribution in $\cos\theta_h$ as before, but now on a simulated sample with all the selection applied (see figure 70). The result is:

$$\begin{aligned} k &= 0.014 \pm 0.001, \\ \mathcal{A}_{\text{FB}} &= 0.0009 \pm 0.0041. \end{aligned} \quad (132)$$

We see that again the \mathcal{A}_{FB} parameter is consistent with zero. We conservatively assign the uncertainty of the fit as a possible systematic error of the result:

$$\sigma_{\mathcal{A}_{\text{FB}}, \mathcal{A}_{\text{CP}}}^{\text{syst}} = 0.004. \quad (133)$$

6.6 UNCERTAINTY DUE TO \mathcal{A}_ε

In order to check the particle-antiparticle reconstruction asymmetry \mathcal{A}_ε with an uncertainty at least matching the statistical precision of the result, we can not rely on the MC simulation. The subtle effects can arise due to different interactions of particles and antiparticles on the material of the detector. These may not be properly modeled by simulation and hence we have to estimate the effect by using an appropriate control data sample.

A good control sample is a sample of the $\Sigma^* \rightarrow \Lambda\pi, \Lambda \rightarrow p\pi$ decay chain events. The Σ^{*+} and Σ^{*-} particles are excited baryons with quark contents uus for Σ^{*+} and dds for Σ^{*-} . They decay strongly with a branching ratio of 0.87 to $\Lambda\pi$. This is a strong decay, where no CP-violation is present and the consequent decay $\Lambda \rightarrow p\pi$ has a measured CP-violating asymmetry of $A_{CP}^\Lambda = 0.006 \pm 0.021$, consistent with 0 [1]. In the previous section, we have shown that the forward-backward asymmetry evens out in the system where θ_h is defined, so the only asymmetry that could be present in this decay mode is the particle-antiparticle reconstruction asymmetry \mathcal{A}_ε .

To measure \mathcal{A}_ε , we repeat the Λ_c decay chain analysis for the Σ^* decay chain. We construct an analysis sample with the same selection criteria used to obtain the Λ_c data sample (see table 14), with $p_{CMS}(\Lambda_c)$ replaced by $p_{CMS}(\Sigma^*)$, to ensure that the momentum distributions of particles are as closely matched to the Λ_c sample as possible.

We fit the Σ^* mass in bins of $\cos\theta_h$, defined in the same way as in the Λ_c decay chain analysis (see figure 31). We use the extended maximum likelihood fit (see chapter 4.5.1) and fit separately the Σ^{*+} and Σ^{*-} masses separately with a simultaneous fit to all bins in $\cos\theta_h$.

The fit model we use to fit the Σ^* mass distributions is:

$$\begin{aligned}
M_G(m_{p\pi\pi}; \vec{p}) &= \sum_{i=1}^{N_{\text{bin}}=10} N_{1,i} \left(G(m_{p\pi\pi}; m_i, \sigma_{1,i}) + n_{12} G(m_{p\pi\pi}; m_i, s_{12}\sigma_{1,i}) + \right. \\
&+ n_{13} G(m_{p\pi\pi}; m_i, s_{13}\sigma_{1,i}) + \\
&+ \left. \frac{n_{1b}(\cos\theta_h)}{1 + n_{12} + n_{13}} \text{CH}(m_{p\pi\pi}; c_1(\cos\theta_h), c_{12}(\cos\theta_h), c_1(\cos\theta_h)) \right), \\
G(x; m, \sigma) &= \frac{1}{\sqrt{2\pi}\sigma} \exp \left[-\frac{(x - m)^2}{2\sigma^2} \right], \\
\text{CH}(x; c_1, c_2) &= 1 + c_1 x + c_2 (x^2 - 1), \\
n_{1b}(x) &= A_b x + B_b, \\
c_1(x) &= A_{c1} x + B_{c1}, \\
c_{12}(x) &= A_{c12} x + B_{c12},
\end{aligned} \tag{134}$$

where we fix the parameters common to all bins: n_{12}, n_{13}, s_{12} and s_{13} to values obtained from fits to the Σ^* signal MC simulation and A_b, B_b to values obtained from the fit with a linear function to the ratio of number of background events and the number of signal events in bins of $\cos\theta_h$, where we obtain the numbers

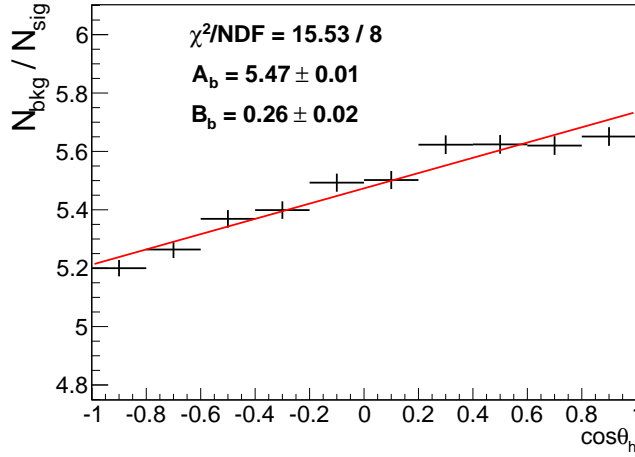


Figure 71: The fit with a linear function on the ratio between numbers of events in the background and the number of events in the signal in bins of $\cos\theta_h$. The numbers of events were obtained from fits on the background and signal MC fits, respectively.

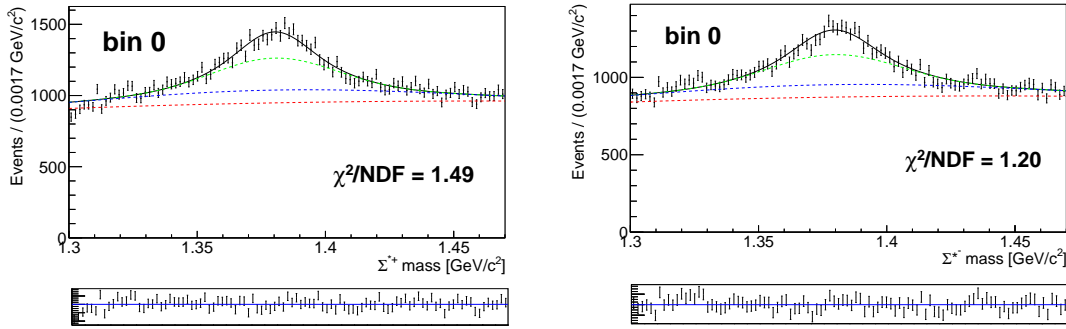


Figure 72: Examples of the Σ^* fits on real data for bin 0 ($-1.0 < \cos\theta_h < -0.8$). Left - fit for Σ^{*+} , right - fit for Σ^{*-} . The black, blue, green and red lines mark the three Gaussians and the Chebyshev polynomial of the 2nd order, respectively. The bottom plots show the fit residuals.

of events for each $\cos\theta_h$ bin from fits to the Σ^* signal and Σ^* background MC simulation, respectively (see figure 71).

Examples of the fit for bin 0 ($-1.0 < \cos\theta_h < -0.8$) are shown on figure 72. Results of fits on all $\cos\theta_h$ bins are shown in appendix A.6.

Next, the numbers of signal events obtained from the fit are deconvoluted using a deconvolution matrix obtained on the Σ^* signal MC simulation (see figure 73) in the same way as in chapter 4.6 and from the deconvoluted numbers of signal events (G_i, \bar{G}_i), the \mathcal{A}_ε is calculated for each bin in $\cos\theta_h$ as :

$$\mathcal{A}_\varepsilon = \frac{G_i - \bar{G}_i}{G_i + \bar{G}_i}. \quad (135)$$

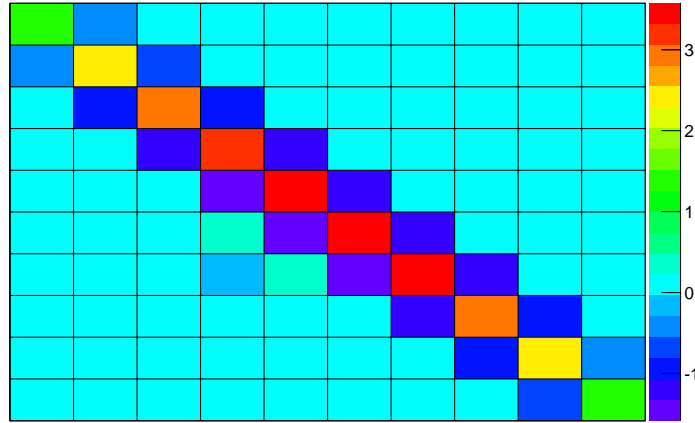


Figure 73: The deconvolution matrix for Σ^* signal events, obtained from the signal MC simulation.

This distribution is then fitted with a multivariate χ^2 fit with a function

$$f(x; k, \mathcal{A}_\varepsilon) = k + \mathcal{A}_\varepsilon \frac{x}{1 + \langle \alpha \rangle x}, \quad (136)$$

where the value for $\langle \alpha \rangle$ is obtained on the Λ_c data sample, as we want to check the \mathcal{A}_ε behavior on this sample. Note that the $\cos\theta_h$ dependence of the \mathcal{A}_ε in equation (69) is a priori not known. Using the control data sample, we want to check a possible contribution of this asymmetry to the \mathcal{A}_{CP} asymmetry. The latter is obtained from a specific difference in the angular distribution of Λ_c^+ and $\overline{\Lambda_c^-}$ decays, leading to the $\cos\theta_h / (1 + \langle \alpha \rangle \cos\theta_h)$ dependence. In order to check a possible contribution of \mathcal{A}_ε to \mathcal{A}_{CP} we thus need to fit the function in equation (136) to a sample known to be free of \mathcal{A}_{CP} .

The fit is shown in figure 74, and the results are:

$$\begin{aligned} k &= 0.048 \pm 0.001, \\ \mathcal{A}_\varepsilon &= 0.002 \pm 0.002. \end{aligned} \quad (137)$$

For the estimate of the systematic uncertainty, we take the error on \mathcal{A}_ε from the fit:

$$\sigma_{\mathcal{A}_\varepsilon, \mathcal{A}_{CP}}^{\text{sys}} = 0.002. \quad (138)$$

6.7 SUMMARY

All the systematic uncertainties are independent, so they need to be summed in quadrature to obtain the whole systematic uncertainty. A summary is shown in table 16.

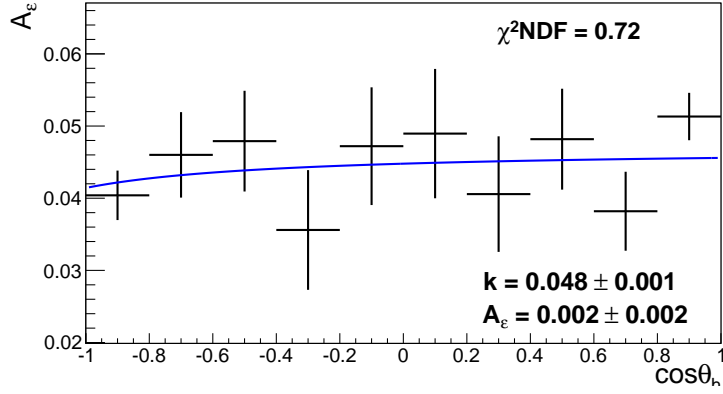


Figure 74: Fit on the \mathcal{A}_ε distribution in bins of $\cos\theta_h$ in the Σ^* analysis sample used to determine the systematic uncertainty.

source	$\sigma_{\langle\alpha\rangle}^{\text{syst}}$	$\sigma_{\mathcal{A}_{\text{CP}}}^{\text{syst}}$
tracking	0.011	n.a.
deconvolution	0.001	negligible
fit model	0.003	0.001
peaking bkg	negligible	negligible
\mathcal{A}_{FB}	n.a.	0.004
\mathcal{A}_ε	n.a.	0.002
sum	0.011	0.005

Table 16: A summary of systematic uncertainties on $\langle\alpha\rangle$ and \mathcal{A}_{CP} .

The systematic errors for $\langle\alpha\rangle$ and \mathcal{A}_{CP} are therefore:

$$\begin{aligned}\sigma_{\langle\alpha\rangle}^{\text{sys}} &= 0.011, \\ \sigma_{\mathcal{A}_{\text{CP}}}^{\text{sys}} &= 0.005.\end{aligned}\tag{139}$$

For $\langle\alpha_{\Lambda_c}\rangle$ and $\mathcal{A}_{\text{CP}}^{\Lambda_c}$, we need to recalculate the systematic uncertainties using equations (75) and (77):

$$\begin{aligned}\sigma_{\langle\alpha_{\Lambda_c}\rangle}^{\text{sys}} &= 0.017, \\ \sigma_{\mathcal{A}_{\text{CP}}^{\Lambda_c}}^{\text{sys}} &= 0.005.\end{aligned}\tag{140}$$

If we assume no CP-violation in the $\Lambda \rightarrow p\pi$ decay, the values for systematic uncertainties remain the same.

SUMMARY

We present a measurement of the weak asymmetry parameter $\langle\alpha_{\Lambda_c}\rangle$ and the CP-violating asymmetry $\mathcal{A}_{\text{CP}}^{\Lambda_c}$ for the $\Lambda_c \rightarrow \Lambda\pi$ decay.

Our method is based on determining the average weak asymmetry parameter for joined Λ_c^+ and $\bar{\Lambda}_c^-$ decays and using this value, determining the weak asymmetry parameter. In the measurement of $\mathcal{A}_{\text{CP}}^{\Lambda_c}$ some sources of the systematic uncertainty (tracking efficiency, ...) cancel out.

The values obtained, assuming the measured CP-violation [1] in the $\Lambda \rightarrow p\pi$ decay, are:

$$\begin{aligned}
|\langle\alpha_{\Lambda_c}\rangle| &= 0.964 \pm 0.014(\text{stat.}) \pm 0.020(\alpha_{\Lambda}) \pm 0.020(\mathcal{A}_{\text{CP}}^{\Lambda}) \pm 0.017(\text{syst.}) = \\
&= 0.964 \pm 0.014(\text{stat.}) \pm 0.033(\text{syst.}), \\
\mathcal{A}_{\text{CP}}^{\Lambda_c} &= -0.012 \pm 0.010(\text{stat.}) \pm 0.021(\mathcal{A}_{\text{CP}}^{\Lambda}) \pm 0.005(\text{syst.}) = \\
&= -0.012 \pm 0.010(\text{stat.}) \pm 0.022(\text{syst.}),
\end{aligned} \tag{141}$$

where in the first step, we separated the uncertainties arising due to the finite accuracy of the weak asymmetry parameter and CP violating asymmetry in the Λ decays.

If we assume no CP-violation in the $\Lambda \rightarrow p\pi$ decay, the results are:

$$\begin{aligned}
|\langle\alpha_{\Lambda_c}\rangle| &= 0.958 \pm 0.014(\text{stat.}) \pm 0.019(\alpha_{\Lambda}) \pm 0.017(\text{syst.}) = \\
&= 0.958 \pm 0.014(\text{stat.}) \pm 0.025(\text{syst.}), \\
\mathcal{A}_{\text{CP}}^{\Lambda_c} &= -0.006 \pm 0.010(\text{stat.}) \pm 0.005(\text{syst.}).
\end{aligned} \tag{142}$$

All values agree with the previous measurements [34] and with the world averages [1] and are consistent with no CP violation in the Λ_c decays. The presented measurements are the most sensitive measurements up to date and are by an order of magnitude more sensitive than the current world averages.

The statistical uncertainties of the results for α_{Λ_c} and $\mathcal{A}_{\text{CP}}^{\Lambda_c}$ are larger than the experimental systematic uncertainties. Hence in the future the sensitivity can be improved by performing measurements at the SuperKEKB collider and Belle II detector, which are currently under construction. Furthermore the sensitivity can be improved by improved measurements of the asymmetries in Λ decays.

 POVZETEK DOKTORSKEGA DELA

8.1 UVOD

8.1.1 *Standardni Model in njegove simetrije*

Standardni Model (SM) je teorija, ki opisuje osnovne delce in interakcije med njimi. Delce opisuje z kvantnimi polji, katerih dinamika je določena preko principa minimalne akcije z Lagrangeovo funkcijo, sestavljeno iz omenjenih kvantnih polj. Opisuje tri interakcije, ki jih najdemo v naravi - elektromagnetno, šibko in močno interakcijo.

SM je relativistična umeritvena teorija, kar pomeni, da je njena Lagrangeova funkcija invariantna na dva seta zveznih transformacij; Poincarejeve transformacije, opisane z Liejevo grupo translacija \times $SO(1,3)$ in umeritvene transformacije, opisane z Liejevo grupo $SU(3)_C \times SU(2)_L \times U(1)_Y$ [2, 3, 4].

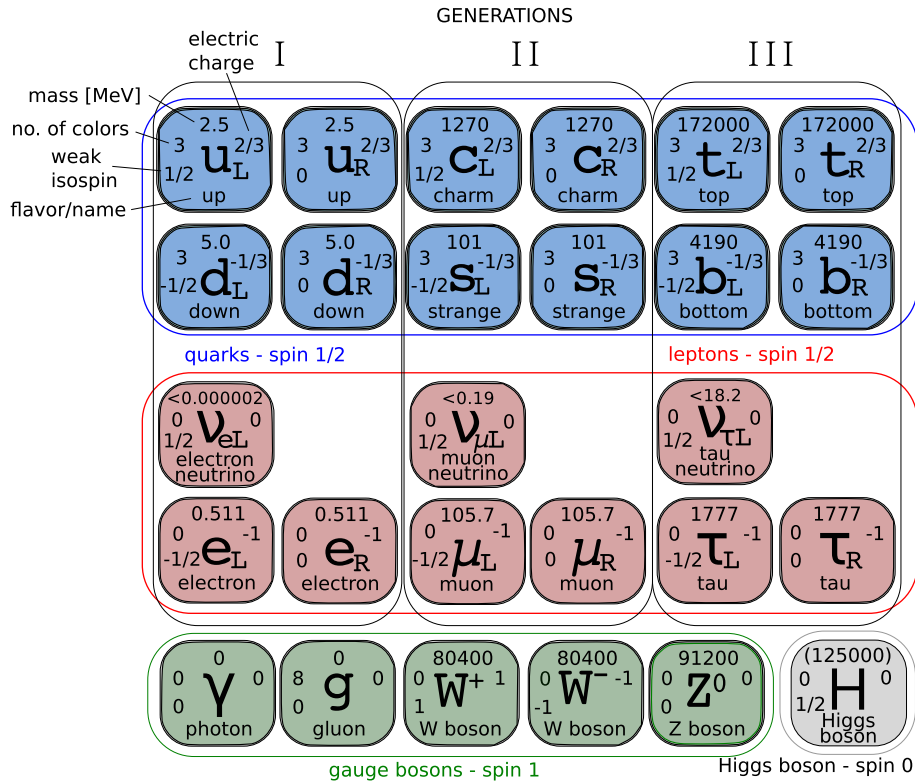
Po Noetherinem teoremu [6] je vsaka simetrija povezana z nekim ohranitvenim zakonom. Pri Poincarejevih transformacijah, ki povezujejo med seboj različne inercialne sisteme, se ohranjajo energija, gibalna količina in vrtilna količina sistema.

Umeritvene transformacije povezujejo med seboj različne konfiguracije kvantnega polja, ki dajo enake opazljive količine. Vsaki interakciji, ki jo opiše SM, lahko priredimo umeritveno simetrijsko grupo. Polja se transformirajo kot grupa $SU(3)_C$ pri močni interakciji, količina, ki se ohranja pri tej transformaciji, pa je barva kvarka. Pri elektrošibki interakciji se polja transformirajo kot grupa $SU(2)_L \times U(1)_Y$, ohranjeni količini pa sta šibki hipernaboj in šibki isospin. V SM je simetrija $SU(3)_C \times SU(2)_L \times U(1)_Y$ spontano zlomljena preko neničelne pričakovane vrednosti vakuuma teorije v simetrijsko grupo $SU(3)_C \times U(1)_{em}$, kar da močno, šibko in elektromagnetno interakcijo.

Fundamentalna kvantna polja v SM lahko razdelimo v več kategorij glede na spin in kvantna števila, ki se ohranjajo pri umeritvenih transformacijah (glej sliko 75).

V prvi kategoriji so umeritveni bozoni z spinom 1, ki prenašajo interakcije. Imamo osem brezmasnih gluonov g , ki prenašajo močno interakcijo, tri masivne šibke bozone W^+ , W^- in Z^0 , ki prenašajo šibko interakcijo in brezmasni foton γ , ki je prenašalec elektromagnetne interakcije.

V drugi kategoriji so fermioni z spinom $\frac{1}{2}$, ki sestavljajo snov. Organiziramo jih lahko v tri generacije, ki se obnašajo enako glede na interakcije, razlika med generacijami je samo v masi fermionov in v okusnem kvantnem številu. V vsaki generaciji imamo par levoročnih kvarkov (tipa u in tipa d), par levoročnih lep-



Slika 75: Delci Standardnega Modela in njihove lastnosti.

tonov (lepton in pripadajoči nevtrino), desnoročna kvarke tipa u in tipa d in desnorčni lepton. Za vsak delec obstaja pripadajoči antidelec, ki ima enako maso in obratna kvantna števila. Tako imamo v SM 3 kvarke tipa u (u, c, t), tri kvarke tipa d (d, s, b), tri tipe leptonov (e, μ, τ) in tri pripadajoče nevtrine (ν_e, ν_μ, ν_τ).

V tretji kategoriji je delec z spinom 0, imenovan Higgsov bozon, ki preko interakcije in spontane zlomitve simetrije delcem generira maso.

Vsi delci, z izjemo Higgsovega bozona, so eksperimentalno potrjeni, v letu 2012 pa sta kolaboraciji ATLAS in CMS odkrili nov delec z lastnostmi, konsistentnimi z Higgsovim bozonom [8, 9].

Poleg točnih fundamentalnih simetrij SM lahko definiramo tudi transformacije, pri katerih se Lagrangeova funkcija v SM le delno ohranja. Definiramo lahko na primer tri diskretne transformacije:

- P - obrat parnosti, ki obrne prostorske koordinate, \vec{r} v $-\vec{r}$,
- C - konjugacija naboja, ki pretvori delec v njegov antidelec z konjugacijo vseh njegovih notranjih kvantnih števil,
- T - obrat časa, ki obrne smer časa, t v $-t$.

Elektromagnetna in močna interakcija sta simetrični glede na vse tri transformacije, šibka interakcija pa krši simetriji P in C maksimalno. Dolgo časa je veljalo, da je SM popolnoma simetričen glede na združeno transformacijo CP, nato pa sta Cronin in Fitch odkrila majhno kršenje simetrije CP v sistemu nevtralnih kaonov [10]. Kršenje simetrije CP so kasneje odkrili tudi v razpadih mezonov B pri

kolaboracijah Belle in Babar [11]. Da se pokazati, da je simetrija CPT fundamentalna simetrija SM [12, 13].

8.1.2 Kršenje simetrije CP in mehanizem Kobayashi-Maskawa

Transformacija CP pretvori delec v njegov antidelec. Kršenje simetrije CP je zato zelo pomembno, saj je eno izmed ključnih stvari, ki lahko pojasni zakaj je vesolje v veliki večini sestavljeno iz snovi in ne iz antisnovi [14].

V SM je edini izvor kršenja simetrije CP pri interakcijah med kvarki pojasnjen z mehanizmom Kobayashi-Maskawa (KM), ki pa ne pojasni celotne asimetrije med snovjo in antisnovjo, izmerjene preko nukleosinteze in kozmičnega mikrovalovnega ozadja [15, 16].

Lagrangeova funkcija za SM je sestavljena iz večih delov:

$$\mathcal{L} = \mathcal{L}_{\text{gaugeKT}} + \mathcal{L}_{\text{fermionKT}} + \mathcal{L}_{\text{Higgs}} + \mathcal{L}_{\text{Yukawa}}. \quad (143)$$

Prva dva dela vsebujeta kinetične člene za umeritvena polja in fermionska polja, tretji del vsebuje Higgsov potencial, četrti pa vsebuje trojno interakcijo Yukawa, kjer interagirajo med seboj Higgsov bozon ter levoročni kvark in desnoročni antikvark (ali obratno). Zadnji člen je edini v SM, ki krši simetrijo CP. Po spontani zlomitvi simetrije se ta člen transformira v člene, ki generirajo maso kvarkov. V interakcijski bazi se člen z Yukawa interakcijo zapiše kot:

$$-\mathcal{L}_{\text{Yukawa}}^{\text{mass}} = (M_d)_{ij} \overline{D}_{Li} D_{Rj} + (M_u)_{ij} \overline{U}_{Li} U_{Rj} + (M_d)^*_{ij} \overline{D}_{Ri} D_{Lj} + (M_u)^*_{ij} \overline{U}_{Ri} U_{Lj}. \quad (144)$$

Da bi iz zgornjih členov izluščili mase kvarkov, je potrebno izraz zapisati v masni bazi, kjer so masne matrike diagonalne. Vedno lahko najdemo dve unitarni matriki V_{qL} in V_{qR} , tako da bo $V_{qL} M_q V_{qR}^\dagger = M_q^{\text{diag}}$, ($q = u, d$). Lastna stanja za maso kvarkov so potem $q'_{Li} = (V_{qL})_{ij} q_{Lj}$, $q'_{Ri} = (V_{qR})_{ij} q_{Rj}$, ($q = u, d$).

V tej bazi so členi v Lagrangeovi funkciji, ki opisujejo šibko interakcijo (1. del Lagrangeove funkcije v enačbi (143)):

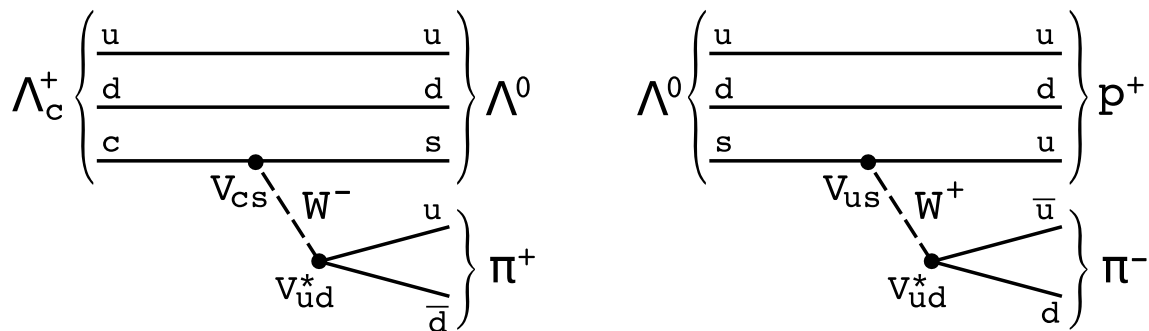
$$-\mathcal{L}_{\text{cc, mass}} = \frac{g}{\sqrt{2}} \begin{bmatrix} \overline{u}'_L & \overline{c}'_L & \overline{t}'_L \end{bmatrix} \gamma^\mu W_\mu^+ (V_{uL} V_{dL}^\dagger) \begin{bmatrix} d'_L \\ s'_L \\ b'_L \end{bmatrix} + \quad (145)$$

$$\frac{g}{\sqrt{2}} \begin{bmatrix} \overline{d}'_L & \overline{s}'_L & \overline{b}'_L \end{bmatrix} \gamma^\mu W_\mu^- (V_{uL} V_{dL}^\dagger)^* \begin{bmatrix} u'_L \\ c'_L \\ t'_L \end{bmatrix}.$$

3×3 unitarna matrika:

$$V_{\text{CKM}} = V_{uL} V_{dL}^\dagger, \quad (146)$$

se imenuje matrika Cabibbo-Kobayashi-Maskawa (CKM). Vrednosti elementov matrike CKM nam povedo kolikšna je verjetnost, da bodo kvarki iz različnih generacij interagirali preko šibke interakcije.

Slika 76: Feynmanovi diagrami razpadne verige bariona Λ_c^+ .

Vsaka 3×3 matrika se da parametrizirati z tremi realnimi parametri in eno kompleksno fazo. Zelo uporabna parametrizacija matrike CKM se imenuje Wolfensteinova parametrizacija:

$$V_{\text{CKM}} = \begin{bmatrix} 1 - \frac{1}{2}\lambda^2 & \lambda & A\lambda^3(\rho - i\eta) \\ -\lambda & 1 - \frac{1}{2}\lambda^2 & A\lambda^2 \\ A\lambda^3(1 - \rho - i\eta) & -A\lambda^2 & 1 \end{bmatrix} + \mathcal{O}(\lambda^4). \quad (147)$$

Vrednosti parametrov lahko določimo iz prilagajanja na vse znane meritve ter z upoštevanjem unitarnosti:

$$\lambda = 0.22535 \pm 0.00065, \quad A = 0.811_{-0.012}^{+0.022}, \quad \rho = 0.131_{-0.013}^{+0.026}, \quad \eta = 0.345_{-0.014}^{+0.013}. \quad (148)$$

Vidimo da je matrika CKM skoraj diagonalna, kar pomeni da je najbolj verjetna šibka sklopitev sklopitev med kvarki iz iste generacije.

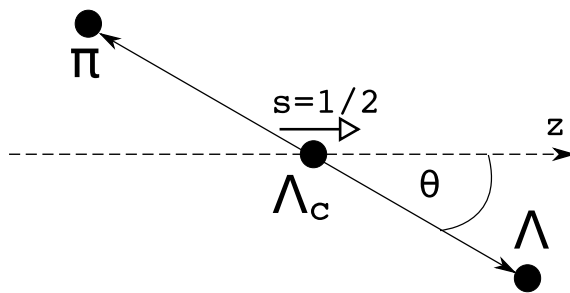
Kompleksna faza matrike CKM je edini izvor kršitve simetrije CP v SM. To lahko vidimo tako, da CP transformiramo del Lagrangeove funkcije (145) in primerjamo transformiran in netransformiran del. Ugotovimo, da če velja $V_{\text{CKM}} = V_{\text{CKM}}^*$, ta del Lagrangeove funkcije ohranja simetrijo CP, ali z drugimi besedami, šibka interakcija ohranja simetrijo CP samo če je kompleksna faza enaka 0.

8.1.3 Kršenje simetrije CP pri razpadu bariona Λ_c

Barion Λ_c je delec z spinom $1/2$, sestavljen iz kvarkov (udc). V tem delu bomo iskali kršenje simetrije CP v specifični razpadni verigi bariona Λ_c , kjer Λ_c razpade z šibko interakcijo v barion Λ , prav tako delec z spinom $1/2$, sestavljen iz kvarkov (uds), in v π^+ , mezon z spinom 0 in kvarkovsko sestavo (u \bar{d}). Barion Λ nato razpade z šibko interakcijo v proton, zopet barion z spinom $1/2$ z kvarkovsko sestavo (uud) in v π^- , mezon z spinom 0 in kvarkovsko sestavo (d \bar{u}). (glej sliko 76).

Šibki razpad bariona z spinom $1/2$ v barion z spinom $1/2$ in mezon z spinom 0 ($B_0 \rightarrow B_1 M$) opišemo z amplitudo:

$$A(B_0 \rightarrow B_1 M) = \overline{u_{B_1}}(p_{B_1}, s_{B_1}) [A_S - \gamma_5 A_P] u_{B_0}(p_{B_0}, s_{B_0}), \quad (149)$$



Slika 77: Definicija kota v kotni porazdelitvi razpada bariona Λ_c v njegovem težiščnem sistemu.

CP-transformirana amplituda pa je:

$$A(B_0 \rightarrow B_1 M) \xrightarrow{CP} \overline{v}_{B_0}(p_{B_0}, s_{B_0}) [A_S + \gamma_5 A_P] v_{B_1}(p_{B_1}, s_{B_1}). \quad (150)$$

Iz amplitude (149) lahko izračunamo kotno porazdelitev razpadnih produktov v razpadu (glej spodaj), ter dobimo da je le-ta linearna funkcija kosinusa polarnega kota. Če je v razpadih ohranjena simetrija CP, bo parameter v kotni porazdelitvi razpada B_0 , α_{B_0} , nasproten parametru pri razpadu antidelca \overline{B}_0 , $\alpha_{\overline{B}_0}$, zaradi (149) in (150). Če definiramo parameter asimetrije

$$\mathcal{A}_{CP}^{B_0} = \frac{\alpha_{B_0} + \alpha_{\overline{B}_0}}{\alpha_{B_0} - \alpha_{\overline{B}_0}}, \quad (151)$$

lahko tako določimo stopnjo kršitve asimetrije CP v razpadih barionov B_0 in \overline{B}_0 .

Pri razpadu bariona Λ_c^+ bo kotna porazdelitev, merjena v težiščnem sistemu bariona Λ (glej sliko 77):

$$\frac{dN}{d \cos \theta} = \psi_f^* \psi_f = 1 + \alpha_{\Lambda_c} \cos \theta, \quad (152)$$

kjer je α_{Λ_c} parameter šibke asimetrije za razpad Λ_c :

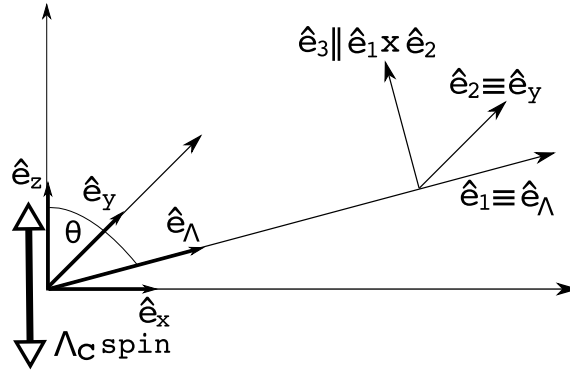
$$\alpha_{\Lambda_c} = \frac{2\text{Re}(A_S^* A_P)}{|A_S|^2 + |A_P|^2}. \quad (153)$$

Definiramo lahko še dva parametra šibke asimetrije za ta razpad:

$$\begin{aligned} \beta_{\Lambda_c} &= \frac{2\text{Im}(A_S^* A_P)}{|A_S|^2 + |A_P|^2}, \\ \gamma_{\Lambda_c} &= \frac{|A_S|^2 - |A_P|^2}{|A_S|^2 + |A_P|^2}. \end{aligned} \quad (154)$$

Če ima Λ_c polarizacijo P_{Λ_c} , se kotna porazdelitev posploši v:

$$\frac{dN}{d \cos \theta} = 1 + P_{\Lambda_c} \alpha_{\Lambda_c} \cos \theta. \quad (155)$$

Slika 78: Definicija emisijskega koordinatnega sistema za Λ .

Ker barion Λ prav tako razpada šibko v barion z spinom $1/2$ in mezon z spinom 0 , lahko tudi za ta razpad zapišemo kotno porazdelitev na enak način kot pri (155):

$$\frac{dN}{d \cos \theta_p} = 1 + P_\Lambda \alpha_\Lambda \cos \theta_p, \quad (156)$$

kjer sta P_Λ in α_Λ polarizacija in parameter šibke asimetrije za razpad bariona Λ .

Če upoštevamo, da ima barion Λ , ki pride iz razpada bariona Λ_c , specifično določeno polarizacijo, ter če se postavimo v posebej definiran emisijski sistem bariona Λ (glej sliko 78), lahko izpeljemo kotne porazdelitve, ki veljajo za združeno razpadno verigo $\Lambda_c \rightarrow \Lambda, \Lambda \rightarrow p\pi$ [22]:

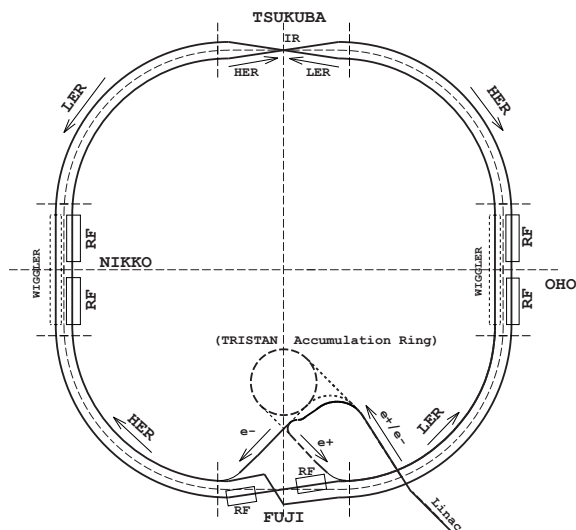
$$\begin{aligned} \frac{dN}{d \cos \vartheta_1} &= 1 + \alpha_{\Lambda_c} \alpha_\Lambda \cos \vartheta_1, & \cos \vartheta_1 &= \hat{e}_p \cdot \hat{e}_1, \\ \frac{dN}{d \cos \vartheta_2} &= 1 + \frac{\pi}{4} P_{\Lambda_c} \beta_{\Lambda_c} \alpha_\Lambda \cos \vartheta_2, & \cos \vartheta_2 &= \hat{e}_p \cdot \hat{e}_2, \\ \frac{dN}{d \cos \vartheta_3} &= 1 + \frac{\pi}{4} P_{\Lambda_c} \gamma_{\Lambda_c} \alpha_\Lambda \cos \vartheta_3, & \cos \vartheta_3 &= \hat{e}_p \cdot \hat{e}_3, \end{aligned} \quad (157)$$

kjer so \hat{e}_1, \hat{e}_2 in \hat{e}_3 smeri osi emisijskega sistema Λ , \hat{e}_p pa je smer emisije protona v težiščnem sistemu Λ .

Iz prve enačbe v (157) vidimo, da lahko določimo parameter α_{Λ_c} ne glede na polarizacijo začetnega vzorca barionov Λ_c .

8.2 TRKALNIK KEKB IN DETEKTOR BELLE

Meritev je bila opravljena na podatkih, zbranih z detektorjem Belle. Belle je detektor osnovnih delcev, postavljen okoli točke, kjer se križata žarka elektronov in pozitronov iz asimetričnega trkalnika KEKB, postavljenega pri mestu Tsukuba na Japonskem. Sledi kratek opis trkalnika KEKB in detektorja Belle. Za popoln opis, glej [24] za opis trkalnika KEKB in [25, 26] za opis detektorja Belle.



Slika 79: Shema trkalnika KEKB [24].

8.2.1 Trkalnik KEKB

Trkalnik KEKB je asimetrični trkalnik elektronov in pozitronov. Ima dva obroča, v enem potujejo elektroni z energijo 8.5 GeV (visokoenergijski obroč HER), v drugem pa pozitroni z energijo 3.5 GeV (nizkoenergijski obroč LER). Obročata se križata v eni točki (interakcijska točka) pod kotom 22mrad (glej sliko 79). Energiji e^- in e^+ sta izbrani tako, da je energija v težiščnem sistemu enaka:

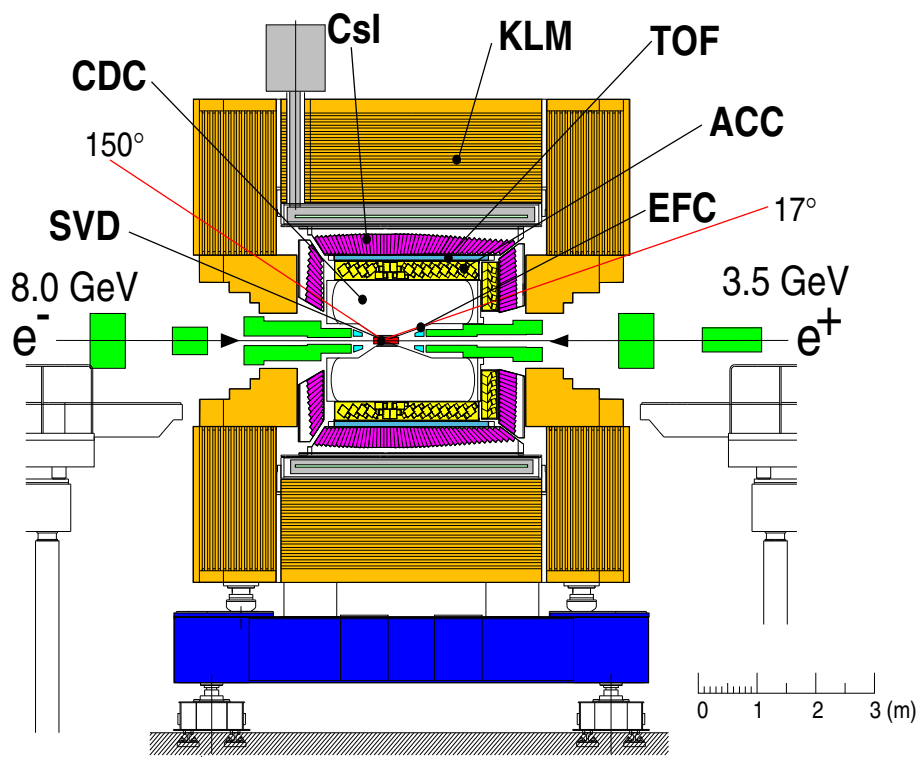
$$E_{CM} = 2\sqrt{E_{HER}E_{LER}} = 10.58 \text{ GeV}, \quad (158)$$

kar ustreza masi resonance $\Upsilon(4S)$, vzbujenemu vezanemu stanju kvarkov $b\bar{b}$ [1]. Ta resonanca razpada izključno v par mezonov B (nabitih ali nevtralnih), saj je njena masa približno enaka masi dveh mezonov B. Sipalni presek za reakcijo $e^+e^- \rightarrow \Upsilon(4S) \rightarrow B\bar{B}$ je pri tej energiji velik, zato trkalnik KEKB proizvede veliko število mezonov B (je t.i. tovarna mezonov B). Zasnova trkalnika je taka, ker je bil glavni cilj kolaboracije Belle meritev kršitve simetrije CP pri mezonih B.

Poleg mezonov B nastajajo pri trkih tudi pari kvarkov drugega okusa, $e^+e^- \rightarrow q\bar{q}$, $q = u, d, s, c$. Trkalnik je tako tudi velik izvor kvarkov c in omogoča študijo fizike čarobnih delcev.

8.2.2 Detektor Belle

Okoli interakcijske točke je postavljen detektor Belle, ki pokriva prostorski kot med 17° in 150° in meri identiteto, energijo in gibalno količino različnih delcev, ki nastanejo kot končni produkti trkov e^+e^- v trkalniku. Postavljen je v superprevodno tuljavo, ki ustvarja homogeno magnetno polje z gostoto 1.5T. Sestavljen je iz večih poddetektorjev, kjer ima vsak poddetektor različne naloge (glej sliko 80).



Slika 8o: Detektor Belle z označenimi poddetektorskimi sistemi [25].

- Silicijev detektor mesta razpada (SVD), ki zelo natančno (na $\sim 100\mu\text{m}$) meri mesto razpada mezonov B (in ostalih kratkoživih delcev), kar omogoča študijo časovno odvisne kršitve simetrije CP pri mezonih B.
- Gledano radialno navzven, sledi večžični ionizacijski detektor (CDC), s katerim rekonstruiramo sledi delcev in preko ukrivljenosti sledi v magnetnem polju določimo njihovo gibalno količino. Relativna natančnost meritve transverzalne gibalne količine je med 0.5% in 1.1%. Poleg tega detektor meri specifično ionizacijo delcev, kar nam omogoča ločevanje med kaoni, pioni in elektroni z gibalnimi količinami pod $0.8 \text{ GeV}/c$ z zanesljivostjo, večjo od 99.7%.
- Radialno navzven sledi pragovni števec sevanja Čerenkova (PID). V njem delci letijo skozi aerogel z lomnim količnikom, izbranim tako, da v območju gibalnih količin med $1.2 \text{ GeV}/c$ in $3.5 \text{ GeV}/c$ pioni sevajo fotone Čerenkova, trikrat težji kaoni pa ne. Tako števec omogoča ločevanje med pioni in kaoni z zanesljivostjo, večjo od 99.7%.
- Sledi merilec časa preleta (TOF), ki meri čas, ki ga delec potrebuje, da preleti razdaljo med interakcijsko točko in TOF. Z pomočjo izmerjenega časa, gibalne količine v CDC in določene razdalje med merilcem TOF in interakcijsko točko lahko izračunamo maso delca. To nam omogoča ločevanje med pioni in kaoni na območju gibalnih količin med $0.8 \text{ GeV}/c$ in $1.2 \text{ GeV}/c$ z zanesljivostjo, večjo od 99.7%.

- Nato sledi elektromagnetni kalorimeter (ECL), ki meri energijo fotonov in elektronov, omogoča pa tudi ločevanje med elektroni in pioni preko meritve deponirane energije in gibalne količine, izmerjene v CDC. Verjetnost za napačno identifikacijo elektronov je okoli 5% za gibalne količine, manjše od 1.0 GeV/c, in pade pod 1% za gibalne količine, večje od 2.0 GeV/c.
- Zunanji detektor je detektor mionov in mezonov K_L (KLM), ki omogoča identifikacijo mionov in mezonov K_L z gibalnimi količinami nad 600 MeV/c z meritvijo penetracijske dolžine. Elektroni se namreč ustavijo že v notranjih poddetektorjih, hadroni se ustavijo v KLM, mioni pa večinoma letijo skozenj. Zanesljivost identifikacije mionov je boljša od 90%, z verjetnostjo napačne identifikacije pod 5%.

8.2.3 Identifikacija nabitih delcev

Tipe nabitih delcev (e, μ, π, K, p) se pri detektorju Belle identificira s kombiniranjem meritev iz različnih poddetektorjev, ki so sposobni ločevati med njimi. Za vsak poddetektor se določi verjetnost, da je neka zaznana nabita sled določenega tipa f ($f = e, \mu, \pi, K, p$) $P_{f,i}$, nato pa se verjetnosti za vsak poddetektor zmnoži; $P_f = \prod_i P_{f,i}$. Ta produkt se nato uporabi za izračun verjetnostnega razmerja, ki loči med delcema tipov f in f' :

$$R_{f/f'} = \frac{P_f}{P_f + P_{f'}}. \quad (159)$$

To razmerje lahko zavzame vrednosti med 0 in 1 in je uporabno, ker s tem lahko ločimo različne tipe delcev z eno samo spremenljivko.

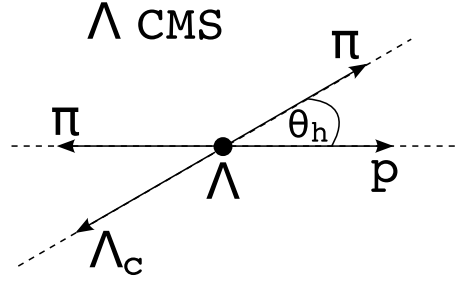
8.3 METODA MERITVE

V tej analizi merimo parameter kršitve simetrije CP $\mathcal{A}_{CP}^{\Lambda_c}$, definiran z enačbo (151) za razpad $\Lambda_c \rightarrow \Lambda \pi$ ¹. Izmerili ga bomo s pomočjo prve enačbe v (157). Da lahko uporabimo to enačbo, moramo izmeriti kotno porazdelitev po kotu θ_h , definiranem kot kot med smerjo gibalne količine protona in smerjo gibalne količine piona iz Λ_c v težiščnem sistemu Λ (glej sliko 81). Ta kot je enak kotu θ_p v enačbah (157). Merjena kotna porazdelitev bo tako oblike

$$\frac{dN}{d \cos \theta_h} = \frac{N}{2}(1 + \alpha \cos \theta_h), \quad (160)$$

kjer je N število rekonstruiranih razpadov v vzorcu, α pa produkt parametrov šibke asimetrije za razpada $\Lambda_c \rightarrow \Lambda \pi$ in $\Lambda \rightarrow p \pi$; $\alpha = \alpha_{\Lambda_c} \alpha_{\Lambda}$.

¹ Kadarkoli pišemo Λ_c brez predznaka, mislimo s tem tako Λ_c^+ kot $\overline{\Lambda_c^-}$.

Slika 81: Definicija kota θ_h , uporabljena v analizi.

8.3.1 Meritev povprečnega parametra šibke asimetrije

Najprej predpostavimo, da je kršenje simetrije CP v razpadu bariona Λ_c majhno, kar pomeni, da je razlika med α za Λ_c^+ in $\bar{\alpha}$ za $\bar{\Lambda}_c^-$ majhna. Tako lahko definiramo povprečni α :

$$d\alpha \ll \langle \alpha \rangle, \quad \langle \alpha \rangle \approx \alpha \approx \bar{\alpha}. \quad (161)$$

Povprečni α lahko izmerimo, če združimo vzorca za Λ_c^+ in $\bar{\Lambda}_c^-$ v enega, ter na njem izmerimo kotno porazdelitev (160). Kotno porazdelitev izmerimo tako, da za vsak rekonstruirani razpad izračunamo $\cos\theta_h$, nato pa razdelimo dogodke v intervale po spremenljivki $\cos\theta_h$.

Za i -ti interval lahko število rekonstruiranih dogodkov v njem izrazimo kot:

$$N_i^{\text{rec,join}}(\cos\theta_{h,i}) = N_i^{0,\text{join}}(\cos\theta_{h,i}) \text{Br}(\Lambda_c \rightarrow \Lambda\pi)(\cos\theta_{h,i}) \quad (162)$$

$$\text{Br}(\Lambda \rightarrow p\pi)(\cos\theta_{h,i}) \langle \epsilon \rangle_i(\cos\theta_{h,i}),$$

kjer je $N_i^{\text{rec,join}}$ število rekonstruiranih Λ_c razpadov v i -tem intervalu, $N_i^{0,\text{join}}$ je število vseh nastalih razpadov Λ_c , ki padejo v i -ti interval, $\text{Br}(\Lambda_c \rightarrow \Lambda\pi)(\cos\theta_{h,i})$ in $\text{Br}(\Lambda \rightarrow p\pi)(\cos\theta_{h,i})$ sta kotno odvisni razvejitevni razmerji za razpada barionov Λ_c in Λ , $\cos\theta_{h,i}$ je vrednost $\cos\theta_h$ v i -tem intervalu, $\langle \epsilon \rangle_i$ pa je učinkovitost za rekonstrukcijo razpadne verige Λ_c v i -tem intervalu.

Kotno odvisnost razvejitvenih razmerij lahko izrazimo preko prve enačbe v (157):

$$\text{Br}(\Lambda_c \rightarrow \Lambda\pi)(\cos\theta_{h,i}) \text{Br}(\Lambda \rightarrow p\pi)(\cos\theta_{h,i}) = \text{Br}^0 \frac{1}{2} (1 + \langle \alpha \rangle \cos\theta_{h,i}), \quad (163)$$

kjer je Br^0 produkt absolutnih razvejitvenih razmerij za Λ_c in Λ razpada.

Kotna odvisnost števila vseh nastalih Λ_c je posledica asimetrije v produkciji; asimetrije naprej-nazaj, ki pa je antisimetrična funkcija glede na delce in antidelce in se tako pokrajša (glej poglavje 8.3.2), ker smo združili vzorca za Λ_c^+ in $\bar{\Lambda}_c^-$.

Tako dobimo za število rekonstruiranih dogodkov v i -tem intervalu izraz

$$N_i^{\text{rec,join}}(\cos\theta_{h,i}) = N_i^{0,\text{join}} \text{Br}^0 \frac{1}{2} (1 + \langle \alpha \rangle \cos\theta_{h,i}) \langle \epsilon \rangle_i(\cos\theta_{h,i}). \quad (164)$$

Za vsak interval določimo število rekonstruiranih dogodkov z funkcijskim prilagajanjem porazdelitve dogodkov po masi Λ_c v tem intervalu, ter ga delimo z učinkovitostjo rekonstrukcije za ta interval, ki jo določimo preko Monte Carlo (MC) simulacije.

Upoštevati je potrebno še resolucijo detektorja za to meritev, ki povzroči da so izmerjene mase in gibalne količine rahlo drugačne od dejanskih, kar pomeni, da se lahko rekonstruirani razpadi premaknejo iz pravega intervala v $\cos\theta_h$. Ta efekt bomo upoštevali tako, da bomo izvedli dekonvolucijo na določenih številnih razpadov v intervalih z dekonvolucijsko matriko, določeno preko MC simulacije.

Po tem postopku dobimo pravo porazdelitev po $\cos\theta_h$, iz katere lahko z prilagajanjem z linearno funkcijo določimo $\langle\alpha\rangle$.

8.3.2 Meritev parametra kršenja simetrije CP

Za to meritev s funkcijskim prilagajanjem porazdelitve dogodkov po masi določimo najprej števila razpadov v intervalih $\cos\theta_h$ za Λ_c^+ in $\bar{\Lambda}_c^-$ razpade posebej, nato pa izračunamo rekonstruirano asimetrijo za vsak interval, kjer je rekonstruirana asimetrija za i -ti interval:

$$\mathcal{A}_i^{\text{rec}}(\cos\theta_{h,i}) = \frac{N_i^{\text{rec}}(\cos\theta_{h,i}) - \bar{N}_i^{\text{rec}}(\cos\theta_{h,i})}{N_i^{\text{rec}}(\cos\theta_{h,i}) + \bar{N}_i^{\text{rec}}(\cos\theta_{h,i})}. \quad (165)$$

Števila rekonstruiranih razpadov N_i^{rec} in \bar{N}_i^{rec} lahko izrazimo na enak način kot v (162):

$$\begin{aligned} N_i^{\text{rec}}(\cos\theta_{h,i}) &= N^0(\cos\theta_{h,i}) \text{Br}(\Lambda_c^+ \rightarrow \Lambda\pi^+)(\cos\theta_{h,i}) \text{Br}(\Lambda \rightarrow p^+\pi^-)(\cos\theta_{h,i}) \varepsilon_i(\cos\theta_{h,i}), \\ \bar{N}_i^{\text{rec}}(\cos\theta_{h,i}) &= \bar{N}^0(\cos\theta_{h,i}) \text{Br}(\bar{\Lambda}_c^- \rightarrow \bar{\Lambda}\pi^-)(\cos\theta_{h,i}) \text{Br}(\bar{\Lambda} \rightarrow \bar{p}^-\pi^+)(\cos\theta_{h,i}) \bar{\varepsilon}_i(\cos\theta_{h,i}), \end{aligned} \quad (166)$$

kjer so količine definirane na enak način kot prej, pri čemer so količine brez črte definirane za razpade Λ_c^+ , količine z črto pa za razpade $\bar{\Lambda}_c^-$.

Kotno odvisnost razvejitenih razmerij lahko izrazimo enako kot v (163):

$$\begin{aligned} \text{Br}(\Lambda_c^+ \rightarrow \Lambda\pi^+)(\cos\theta_{h,i}) \text{Br}(\Lambda \rightarrow p^+\pi^-)(\cos\theta_{h,i}) &= \text{Br}^0 \frac{1}{2} (1 + \alpha \cos\theta_{h,i}), \quad (167) \\ \text{Br}(\bar{\Lambda}_c^- \rightarrow \bar{\Lambda}\pi^-)(\cos\theta_{h,i}) \text{Br}(\bar{\Lambda} \rightarrow \bar{p}^-\pi^+)(\cos\theta_{h,i}) &= \text{Br}^0 \frac{1}{2} (1 + \bar{\alpha} \cos\theta_{h,i}). \end{aligned}$$

Tako dobimo za števili rekonstruiranih razpadov v i -tem intervalu:

$$\begin{aligned} N_i^{\text{rec}}(\cos\theta_{h,i}) &= N^0(\cos\theta_{h,i}) \text{Br}^0 \frac{1}{2} (1 + \alpha \cos\theta_{h,i}) \varepsilon_i(\cos\theta_{h,i}), \quad (168) \\ \bar{N}_i^{\text{rec}}(\cos\theta_{h,i}) &= \bar{N}^0(\cos\theta_{h,i}) \text{Br}^0 \frac{1}{2} (1 + \bar{\alpha} \cos\theta_{h,i}) \bar{\varepsilon}_i(\cos\theta_{h,i}). \end{aligned}$$

Sedaj poleg majhnosti kršitve simetrije CP predpostavimo še majhno asimetrijo naprej-nazaj, kar pomeni da je število vseh nastalih Λ_c^+ in $\bar{\Lambda}_c^-$ približno

enako, ter da sta učinkovitosti za rekonstrukcijo razpadov Λ_c^+ in $\bar{\Lambda}_c^-$ približno enaki:

$$\begin{aligned} N_i^0 &\approx \bar{N}_i^0 \approx \langle N^0 \rangle_i, \\ \varepsilon_i &\approx \bar{\varepsilon}_i \approx \langle \varepsilon \rangle_i. \end{aligned} \quad (169)$$

S temi predpostavkami lahko količine razvijemo do prvega reda v majhnih količinah dN^0 , $d\alpha$ in $d\varepsilon$:

$$\begin{aligned} N_i^0 &= \langle N^0 \rangle_i + dN_i^0, \quad dN_i^0 \ll \langle N^0 \rangle_i, \\ \bar{N}_i^0 &= \langle N^0 \rangle_i - dN_i^0, \\ \alpha &= \langle \alpha \rangle + d\alpha, \quad d\alpha \ll \langle \alpha \rangle, \\ \bar{\alpha} &= \langle \alpha \rangle - d\alpha, \\ \varepsilon_i &= \langle \varepsilon \rangle_i + d\varepsilon_i, \quad d\varepsilon_i \ll \langle \varepsilon \rangle_i, \\ \bar{\varepsilon}_i &= \langle \varepsilon \rangle_i - d\varepsilon_i. \end{aligned} \quad (170)$$

Če te razvoje vstavimo v enačbo za rekonstruirano asimetrijo (165), dobimo do prvega reda:

$$\begin{aligned} \mathcal{A}_i^{\text{rec}}(\cos \theta_{h,i}) &= \mathcal{A}_i^{\text{FB}}(\cos \theta_{h,i}) + \mathcal{A}_i^\varepsilon(\cos \theta_{h,i}) + \mathcal{A}_{\text{CP}} \frac{\cos \theta_{h,i}}{1 + \langle \alpha \rangle \cos \theta_{h,i}}, \\ \mathcal{A}_i^{\text{FB}} &= \frac{N_i^0 - \bar{N}_i^0}{N_i^0 + \bar{N}_i^0}, \\ \mathcal{A}_i^\varepsilon &= \frac{\varepsilon_i - \bar{\varepsilon}_i}{\varepsilon_i + \bar{\varepsilon}_i}, \\ \mathcal{A}_{\text{CP}} &= \frac{\alpha - \bar{\alpha}}{\alpha + \bar{\alpha}}. \end{aligned} \quad (171)$$

Tu smo definirali asimetrijo naprej-nazaj (\mathcal{A}^{FB}) in asimetrijo pri rekonstrukciji Λ_c^+ ali $\bar{\Lambda}_c^-$ (\mathcal{A}^ε). Za asimetrijo \mathcal{A}^{FB} vemo, da je antisimetrična funkcija polarnega kota [1, 35] v težiščnem sistemu e^+e^- , asimetrija \mathcal{A}^ε pa je lahko odvisna od polarnega kota v laboratorijskem sistemu zaradi geometrije detektorja. Ker pa je $\cos \theta_h$ definiran v svojem sistemu (emisijem sistemu za Λ) za vsak razpad posebej, predpostavimo da se odvisnosti \mathcal{A}^{FB} in \mathcal{A}^ε od $\cos \theta_h$ izpovprečita. Ti predpostavki lahko preverimo; za \mathcal{A}^{FB} tako, da jo preverimo na MC simulaciji, za \mathcal{A}^ε pa tako, da rekonstruiramo razpadno verigo $\Sigma^* \rightarrow \Lambda\pi$, $\Lambda \rightarrow p\pi$, ki ima enake končne produkte kot naša merjena razpadna veriga, vendar ne vsebuje asimetrije CP, saj poteka razpad bariona Σ^* preko močne interakcije, razpad Λ pa ima izmerjeno asimetrijo CP konsistentno z 0 v okviru napake [1].

S temi predpostavkami lahko zapišemo izraz za rekonstruirano asimetrijo kot:

$$\mathcal{A}_i^{\text{rec}}(\cos \theta_{h,i}) = \mathcal{A}_i^{\text{FB}} + \mathcal{A}_i^\varepsilon + \mathcal{A}_{\text{CP}} \frac{\cos \theta_{h,i}}{1 + \langle \alpha \rangle \cos \theta_{h,i}}. \quad (172)$$

Asimetrijo \mathcal{A}_{CP} lahko tako izmerimo z prilagajanjem funkcije $f(x) = k + \mathcal{A}_{CP}(x/(1 + \langle \alpha \rangle x))$ na porazdelitev rekonstruirane asimetrije po intervalih v $\cos\theta_{hr}$, z uporabo prej izmerjenega parametra $\langle \alpha \rangle$.

8.3.3 Določanje parametrov za razpad Λ_c

Za določanje parametrov α_{Λ_c} in $\mathcal{A}_{CP}^{\Lambda_c}$ uporabimo izmerjene vrednosti za α_{Λ} in $\mathcal{A}_{CP}^{\Lambda}$ [1]:

$$\begin{aligned}\alpha_{\Lambda} &= 0.642 \pm 0.013, \\ \mathcal{A}_{CP}^{\Lambda} &= \frac{\alpha_{\Lambda} + \alpha_{\bar{\Lambda}}}{\alpha_{\Lambda} - \alpha_{\bar{\Lambda}}} = 0.006 \pm 0.021.\end{aligned}\tag{173}$$

Z temi vrednostmi lahko izračunamo željena parametra po enačbah

$$\begin{aligned}\langle \alpha_{\Lambda_c} \rangle &= \frac{\langle \alpha \rangle}{\alpha_{\Lambda}} (1 + \mathcal{A}_{CP}^{\Lambda}), \\ \mathcal{A}_{CP}^{\Lambda_c} &= \frac{\alpha_{\Lambda_c} + \alpha_{\bar{\Lambda}_c}}{\alpha_{\Lambda_c} - \alpha_{\bar{\Lambda}_c}} = \frac{\mathcal{A}_{CP} - \mathcal{A}_{CP}^{\Lambda}}{1 - \mathcal{A}_{CP} \mathcal{A}_{CP}^{\Lambda}},\end{aligned}\tag{174}$$

oziroma, če predpostavimo da je kršenje simetrije CP v razpadu $\Lambda \rightarrow p\pi$ zanemarljivo, po enačbah

$$\begin{aligned}\langle \alpha_{\Lambda_c} \rangle &= \frac{\langle \alpha \rangle}{\alpha_{\Lambda}}, \\ \mathcal{A}_{CP}^{\Lambda_c} &= \mathcal{A}_{CP}.\end{aligned}\tag{175}$$

8.4 RAZVOJ METODE MERITVE NA SIMULIRANIH PODATKIH

Da se prepričamo, da je metoda nepristranska, jo najprej preverimo na podatkih, simuliranih z Monte Carlo simulacijo.

8.4.1 Rekonstrukcija razpadne verige Λ_c

Preden rekonstruiramo razpadno verigo za Λ_c , morajo vsi dogodki ustrezati t.i. preselekciji HadronB. Ta preselekcija vsebuje nekatere splošne zahteve, ki jim mora ustrezati vsak zabeležen e^+e^- trk (dogodek) v detektorju, njen namen pa je da ohrani čim večje število dogodkov $e^+e^- \rightarrow \Upsilon(4S) \rightarrow B\bar{B}$ in $e^+e^- \rightarrow q\bar{q}$, $q=u,d,s,c$ in zavrže čim večje število nehadronskih dogodkov (dvo fotonski dogodki, produkcija τ leptonov, i.t.d.). Po preselekciji ostane v vzorcu 99% dogodkov $e^+e^- \rightarrow \Upsilon(4S) \rightarrow B\bar{B}$, 79.5% $e^+e^- \rightarrow q\bar{q}$ dogodkov in samo 5% nehadronskih dogodkov.

V preselektiranem vzorcu nato rekonstruiramo razpadno verigo Λ_c . To storimo tako, da vzamemo rekonstruirane nabite sledi v dogodku, ter z uporabo ustreznih spremenljivk $R_{f/f'}$, definiranih v poglavju 8.2.3, identificiramo sledi kot pione ($R_{\pi/K}, R_{\pi/p}, R_{\pi/e}, R_{\pi/\mu}$) in protone ($R_{p/K}, R_{p/\pi}$). Z pomočjo rekonstruiranega

seleksijska spremenljivka	vrednost
$R_{\pi/K}, R_{\pi/p}, R_{p/K}, R_{p/\pi}$	≥ 0.6
$R_{\pi/e}, R_{\pi/\mu}$	≤ 0.9
$m(p\pi)$	$\geq 1.10 \text{ GeV}/c^2, \leq 1.13 \text{ GeV}/c^2$
$m(p\pi\pi)$	$\geq 2.19 \text{ GeV}/c^2, \leq 2.38 \text{ GeV}/c^2$
$p_{CMS}(\Lambda_c)$	$\geq 1.5 \text{ GeV}/c$

Tabela 17: Seleksijski kriteriji, uporabljeni za konstrukcijo večjega vzorca dogodkov iz vseh dogodkov v generični MC simulaciji.

naboja sledi jih ločimo še na π^+, π^- in p^+, p^- . Nato tvorimo vse kombinacije vseh tako identificiranih π^- in protonov (π^+ in antiprotonov) in s tem dobimo barione Λ ($\bar{\Lambda}$), ter nato tvorimo kombinacije Λ ($\bar{\Lambda}$) ter π^+ (π^-) v barione Λ_c ($\bar{\Lambda}_c$). Na koncu iz vseh dobljenih barionov Λ_c^+ ($\bar{\Lambda}_c^-$) izberemo najboljšega kandidata tako, da naredimo prilagajanje sledi π in Λ na skupni vertex, in vzamemo kombinacijo z najboljšo stopnjo zaupanja prilagajanja.

8.4.2 Primerjava vzorcev iz simulacije in pravih podatkov

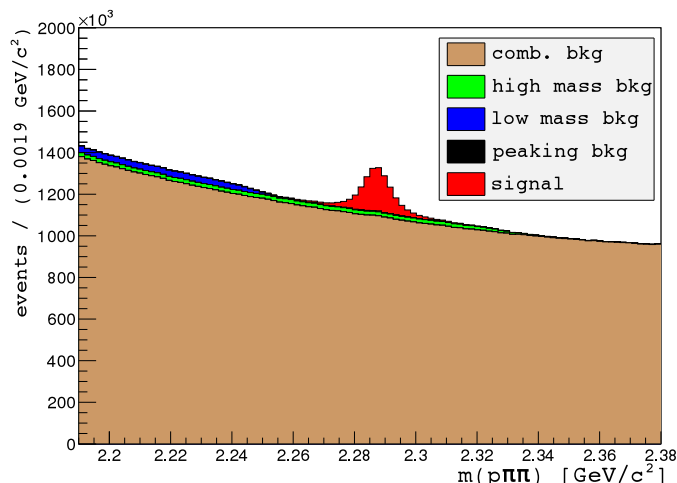
Če hočemo preveriti metodo moramo vzorec, dobljen iz MC simulacije, primerjati z vzorcem, dobljenim iz pravih podatkov, da se prepričamo v pravilnost opisa pomembnih procesov v MC simulaciji. Razlika med simulacijo in pravimi podatki se pojavi predvsem zaradi neustreznega opisa fragmentacije kvarkov $c\bar{c}$ v hadrone. V ta namen najprej selektiramo vzorec z pomočjo ohlapnih selekcijskih kriterijev, naštetih v tabeli 17. Poleg spremenljivk R uporabimo še kriterije za invariantno maso Λ ter za gibalno količino Λ_c v težiščnem sistemu e^+e^- , pri čemer je invariantna masa delca P definirana preko ohranitve njegovega četverca gibalne količine P_P z:

$$m_P = m(P_0 \dots P_N) = \sqrt{P_P^2} = \sqrt{E_P^2 - |\vec{p}_P|^2} = \sqrt{\left(\sum_i \sqrt{|\vec{p}_i|^2 + m_i^2} \right)^2 - \left| \sum_i \vec{p}_i \right|^2}, \quad (176)$$

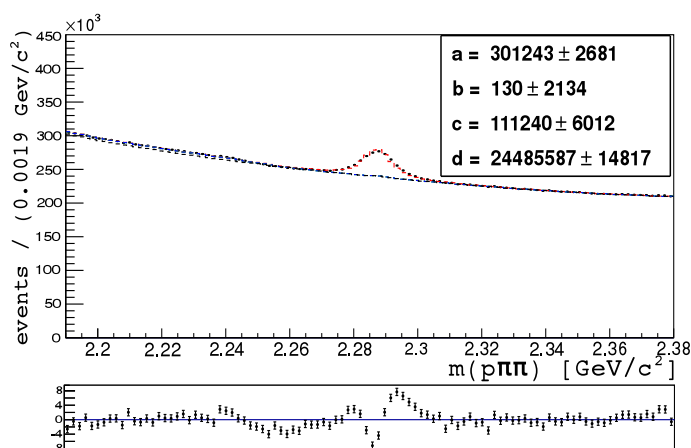
kjer N teče po vseh končnih produktih, ki tvorijo delec P .

Za dobljeni vzorec razdelimo vsak dogodek glede na izvor bariona Λ_c (glej sliko 82). Identificiramo lahko pet različnih prispevkov:

- Signalne dogodke, ki vsebujejo prave razpade Λ_c , kjer Λ_c prihaja direktno iz fragmentacije, iz razpadov mezonov B , ter iz razpadov barionov Σ_c .
- Dogodke iz ozadja, ki imajo enako porazdelitev kot signalni dogodki, ki prihajajo iz razpadov $\Lambda_c^+ \rightarrow f_0 p^+$, $f_0 \rightarrow \pi^+ \pi^-$; $\Lambda_c^+ \rightarrow K^0 p^+$, $K^0 \rightarrow K_S^0 \rightarrow \pi^+ \pi^-$ in $\Lambda_c^+ \rightarrow p^+ \pi^+ \pi^-$.
- Dogodke iz ozadja z nižjo maso, ki prihajajo iz razpada $\Sigma^0 \rightarrow \Lambda \gamma$, $\Lambda \rightarrow p^+ \pi^-$, kjer fotona nismo rekonstruirali.



Slika 82: Dogodki v večjem vzorcu, razdeljeni glede na izvor rekonstruiranega bariona Λ_c .

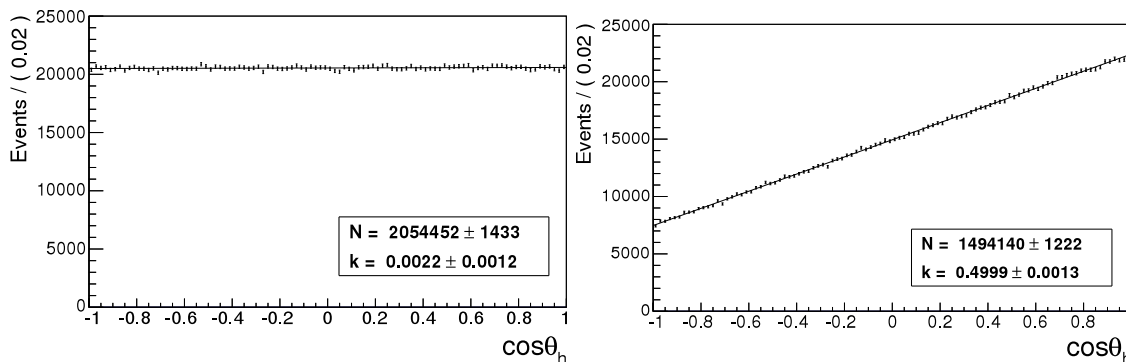


Slika 83: Prilaganje na porazdelitev po invariantni masi $m(p\pi\pi)$, s katerim dobimo koeficiente za popravljanje vzorca iz MC simulacije.

- Dogodke iz ozadja z višjo maso, ki prihajajo iz različnih razpadov barionov Ξ_c .
- Kombinatorne dogodke iz ozadja, ki so večinoma naključne kombinacije končnih produktov.

Vzorec zdaj primerjamo z pravimi podatki, tako da za vsak identificiran prispevek iz porazdelitve po invariantni masi $m(p\pi\pi)$ tvorimo verjetnostno gostoto, definiramo funkcijo, ki je seštevek posameznih verjetnostnih gostot, pomnoženih z prostim parametrom, ter to funkcijo prilagajamo na porazdelitev po invariantni masi $m(p\pi\pi)$ za prave podatke. Tako dobimo koeficiente, s katerimi moramo pomnožiti vsakega od prispevkov v vzorcu iz MC simulacije, da dobimo vzorec, najbolj podoben pravim podatkom (glej sliko 83).

V MC simulaciji prav tako ni simulirana linearna odvisnost kotne porazdelitve po $\cos\theta_h$, zato simulacijo dodatno preutežimo z naključnim odvzemanjem dogodkov na tak način, da dobimo linearno odvisnost z parametrom $\alpha = 0.5$ (dobljenim iz [34]) (glej sliko 84).



Slika 84: Preuteževanje kotne porazdelitve po $\cos\theta_h$ na vzorcu, dobljenem iz MC simulacije. Levo - kotna porazdelitev pred preuteževanjem, desno - kotna porazdelitev po preuteževanju.

seleksijska spremenljivka	vrednost
$R_{\pi/K}, R_{\pi/p}$ (za oba piona)	≥ 0.6
$R_{\pi/e}, R_{\pi/\mu}$ (za oba piona)	≤ 0.9
$R_{p/K}, R_{p/\pi}$	≥ 0.6
$p\pi, p\pi\pi$ st. zaupanja	$\geq 10^{-3}$
$m(p\pi)$	$\geq 1.1126 \text{ GeV}/c^2, \leq 1.1186 \text{ GeV}/c^2$
$m(p\pi\pi)$	$\geq 2.19 \text{ GeV}/c^2, \leq 2.38 \text{ GeV}/c^2$
$p_{CMS}(\Lambda_c)$	$\geq 2.2 \text{ GeV}/c$

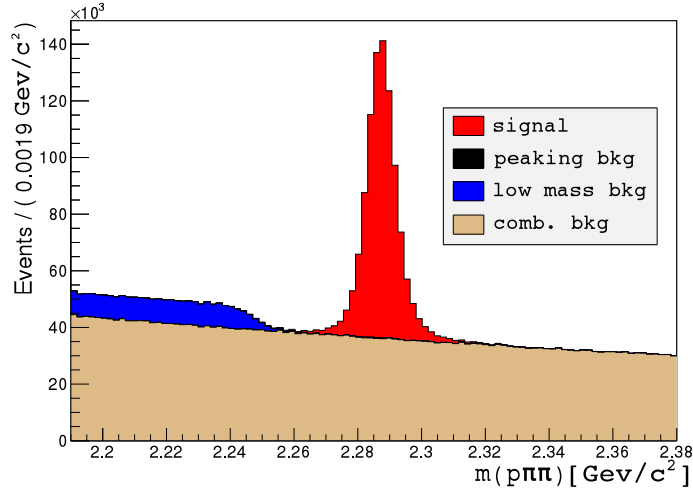
Tabela 18: Optimizirani seleksijski kriteriji uporabljeni za konstrukcijo analiznega vzorca.

8.4.3 Konstrukcija analiznega vzorca

Analizni vzorec konstruiramo tako, da vzamemo večji vzorec, ki smo ga konstruirali v prejšnjem poglavju, ter optimiziramo seleksijske kriterije. Optimizacija je definirana tako, da za vsak seleksijski kriterij izračunamo funkcijo

$$\text{FOM} = \varepsilon \cdot P, \quad (177)$$

kjer je ε učinkovitost za rekonstrukcijo, P pa čistost vzorca. Seleksijski kriterij je optimiziran, ko je funkcija FOM pri optimizirani vrednosti maksimalna. Taka optimizacija nam da največjo signifikanco signala v vzorcu. Za analizni vzorec uporabimo vse seleksijske kriterije, našteje v tabeli 17, poleg njih pa še vrednosti stopnje zaupanja, dobljene iz prilagajanja skupnega verteksa sledi π in p , ter π, π in p . Optimizirani seleksijski kriteriji so našteji v tabeli 18, končna porazdelitev po invariantni masi $m(p\pi\pi)$, razdeljena glede na tip dogodkov, pa je prikazana na sliki 85.



Slika 85: Porazdelitev po invariantni masi $m(p\pi\pi)$ za analizni vzorec, ločena glede na tip dogodka.

8.4.4 Prilagajanje porazdelitev po masi Λ_c v intervalih $\cos\theta_h$

Celotni interval $[-1, 1]$ spremenljivke $\cos\theta_h$ razdelimo na 10 enako širokih intervalov, ter za vsakega določimo porazdelitev po invariantni masi $m(p\pi\pi)$. Na vsako izmed porazdelitev z prilagajanjem določimo funkcijo, iz katere lahko izračunamo število signalnih dogodkov v tem intervalu.

Za vsako porazdelitev vzamemo enak funkcijski model z nekim naborom parametrov (ki je lahko sestavljen iz večih modelov, od katerih vsak opiše del porazdelitve), normiran na celotno število dogodkov v vseh intervalih $\cos\theta_h$.

$$M(x; \vec{p}) = \sum_i N_i M_i(x; \vec{p}_i), \quad \int M(x; \vec{p}) dx \equiv N_{\text{exp}}(\vec{p}). \quad (178)$$

Tu je M model za celotno porazdelitev, M_i so modeli za posamezne dele porazdelitev, x je opazljivka, glede na katero prilagajamo, N_i je število dogodkov, ki jih opiše model M_i , \vec{p} je vektor vseh parametrov modela, \vec{p}_i je podnabor parametrov za model i , N_{exp} pa je število vseh dogodkov v vseh intervalih $\cos\theta_h$.

Model prilagajamo na porazdelitve v vseh intervalih istočasno, tako da minimiziramo funkcijo $-\ln L$:

$$-\ln L(\vec{p}) = - \sum_{j=1}^{N_{\text{bin}}=10} \sum_{H_j(x_i)} M(x_i; \vec{p}_j) - \text{Poisson}(N_{\text{obs}} | \sum_{j=1}^{N_{\text{bin}}=10} N_{\text{exp},j}(\vec{p}_j)), \quad (179)$$

kjer indeks j teče po intervalih v $\cos\theta_h$, $H_j(x_i)$ je histogram za j -ti interval z i razdelki, x_i je središče i -tega razdelka histograma H_j , \vec{p}_j je nabor parametrov, ki opiše model za porazdelitev v j -tem intervalu $\cos\theta_h$, N_{obs} pa je opaženo število dogodkov v vseh porazdelitvah, modelirano z Poissonsko porazdelitvijo z pričakovanim številom dogodkov v vseh intervalih kot povprečjem.

Da zagotovimo konvergenco postopka prilagajanja, najprej prilagajamo samo signalne dogodke, nato pa pri prilagajanju na vse dogodke nekatere parametre

parameter	value
n_{12}	0.710 ± 0.060
n_{13}	0.156 ± 0.010
s_{12}	1.741 ± 0.018
s_{13l}	4.008 ± 0.056
s_{13r}	4.856 ± 0.071

Tabela 19: Vrednosti fiksiiranih parametrov za prilagajanje porazdelitev na generični MC simulaciji.

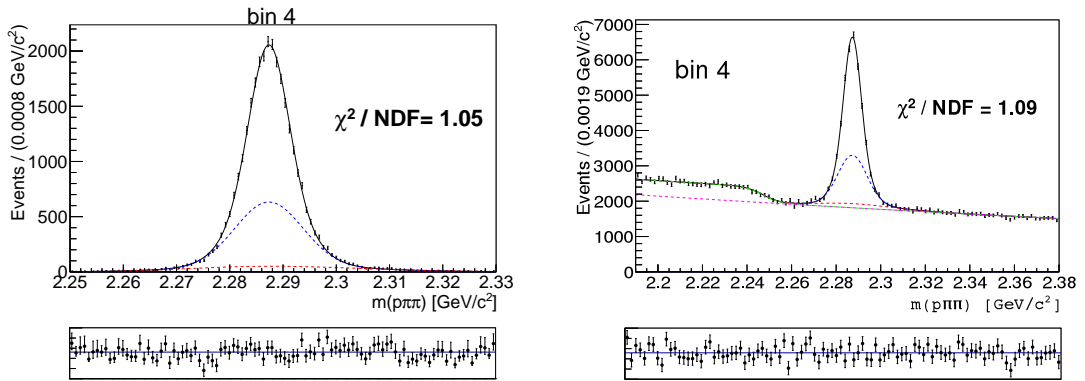
fiksiramo na vrednosti, dobljene iz tega prilagajanja. Model, ki ga uporabimo za prilagajanje na signalne dogodke, je sestavljen iz dveh Gaussovih funkcij in ene asimetrične Gaussove funkcije, pri čemer je nekaj parametrov skupnih za vse intervale $\cos\theta_h$:

$$\begin{aligned}
M_S(m_{p\pi\pi}; \vec{p}) &= \sum_{i=1}^{N_{bin}=10} N_{1,i} [G(m_{p\pi\pi}; m_i, \sigma_{1,i}) + n_{12}G(m_{p\pi\pi}; m_i, s_{12}\sigma_{1,i}) + \\
&\quad + n_{13}AG(m_{p\pi\pi}; m_i, s_{13l}\sigma_{1,i}, s_{13r}\sigma_{1,i})], \\
G(x; m, \sigma) &= \frac{1}{\sqrt{2\pi}\sigma} \exp\left[-\frac{(x-m)^2}{2\sigma^2}\right], \tag{180} \\
AG(x; m, \sigma_l, \sigma_r) &= \frac{1}{\sqrt{2\pi}\sigma_l} (1 - \theta(x-m)) \exp\left[-\frac{(x-m)^2}{2\sigma_l^2}\right] + \\
&\quad + \frac{1}{\sqrt{2\pi}\sigma_r} \theta(x-m) \exp\left[-\frac{(x-m)^2}{2\sigma_r^2}\right],
\end{aligned}$$

kjer je $\theta(x)$ Heavisideova funkcija.

Dobljene vrednosti, ki jih fiksiramo, so našteje v tabeli 19. Za prilagajanje porazdelitve vseh dogodkov uporabimo model, sestavljen iz prejšnjega modela z nekaj parametri, fiksiiranimi na vrednosti dobljene iz prilagajanja na signalne dogodke, ter sigmoidno funkcijo za opis dogodkov iz ozadja z nižjo maso in polinomom Čebiševa druge stopnje za opis kombinatornega ozadja:

$$\begin{aligned}
M_G(m_{p\pi\pi}; \vec{p}) &= \sum_{i=1}^{N_{bin}=10} \left[N_{1,i} (G(m_{p\pi\pi}; m_i, \sigma_{1,i}) + n_{12}G(m_{p\pi\pi}; m_i, s_{12}\sigma_{1,i}) + \right. \\
&\quad + n_{13}AG(m_{p\pi\pi}; m_i, s_{13l}\sigma_{1,i}, s_{13r}\sigma_{1,i})) + \\
&\quad \left. + N_{b1,i}S(m_{p\pi\pi}; m_b, w_b) + N_{b2,i}CH(m_{p\pi\pi}; c_1, c_2) \right], \tag{181}
\end{aligned}$$



Slika 86: Primera prilaganja na signalne dogodke - levo in vse dogodke - desno za interval 4 ($-0.2 < \cos\theta_h < 0.0$). Črna, modra in rdeča črta označujejo obe Gaussovi funkciji in asimetrično Gaussovo funkcijo, ki opisujejo signalne dogodke, zelena in vijolična črta pa označujeta sigmoidno funkcijo in polinom Čebiševa drugega reda, ki opisujeta dogodke iz ozadja. Spodnji grafi prikazujejo residue prilaganja.

$$G(x; m, \sigma) = \frac{1}{\sqrt{2\pi}\sigma} \exp\left[-\frac{(x-m)^2}{2\sigma^2}\right],$$

$$AG(x; m, \sigma_l, \sigma_r) = \frac{1}{\sqrt{2\pi}\sigma_l} (1 - \theta(x-m)) \exp\left[-\frac{(x-m)^2}{2\sigma_l^2}\right] +$$

$$+ \frac{1}{\sqrt{2\pi}\sigma_r} \theta(x-m) \exp\left[-\frac{(x-m)^2}{2\sigma_r^2}\right],$$

$$S(x; m, w) = \frac{1}{1 + \exp\left[\frac{x-m}{w}\right]},$$

$$CH(x; c_1, c_2) = 1 + c_1x + c_2(x^2 - 1).$$

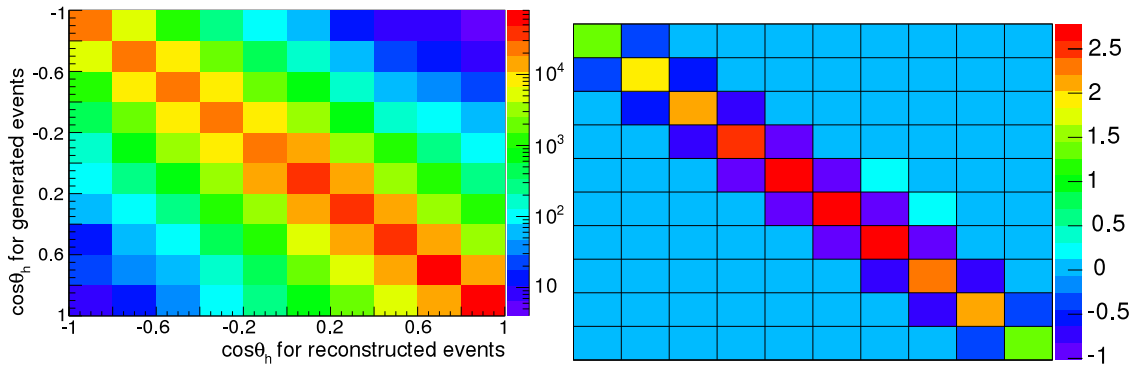
Primera prilaganja za signalne in vse dogodke sta prikazana na sliki 86, za rezultate prilaganja na vse intervale pa glej dodatka A.1 in A.2. Števila signalnih dogodkov R_i v vsakem intervalu $\cos\theta_h$ potem dobimo iz parametrov prilaganja kot:

$$R_i = N_{1,i}(1 + n_{12} + n_{13}), \quad \sigma_{R_i} = \sigma_{N_{1,i}}(1 + n_{12} + n_{13}). \quad (182)$$

8.4.5 Dekonvolucija

Ker ima detektor Belle končno resolucijo meritve kota θ_h , se lahko zgodi, da izmerjen kot za nek dogodek pade v drug interval v $\cos\theta_h$ kot dejanski kot, kar povzroči migracijo dogodkov med intervali. Matematično to pomeni, da je prava porazdelitev dogodkov po $\cos\theta_h$ konvoluirana z resolucijsko funkcijo:

$$\left(\frac{dN}{d\cos\theta_h}\right)_{\text{rec}} = \left(\frac{dN}{d\cos\theta_h}\right) \otimes \text{Res}(\cos\theta_h). \quad (183)$$



Slika 87: Levo - resolucijska matrika, desno - dekonvolucijska matrika, dobljeni iz generične MC simulacije. (Pri resolucijski matriki je barvna os v logaritemski skali.)

Če hočemo iz rekonstruirane porazdelitve dobiti pravo, moramo porazdelitev dekonvoluirati z pomočjo dekonvolucijske matrike, ki jo določimo iz MC simulacije na naslednji način:

Dogodke razporedimo v 2D razdelke, glede na interval v katerega pade rekonstruirana in prava vrednost $\cos \theta_h$. Tako dobljeno resolucijsko matriko (M_{ij}) normiramo po vrsticah, da iz nje dobimo elemente konvolucijske matrike ($p_{ij} = M_{ij} / \sum_k M_{kj}$). Nato konvolucijsko matriko invertiramo, da dobimo elemente dekonvolucijske matrike (q_{ij}). Resolucijska in dekonvolucijska matrika sta prikazani na sliki 87.

Število dekonvoluiranih dogodkov (G_i) in napaka na tem številu (σ_{G_i}) za i -ti interval v $\cos \theta_h$ se izračuna po (glej dodatek B.3):

$$G_i = \sum_j q_{ij} R_j, \quad (184)$$

$$\sigma_{G_i}^2 = \sum_j R_j^2 \sigma_{q_{ij}}^2 + \sum_j \sum_k q_{ij} q_{ik} R_{jk} \sigma_{R_j} \sigma_{R_k},$$

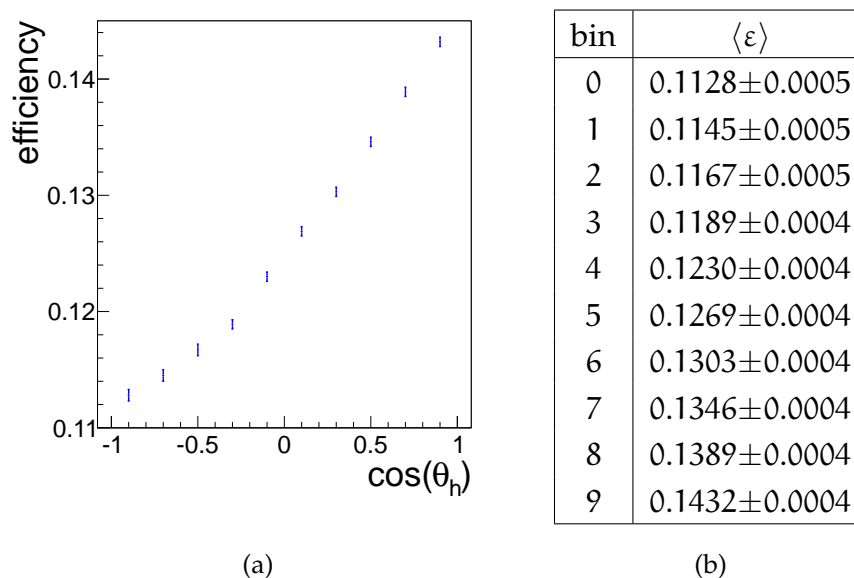
kjer je R_{jk} korelacijski koeficient med številoma dogodkov R_j in R_k , dobljen iz prilaganja, q_{ij} element dekonvolucijske matrike, $\sigma_{q_{ij}}$ pa napaka na tem elementu, izračunana po (glej dodatek B.4):

$$\sigma_{q_{ij}}^2 = \sum_a \sum_b q_{ia}^2 \frac{M_{ab} \sum_{c \neq a} M_{cb}}{(\sum_c M_{ab})^3} q_{bj}^2. \quad (185)$$

8.4.6 Učinkovitost rekonstrukcije za razpad Λ_c

Učinkovitost rekonstrukcije za razpad Λ_c za vsak interval v $\cos \theta_h$ določimo iz MC simulacije kot:

$$\langle \varepsilon_i \rangle = \frac{N_{R,i}}{N_{G,i}}. \quad (186)$$



Slika 88: Slika 88a kaže grafično predstavitev učinkovitosti rekonstrukcije, tabela 88b pa vsebuje numerične vrednosti za vsak interval v $\cos \theta_h$. Opomba: os grafa na sliki 88a se ne začne pri 0, celotna sprememba vrednosti za učinkovitost rekonstrukcije preko celotnega intervala za $\cos \theta_h$ je tako samo okoli 2% – 3%.

kjer sta $N_{R,i}$ in $N_{G,i}$ števili rekonstruiranih in generiranih razpadov Λ_c v i -tem intervalu. Napaka na tako določeni učinkovitosti se izračuna Poissonsko:

$$\sigma_{\langle \varepsilon \rangle_i} = \sqrt{\frac{N_{R,i}(N_{G,i} + N_{R,i})}{N_{G,i}^3}}. \quad (187)$$

Vrednosti za učinkovitost, določene iz MC simulacije, so predstavljene grafično na sliki 88a in numerično v tabeli 88b.

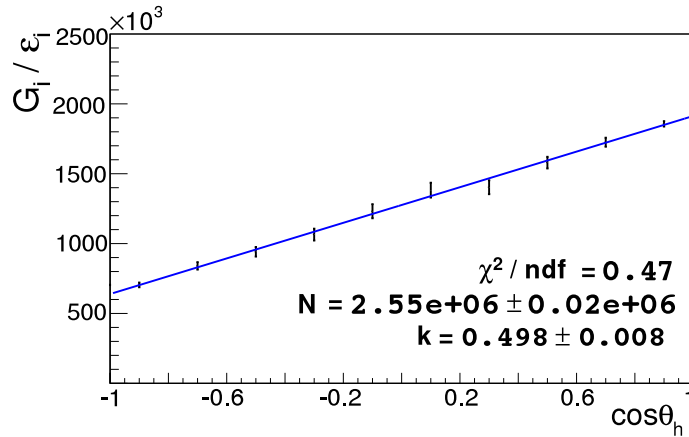
8.4.7 Določanje povprečnega parametra šibke asimetrije

Za določanje $\langle \alpha \rangle$ prilagajamo funkcijo oblike $f(x; N, \langle \alpha \rangle) = \frac{1}{2}N(1 + \langle \alpha \rangle x)$ na dekonvoluirana števila dogodkov v intervalih $\cos \theta_h$, popravljena z učinkovitostjo rekonstrukcije za vsak interval ($T_i = G_i / \langle \varepsilon \rangle_i$). Ker napaki na G_i in $\langle \varepsilon \rangle_i$ nista korelirani, ju seštejemo v kvadratu.

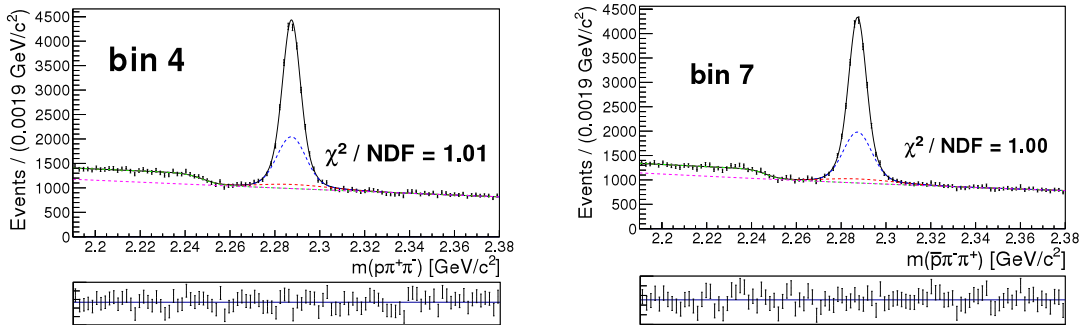
Prilagajanje izvedemo z minimiziranjem funkcije

$$\chi^2(N, \langle \alpha \rangle) = (\vec{T} - \vec{f}(x; N, \langle \alpha \rangle))^T V^{-1} (\vec{T} - \vec{f}(x; N, \langle \alpha \rangle)), \quad (188)$$

kjer je \vec{T} vektor izračunanih vrednosti T_i , V pa kovariančna matrika za vrednosti T_i (glej dodatek B.2). Tak način prilagajanja je potreben, ker so vrednosti T_i zaradi dekonvolucije med seboj korelirane. Rezultat prilagajanja je prikazan na sliki



Slika 89: Rezultat prilaganja linearne funkcije na dekonvoluirana števila dogodkov v intervalih $\cos\theta_h$, popravljena z učinkovitostjo rekonstrukcije za vsak interval, uporabljenega za določanje parametra $\langle\alpha\rangle$.



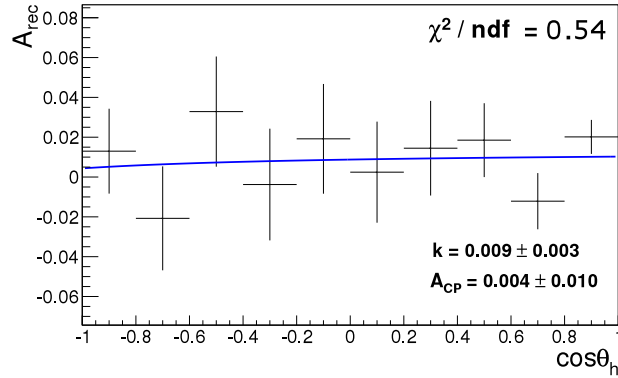
Slika 90: Primeri prilaganja na vzorca za Λ_c^+ in $\bar{\Lambda}_c^-$ za interval 7 ($0.4 < \cos\theta_h < 0.6$). Črna, modra in rdeča črta označujejo obe Gaussovi funkciji in asimetrično Gaussovo funkcijo, ki opisujejo signalne dogodke, zelena in vijolična črta pa označujeta sigmoidno funkcijo in polinom Čebiševa drugega reda, ki opisujeta dogodke iz ozadja. Spodnji grafi prikazujejo residue prilaganja.

89. Rezultat, ki ga dobimo iz prilaganja primerjamo z dejansko vrednostjo, dobljeno iz MC simulacije in dobimo dobro ujemanje v okviru napake:

$$\langle\alpha\rangle_{\text{rec}} = 0.498 \pm 0.008, \quad \langle\alpha\rangle_{\text{st12gen}} = 0.501 \pm 0.001. \quad (189)$$

8.4.8 Določanje parametra \mathcal{A}_{CP}

Za določanje parametra \mathcal{A}_{CP} prejšnji vzorec razdelimo na vzorec za Λ_c^+ in na vzorec za $\bar{\Lambda}_c^-$. Za vsak vzorec posebej določimo števila razpadov Λ_c^+ in $\bar{\Lambda}_c^-$ (R_i, \bar{R}_i) v intervalih $\cos\theta_h$ z prilaganjem na enak način kot v prejšnjem poglavju, torej z minimiziranjem funkcije (179) in uporabo modela (181), pri čemer so vrednosti za fiksirane parametre pri obeh prilaganjih vzete iz tabele 19. Primeri prilaganja sta prikazana na sliki 90, za rezultate prilaganj na vse intervale pa glej dodatek A.3.



Slika 91: Rezultat prilaganja z funkcijo (192) na porazdelitev rekonstruirane asimetrije po intervalih $\cos\theta_h$, uporabljenega za določanje parametra \mathcal{A}_{CP} .

Števila dogodkov nato dekonvoluiramo z pomočjo dekonvolucijske matrike, določene v poglavju 8.4.5, nato pa iz dekonvoluiranih dogodkov (G_i, \bar{G}_i) izračunamo rekonstruirano asimetrijo (A_{rec}) za vsak interval $\cos\theta_h$:

$$\mathcal{A}_{rec}^i = \frac{G_i - \bar{G}_i}{G_i + \bar{G}_i}. \quad (190)$$

Napako na \mathcal{A}_{rec}^i lahko izrazimo kot (glej dodatek B.6):

$$\begin{aligned} \sigma_{\mathcal{A}_{rec}^i}^2 = & \frac{4}{(G_i + \bar{G}_i)^4} \left(\bar{G}_i^2 \sum_k \sum_l q_{ik} q_{il} R_{kl} \sigma_{R_k} \sigma_{R_l} + \right. \\ & \left. + G_i^2 \sum_k \sum_l q_{ik} q_{il} \bar{R}_{kl} \sigma_{\bar{R}_k} \sigma_{\bar{R}_l} + \sum_k (R_k \bar{G}_i - \bar{R}_k G_i)^2 \sigma_{q_{ik}}^2 \right), \end{aligned} \quad (191)$$

kjer so R_{kl} in \bar{R}_{kl} korelacijski koeficienti med števili dogodkov, določenimi iz prilaganja, q_{ik} pa koeficienti dekonvolucijske matrike.

Parameter \mathcal{A}_{CP} sedaj določimo tako, da na porazdelitev A_{rec} po intervalih v $\cos\theta_h$ prilagajamo funkcijo oblike

$$g(x; k, \mathcal{A}_{CP}) = k + \mathcal{A}_{CP} \frac{x}{1 + \langle \alpha \rangle x}, \quad (192)$$

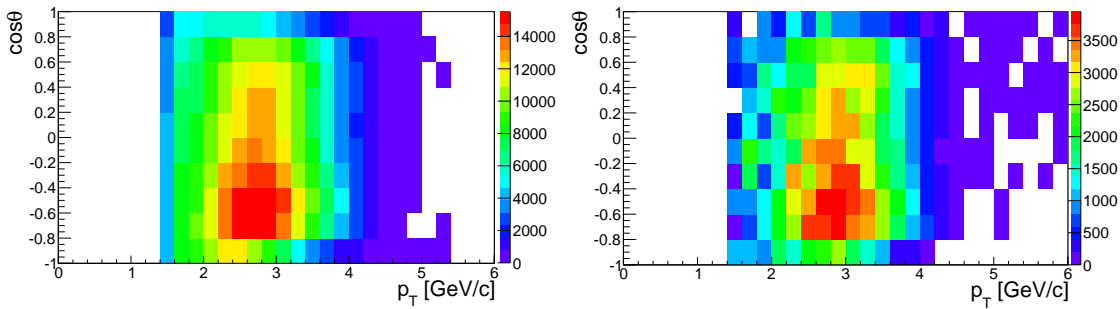
z minimiziranjem funkcije

$$\chi^2(k, \mathcal{A}_{CP}) = (\vec{A}_{rec} - \vec{g}(x; k, \mathcal{A}_{CP}))^T V^{-1} (\vec{A}_{rec} - \vec{g}(x; k, \mathcal{A}_{CP})), \quad (193)$$

kjer je \vec{A}_{rec} vektor vrednosti rekonstruirane asimetrije po intervalih $\cos\theta_h$, V pa kovariančna matrika za vrednosti \mathcal{A}_{rec}^i (glej dodatek B.5).

Rezultat prilaganja je prikazan na sliki 91. Če ga primerjamo z dejansko vrednostjo, dobjeno iz MC simulacije, dobimo dobro ujemanje v okviru napake:

$$\mathcal{A}_{CP}^{rec} = 0.004 \pm 0.010 \quad \mathcal{A}_{CP}^{gen} = -0.003 \pm 0.003. \quad (194)$$



Slika 92: Porazdelitev po $(p_T, \cos \theta)$ za levo - signalne dogodke iz MC simulacije, desno - dogodke iz pravih podatkov dobljene z odštevanjem stranskega okna od signalnega okna.

Postopek smo preverili še na vzorcih, generiranih z drugačnimi vrednostmi parametrov $\langle \alpha \rangle$ in \mathcal{A}_{CP} , ter na vseh dobili konsistentne rezultate.

8.5 REZULTATI

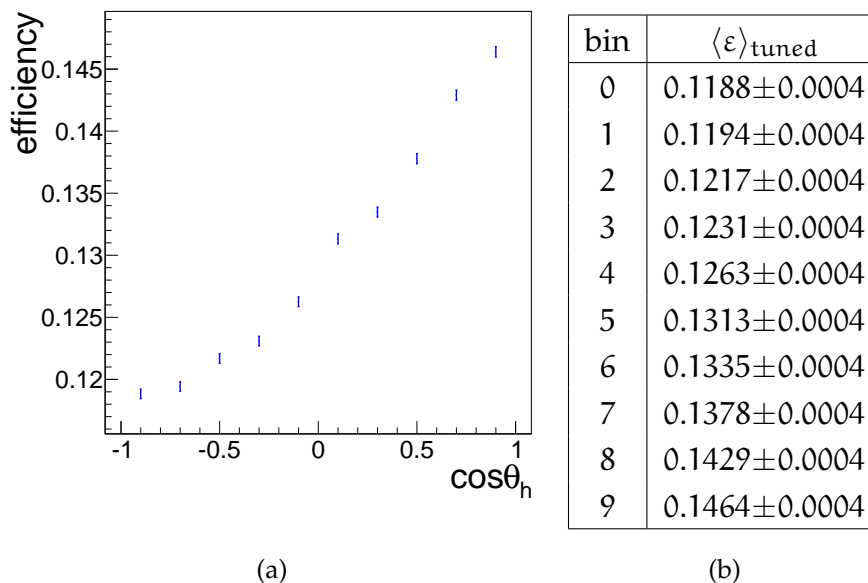
8.5.1 Popravljanje MC simulacije

Preden uporabimo metodo iz prejšnjega poglavja, moramo zopet primerjati MC simulacijo in prave podatke, saj se zaradi majhnih razlik, ki pridejo iz nezadostnega opisa fragmentacije kvarkov $c\bar{c}$, razlikujejo tudi gibalne količine hadronov, kar se nato odraža v nekoliko drugačni porazdelitvi dogodkov po $\cos \theta_h$. Zaradi omenjenih razlik moramo popraviti tiste količine, določene iz MC simulacije, ki se na pravih podatkih spremenijo. Za našo analizo sta taki količini dve, optimiziran selekcijski kriterij za gibalno količino Λ_c v težiščnem sistemu e^+e^- in učinkovitost rekonstrukcije.

Najprej popravimo MC simulacijo tako, da primerjamo 2D porazdelitev signalnih dogodkov iz MC simulacije in iz pravih podatkov po spremenljivkah $(p_T, \cos \theta)$, kjer je p_T transverzalna komponenta gibalne količine Λ_c v težiščnem sistemu e^+e^- , θ pa polarni kot smeri letenja Λ_c v težiščnem sistemu e^+e^- . Za prave podatke dobimo to porazdelitev za signalne dogodke tako, da določimo signalno ter stransko okno z enakim številom dogodkov, nato pa stransko okno odštejemo od signalnega. Obe dobljeni porazdelitvi sta prikazani na sliki 92.

MC simulacijo nato popravimo tako, da za obe porazdelitvi z normiranjem na števili dogodkov konstruiramo verjetnostni porazdelitvi, nato pa izračunamo razmerje med porazdelitvama za prave podatke in simulirane podatke za vsak 2D interval. S temi razmerji nato pomnožimo ustrezna števila dogodkov v MC simulaciji. S tem dobimo MC simulacijo, ki ima enako porazdelitev po $(p_T, \cos \theta)$ kot realni podatki.

S tako popravljeno MC simulacijo nato še enkrat optimiziramo selekcijski kriterij za gibalno količino Λ_c v težiščnem sistemu e^+e^- , ter ugotovimo, da moramo kriterij dvigniti iz $p_{CMS}(\Lambda_c) > 2.2\text{GeV}$ na $p_{CMS}(\Lambda_c) > 2.325\text{GeV}$, ker imajo dogodki v pravih podatkih večji povprečni $p_{CMS}(\Lambda_c)$.



Slika 93: Slika 93a kaže grafično predstavitev popravljene učinkovitosti rekonstrukcije, tabela 93b pa vsebuje numerične vrednosti za vsak interval v $\cos \theta_h$. Opomba: os grafa na sliki 93a se ne začne pri 0, celotna sprememba vrednosti za učinkovitost rekonstrukcije preko celotnega intervala za $\cos \theta_h$ je tako samo okoli 2% – 3%.

S popravljeno MC simulacijo določimo še novo učinkovitost rekonstrukcije, na isti način kot v poglavju 8.4.6. Rezultati so prikazani grafično na sliki 93a in numerično v tabeli 93b.

8.5.2 Rezultati

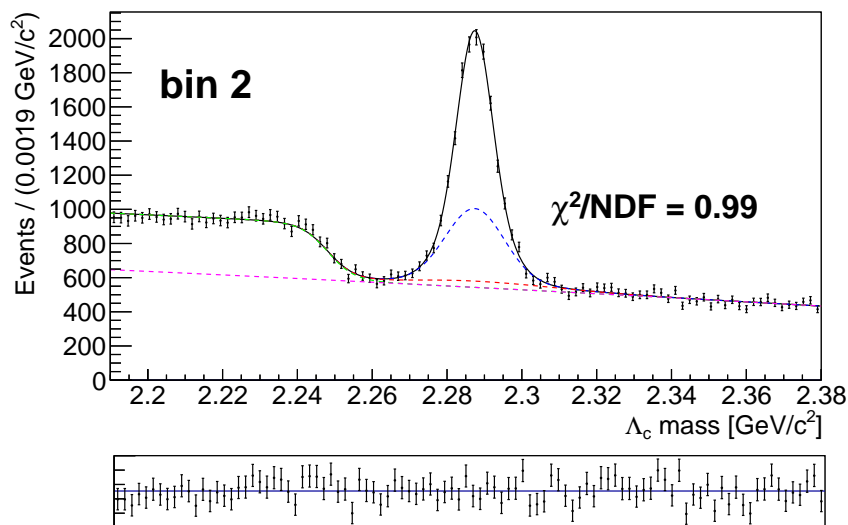
Analizni vzorec za prave podatke naredimo tako, da na celotnem vzorcu uporabimo selekcijske kriterije, naštete v tabeli 18, le kriterij za $p_{\text{CMS}}(\Lambda_c)$ spremenimo tako, kot smo določili v zgornjem poglavju.

Za ta vzorec nato z določimo števila signalnih dogodkov za vse intervale v $\cos \theta_h$ tako kot v poglavju 8.4.4 (za primer prilagajanja glej sliko 94, za rezultate prilagajanj na vse intervale pa glej dodatek A.4). Ta števila dekonvoluiramo z dekonvolucijsko matriko, določeno v poglavju 8.4.5, ter dekonvoluirana števila dogodkov za vsak interval delimo z popravljeno učinkovitostjo rekonstrukcije za ta interval (glej tabelo 93b).

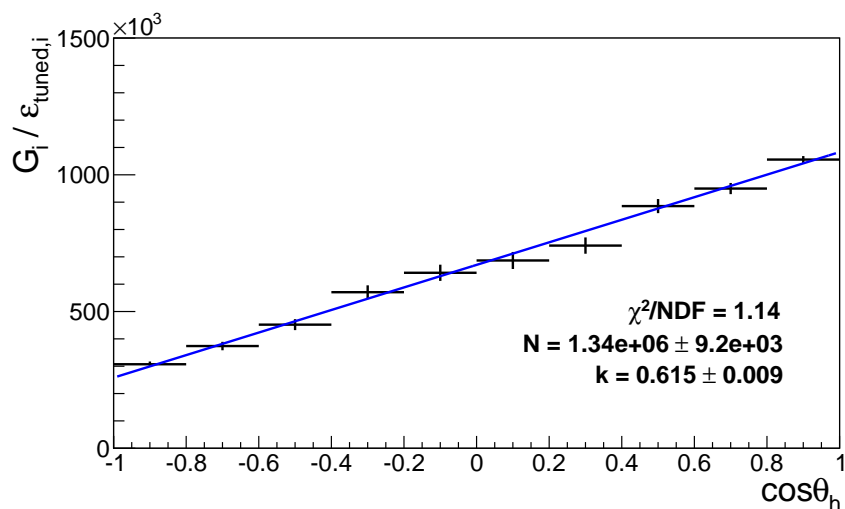
Na porazdelitev dekonvoluiranih števil dogodkov, popravljenih z učinkovitostjo rekonstrukcije po intervalih $\cos \theta_h$ nato prilagajamo funkcijo $f(x; N, \langle \alpha \rangle) = \frac{1}{2}N(1 + \langle \alpha \rangle x)$, da določimo $\langle \alpha \rangle$ (glej sliko 95). Za rezultat dobimo:

$$\langle \alpha \rangle = 0.615 \pm 0.009, \quad (195)$$

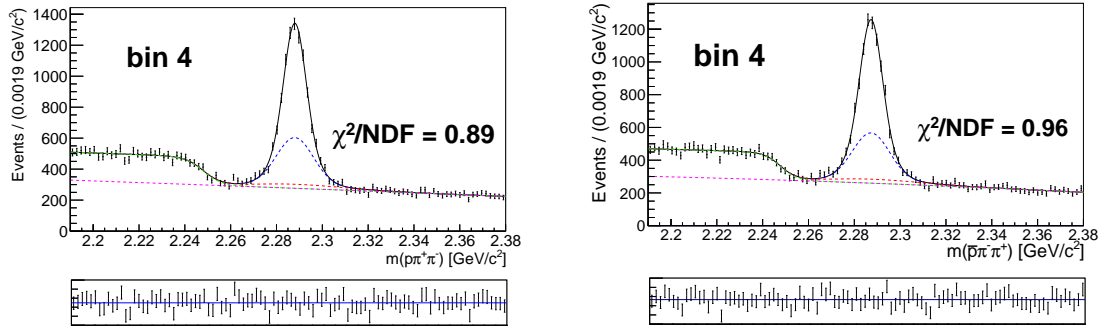
kjer je napaka samo statistična.



Slika 94: Primer prilagajanja na vzorec za Λ_c na pravih podatkih za interval 2 ($0.4 < \cos\theta_h < 0.6$). Črna, modra in rdeča črta označujejo obe Gaussovi funkciji in asimetrično Gaussovo funkcijo, ki opisujejo signalne dogodke, zelena in vijolična črta pa označujeta sigmoidno funkcijo in polinom Čebiševa drugega reda, ki opisujeta dogodke iz ozadja. Spodnji grafi prikazujejo residue prilagajanja.



Slika 95: Rezultat prilagajanja linearne funkcije na dekonvoluirana števila dogodkov v intervalih $\cos\theta_h$ na pravih podatkih, popravljena z učinkovitostjo rekonstrukcije za vsak interval, uporabljenega za določevanje parametra $\langle\alpha\rangle$.



Slika 96: Primera prilaganja na vzorca za levo - Λ_c^+ in desno - $\bar{\Lambda}_c^-$ na pravih podatkih za interval 4 ($-0.2 < \cos\theta_h < 0.0$). Črna, modra in rdeča črta označujejo obe Gaussovi funkciji in asimetrično Gaussovo funkcijo, ki opisujejo signalne dogodke, zelena in vijolična črta pa označujeta sigmoidno funkcijo in polinom Čebiševa drugega reda, ki opisujeta dogodke iz ozadja. Spodnji grafi prikazuje residue prilaganja.

Iz tega rezultata dobimo parameter $\langle\alpha_{\Lambda_c}\rangle$ tako, da upoštevamo enačbo (174) ter dobimo:

$$|\langle\alpha_{\Lambda_c}\rangle| = 0.964 \pm 0.014(\text{stat.}) \pm 0.020(\alpha_\Lambda) \pm 0.020(\mathcal{A}_{CP}^\Lambda) = 0.964 \pm 0.032, \quad (196)$$

kjer smo napako razdelili na statistično napako ter na napaki meritve parametrov α_Λ in \mathcal{A}_{CP}^Λ .

Če predpostavimo, da v razpadu $\Lambda \rightarrow p\pi$ ni kršitve simetrije CP, uporabimo enačbo (175), ter dobimo:

$$|\langle\alpha_{\Lambda_c}\rangle| = 0.958 \pm 0.014(\text{stat.}) \pm 0.019(\alpha_\Lambda) = 0.958 \pm 0.024, \quad (197)$$

kjer je prvi del napake statistična napaka, drugi pa napaka meritve parametra α_Λ .

Oba rezultata se ujemata z trenutnim svetovnim povprečjem [1] (-0.91 ± 0.15) in imata za velikostni red manjšo napako.

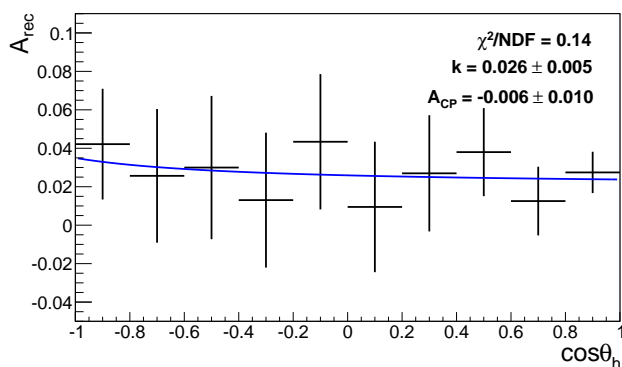
Parameter \mathcal{A}_{CP} določimo tako, da analizni vzorec za prave podatke razdelimo na vzorca za Λ_c^+ in $\bar{\Lambda}_c^-$, ter z prilaganjem, opisanim v poglavju 8.4.8 (za primer prilaganja glej sliko 96, za rezultate prilaganja na vse intervale pa glej dodatek A.5), določimo števila signalnih dogodkov za Λ_c^+ in $\bar{\Lambda}_c^-$ po intervalih v $\cos\theta_h$, oba seta števil dekonvoluiramo, ter izračunamo rekonstruirano asimetrijo. Po razdelitvi rekonstruirane asimetrije nato prilagajamo z funkcijo (192) (glej sliko 97), ter dobimo rezultat:

$$\mathcal{A}_{CP} = -0.006 \pm 0.010, \quad (198)$$

kjer je napaka statistična.

Za določitev parametra $\mathcal{A}_{CP}^{\Lambda_c}$ uporabimo enačbo (174), ter dobimo:

$$\mathcal{A}_{CP}^{\Lambda_c} = -0.012 \pm 0.010(\text{stat.}) \pm 0.021(\mathcal{A}_{CP}^\Lambda) = -0.012 \pm 0.023. \quad (199)$$



Slika 97: Prilaganje z funkcijo (192) na rekonstruirano asimetrijo, uporabljeno za določanje parametra \mathcal{A}_{CP} .

kjer je prvi del napake statistična napaka, drugi pa napaka meritve parametra $\mathcal{A}_{CP}^{\wedge}$.

Če predpostavimo, da v razpadu $\Lambda \rightarrow p\pi$ ni kršitve simetrije CP, je parameter $\mathcal{A}_{CP}^{\wedge c}$ kar enak parametru \mathcal{A}_{CP} (enačba (175)):

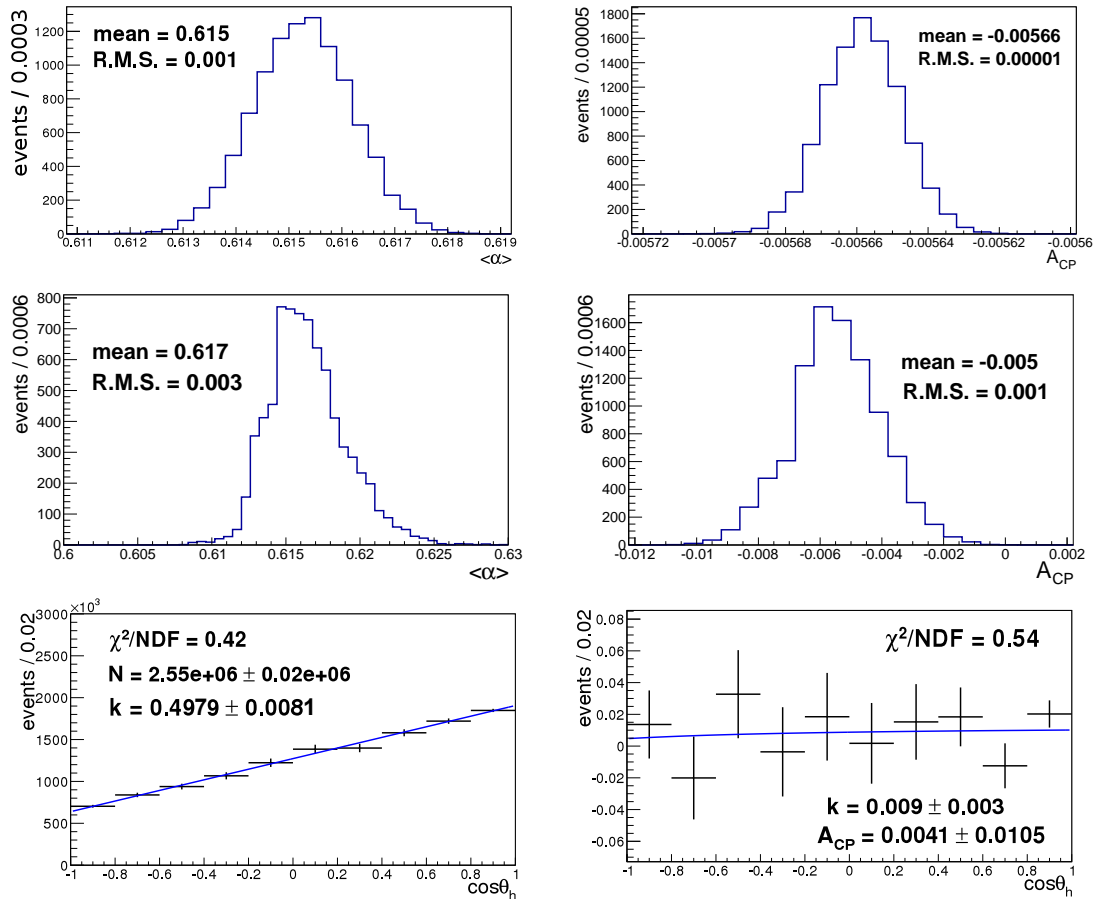
$$\mathcal{A}_{CP}^{\wedge c} = -0.006 \pm 0.010. \quad (200)$$

Oba rezultata sta konsistentna z odsotnostjo kršitve simetrije CP in se ujemata z trenutnim svetovnim povprečjem [1] (-0.07 ± 0.19), ter imata za velikostni red manjšo napako.

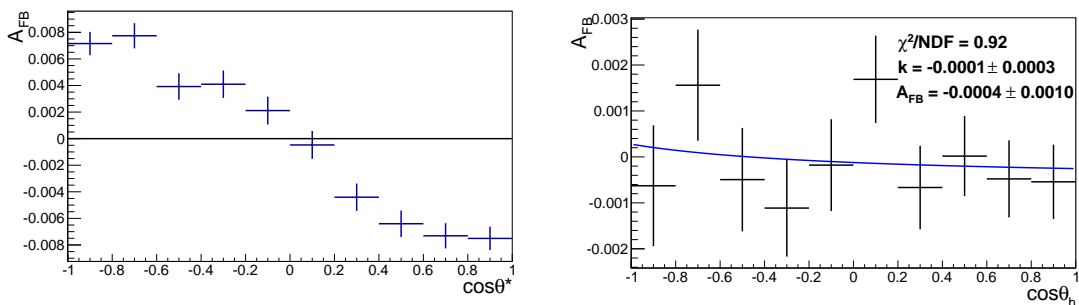
8.6 SISTEMATSKA NAPAKA

Za sistematsko napako smo določili več izvorov:

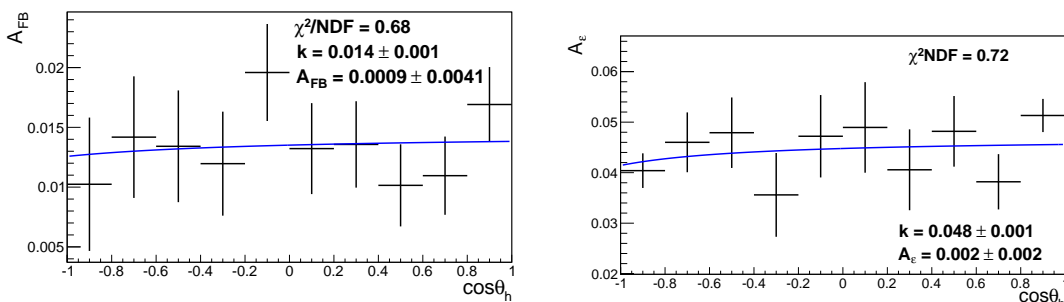
- Razlika v učinkovitosti določanja sledi pri MC simulaciji in pri podatkih. Ta napaka vpliva samo na rezultat za parameter $\langle \alpha \rangle$, saj se pri določanju parametra \mathcal{A}_{CP} pokrajša. Za vsako sled z gibalno količino večjo od 200 MeV/c, uporabljeno v rekonstrukciji Λ_c , znaša napaka 0.35% [38]. Ker uporabimo 3 sledi, ocenimo to napako na 1.05% vrednosti rezultata.
- Napaka zaradi uporabe določenih števil dogodkov v resolucijski matriki. To napako ocenimo tako, da variiramo števila dogodkov naključno po Gaussovi porazdelitvi v vsakem 2D intervalu resolucijske matrike, ter ponovno izračunamo rezultate. Koren variance tako dobljene porazdelitve vzamemo za oceno napake (glej sliko 98).
- Napaka zaradi fiksiranih parametrov v modelu, uporabljenem za prilaganje. To napako ocenimo tako, da variiramo fiksirane parametre naključno po Gaussovi porazdelitvi, ter ponovno izračunamo rezultate. Koren variance tako dobljene porazdelitve vzamemo za oceno napake (glej sliko 98).
- Napaka zaradi zanemaritve ozadja z enako porazdelitvijo po invariantni masi kot pri signalnih dogodkih. To napako ocenimo tako, da iz vzorca



Slika 98: Porazdelitve, uporabljene za določevanje sistematskih napak: levo zgoraj - določanje napake na $\langle\alpha\rangle$ zaradi dekonvolucije, desno zgoraj - določanje napake na \mathcal{A}_{CP} zaradi dekonvolucije, levo v sredini - določanje napake na $\langle\alpha\rangle$ zaradi modela prilagajanja, desno v sredini - določanje napake na \mathcal{A}_{CP} zaradi modela prilagajanja, levo spodaj - določanje napake na $\langle\alpha\rangle$ zaradi zanemaritve podobnega ozadja, desno spodaj - določanje napake na \mathcal{A}_{CP} zaradi zanemaritve podobnega ozadja.



Slika 99: Preverjanje izpovprečevanja \mathcal{A}_{FB} . Levo - porazdelitev \mathcal{A}_{FB} po $\cos \theta^*$, desno - porazdelitev \mathcal{A}_{FB} po $\cos \theta_h$.



Slika 100: Določevanje sistemske napake zaradi odvisnosti asimetrij od $\cos \theta_h$. Levo - določanje napake zaradi \mathcal{A}_{FB} , desno - določanje napake zaradi \mathcal{A}_ϵ .

izpustimo to ozadje, ter ponovno izračunamo rezultate. Za oceno napake nato vzamemo razliko med rezultatoma (glej sliko 98).

- Napaka zaradi predpostavke, da asimetrija naprej nazaj (\mathcal{A}_{FB}) ni funkcija $\cos \theta_h$. To napako ocenimo tako, da vzamemo vzorec signalnih dogodkov iz MC simulacije v kateri je ta asimetrija simulirana, pri izbiri vzorca pa ne uporabimo nikakršnih selekcijskih kriterijev. Nato preštejemo razpade Λ_c^+ in $\overline{\Lambda}_c$ posebej, izračunamo asimetrijo, ter jo razvrstimo v enake intervale po $\cos \theta_h$ kot pri originalni analizi. Tako vidimo, če se odvisnost po $\cos \theta_h$ izpovpreči (glej sliko 99). Nato vzamemo vzorec signalnih dogodkov, izbran z enakimi kriteriji kot pri originalni analizi, ter znova tvorimo porazdelitev asimetrije po intervalih v $\cos \theta_h$. Na to porazdelitev prilagajamo enako funkcijo kot pri določitvi parametra \mathcal{A}_{CP} , ter za oceno napake vzamemo napako, ki jo dobimo iz prilagajanja (glej sliko 100).
- Napaka zaradi predpostavke, da asimetrija zaradi rekonstrukcije delcev in antidelcev (\mathcal{A}_ϵ) ni funkcija $\cos \theta_h$. To napako ocenimo tako, da na enak način rekonstruiramo razpadno verigo $\Sigma^* \rightarrow \Lambda\pi, \Lambda \rightarrow p\pi$, za katero vemo, da ne vsebuje nobene druge asimetrije. Za to razpadno verigo nato določimo porazdelitev asimetrije po intervalih v $\cos \theta_h$, ter na to porazdelitev prilagajamo enako funkcijo kot pri določitvi parametra \mathcal{A}_{CP} , ter za oceno napake vzamemo napako, ki jo dobimo iz prilagajanja (glej sliko 100).

izvor	$\sigma_{\langle\alpha\rangle}^{\text{sys}}$	$\sigma_{\mathcal{A}_{\text{CP}}}^{\text{sys}}$
nabite sledi	0.011	n.a.
dekonvolucija	0.001	zanemarljivo
fiksirani par.	0.003	0.001
ozadje z enako porazd.	zanemarljivo	zanemarljivo
\mathcal{A}_{FB}	n.a.	0.004
$\mathcal{A}_{\varepsilon}$	n.a.	0.002
vsota	0.011	0.005

Tabela 20: Sistematske napake na parametrih $\langle\alpha\rangle$ and \mathcal{A}_{CP} .

Vsi izvori sistematske napake so neodvisni, zato vse prispevke seštejemo v kvadratu, in dobimo za sistematski napaki na $\langle\alpha\rangle$ ter \mathcal{A}_{CP} rezultat, prikazan v tabeli 20.

8.7 POVZETEK

Izmerili smo parameter šibke asimetrije $\langle\alpha_{\Lambda_c}\rangle$ ter parameter kršitve simetrije CP $\mathcal{A}_{\text{CP}}^{\Lambda_c}$ za razpad $\Lambda_c \rightarrow \Lambda\pi$.

Naša metoda meritve je zasnovana tako, da najprej izmerimo povprečni parameter šibke asimetrije za združena vzorca razpadov Λ_c^+ in $\overline{\Lambda_c^-}$, nato pa z uporabo te vrednosti določimo parameter kršitve simetrije CP. Pri meritvi $\mathcal{A}_{\text{CP}}^{\Lambda_c}$ se tako nekateri izvori sistematske napake pokrajšajo.

Če privzamemo izmerjeno kršitev simetrije CP v razpadu $\Lambda \rightarrow p\pi$ [1], so izmerjene vrednosti enake:

$$\begin{aligned}
|\langle\alpha_{\Lambda_c}\rangle| &= 0.964 \pm 0.014(\text{stat.}) \pm 0.020(\alpha_{\Lambda}) \pm 0.020(\mathcal{A}_{\text{CP}}^{\Lambda}) \pm 0.017(\text{syst.}) = \\
&= 0.964 \pm 0.014(\text{stat.}) \pm 0.033(\text{syst.}), \\
\mathcal{A}_{\text{CP}}^{\Lambda_c} &= -0.012 \pm 0.010(\text{stat.}) \pm 0.021(\mathcal{A}_{\text{CP}}^{\Lambda}) \pm 0.005(\text{syst.}) = \\
&= -0.012 \pm 0.010(\text{stat.}) \pm 0.022(\text{syst.}),
\end{aligned} \tag{201}$$

kjer smo v prvem koraku razdelili mersko napako na napaki meritev parametrov šibke asimetrije in kršitve simetrije CP v razpadu $\Lambda \rightarrow p\pi$.

Če predpostavimo, da kršitve v razpadu $\Lambda \rightarrow p\pi$ ni, pa so izmerjene vrednosti enake:

$$\begin{aligned}
|\langle\alpha_{\Lambda_c}\rangle| &= 0.958 \pm 0.014(\text{stat.}) \pm 0.019(\alpha_{\Lambda}) \pm 0.017(\text{syst.}) = \\
&= 0.958 \pm 0.014(\text{stat.}) \pm 0.025(\text{syst.}), \\
\mathcal{A}_{\text{CP}}^{\Lambda_c} &= -0.006 \pm 0.010(\text{stat.}) \pm 0.005(\text{syst.}).
\end{aligned} \tag{202}$$

Vse vrednosti se ujemajo z prejšnjimi meritvami [34] in z svetovnimi povprečji [1] ter so konsistentni z odsotnostjo kršitve simetrije CP v razpadu $\Lambda_c \rightarrow \Lambda\pi$. Predstavljene meritve so najbolj natančne meritve do sedaj, ter imajo za velikostni red manjšo napako kot trenutna svetovna povprečja.

Statistične napake rezultatov za α_{Λ_c} in $\mathcal{A}_{\text{CP}}^{\Lambda_c}$ so večje kot eksperimentalne sistemske napake. Tako lahko v prihodnosti izboljšamo napake z meritvami na trkalniku SuperKEKB in detektorju Belle II, ki sta trenutno v izgradnji. Napaka se lahko izboljša tudi z izboljšanimi meritvami asimetrij v razpadu $\Lambda \rightarrow p\pi$.

FIT RESULTS

A.1 Λ_c SIGNAL MC SIMULATION FIT

The parameters obtained from the Λ_c signal MC simulation fit from section 4.5.2 are listed in table 21, and the fits for all bins are shown in figures 101 and 102.

A.2 Λ_c GENERIC MC SIMULATION FIT

The parameters obtained from the Λ_c generic MC simulation fit from section 4.5.3 are listed in table 22, and the fits for all bins are shown in figures 103 and 104.

A.3 Λ_c^+ AND $\overline{\Lambda}_c^-$ GENERIC MC SIMULATION FIT

The parameters obtained from the Λ_c^+ and $\overline{\Lambda}_c^-$ MC simulation fit from section 4.9 are listed in tables 23 and 24, and the fits for all bins are shown in figures 105, 106, 107 and 108.

A.4 Λ_c REAL DATA FIT

The parameters obtained from the Λ_c fit on real data from section 5.2 are listed in table 25, and the fits for all bins are shown in figures 109 and 110.

A.5 Λ_c^+ AND $\overline{\Lambda}_c^-$ REAL DATA FIT

The parameters obtained from the Λ_c^+ and $\overline{\Lambda}_c^-$ fit on real data from section 5.4 are listed in tables 26 and 27, and the fits for all bins are shown in figures 111, 112, 113 and 114.

A.6 Σ^{*+} AND Σ^{*-} REAL DATA FIT

The Σ^{*+} and Σ^{*-} fits on real data from section 6.6 for all bins are shown in figures 115, 116, 117 and 118.

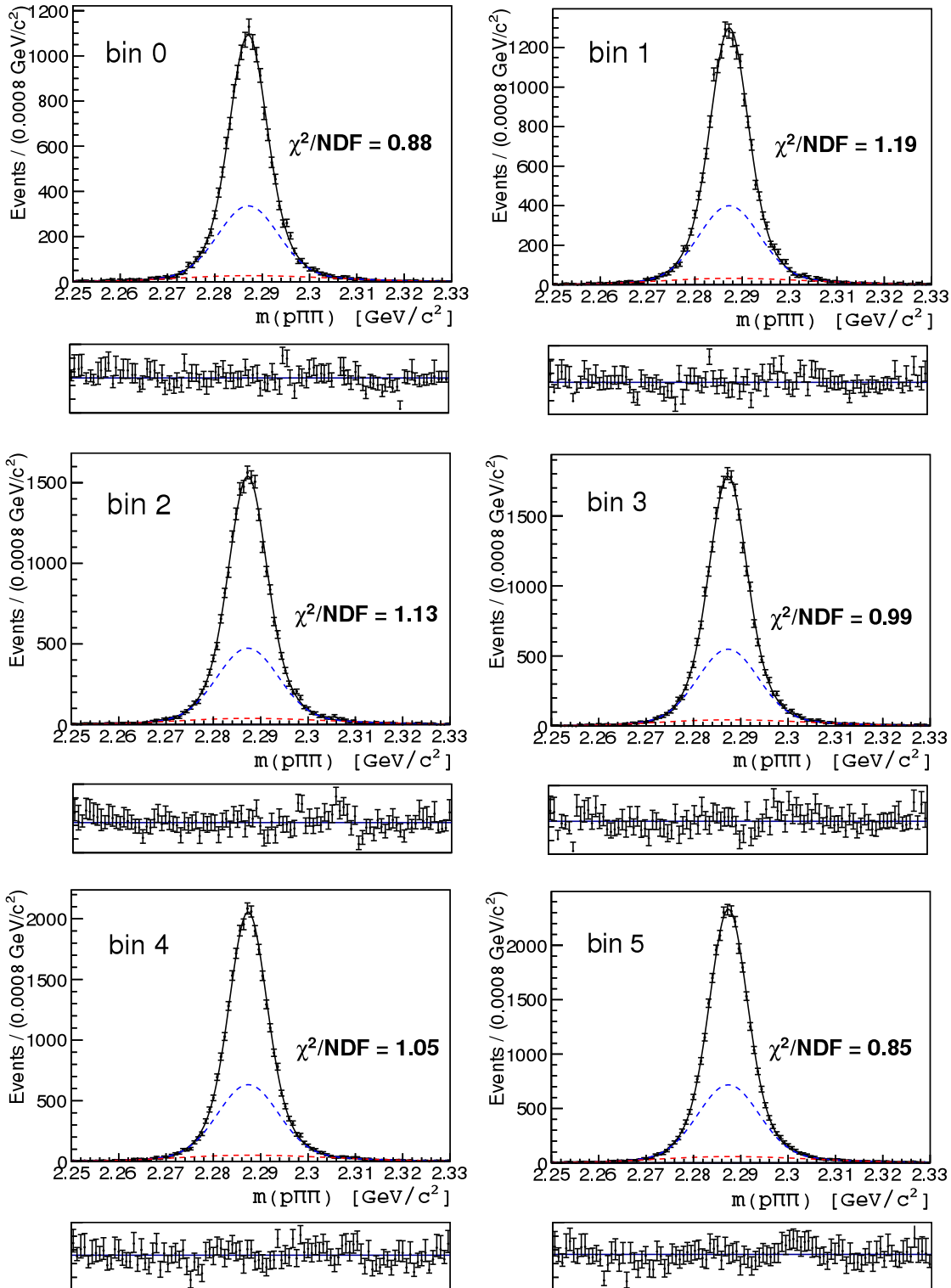


Figure 101: The Λ_c signal MC simulation fit for bins 0 – 5. The black, blue and red lines mark the narrow Gaussian, the wide Gaussian and the asymmetric Gaussian. The bottom plots show the fit residuals.

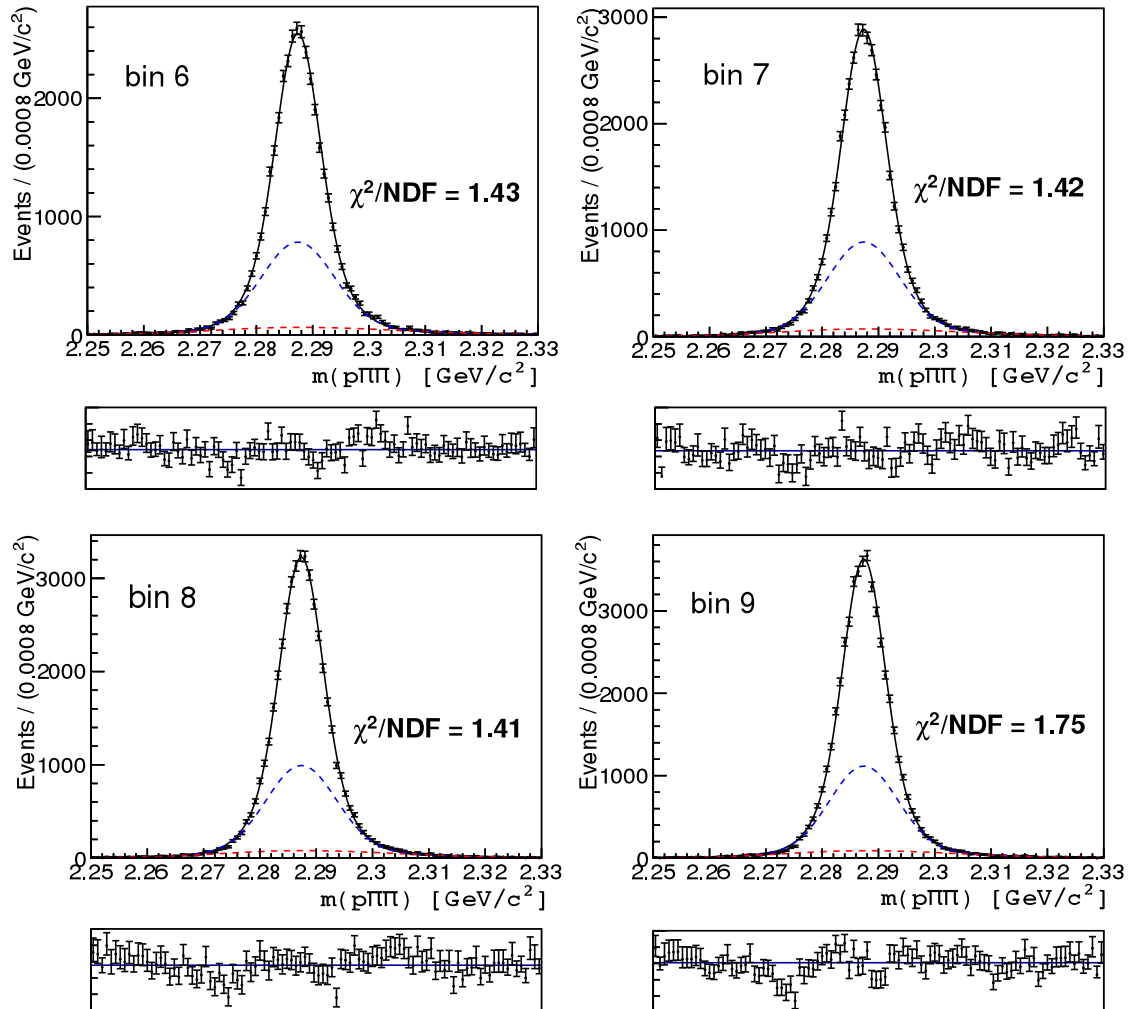


Figure 102: The Λ_c signal MC simulation fit for bins 6 – 9. The black, blue and red lines mark the narrow Gaussian, the wide Gaussian and the asymmetric Gaussian. The bottom plots show the fit residuals.

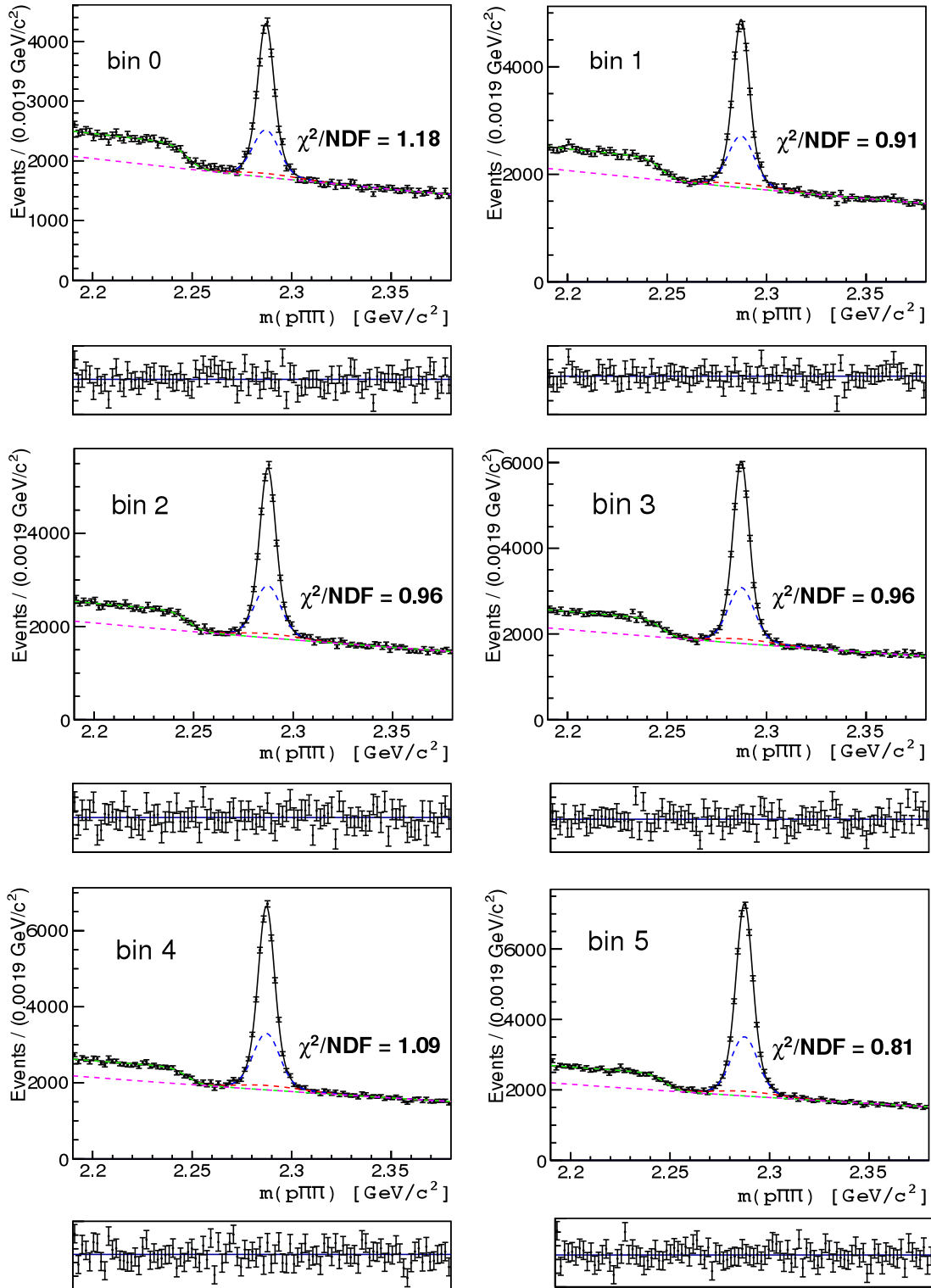


Figure 103: The Λ_c generic MC simulation fit for bins 0 – 5. The black, blue, red, green and purple lines mark the narrow Gaussian, the wide Gaussian, the asymmetric Gaussian (all describing signal events), the sigmoid function and the 2nd order Chebyshev polynomial (all describing the backgrounds), respectively. The bottom plots show the fit residuals.

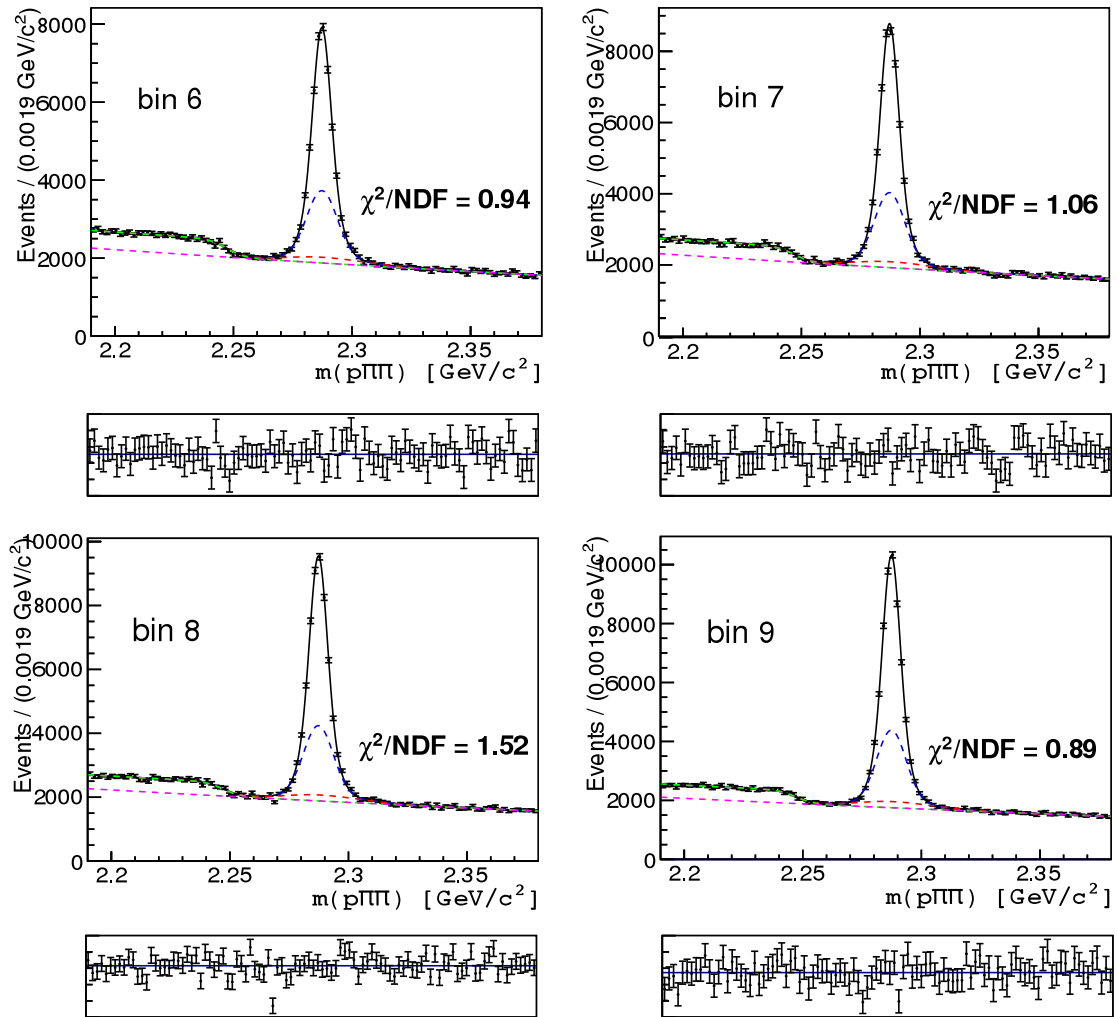


Figure 104: The Λ_c generic MC simulation fit for bins 6 – 9. The black, blue, red, green and purple lines mark the narrow Gaussian, the wide Gaussian, the asymmetric Gaussian (all describing signal events), the sigmoid function and the 2nd order Chebyshev polynomial (all describing the backgrounds), respectively. The bottom plots show the fit residuals.

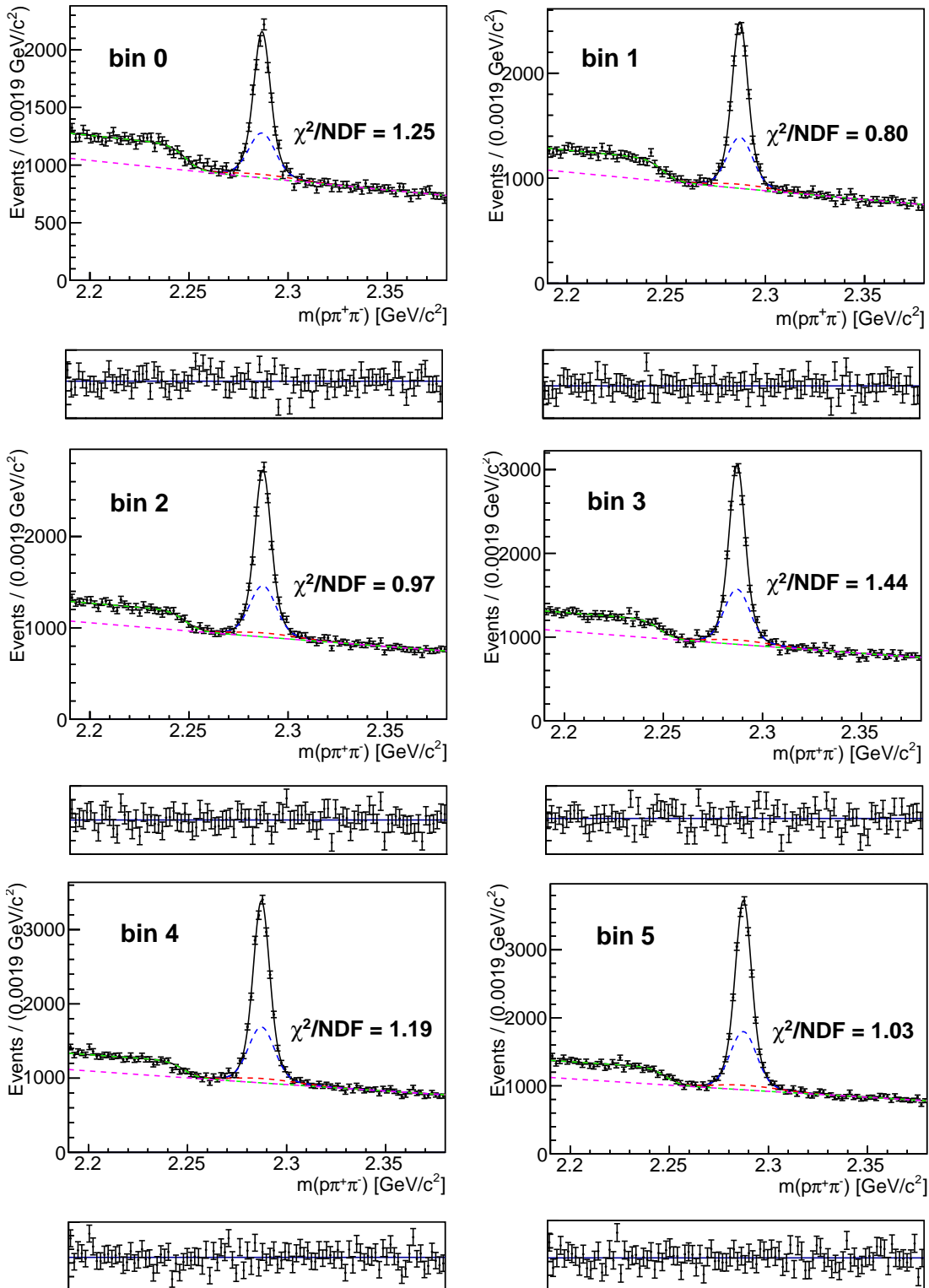


Figure 105: The Λ_c^+ MC simulation fit for bins 0 – 5. The black, blue, red, green and purple lines mark the narrow Gaussian, the wide Gaussian, the asymmetric Gaussian (all describing signal events), the sigmoid function and the 2nd order Chebyshev polynomial (all describing the backgrounds), respectively. The bottom plots show the fit residuals.

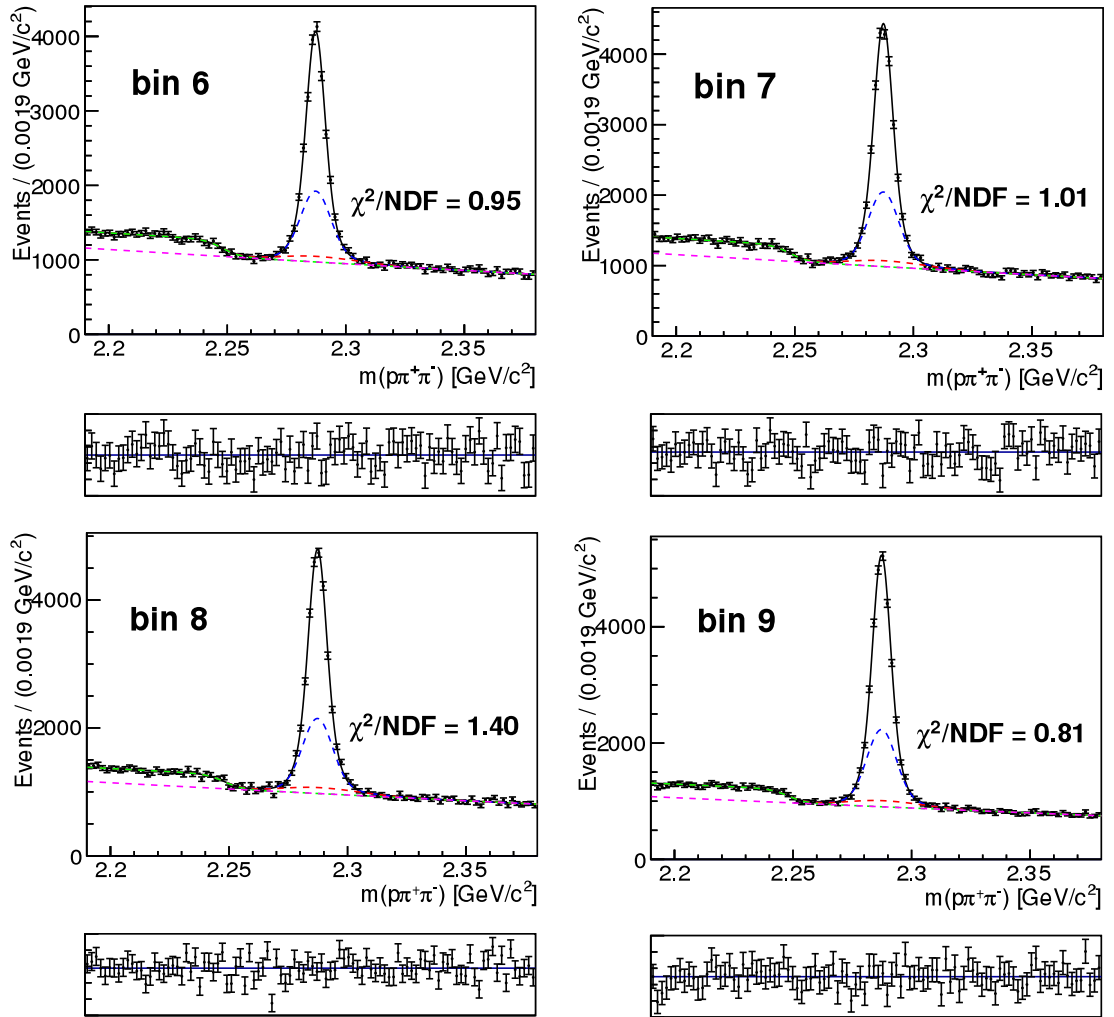


Figure 106: The Λ_c^+ MC simulation fit for bins 6 – 9. The black, blue, red, green and purple lines mark the narrow Gaussian, the wide Gaussian, the asymmetric Gaussian (all describing signal events), the sigmoid function and the 2nd order Chebyshev polynomial (all describing the backgrounds), respectively. The bottom plots show the fit residuals.

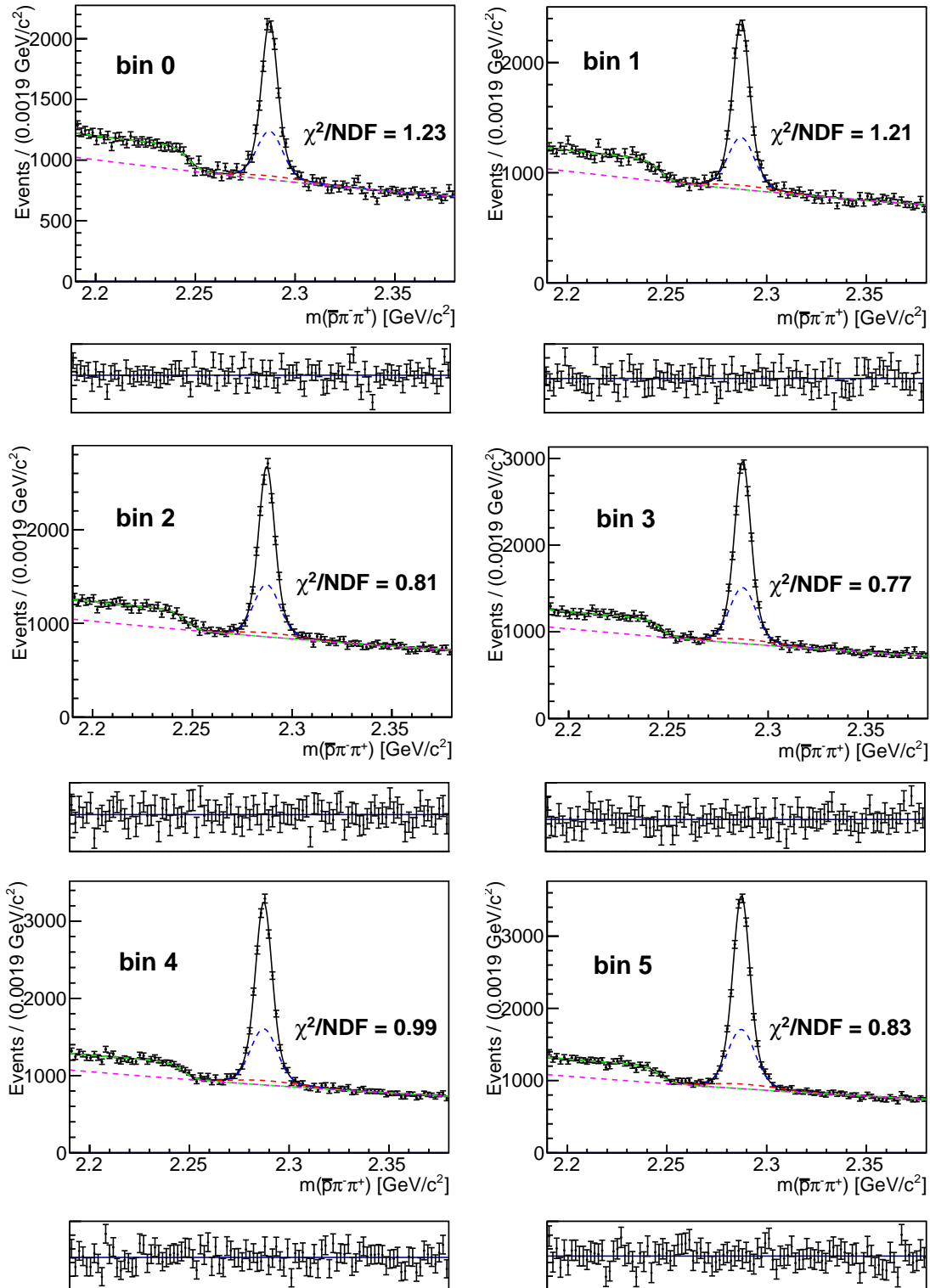


Figure 107: The $\bar{\Lambda}_c^-$ MC simulation fit for bins 0 – 5. The black, blue, red, green and purple lines mark the narrow Gaussian, the wide Gaussian, the asymmetric Gaussian (all describing signal events), the sigmoid function and the 2nd order Chebyshev polynomial (all describing the backgrounds), respectively. The bottom plots show the fit residuals.

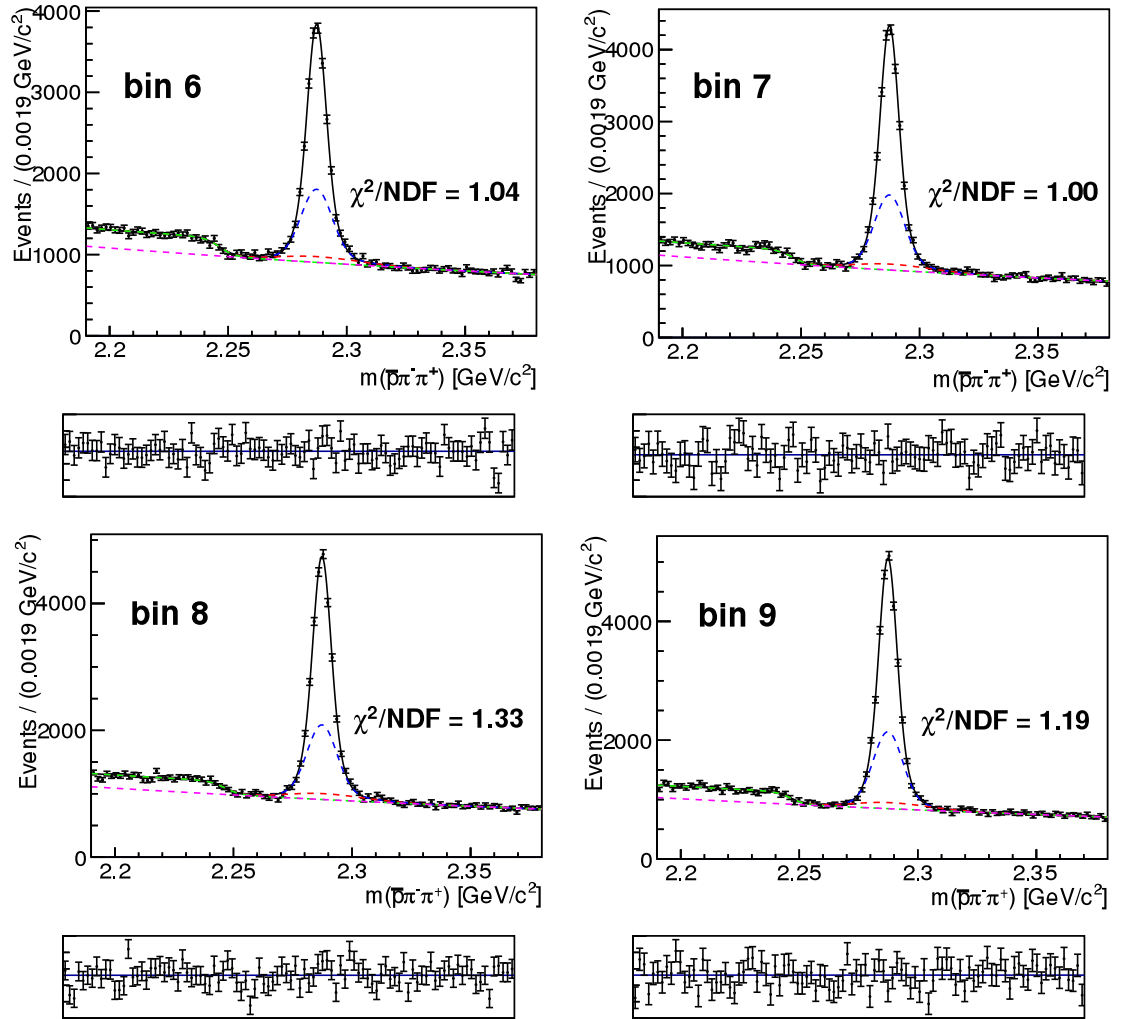


Figure 108: The $\bar{\Lambda}_c^-$ MC simulation fit for bins 6 – 9. The black, blue, red, green and purple lines mark the narrow Gaussian, the wide Gaussian, the asymmetric Gaussian (all describing signal events), the sigmoid function and the 2nd order Chebyshev polynomial (all describing the backgrounds), respectively. The bottom plots show the fit residuals.

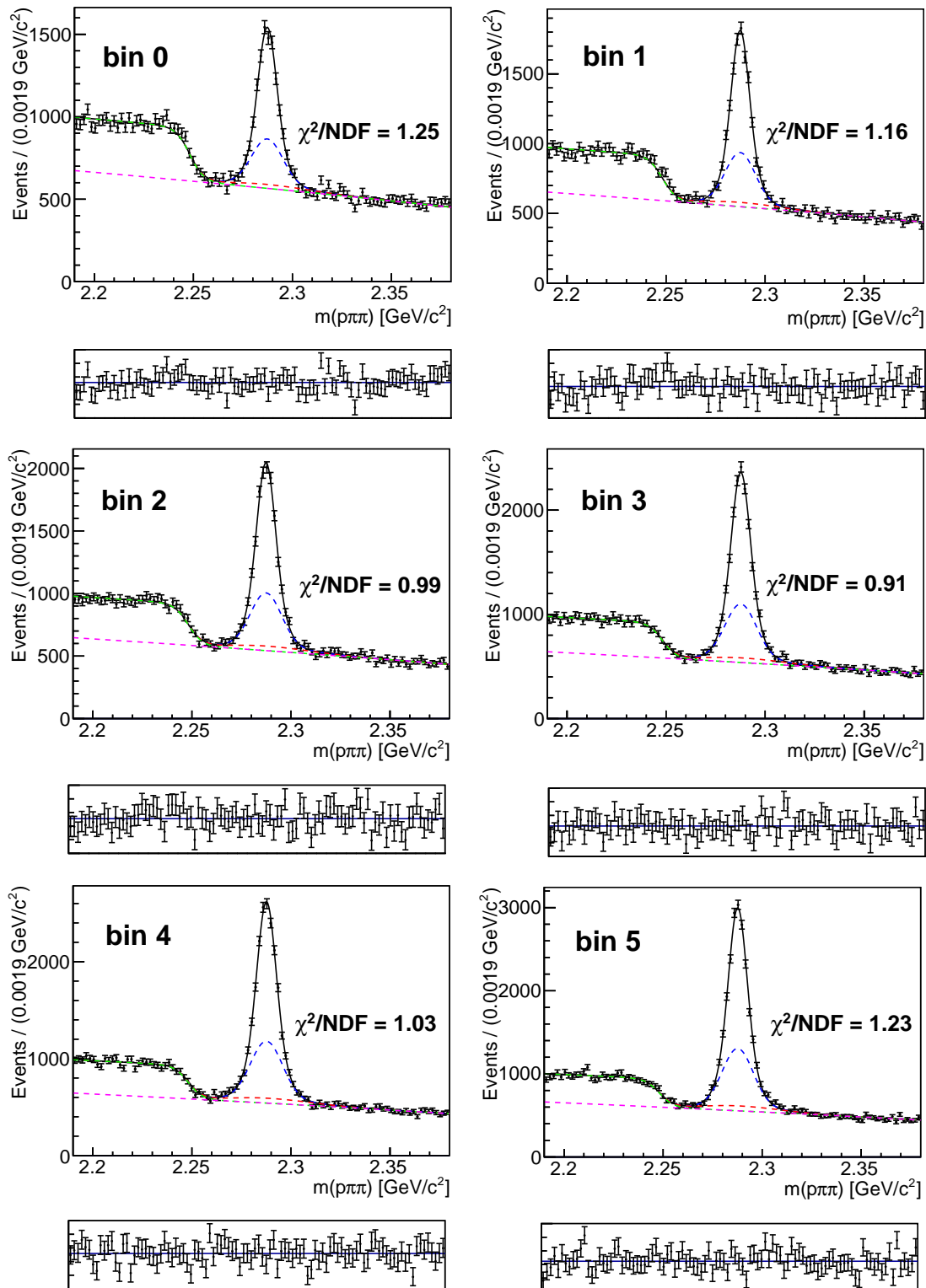


Figure 109: The Λ_c real data fit for bins 0 – 5. The black, blue, red, green and purple lines mark the narrow Gaussian, the wide Gaussian, the asymmetric Gaussian (all describing signal events), the sigmoid function and the 2nd order Chebyshev polynomial (all describing the backgrounds), respectively. The bottom plots show the fit residuals.

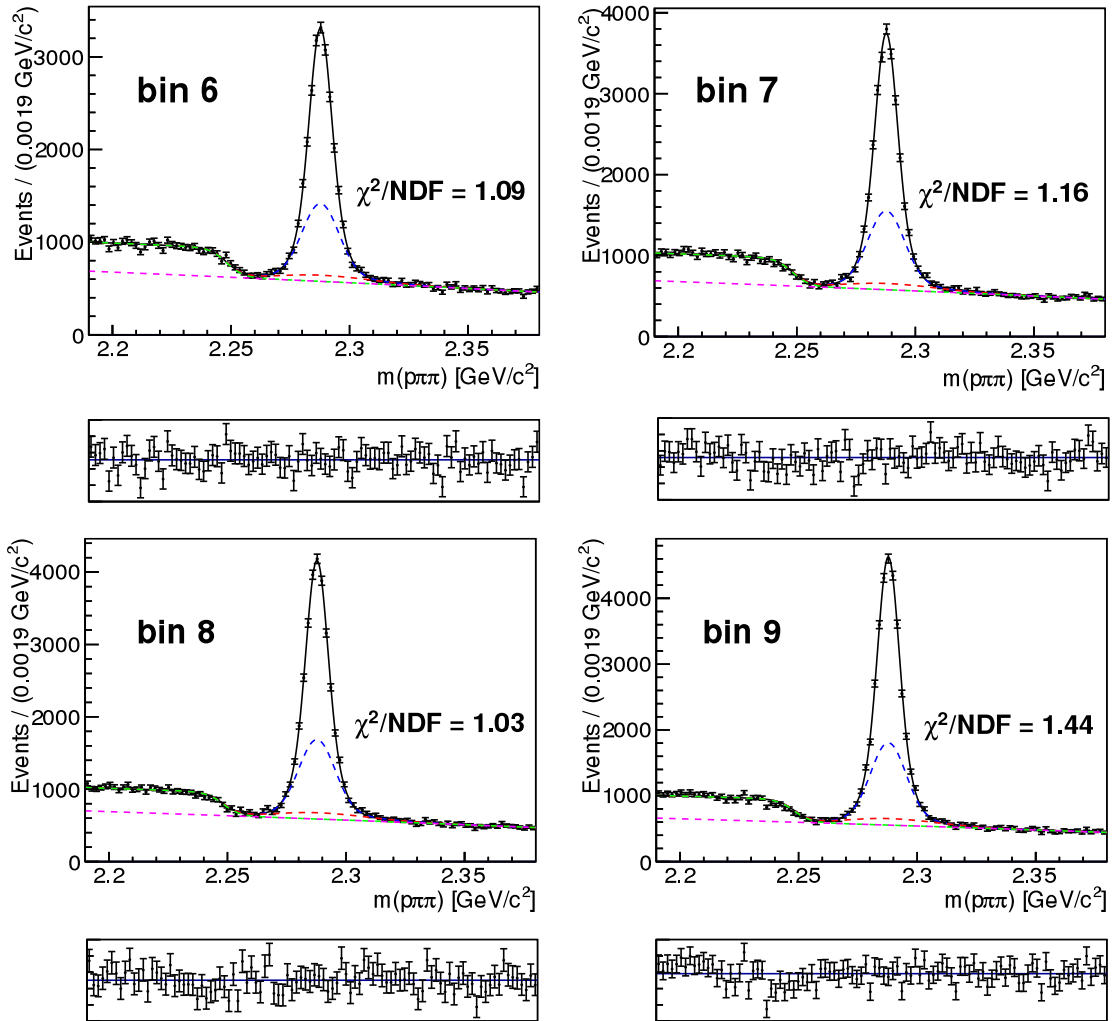


Figure 110: The Λ_c real data fit for bins 6 – 9. The black, blue, red, green and purple lines mark the narrow Gaussian, the wide Gaussian, the asymmetric Gaussian (all describing signal events), the sigmoid function and the 2nd order Chebyshev polynomial (all describing the backgrounds), respectively. The bottom plots show the fit residuals.

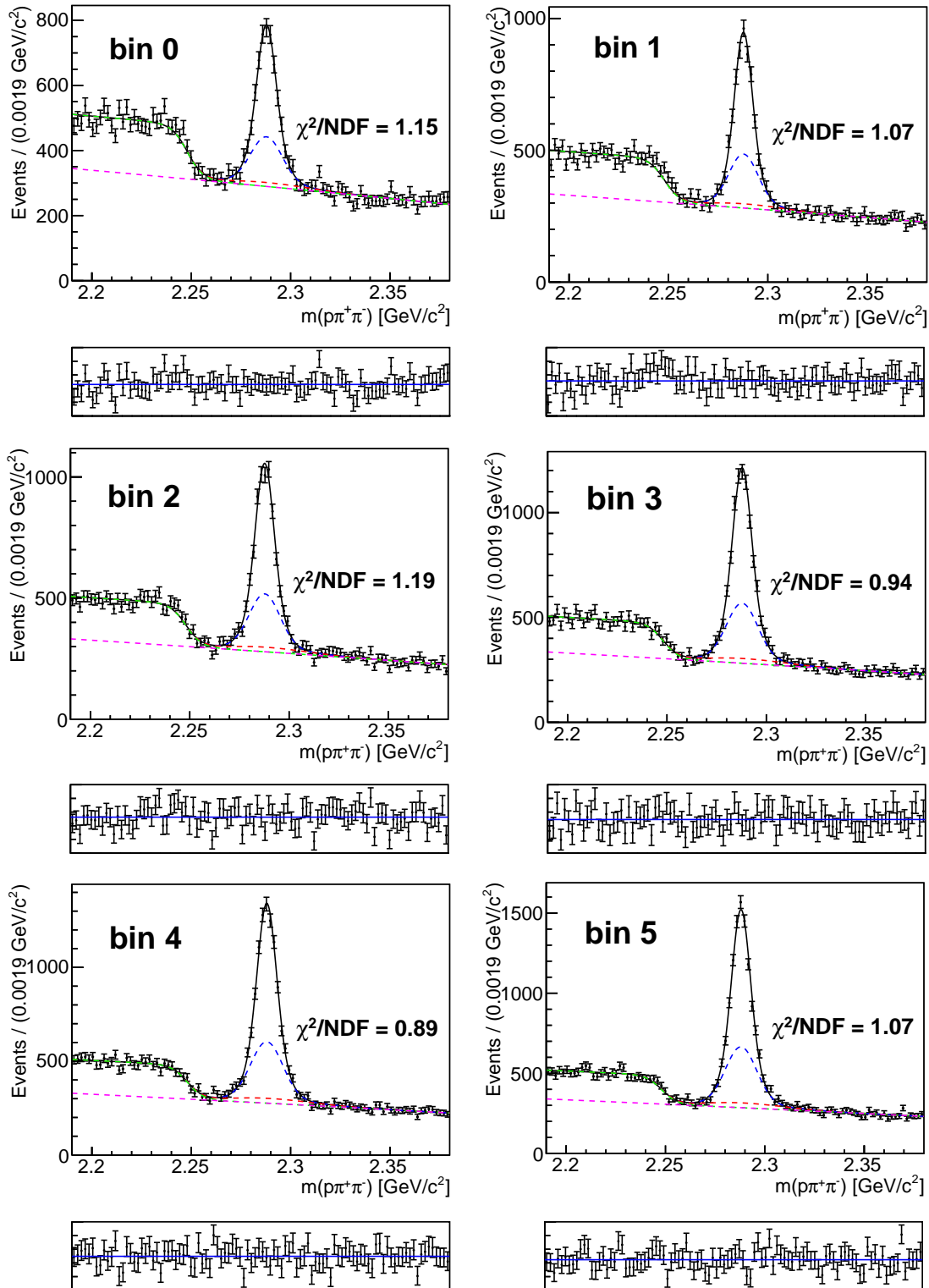


Figure 111: The Λ_c^+ fit on real data for bins 0–5. The black, blue, red, green and purple lines mark the narrow Gaussian, the wide Gaussian, the asymmetric Gaussian (all describing signal events), the sigmoid function and the 2nd order Chebyshev polynomial (all describing the backgrounds), respectively. The bottom plots show the fit residuals.

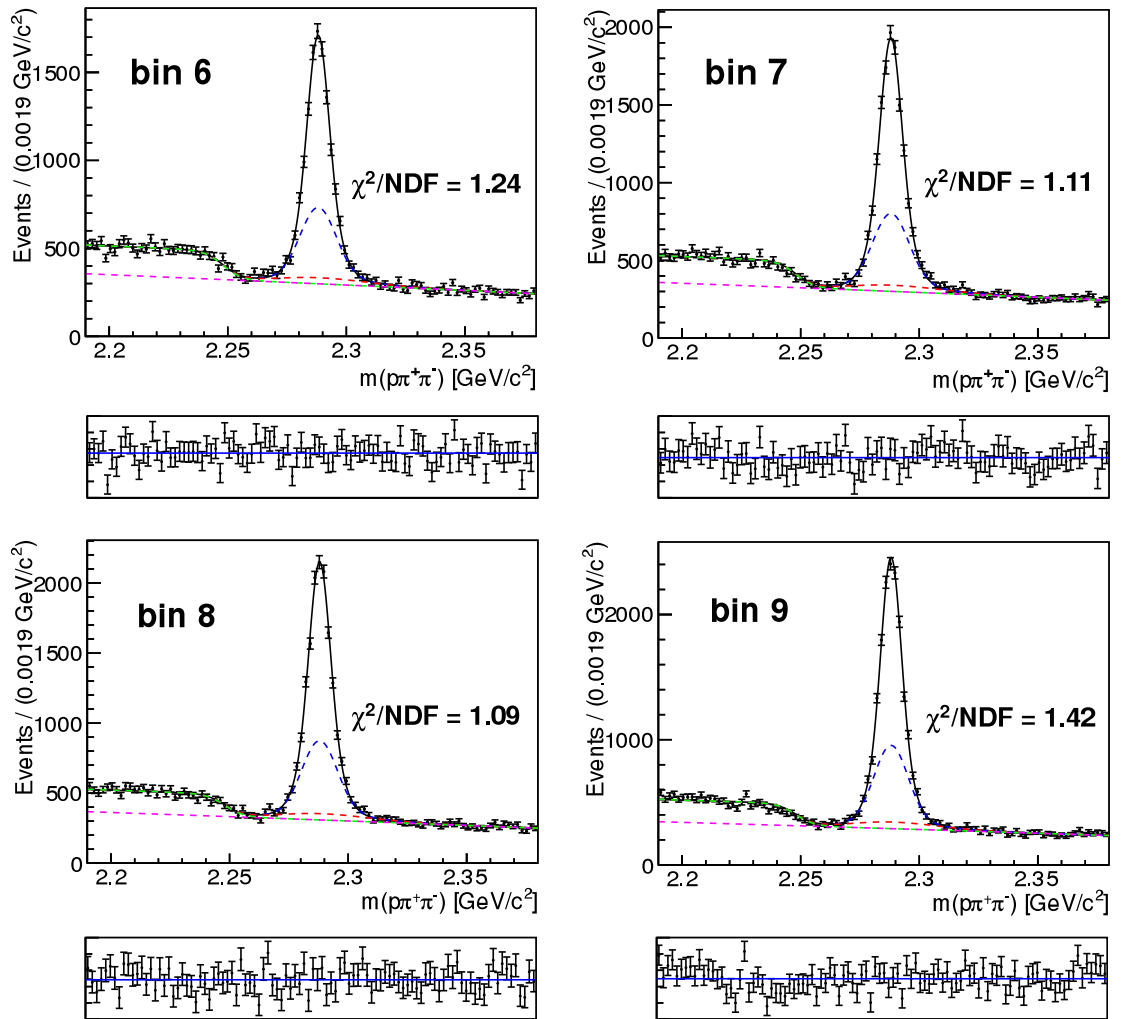


Figure 112: The Λ_c^+ fit on real data for bins 6 – 9. The black, blue, red, green and purple lines mark the narrow Gaussian, the wide Gaussian, the asymmetric Gaussian (all describing signal events), the sigmoid function and the 2nd order Chebyshev polynomial (all describing the backgrounds), respectively. The bottom plots show the fit residuals.

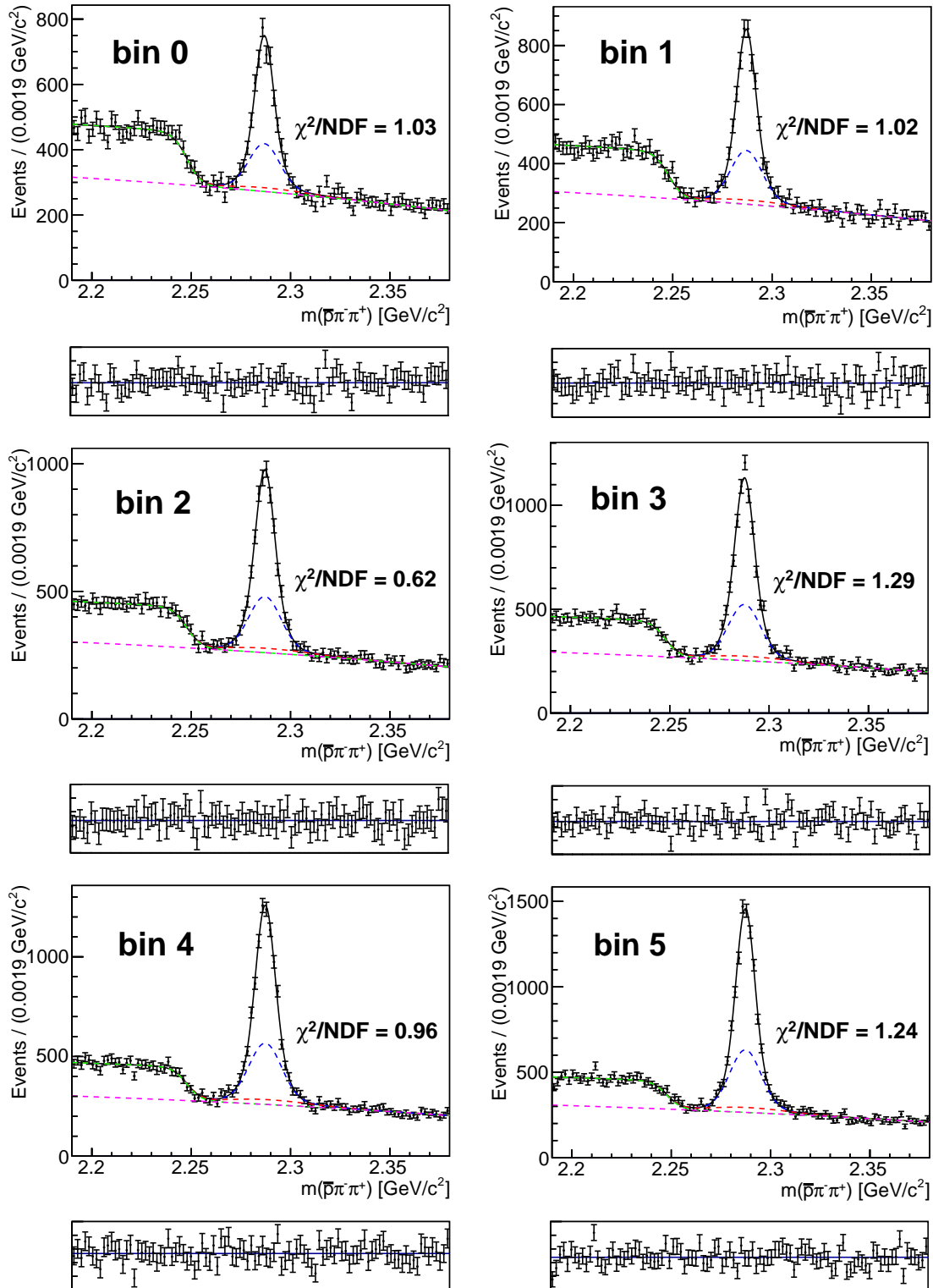


Figure 113: The $\bar{\Lambda}_c^-$ fit on real data for bins 0 – 5. The black, blue, red, green and purple lines mark the narrow Gaussian, the wide Gaussian, the asymmetric Gaussian (all describing signal events), the sigmoid function and the 2nd order Chebyshev polynomial (all describing the backgrounds), respectively. The bottom plots show the fit residuals.

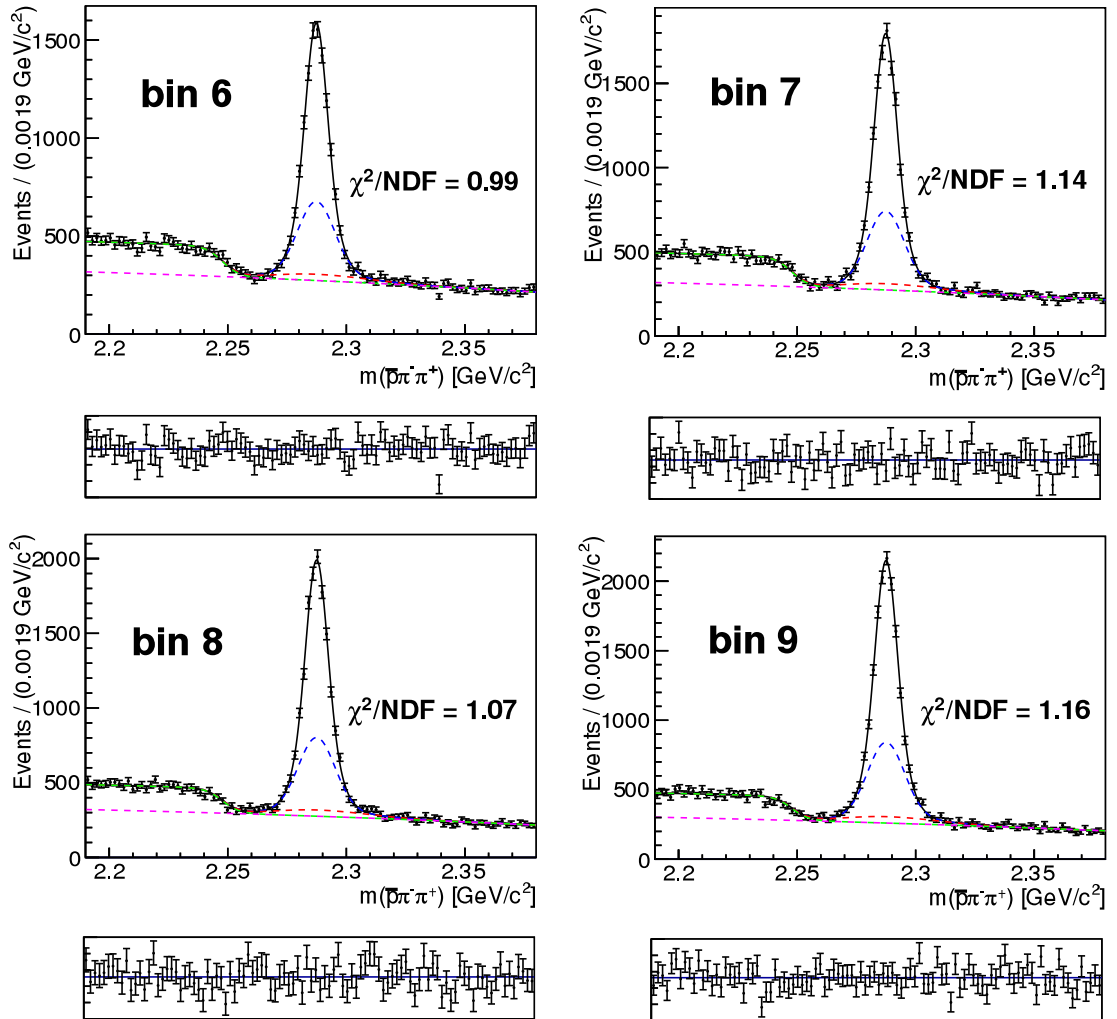


Figure 114: The $\bar{\Lambda}_c^-$ fit on real data for bins 6 – 9. The black, blue, red, green and purple lines mark the narrow Gaussian, the wide Gaussian, the asymmetric Gaussian (all describing signal events), the sigmoid function and the 2nd order Chebyshev polynomial (all describing the backgrounds), respectively. The bottom plots show the fit residuals.

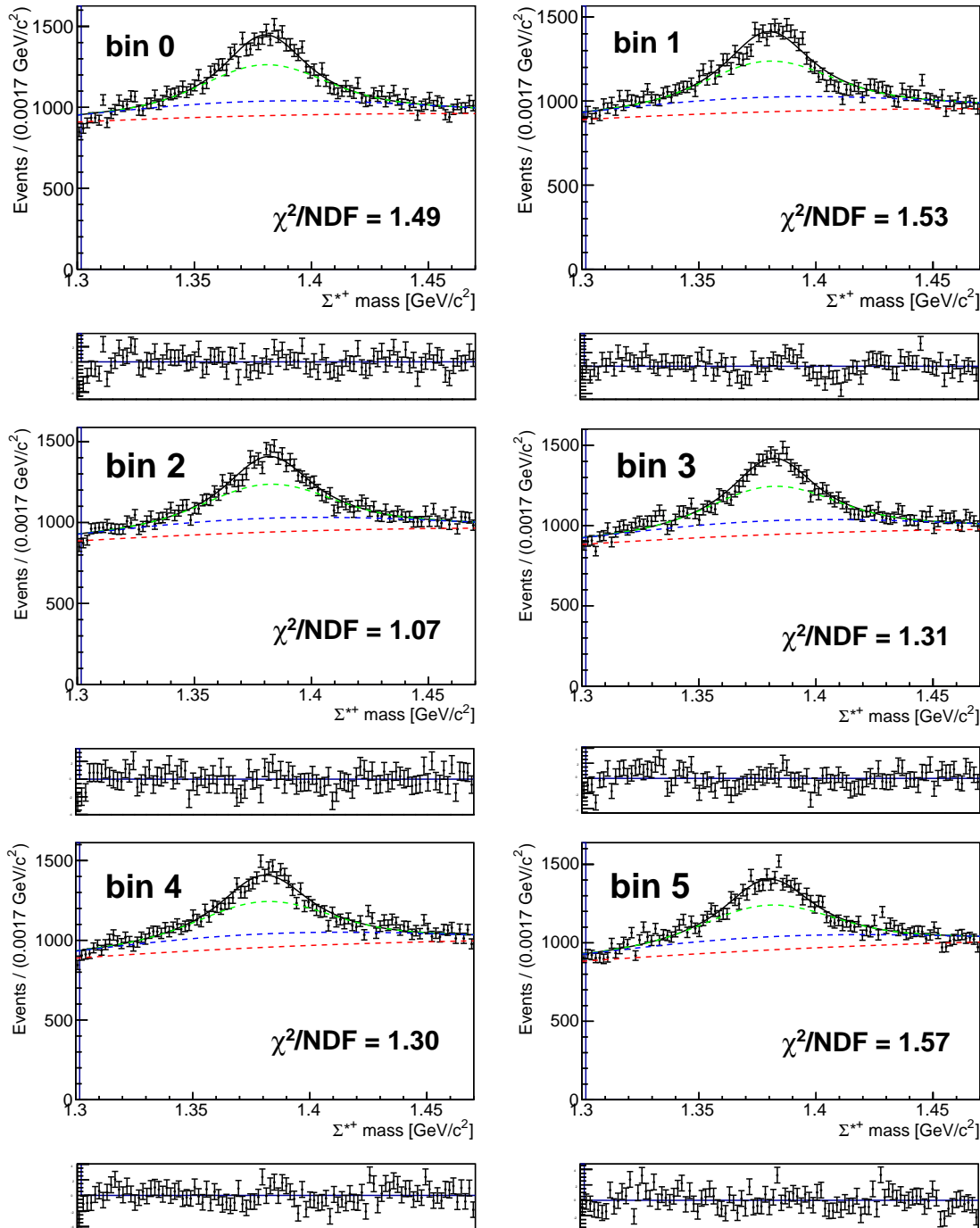


Figure 115: The Σ^{*+} real data fit for bins 0 – 5. The black, green and blue lines mark the three Gaussian functions (all describing signal events) and the red line marks the 2nd order Chebyshev polynomial (describing the background). The bottom plots show the fit residuals.

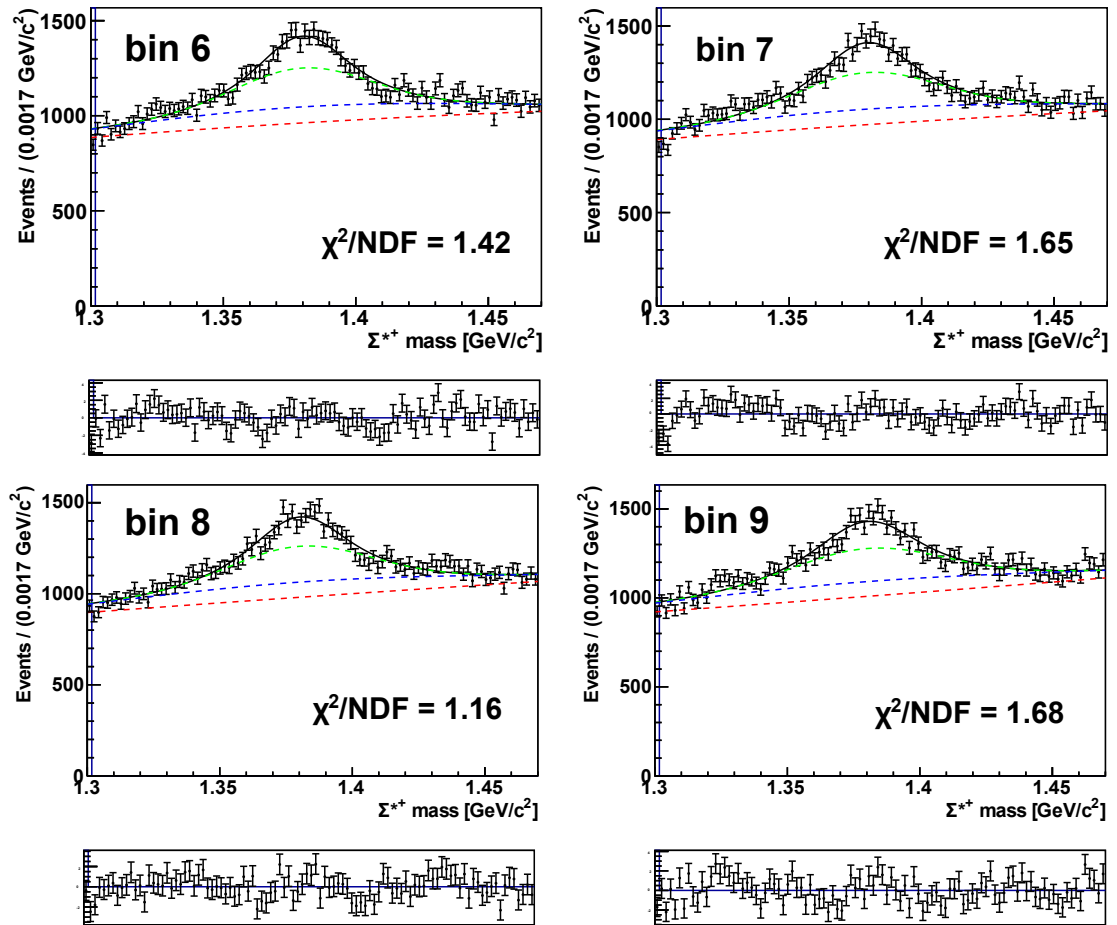


Figure 116: The Σ^{*+} real data fit for bins 6 – 9. The black, green and blue lines mark the three Gaussian functions (all describing signal events) and the red line marks the 2nd order Chebyshev polynomial (describing the background). The bottom plots show the fit residuals.

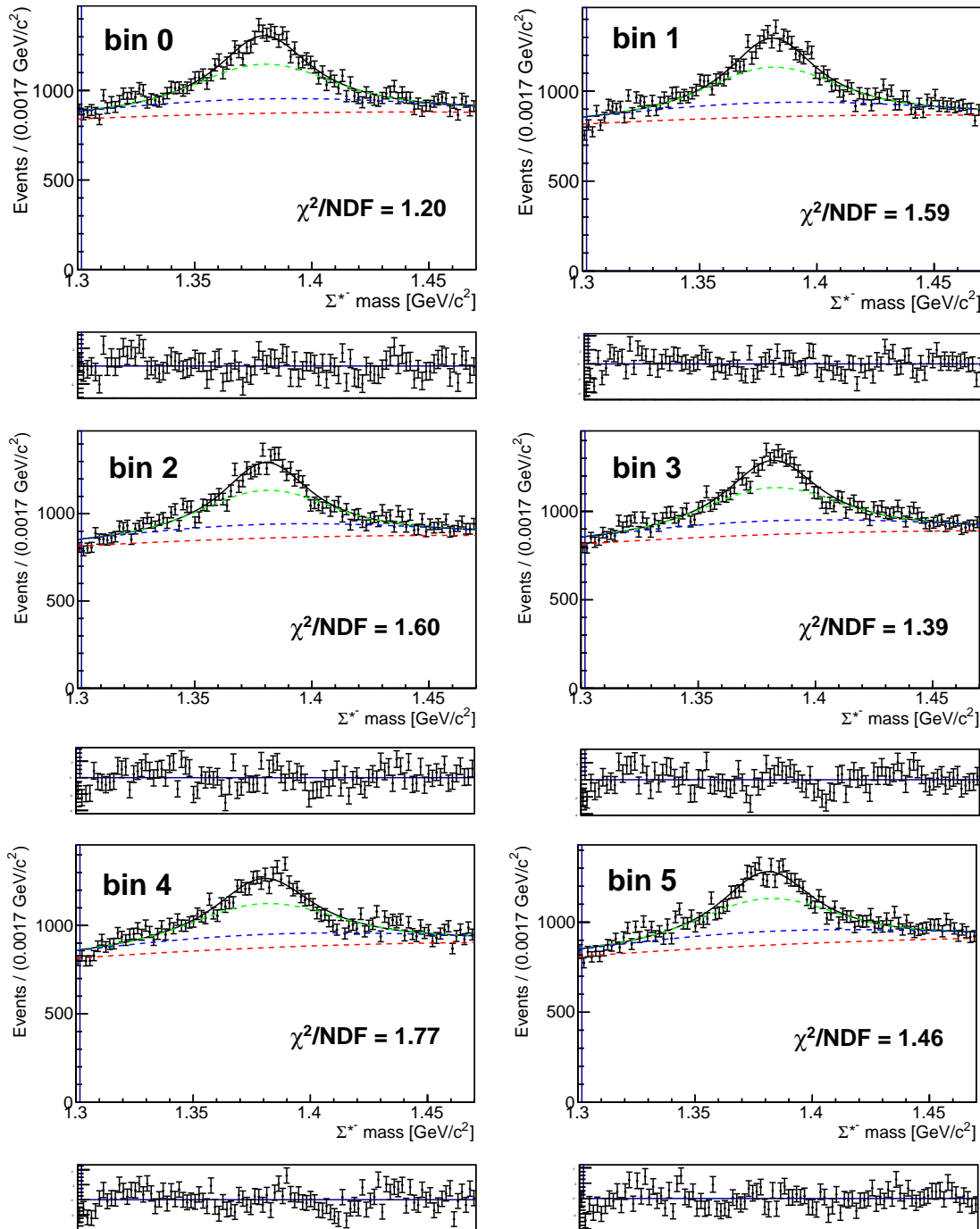


Figure 117: The Σ^{*-} real data fit for bins 0 – 5. The black, green and blue lines mark the three Gaussian functions (all describing signal events) and the red line marks the 2nd order Chebyshev polynomial (describing the background). The bottom plots show the fit residuals.

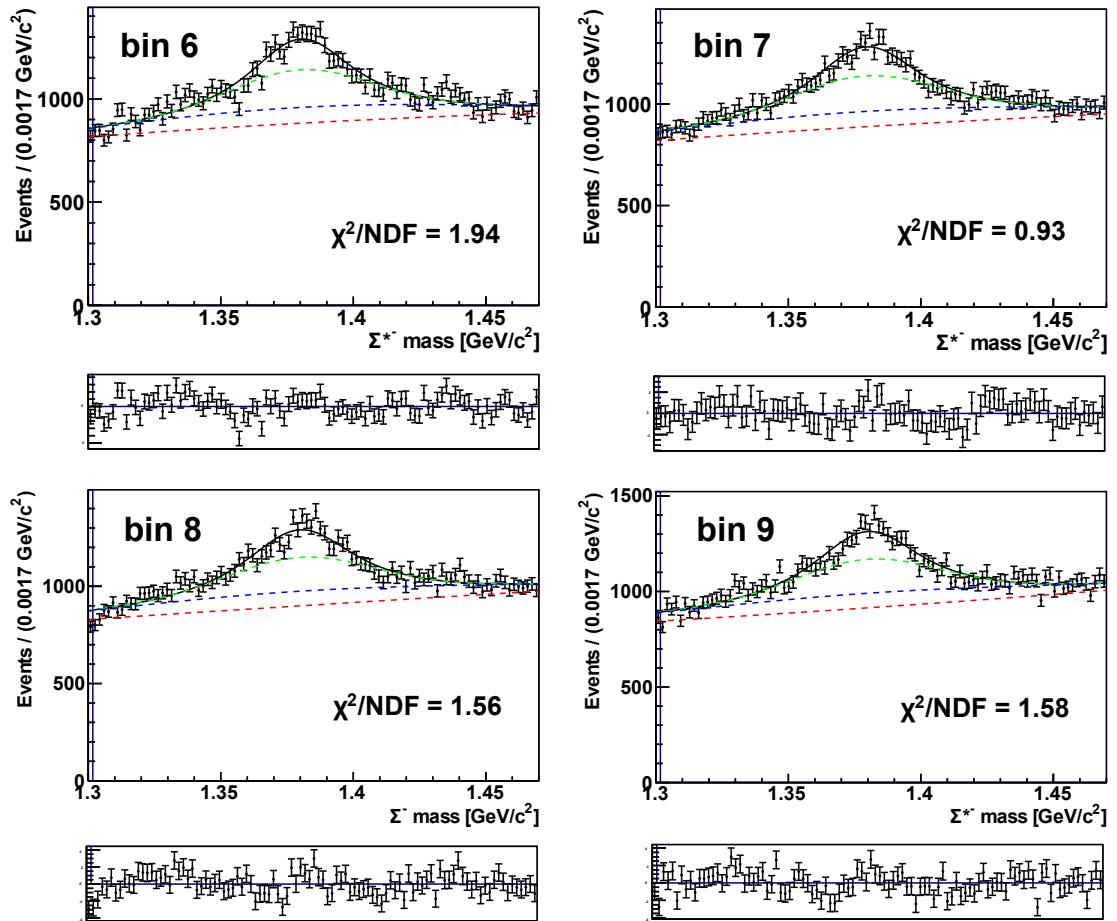


Figure 118: The Σ^{*-} real data fit for bins 6 – 9. The black, green and blue lines mark the three Gaussian functions (all describing signal events) and the red line marks the 2nd order Chebyshev polynomial (describing the background). The bottom plots show the fit residuals.

bin	χ^2/NDF	$N_{1,i}$	m_i	$\sigma_{1,i}$
0	0.88	8562 ± 327	2.28705 ± 0.00004	0.00361 ± 0.00005
1	1.19	10245 ± 390	2.28724 ± 0.00004	0.00363 ± 0.00005
2	1.13	12266 ± 466	2.28727 ± 0.00003	0.00367 ± 0.00005
3	0.99	14041 ± 532	2.28731 ± 0.00003	0.00363 ± 0.00005
4	1.05	16225 ± 614	2.28735 ± 0.00003	0.00364 ± 0.00005
5	0.85	18523 ± 699	2.28740 ± 0.00003	0.00366 ± 0.00005
6	1.43	20302 ± 766	2.28737 ± 0.00003	0.00367 ± 0.00005
7	1.42	22678 ± 855	2.28740 ± 0.00003	0.00362 ± 0.00005
8	1.41	24917 ± 938	2.28736 ± 0.00002	0.00356 ± 0.00005
9	1.75	27206 ± 1024	2.28740 ± 0.00002	0.00345 ± 0.00004
n_{12}	n_{13}	s_{12}	s_{13l}	s_{13r}
0.710 ± 0.060	0.156 ± 0.010	1.741 ± 0.018	4.008 ± 0.056	4.856 ± 0.071

Table 21: Values of parameters obtained from the Λ_c signal MC simulation fit.

bin	χ^2/NDF	$N_{1,i}$	m_i	$\sigma_{1,i}$
0	1.18	8674 ± 130	2.28706 ± 0.00007	0.00369 ± 0.00006
1	0.91	10424 ± 134	2.28719 ± 0.00006	0.00365 ± 0.00005
2	0.96	12155 ± 139	2.28728 ± 0.00005	0.00365 ± 0.00005
3	0.96	14078 ± 143	2.28724 ± 0.00005	0.00363 ± 0.00004
4	1.09	16431 ± 150	2.28730 ± 0.00004	0.00372 ± 0.00004
5	0.81	18747 ± 156	2.28737 ± 0.00004	0.00375 ± 0.00004
6	0.94	20236 ± 158	2.28731 ± 0.00004	0.00367 ± 0.00003
7	1.06	22553 ± 162	2.28734 ± 0.00003	0.00360 ± 0.00003
8	1.52	25088 ± 166	2.28733 ± 0.00003	0.00358 ± 0.00003
9	0.89	27452 ± 166	2.28737 ± 0.00003	0.00351 ± 0.00002
bin		$N_{b1,i}$	$N_{b2,i}$	common par.
0		12587 ± 543	174142 ± 755	$m_b = 2.2472 \pm 0.0003$
1		12149 ± 544	176753 ± 757	$w_b = 0.0037 \pm 0.0003$
2		12767 ± 548	177257 ± 763	$c_1 = -0.184 \pm 0.005$
3		12795 ± 553	179416 ± 769	$c_2 = 0.007 \pm 0.002$
4		13211 ± 564	182959 ± 784	
5		14780 ± 577	184474 ± 798	
6		13609 ± 575	189205 ± 798	
7		12909 ± 579	194089 ± 804	
8		13071 ± 571	190137 ± 795	
9		13404 ± 544	176755 ± 759	

Table 22: Values of parameters obtained from the Λ_c generic MC simulation fit.

bin	χ^2/NDF	$N_{1,i}$	m_i	$\sigma_{1,i}$
0	1.25	4360 ± 93	2.28686 ± 0.00010	0.00376 ± 0.00009
1	0.80	5178 ± 95	2.28715 ± 0.00008	0.00358 ± 0.00008
2	0.97	6162 ± 101	2.28729 ± 0.00008	0.00369 ± 0.00007
3	1.44	7075 ± 102	2.28720 ± 0.00007	0.00361 ± 0.00006
4	1.19	8290 ± 107	2.28731 ± 0.00006	0.00370 ± 0.00006
5	1.03	9432 ± 111	2.28737 ± 0.00006	0.00371 ± 0.00005
6	0.95	10218 ± 113	2.28728 ± 0.00005	0.00361 ± 0.00005
7	1.01	11384 ± 116	2.28737 ± 0.00005	0.00361 ± 0.00004
8	1.40	12528 ± 119	2.28735 ± 0.00004	0.00359 ± 0.00004
9	0.81	13903 ± 119	2.28734 ± 0.00004	0.00352 ± 0.00004
bin		$N_{b1,i}$	$N_{b2,i}$	common par.
0		6621 ± 395	89344 ± 547	$m_b = 2.2480 \pm 0.0004$
1		6346 ± 391	90936 ± 543	$w_b = 0.0039 \pm 0.0004$
2		6532 ± 393	90686 ± 549	$c_1 = -0.181 \pm 0.006$
3		6824 ± 399	91870 ± 554	$c_2 = 0.003 \pm 0.004$
4		6690 ± 408	94171 ± 565	
5		7664 ± 413	94785 ± 571	
6		6800 ± 413	97816 ± 573	
7		7003 ± 417	99285 ± 578	
8		6788 ± 414	98136 ± 575	
9		7115 ± 392	91057 ± 546	

Table 23: Values of parameters obtained from the Λ_c^+ MC simulation fit.

bin	χ^2/NDF	$N_{1,i}$	m_i	$\sigma_{1,i}$
0	1.23	4294 ± 90	2.28726 ± 0.00010	0.00361 ± 0.00009
1	1.21	5223 ± 94	2.28723 ± 0.00009	0.00372 ± 0.00008
2	0.81	5974 ± 96	2.28727 ± 0.00007	0.00360 ± 0.00007
3	0.77	6976 ± 100	2.28727 ± 0.00007	0.00364 ± 0.00006
4	0.99	8100 ± 105	2.28731 ± 0.00006	0.00374 ± 0.00006
5	0.83	9275 ± 109	2.28737 ± 0.00006	0.00380 ± 0.00005
6	1.04	9983 ± 111	2.28734 ± 0.00005	0.00372 ± 0.00005
7	1.00	11131 ± 113	2.28731 ± 0.00005	0.00358 ± 0.00004
8	1.33	12521 ± 116	2.28731 ± 0.00004	0.00358 ± 0.00004
9	1.19	13500 ± 116	2.28741 ± 0.00004	0.00350 ± 0.00003
bin		$N_{b1,i}$	$N_{b2,i}$	common par.
0		5878 ± 351	84887 ± 502	$m_b = 2.2464 \pm 0.0003$
1		5708 ± 355	85910 ± 509	$w_b = 0.0033 \pm 0.0004$
2		6121 ± 359	86677 ± 512	$c_1 = -0.190 \pm 0.006$
3		5901 ± 357	87610 ± 512	$c_2 = 0.011 \pm 0.003$
4		6394 ± 367	88919 ± 524	
5		7005 ± 376	89806 ± 536	
6		6694 ± 374	91507 ± 534	
7		5823 ± 375	94872 ± 537	
8		6183 ± 369	92100 ± 529	
9		6196 ± 354	85795 ± 508	

Table 24: Values of parameters obtained from the $\overline{\Lambda}_c^-$ MC simulation fit.

bin	χ^2/NDF	$N_{1,i}$	m_i	$\sigma_{1,i}$
0	1.25	4004 ± 86	2.28732 ± 0.00012	0.00448 ± 0.00011
1	1.16	4960 ± 89	2.28745 ± 0.00010	0.00429 ± 0.00009
2	0.99	6162 ± 95	2.28741 ± 0.00009	0.00449 ± 0.00008
3	0.91	7544 ± 100	2.28773 ± 0.00007	0.00452 ± 0.00007
4	1.03	8778 ± 103	2.28766 ± 0.00007	0.00462 ± 0.00006
5	1.23	9927 ± 107	2.28769 ± 0.00006	0.00445 ± 0.00006
6	1.09	11034 ± 110	2.28775 ± 0.00006	0.00442 ± 0.00005
7	1.16	12730 ± 116	2.28774 ± 0.00005	0.00440 ± 0.00005
8	1.03	14261 ± 119	2.28775 ± 0.00005	0.00437 ± 0.00004
9	1.44	15866 ± 121	2.28786 ± 0.00004	0.00426 ± 0.00004
bin		$N_{b1,i}$	$N_{b2,i}$	common par.
0		9905 ± 328	56644 ± 447	$m_b = 2.2481 \pm 0.0002$
1		9796 ± 333	54898 ± 454	$w_b = 0.0035 \pm 0.0002$
2		10133 ± 326	54390 ± 452	$c_1 = -0.196 \pm 0.009$
3		10356 ± 328	53934 ± 447	$c_2 = -0.005 \pm 0.005$
4		10525 ± 330	54182 ± 453	
5		10411 ± 338	55662 ± 461	
6		9602 ± 346	57774 ± 475	
7		10492 ± 352	57970 ± 492	
8		9845 ± 350	58971 ± 483	
9		10572 ± 337	55564 ± 467	

Table 25: Values of parameters obtained from the Λ_c fit on real data.

bin	χ^2/NDF	$N_{1,i}$	m_i	$\sigma_{1,i}$
0	1.15	2065 ± 62	2.28786 ± 0.00017	0.00454 ± 0.00016
1	1.07	2538 ± 61	2.28777 ± 0.00013	0.00416 ± 0.00011
2	1.19	3141 ± 66	2.28768 ± 0.00012	0.00442 ± 0.00011
3	0.94	3827 ± 70	2.28783 ± 0.00010	0.00449 ± 0.00010
4	0.89	4487 ± 73	2.28802 ± 0.00010	0.00461 ± 0.00009
5	1.07	5042 ± 76	2.28802 ± 0.00009	0.00446 ± 0.00008
6	1.24	5624 ± 78	2.28814 ± 0.00008	0.00436 ± 0.00007
7	1.11	6514 ± 82	2.28808 ± 0.00007	0.00437 ± 0.00006
8	1.09	7227 ± 84	2.28800 ± 0.00007	0.00430 ± 0.00006
9	1.42	8091 ± 85	2.28813 ± 0.00006	0.00409 ± 0.00005
bin		$N_{b1,i}$	$N_{b2,i}$	common par.
0		5085 ± 200	29068 ± 293	$c_1 = -0.190 \pm 0.009$ $c_2 = -0.003 \pm 0.006$
1		5056 ± 196	28191 ± 284	
2		5354 ± 196	27976 ± 288	
3		5205 ± 198	28257 ± 292	
4		5512 ± 197	27735 ± 291	
5		5492 ± 201	28693 ± 296	
6		4983 ± 205	30000 ± 302	
7		5252 ± 207	30213 ± 305	
8		4875 ± 209	30975 ± 309	
9		5420 ± 203	29103 ± 296	

Table 26: Values of parameters obtained from the Λ_c^+ fit on real data.

bin	χ^2/NDF	$N_{1,i}$	m_i	$\sigma_{1,i}$
0	1.03	1914 ± 51	2.28680 ± 0.00017	0.00438 ± 0.00012
1	1.02	2398 ± 57	2.28707 ± 0.00014	0.00443 ± 0.00010
2	0.62	2979 ± 68	2.28713 ± 0.00012	0.00455 ± 0.00012
3	1.29	3658 ± 71	2.28761 ± 0.00011	0.00454 ± 0.00010
4	0.96	4230 ± 74	2.28730 ± 0.00010	0.00463 ± 0.00009
5	1.24	4832 ± 78	2.28734 ± 0.00009	0.00443 ± 0.00009
6	0.99	5339 ± 79	2.28733 ± 0.00008	0.00445 ± 0.00007
7	1.14	6139 ± 85	2.28736 ± 0.00007	0.00441 ± 0.00007
8	1.07	6940 ± 87	2.28749 ± 0.00007	0.00443 ± 0.00007
9	1.16	7691 ± 89	2.28753 ± 0.00006	0.00445 ± 0.00006
bin		$N_{b1,i}$	$N_{b2,i}$	common par.
0		4932 ± 343	27019 ± 405	$m_b = 2.2477 \pm 0.0003$
1		4832 ± 351	26115 ± 413	$w_b = 0.0036 \pm 0.0005$
2		4839 ± 348	25823 ± 426	$c_1 = -0.191 \pm 0.022$
3		5216 ± 337	25102 ± 414	$c_2 = -0.016 \pm 0.010$
4		5102 ± 341	25806 ± 421	
5		4998 ± 363	26324 ± 449	
6		4708 ± 370	27207 ± 450	
7		5353 ± 383	27165 ± 474	
8		5069 ± 378	27434 ± 467	
9		5280 ± 370	25880 ± 462	

Table 27: Values of parameters obtained from the $\overline{\Lambda}_c^-$ fit on real data.

B

DERIVATIONS OF COVARIANCE MATRICES AND ERRORS

In this appendix, we give the derivations of covariance matrices and errors of the efficiency corrected deconvoluted numbers of events used in the fits which determine the $\langle\alpha\rangle$ and \mathcal{A}_{CP} .

B.1 ERROR PROPAGATION

We have n quantities $\vec{\theta} = (\theta_1, \dots, \theta_n)$, and m functions $\vec{\eta}(\vec{\theta}) = (\eta_1(\vec{\theta}), \dots, \eta_m(\vec{\theta}))$. We know the estimated values $\hat{\vec{\theta}} = (\hat{\theta}_1, \dots, \hat{\theta}_n)$ and the covariance matrix $V_{ij} = \text{cov}[\hat{\theta}_i, \hat{\theta}_j]$.

The goal of error propagation is to determine the covariance matrix for the functions $\vec{\eta}(\vec{\theta})$, $U_{ij} = \text{cov}[\hat{\eta}_i, \hat{\eta}_j]$, where $\hat{\eta}_i = \eta_i(\hat{\vec{\theta}})$.

We can find U_{ij} by expanding the functions $\vec{\eta}(\vec{\theta})$ about the estimates $\hat{\vec{\theta}}$ to the first order in a Taylor series:

$$U_{ij} \approx \sum_k \sum_l \frac{\partial \eta_i}{\partial \theta_k} \frac{\partial \eta_j}{\partial \theta_l} \Big|_{\hat{\vec{\theta}}} V_{kl}. \quad (203)$$

Or in matrix notation:

$$U \approx A V A^T, \quad A_{ij} = \frac{\partial \eta_i}{\partial \theta_j} \Big|_{\hat{\vec{\theta}}}. \quad (204)$$

This approximation is exact if $\vec{\eta}(\vec{\theta})$ is linear, and can break down if it is significantly nonlinear close to $\hat{\vec{\theta}}$ in a region of a size comparable to the standard deviation of $\hat{\vec{\theta}}$.

B.2 COVARIANCE MATRIX FOR THE $\langle\alpha\rangle$ FIT

We fit the quantities

$$T_i = \frac{G_i}{\langle\varepsilon\rangle_i} = \frac{\sum_c q_{ic} R_c}{\langle\varepsilon\rangle_i}, \quad (205)$$

so we form the vector $\vec{\theta}$ out of:

- 10 quantities R_i with an error of σ_{R_i} , defined in (87) and the correlation matrix R_{ij} ,

- 10 quantities $\langle \varepsilon \rangle_i$ with an error of $\sigma_{\langle \varepsilon \rangle_i}$, defined in (99) which are not correlated, so the correlation matrix is δ_{ij} ,
- 100 quantities q_{ij} with an error of $\sigma_{q_{ij}}$, defined in (97) which are not correlated, so the correlation matrix is $Q_{ia,jb} = \delta_{ij}\delta_{ab}$.

We also know that R_i , $\langle \varepsilon \rangle_i$, and q_{ij} are uncorrelated.

The vector $\vec{\theta}$ is therefore:

$$\vec{\theta} = (R_1, \dots, R_{10}, \langle \varepsilon \rangle_1, \dots, \langle \varepsilon \rangle_{10}, q_{00}, \dots, q_{09}, q_{10}, \dots, q_{19}, \dots, q_{90}, \dots, q_{99}), \quad (206)$$

and the covariance matrix for these quantities is

$$V_{ij} = \begin{bmatrix} R_{ij}\sigma_{R_i}\sigma_{R_j} & \emptyset & \emptyset \\ \emptyset & \delta_{ij}\sigma_{\langle \varepsilon \rangle_i}\sigma_{\langle \varepsilon \rangle_j} & \emptyset \\ \emptyset & \emptyset & \delta_{ij}\delta_{ab}\sigma_{q_{ia}}\sigma_{q_{ib}} \end{bmatrix}. \quad (207)$$

According to (203), we calculate the covariance matrix for T_i as follows:

$$\begin{aligned} U_{ij} &= \sum_k \sum_l \left(\frac{\partial T_i}{\partial \theta_k} \right) \left(\frac{\partial T_j}{\partial \theta_l} \right) V_{kl} = \\ &= \sum_k \sum_l \left(\frac{\partial T_i}{\partial R_k} \right) \left(\frac{\partial T_j}{\partial R_l} \right) R_{kl}\sigma_{R_k}\sigma_{R_l} + \\ &\quad + \sum_k \sum_l \left(\frac{\partial T_i}{\partial \langle \varepsilon \rangle_k} \right) \left(\frac{\partial T_j}{\partial \langle \varepsilon \rangle_l} \right) \delta_{kl}\sigma_{\langle \varepsilon \rangle_k}\sigma_{\langle \varepsilon \rangle_l} + \\ &\quad + \sum_k \sum_l \sum_a \sum_b \left(\frac{\partial T_i}{\partial q_{ka}} \right) \left(\frac{\partial T_j}{\partial q_{lb}} \right) \delta_{kl}\delta_{ab}\sigma_{q_{ka}}\sigma_{q_{lb}}. \end{aligned} \quad (208)$$

We calculate the derivatives:

$$\begin{aligned} \frac{\partial T_i}{\partial R_k} &= \frac{\partial}{\partial R_k} \left(\frac{\sum_c q_{ic}R_c}{\langle \varepsilon \rangle_i} \right) = \frac{\delta_{ck}q_{ic}}{\langle \varepsilon \rangle_i}, \\ \frac{\partial T_i}{\partial \langle \varepsilon \rangle_k} &= \frac{\partial}{\partial \langle \varepsilon \rangle_k} \left(\frac{\sum_c q_{ic}R_c}{\langle \varepsilon \rangle_i} \right) = \frac{\delta_{ik}\sum_c q_{ic}R_c}{-\langle \varepsilon \rangle_i^2} = -\frac{\delta_{ik}G_i}{\langle \varepsilon \rangle_i^2}, \\ \frac{\partial T_i}{\partial q_{ka}} &= \frac{\partial}{\partial q_{ka}} \left(\frac{\sum_c q_{ic}R_c}{\langle \varepsilon \rangle_i} \right) = \delta_{ik}\delta_{ac}\frac{R_c}{\langle \varepsilon \rangle_i}. \end{aligned} \quad (209)$$

We put the derivatives into (208):

$$\begin{aligned}
 U_{ij} &= \sum_k \sum_l \frac{\delta_{ck} q_{ic}}{\langle \varepsilon \rangle_i} \frac{\delta_{dl} q_{jd}}{\langle \varepsilon \rangle_j} R_{kl} \sigma_{R_k} \sigma_{R_l} + \sum_k \sum_l \frac{\delta_{ik} G_i}{-\langle \varepsilon \rangle_i^2} \frac{\delta_{jl} G_j}{-\langle \varepsilon \rangle_j^2} \delta_{kl} \sigma_{\langle \varepsilon \rangle_k} \sigma_{\langle \varepsilon \rangle_l} + \\
 &+ \sum_k \sum_l \sum_a \sum_b \frac{\delta_{ik} \delta_{ac} R_c}{\langle \varepsilon \rangle_i} \frac{\delta_{jl} \delta_{bd} R_d}{\langle \varepsilon \rangle_j} \delta_{kl} \delta_{ab} \sigma_{q_{ka}} \sigma_{q_{lb}} = \\
 &= \sum_k \sum_l \frac{q_{ik} q_{jl}}{\langle \varepsilon \rangle_i \langle \varepsilon \rangle_j} R_{kl} \sigma_{R_k} \sigma_{R_l} + \frac{G_i G_j}{\langle \varepsilon \rangle_i^2 \langle \varepsilon \rangle_j^2} \delta_{ij} \sigma_{\langle \varepsilon \rangle_i} \sigma_{\langle \varepsilon \rangle_j} + \delta_{ij} \sum_a \frac{R_a^2 \sigma_{q_{ia}} \sigma_{q_{ja}}}{\langle \varepsilon \rangle_i \langle \varepsilon \rangle_j} + \\
 &= T_i T_j \left(\frac{\sum_k \sum_l q_{ik} q_{jl} R_{kl} \sigma_{R_k} \sigma_{R_l}}{G_i G_j} + \delta_{ij} \frac{\sum_k R_k^2 \sigma_{q_{ik}} \sigma_{q_{jk}}}{G_i G_j} + \delta_{ij} \frac{\sigma_{\langle \varepsilon \rangle_i} \sigma_{\langle \varepsilon \rangle_j}}{\langle \varepsilon \rangle_i \langle \varepsilon \rangle_j} \right). \tag{210}
 \end{aligned}$$

With this, we have derived the equation (104).

B.3 ERROR FOR THE $\langle \alpha \rangle$ FIT

Errors are defined as the square of the variance, so we just need the diagonal elements of the covariance matrix (210):

$$\begin{aligned}
 \sigma_{T_i}^2 &= U_{ii} = \\
 &= T_i^2 \left(\frac{\sum_k \sum_l q_{ik} q_{il} R_{kl} \sigma_{R_k} \sigma_{R_l}}{G_i^2} + \frac{\sigma_{\langle \varepsilon \rangle_i}^2}{\langle \varepsilon \rangle_i^2} + \frac{\sum_k R_k^2 \sigma_{q_{ik}}^2}{G_i^2} \right). \tag{211}
 \end{aligned}$$

To get the error on G_i , we just use equations (102) and (100) to get:

$$\sigma_{G_i}^2 = \sum_k \sum_l q_{ik} q_{il} R_{kl} \sigma_{R_k} \sigma_{R_l} + \sum_k R_k^2 \sigma_{q_{ik}}^2. \tag{212}$$

which is the equation (96).

B.4 ERROR ON THE DECONVOLUTION MATRIX ELEMENT

The error on the deconvolution matrix element $\sigma_{q_{ij}}$ can be expressed with the numbers of events in bins of the resolution map M_{ij} in the following way. We know that the deconvolution matrix is an inverse of the convolution matrix. If we know the error on the convolution matrix, the error on its inverse can be calculated as [39]:

$$\sigma_{q_{ij}}^2 = \sum_a \sum_b q_{ia}^2 \sigma_{p_{ab}}^2 q_{bj}^2. \tag{213}$$

We know that the the element of the convolution matrix P is calculated from the resolution map as:

$$p_{ab} = \frac{M_{ab}}{\sum_c N_{cb}}. \tag{214}$$

The M_{ij} are uncorrelated, so the error on p_{ab} is calculated as:

$$\sigma_{p_{ab}}^2 = \sum_d \left(\frac{\partial p_{ab}}{\partial M_{db}} \right)^2 \sigma_{M_{db}}^2. \quad (215)$$

For the error on M_{db} we can just take the square root of M_{db} as this is a statistical error:

$$\sigma_{M_{db}}^2 = M_{db}. \quad (216)$$

We also need to calculate the derivative:

$$\frac{\partial p_{ab}}{\partial M_{db}} = \begin{cases} -\frac{M_{ab}}{(\sum_c M_{cb})^2} & d \neq a, \\ \frac{\sum_{c \neq a} M_{cb}}{(\sum_c M_{cb})^2} & d = a. \end{cases} \quad (217)$$

We can now put (217) and (216) into (214), and get:

$$\begin{aligned} \sigma_{p_{ab}}^2 &= \sum_{d \neq a} \left(-\frac{M_{ab}}{(\sum_c M_{cb})^2} \right)^2 M_{db} + \left(\frac{\sum_{c \neq a} M_{cb}}{(\sum_c M_{cb})^2} \right)^2 M_{ab} = \\ &= \frac{M_{ab}^2}{(\sum_c M_{cb})^4} \sum_{d \neq a} M_{db} + \frac{(\sum_{c \neq a} M_{cb})^2}{(\sum_c M_{cb})^4} M_{ab} = \\ &= \frac{M_{ab}(\sum_{c \neq a} M_{cb})(M_{ab} + \sum_{c \neq a} M_{cb})}{(\sum_c M_{cb})^4} = \\ &= \frac{M_{ab}(\sum_{c \neq a} M_{cb})(\sum_c M_{cb})}{(\sum_c M_{cb})^4} = \frac{M_{ab}(\sum_{c \neq a} M_{cb})}{(\sum_c M_{cb})^3}. \end{aligned} \quad (218)$$

If we put this result into equation (213), we come to the equation (97).

B.5 COVARIANCE MATRIX FOR THE \mathcal{A}_{CP} FIT

We fit the quantities:

$$\mathcal{A}_{\text{rec}}^i = \frac{G_i - \bar{G}_i}{G_i + \bar{G}_i} = \frac{\sum_j q_{ij} R_j - \sum_j q_{ij} \bar{R}_j}{\sum_j q_{ij} R_j + \sum_j q_{ij} \bar{R}_j}, \quad (219)$$

so we form the vector $\vec{\theta}$ out of:

- 10 quantities R_i with an error of σ_{R_i} , defined in (106) and the correlation matrix R_{ij} ,
- 10 quantities \bar{R}_i with an error of $\sigma_{\bar{R}_i}$, defined in (106) and the correlation matrix \bar{R}_{ij} ,
- 100 quantities q_{ij} with an error of $\sigma_{q_{ij}}$, defined in (97), which are not correlated, so the correlation matrix is $Q_{ia,jb} = \delta_{ij} \delta_{ab}$.

We also know that R_i , \bar{R}_i , and q_{ij} are uncorrelated. The vector $\vec{\theta}$ is therefore:

$$\vec{\theta} = (R_1, \dots, R_{10}, \bar{R}_1, \dots, \bar{R}_{10}, q_{00}, \dots, q_{09}, q_{10}, \dots, q_{19}, \dots, q_{90}, \dots, q_{99}), \quad (220)$$

and the covariance matrix for these quantities is

$$V_{ij} = \begin{bmatrix} R_{ij} \sigma_{R_i} \sigma_{R_j} & \emptyset & \emptyset \\ \emptyset & \bar{R}_{ij} \sigma_{\bar{R}_i} \sigma_{\bar{R}_j} & \emptyset \\ \emptyset & \emptyset & \delta_{ij} \delta_{ab} \sigma_{q_{ia}} \sigma_{q_{ib}} \end{bmatrix}. \quad (221)$$

According to (203), we calculate the covariance matrix for $\mathcal{A}_{\text{rec}}^i$ as follows:

$$\begin{aligned} U_{ij} &= \sum_k \sum_l \left(\frac{\partial \mathcal{A}_{\text{rec}}^i}{\partial \theta_k} \right) \left(\frac{\partial \mathcal{A}_{\text{rec}}^j}{\partial \theta_l} \right) V_{kl} = \\ &= \sum_k \sum_l \left(\frac{\partial \mathcal{A}_{\text{rec}}^i}{\partial R_k} \right) \left(\frac{\partial \mathcal{A}_{\text{rec}}^j}{\partial R_l} \right) R_{kl} \sigma_{R_k} \sigma_{R_l} + \\ &\quad + \sum_k \sum_l \left(\frac{\partial \mathcal{A}_{\text{rec}}^i}{\partial \bar{R}_k} \right) \left(\frac{\partial \mathcal{A}_{\text{rec}}^j}{\partial \bar{R}_l} \right) \bar{R}_{kl} \sigma_{\bar{R}_k} \sigma_{\bar{R}_l} + \\ &\quad + \sum_k \sum_l \sum_a \sum_b \left(\frac{\partial \mathcal{A}_{\text{rec}}^i}{\partial q_{ka}} \right) \left(\frac{\partial \mathcal{A}_{\text{rec}}^j}{\partial q_{lb}} \right) \delta_{kl} \delta_{ab} \sigma_{q_{ka}} \sigma_{q_{lb}}. \end{aligned} \quad (222)$$

We calculate the derivatives:

$$\begin{aligned} \frac{\partial \mathcal{A}_{\text{rec}}^i}{\partial R_k} &= \frac{\partial}{\partial R_k} \left(\frac{\sum_c q_{ic} R_c - \sum_c q_{ic} \bar{R}_c}{\sum_c q_{ic} R_c + \sum_c q_{ic} \bar{R}_c} \right) = \\ &= \delta_{dk} q_{id} \frac{2 \sum_c q_{ic} \bar{R}_c}{(\sum_c q_{ic} R_c + \sum_c q_{ic} \bar{R}_c)^2} = 2 \delta_{dk} q_{id} \frac{\bar{G}_i}{(G_i + \bar{G}_i)^2}, \quad (223) \\ \frac{\partial \mathcal{A}_{\text{rec}}^i}{\partial \bar{R}_k} &= \frac{\partial}{\partial \bar{R}_k} \left(\frac{\sum_c q_{ic} R_c - \sum_c q_{ic} \bar{R}_c}{\sum_c q_{ic} R_c + \sum_c q_{ic} \bar{R}_c} \right) = \\ &= \delta_{dk} q_{id} \frac{-2 \sum_c q_{ic} R_c}{(\sum_c q_{ic} R_c + \sum_c q_{ic} \bar{R}_c)^2} = -2 \delta_{dk} q_{id} \frac{G_i}{(G_i + \bar{G}_i)^2}, \\ \frac{\partial \mathcal{A}_{\text{rec}}^i}{\partial q_{ka}} &= \frac{\partial}{\partial q_{ka}} \left(\frac{\sum_c q_{ic} R_c - \sum_c q_{ic} \bar{R}_c}{\sum_c q_{ic} R_c + \sum_c q_{ic} \bar{R}_c} \right) = \\ &= 2 \delta_{ik} \delta_{ad} \frac{R_d \sum_c q_{ic} \bar{R}_c - \bar{R}_d \sum_c q_{ic} R_c}{(\sum_c q_{ic} R_c + \sum_c q_{ic} \bar{R}_c)^2} = \\ &= 2 \delta_{ik} \delta_{ad} \frac{R_d \bar{G}_i - \bar{R}_d G_i}{(G_i + \bar{G}_i)^2}. \end{aligned}$$

We put the derivatives into (222):

$$\begin{aligned}
U_{ij} &= \sum_k \sum_l \frac{2\delta_{dk}q_{id}\bar{G}_i}{(G_i + \bar{G}_i)^2} \frac{2\delta_{ek}q_{je}\bar{G}_j}{(G_j + \bar{G}_j)^2} R_{kl}\sigma_{R_k}\sigma_{R_l} + \\
&+ \sum_k \sum_l \frac{-2\delta_{dk}q_{id}G_i}{(G_i + \bar{G}_i)^2} \frac{-2\delta_{ek}q_{je}G_j}{(G_j + \bar{G}_j)^2} \bar{R}_{kl}\sigma_{\bar{R}_k}\sigma_{\bar{R}_l} + \\
&+ \sum_k \sum_l \sum_a \sum_b \left(\frac{2\delta_{ik}\delta_{ad}(R_d\bar{G}_i - \bar{R}_dG_i)}{(G_i + \bar{G}_i)^2} \right. \\
&\quad \left. \frac{2\delta_{jl}\delta_{be}(R_e\bar{G}_j - \bar{R}_eG_j)}{(G_j + \bar{G}_j)^2} \delta_{kl}\delta_{ab}\sigma_{q_{ka}}\sigma_{q_{kb}} \right) = \\
&= \frac{4}{(G_i + \bar{G}_i)^2(G_j + \bar{G}_j)^2} \left(\bar{G}_i\bar{G}_j \sum_k \sum_l q_{ik}q_{jl}R_{kl}\sigma_{R_k}\sigma_{R_l} + \right. \\
&\quad + G_iG_j \sum_k \sum_l q_{ik}q_{jl}\bar{R}_{kl}\sigma_{\bar{R}_k}\sigma_{\bar{R}_l} + \\
&\quad \left. + \delta_{ij} \sum_k (R_k\bar{G}_i - \bar{R}_kG_i)(R_k\bar{G}_j - \bar{R}_kG_j)\sigma_{q_{ik}}\sigma_{q_{jk}} \right). \tag{224}
\end{aligned}$$

With this, we have derived the equation (112).

B.6 ERROR ON THE \mathcal{A}_{CP} FIT

Errors are defined as the square of the variance, so we just need the diagonal elements of the covariance matrix (224):

$$\begin{aligned}
\sigma_{\mathcal{A}_{rec}}^2 &= U_{ii} = \\
&= \frac{4}{(G_i + \bar{G}_i)^4} \left(\bar{G}_i^2 \sum_k \sum_l q_{ik}q_{il}R_{kl}\sigma_{R_k}\sigma_{R_l} + \right. \\
&\quad \left. + G_i^2 \sum_k \sum_l q_{ik}q_{il}\bar{R}_{kl}\sigma_{\bar{R}_k}\sigma_{\bar{R}_l} + \sum_k (R_k\bar{G}_i - \bar{R}_kG_i)^2\sigma_{q_{ik}}^2 \right). \tag{225}
\end{aligned}$$

With this, we have come to the equation (110).

BIBLIOGRAPHY

- [1] J. Beringer et al. Review of Particle Physics (RPP). *Phys.Rev.*, D86:010001, 2012. (Cited on pages [vii](#), [ix](#), [15](#), [17](#), [39](#), [43](#), [45](#), [46](#), [66](#), [82](#), [84](#), [91](#), [97](#), [105](#), [110](#), [111](#), [125](#), [126](#), and [129](#).)
- [2] S.L. Glashow. Partial Symmetries of Weak Interactions. *Nucl.Phys.*, 22:579–588, 1961. (Cited on pages [1](#) and [99](#).)
- [3] A. Salam and J. C. Ward. Electromagnetic and weak interactions. *Phys.Lett.*, 13:168–171, 1964. (Cited on pages [1](#) and [99](#).)
- [4] S. Weinberg. A Model of Leptons. *Phys.Rev.Lett.*, 19:1264–1266, 1967. (Cited on pages [1](#) and [99](#).)
- [5] P. W. Higgs. Broken symmetries, massless particles and gauge fields. *Phys.Lett.*, 12:132–133, 1964. (Cited on page [1](#).)
- [6] E. Noether. Invariant Variation Problems. *Gott.Nachr.*, 1918:235–257, 1918. (Cited on pages [1](#) and [99](#).)
- [7] E.C. Zeeman. Causality implies the Lorentz group. *J. Math. Phys.*, 5:490–493, 1964. (Cited on page [1](#).)
- [8] S. Chatrchyan et al. Observation of a new boson at a mass of 125 GeV with the CMS experiment at the LHC. *Phys. Lett. B*, 716(1):30–61, 2012. (Cited on pages [3](#) and [100](#).)
- [9] G. Aad et al. Observation of a new particle in the search for the Standard Model Higgs boson with the ATLAS detector at the LHC. *Phys. Lett. B*, 716(1):1–29, 2012. (Cited on pages [3](#) and [100](#).)
- [10] J.H. Christenson, J.W. Cronin, V.L. Fitch, and R. Turlay. Evidence for the 2π Decay of the K^0 Meson. *Phys.Rev.Lett.*, 13:138–140, 1964. (Cited on pages [4](#) and [100](#).)
- [11] Y. Amhis et al. Averages of b-hadron, c-hadron, and tau-lepton properties as of early 2012. 2012. (Cited on pages [4](#) and [101](#).)
- [12] G. Luders. On the Equivalence of Invariance under Time Reversal and under Particle-Antiparticle Conjugation for Relativistic Field Theories. *Kong.Dan.Vid.Sel.Mat.Fys.Med.*, 28N5:1–17, 1954. (Cited on pages [4](#) and [101](#).)
- [13] O.W. Greenberg. CPT violation implies violation of Lorentz invariance. *Phys.Rev.Lett.*, 89:231602, 2002. (Cited on pages [4](#) and [101](#).)
- [14] A.D. Sakharov. Violation of CP Invariance, C Asymmetry, and Baryon Asymmetry of the Universe. *Pisma Zh.Eksp.Teor.Fiz.*, 5:32–35, 1967. (Cited on pages [4](#) and [101](#).)

- [15] S. Dimopoulos and L. Susskind. Baryon number of the universe. *Phys. Rev. D*, 18:4500–4509, 1978. (Cited on pages 4 and 101.)
- [16] E. Komatsu et al. Seven-Year Wilkinson Microwave Anisotropy Probe (WMAP) Observations: Cosmological Interpretation. *Astrophys.J.Suppl.*, 192:18, 2011. (Cited on pages 4 and 101.)
- [17] Y. Nir. Flavour physics and CP violation. 2010. (Cited on page 5.)
- [18] Z. Ligeti. Introduction to heavy meson decays and CP asymmetries. *eConf, Co20805:Lo2*, 2002. (Cited on page 5.)
- [19] M. Dine. TASI lectures on the strong CP problem. pages 349–369, 2000. (Cited on page 6.)
- [20] L. Wolfenstein. Parametrization of the Kobayashi-Maskawa Matrix. *Phys.Rev.Lett.*, 51:1945, 1983. (Cited on page 7.)
- [21] B.T. Cleveland, T. Daily, Jr. Davis, R., J.R. Distel, K. Lande, et al. Measurement of the solar electron neutrino flux with the Homestake chlorine detector. *Astrophys.J.*, 496:505–526, 1998. (Cited on page 8.)
- [22] W. Koch. Determination of the Ξ decay parameters. In (Ed.) Lock, W.O., (Ed.) Nikolic, M., and (Ed.) Van Hove, L., editors, *1964 Easter school for physicists using the CERN proton synchrotron, Herceg-Novi, Yugoslavia, 18-31 May 1964: Proceedings. 2.*, pages 75–112. CERN, 1964. (Cited on pages 10 and 104.)
- [23] K.K. Sharma and R.C. Verma. A Study of weak mesonic decays of Λ_c and Ξ_c baryons on the basis of HQET results. *Eur.Phys.J.*, C7:217–224, 1999. (Cited on page 11.)
- [24] S. Kurokawa and E. Kikutani. Overview of the KEKB accelerators. *Nucl.Instrum.Meth.*, A499:1–7, 2003. (Cited on pages 15, 16, 104, and 105.)
- [25] A. Abashian, K. Gotow, N. Morgan, L. Piilonen, S. Schrenk, et al. The Belle Detector. *Nucl.Instrum.Meth.*, A479:117–232, 2002. (Cited on pages 15, 16, 18, 19, 20, 21, 22, 23, 24, 25, 26, 27, 28, 29, 30, 31, 32, 34, 37, 38, 48, 104, and 106.)
- [26] Z. Natkaniec, H. Aihara, Y. Asano, T. Aso, A. Bakich, et al. Status of the Belle silicon vertex detector. *Nucl.Instrum.Meth.*, A560:1–4, 2006. (Cited on pages 15, 20, and 104.)
- [27] URL http://belle.kek.jp/bdocs/lumi_belle.png. (Cited on page 18.)
- [28] K. Hanagaki, H. Kakuno, H. Ikeda, T. Iijima, and T. Tsukamoto. Electron identification in Belle. *Nucl.Instrum.Meth.*, A485:490–503, 2002. (Cited on page 37.)
- [29] A. Abashian, K. Abe, K. Abe, P.K. Behera, F. Handa, et al. Muon identification in the Belle experiment at KEKB. *Nucl.Instrum.Meth.*, A491:69–82, 2002. (Cited on page 38.)

- [30] D.J. Lange. The EvtGen particle decay simulation package. *Nucl.Instrum.Meth.*, A462:152–155, 2001. (Cited on page 39.)
- [31] T. Sjostrand. High-energy physics event generation with PYTHIA 5.7 and JETSET 7.4. *Comput.Phys.Commun.*, 82:74–90, 1994. (Cited on page 39.)
- [32] B. Andersson, G. Gustafson, G. Ingelman, and T. Sjostrand. Parton Fragmentation and String Dynamics. *Phys.Rept.*, 97:31–145, 1983. (Cited on page 39.)
- [33] R. Brun, F. Bruyant, M. Maire, A.C. McPherson, and P. Zancarini. GEANT3. 1987. (Cited on page 39.)
- [34] J.M. Link et al. Study of the decay asymmetry parameter and CP violation parameter in the $\Lambda_c^+ \rightarrow \Lambda\pi^+$ decay. *Phys.Lett.*, B634:165–172, 2006. (Cited on pages 41, 52, 97, 113, and 129.)
- [35] B. Aubert et al. Search for CP violation in the decays $D^0 \rightarrow K^-K^+$ and $D^0 \rightarrow \pi^-\pi^+$. *Phys. Rev. Lett.*, 100:061803, 2008. (Cited on pages 45 and 110.)
- [36] O. E. Overseth and R. F. Roth. Time reversal invariance in Λ^0 decay. *Phys. Rev. Lett.*, 19:391–393, 1967. (Cited on page 46.)
- [37] P. D. Barnes et al. Observables in high-statistics measurements of the reaction $\bar{p}p \rightarrow \bar{\Lambda}\Lambda$. *Phys. Rev. C*, 54:1877–1886, 1996. (Cited on page 46.)
- [38] B. Bhuyan. High p_T tracking efficiency using partially reconstructed D^* decays. *Internal Belle note*, 1165. (Cited on pages 85 and 126.)
- [39] Lefebvre M., Keeler R.K., Sobie R., and White J. Propagation of errors for matrix inversion. *Nucl.Instrum.Meth.*, A451(2):520–528, 2000. (Cited on page 159.)

DEKLARACIJA

Izjavljam, da je disertacija rezultat mojega samostojnega raziskovalnega dela.

Ljubljana, 24. januar 2013

Peter Smerkol